



**UNIVERSITA' DEGLI STUDI DI NAPOLI FEDERICO II**  
**Scuola di Dottorato in Ingegneria dell'Informazione**  
**Dottorato di Ricerca in Ingegneria Informatica ed Automatica**



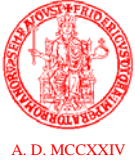
Comunità Europea  
Fondo Sociale Europeo

**Advanced measurement systems based on digital processing techniques  
for superconducting LHC magnets**

**Alessandro Masi**

**Tesi di Dottorato di Ricerca**

**Novembre 2005**



**UNIVERSITA' DEGLI STUDI DI NAPOLI FEDERICO II**  
**Scuola di Dottorato in Ingegneria dell'Informazione**  
**Dottorato di Ricerca in Ingegneria Informatica ed Automatica**



**Advanced measurement systems based on digital processing techniques  
for superconducting LHC magnets**

**Alessandro Masi**

**Tesi di Dottorato di Ricerca**

**(XVIII ciclo)**

**Novembre 2005**

**Il Tutore**

**Prof. Felice Cennamo**

**Il Coordinatore del Dottorato**

**Prof. Luigi Cordella**

**Il Co-Tutore**

**Dott. Ing. Luca Bottura**

**Dipartimento di Informatica e Sistemistica**

*To my parents*

## **ABSTRACT**

The Large Hadron Collider (LHC), a particle accelerator aimed at exploring deeper into matter than ever before, is currently being constructed at CERN. Beam optics of the LHC, requires stringent control of the field quality of about 8400 superconducting magnets, including 1232 main dipoles and 360 main quadrupoles to assure the correct machine operation. The measurement challenges are various: accuracy on the field strength measurement up to 50 ppm, harmonics in the ppm range, measurement equipment robustness, low measurement times to characterize fast field phenomena.

New magnetic measurement systems, principally based on analog solutions, were developed at CERN to achieve these goals. This work proposes the introduction of digital technologies to improve measurement performance of three systems, aimed at different measurement target and characterized by different accuracy levels.

The high accuracy measurement systems, based on rotating coils, exhibit high performance in static magnetic field. With varying magnetic field the system accuracy gets worse, independently from coil speed, due to the limited resolution of the digital integrator currently used, and the restrictions of the standard analysis. A new integrator based on ADC conversion and numerical integration is proposed. The experimental concept validation by emulating the proposed approach on a PXI platform is detailed along with the improvements with respect to the old integrators. Two new analysis

algorithms to reduce the errors in dynamic measurements are presented. The first combines quadrature detection and short time Fourier transform (STFT) of the acquired magnetic flux samples; the second approach is based on the extrapolation of the magnetic flux samples. Unlike other algorithms presented in the literature, both the proposals do not require the information about the magnet current and are able to work in real time so, can be easily implemented in firmware on DSP. The performance of the new proposals is assessed in simulation.

As far as medium accuracy systems are concerned, at CERN was originally developed a probe to measure the sextupolar and decapolar field harmonics of the superconducting dipoles using a suitable Hall plates arrangement for the bucking of the main dipolar field, which is, 4 orders of magnitude higher than the measurement target. The output signals of each Hall plate belonging to the same measurement ring are mixed using analog cards. The resultant signal is proportional to the field harmonic to measure. A complete metrological characterization of this sensor was carried out, showing the limitation of a fully analog solution. The main problems found were the instability of the analog compensation cards and the impossibility to correct the non linearity effects beyond the first order. An automatic calibration procedure implemented in the new instrument software is presented to guarantee measurement repeatability. In alternative a digital bucking solution, namely the compensation of the main field after the sampling of each hall plate signal by means of numerical sum, is proposed. An implementation of this approach, based on 18 bit ADC converter, over-sampling and dithering techniques as well as compensation of the Hall plates non linearity in real time is analyzed.

Finally, as far as the low accuracy measurement systems are concerned, the design of an instrument based on a rotating Hall plate to check the polarity of all LHC magnets is presented. Even if this architecture is characterized by low accuracy in the measurement of field strength and phase, the results are sufficient to identify main harmonic order, type and polarity with practically no errors, thanks to an accurate definition of the measurement algorithm. A complete metrological characterization of the prototype developed and a correction of all the systematic measurement errors was carried out. This instrument, integrated in a test bench developed ad hoc, is become the standard at CERN for the polarity test of all the magnets will compose the machine.

## **ACKNOWLEDGEMENTS**

First of all, I would like to express my sincere gratitude to Dr. Luca Bottura, my CERN supervisor, whom I admire professionally. His wise guide and supervision and his smart suggestions are the main ingredients for the good accomplishment of my PhD thesis. He will be always the model to imitate in my career. I would like to thank Dr. Marco Buzio, for his support and useful suggestions. I render thanks to all the MTM group, Dr. Juan Garcia Perez and Dr. Stephane Sanfilippo for their help and support. Nicholas Sammut and Tatiana Pieloni for their important inputs. In particular A. Tikov, the great Peter Galbraith and David Giloteaux that helped me patiently in all the experimental measurements.

I am extremely grateful to the Prof. Felice Cennamo, my University supervisor, that encouraged me to start the CERN experience; he is a great person and a great teacher. For me he is a teacher of life. Many thanks to the professors of the measurement group of the University of Naples and in particular to the Prof. Aldo Baccigalupi for the useful advisements and Prof. Leopoldo Angrisani for the profitable collaboration. A special thank to Rosario Schiano Lo Moriello for his important contribution to the simulating work, and to all the other “measurement friends” Mauro, Michele, Antonio, Nicola, Umberto and Annalisa.

At the last but not the least, I am obliged to Prof. Pasquale Arpaia of the University of Sannio for his precious contribution in the review of the present work. I have learned from him the importance of the “scientific excellence”. He was a professor of mine and now he is a great friend. I hope this is only the start of a long collaboration.

My sincere gratitude to my Master Degree thesis students Gabriele Greco and Pasquale Russiello that with their work gave an important part to the results presented in this work.

I cannot avoid to express my grateful to the Napolitan team of “Young Lions”: Giovanni, Pierluigi, Mario, Stefano and Vitaliano for their help in the final graphical revision of this work.

Special tanks to the friend that allowed enjoyable my stay in Geneve, Mirco and Chiara, Marco, my “socio” Stefano and Tatiana, Esther, Toni, Boris, Federico, Stefano Pauletta, Mirko Pojer and all the others.

My family has always been close to me and supported me since I left my beloved Napoli to come to Geneva. I want to sincerely thank Nicola (papa’), Angela (mamma), Adele. The motivation for me to make them proud of me is the main engine for all I do. All my relatives and, in particular, my grandmother Michela and zio Pino.

I cannot conclude this list without to express my appreciation for Roberto Losito, my current work supervisor, that was so comprehensive during the hard days of thesis writing, even in presence of a not negligible workload.

# Contents

Introduction.....	
Chapter I - The Large Hadron Collider .....	I-1
I.1 - The LHC Project .....	I-1
I.2 - Particle Circular Accelerators .....	I-3
I.3 - The LHC Dipole and Quadrupole Magnets .....	I-4
I.3.1 - The superconducting cables .....	I-5
I.4 - Multipoles and Field quality .....	I-7
I.5 - Harmonics tolerances from the beam dynamics .....	I-9
I.6 - Field error sources in LHC dipoles .....	I-9
I.6.1 - Static errors .....	I-10
I.6.2 - Dynamic errors.....	I-11
I.7 - Field Errors compensation in the LHC .....	I-13
I.8 - The reference magnetic system project.....	I-15
I.9 - References .....	I-18
Chapter II - State of the Art .....	II-1
II.1 - Outline .....	II-1
II.2 - HIGH ACCURACY SYSTEMS BASED ON ROTATING COILS .....	II-2
II.2.1 - The measurement principle: The Faraday-Lenz`s law .....	II-2
II.2.2 - Experimental Setup.....	II-6
II.2.3 - The new measurement requirements .....	II-11
II.2.4 - New integrators: State of the art .....	II-15
II.2.5 - New analysis algorithms: State of the art .....	II-18
II.3 - Systems based on fixed hall plates .....	II-19
II.3.1 - The measurement principle.....	II-20
II.3.2 - The measurement probe developed at CERN.....	II-24
II.3.3 - The measurement problem.....	II-27
II.4 - System based on rotating hall plates.....	II-28
II.5 - References.....	II-30

Chapter III - high accuracy systems:the numerical integrators .....	III-1
III.1 - Measurement problem .....	III-1
III.2 - Working principle of the proposed digital integrator .....	III-2
III.2.1 - System Resolution .....	III-3
III.2.2 - Offset and gain calibration .....	III-4
III.2.3 - Trigger uncertainty .....	III-4
III.2.4 - Integration noise .....	III-5
III.2.5 - Advantages .....	III-7
III.3 - Experimental validation.....	III-8
III.3.1 - Solution based on hardware interrupts for angular synchronization	III-9
III.3.2 - PXI Integrator Solution 1: Metrological Characterization .....	III-12
III.3.2 Solution based on encoder signal acquisition and rising edges detection	III
III.3.3 - Comparison with PDI integrators .....	III-22
III.4 - Architecture Overview .....	III-31
III.4.1 - The new integrators boards: general layout.....	III-32
III.4.2 - Measurement execution.....	III-41
III.4.3 - The prescaler board .....	III-42
III.4.4 - Consideration on the instrument bus and platform.....	III-44
III.5 - Preliminary test results of the new integrator boards analogic front-end	III-45
Chapter IV - Rotating coils system: the new measurement algorithms.....	IV-1
IV.1 - Introduction .....	IV-1
IV.2 - The standard analysis .....	IV-2
IV.3 - The rotating coil simulator .....	IV-5
IV.3.1 - The flux construction .....	IV-6
IV.3.2 - Current types .....	IV-8
IV.3.3 - Exponential current ramp.....	IV-8
IV.3.4 - Linear current ramp.....	IV-9
IV.3.5 - The software implementation.....	IV-9
IV.4 - Performance assessment of the standard analysis.....	IV-12
IV.4.1 - Parabolic current ramp .....	IV-14

IV.4.2 - Exponential current ramp .....	IV-15
IV.4.3 - Discussion of results.....	IV-16
IV.5 - The method based on the flux demodulation .....	IV-17
IV.5.1 - Demodulation of the main field harmonic .....	IV-17
IV.5.2 - The higher-order multipoles estimation by STFT .....	IV-20
IV.6 - The method based on the extrapolation and interpolation of magnetic flux samples.....	IV-22
IV.7 - Comparison of the different methods.....	IV-25
IV.7.1 - Linear current ramp .....	IV-26
IV.7.2 - Parabolic current ramp .....	IV-27
IV.7.3 - Exponential current ramp .....	IV-28
IV.7.4 - Discussion .....	IV-28
IV.8 - Experimental Validation .....	IV-29
IV.9 - References .....	IV-33
Chapter V - The Snapback analyzer: an instrument to measure b3 and b5 harmonics	V
V.1 - Introduction .....	V-1
V.2 - The solution based on the analogic bucking.....	V-3
V.2.1 - Hardware overview.....	V-3
V.2.2 - The measurement uncertainty sources.....	V-9
V.2.3 - The off-line calibration .....	V-20
V.2.4 - The software .....	V-22
V.2.5 - Measurements and results.....	V-26
V.2.6 - The new analogic bucking cards .....	V-29
V.3 - The solution based on digital bucking .....	V-31
V.3.1 - The working principle .....	V-31
V.3.2 - The proof demonstration .....	V-37
V.3.3 - The hardware proposed for the digital bucking.....	V-38
V.3.4 - Digital bucking tests on the new DAQ cards .....	V-38
V.3.5 - The software developed: architecture overview .....	V-41

V.3.6 - Conclusions .....	V-42
V.4 - References .....	V-43
Chapter VI - The polarity checker .....	VI-1
VI.1 - The measurement problem .....	VI-1
VI.2 - Measurement principle based on a single rotating hall plate .....	VI-3
VI.3 - Instrument description .....	VI-5
VI.3.1 - The mechanical layout .....	VI-6
VI.3.2 - The electronic hardware architecture .....	VI-8
VI.3.3 - The instrument software .....	VI-10
VI.4 - System characterization .....	VI-13
VI.4.1 - Hall plate static characteristic evaluation .....	VI-13
VI.4.2 - Systematic errors investigation .....	VI-15
VI.4.3 - Measurement uncertainty evaluation .....	VI-18
VI.5 - The automatic polarity test .....	VI-19
VI.6 - Results .....	VI-22
VI.7 - References .....	VI-24
Conclusions .....	
Appendix A .....	A-1
Appendix B .....	B-1
Appendix C .....	C-1
Appendix D .....	D-1

## **INTRODUCTION**

The Large Hadron Collider (LHC) is a particle accelerator which will probe deeper into matter than ever before. Due to come on-line in 2007, it will ultimately collide beams of protons at an energy of 14 TeV . Beams of lead nuclei will be also accelerated, colliding them at an energy of 1150 TeV.

This accelerator will help to complete understanding of the Universe. In particular, the Standard Model [1], at current the most qualified, leaves many unsolved questions. Among them, the reason why elementary particles have mass, and why their masses are different is the most perplexing one. It is remarkable that such a familiar concept is so poorly understood.

The answer may lie within the Standard Model, in an idea called the Higgs mechanism. According to this, the whole of space is filled with a 'Higgs field', and by interacting with this field, particles acquire their masses. Particles which interact strongly with the Higgs field are heavy, whilst those which interact weakly are light. The Higgs field has at least one new particle associated with it, the Higgs boson. If such particle exists, the LHC will be able to make it detectable.

The LHC will also help us solve the riddle of antimatter. It was once thought that antimatter was a perfect 'reflection' of matter. Now is known that the reflection is imperfect, and this could have led to the matter-antimatter imbalance.

The LHC will be a very good 'antimatter-mirror', allowing us to put the Standard Model through one of its most gruelling tests yet. These are just a few of the questions the LHC should answer, but history has shown that the greatest advances in science are often unexpected. Although there is a good idea of what it is expected to find at the LHC, nature may well have surprises in store. One thing is certain, the LHC will change our view of the Universe.

On the other side, The LHC represents one of the biggest technological challenges nowadays.

Particles beams are accelerated at the speed of light and at the nominal energy over the 27 Km circular trajectory thanks to four Radio Frequency Cavities. A total of 1232 dipole field magnets will be installed in the arcs to bend the beam on the reference trajectory. They will produce a bore field of 8.33 T, which will bend the beam at nominal energy on a circular trajectory with a curvature radius of 2803 m. Furthermore, during their revolution particle beams must maintain proper intensity and size. For this reason, 360 quadrupole magnets will be used to focus the particles around the nominal orbit. The quadrupoles gradient necessary to achieve the nominal working point is  $223 \text{ T m}^{-1}$ , which corresponds to a peak field of about 7 T on the coil.

The high strength of magnetic field to be achieved in the LHC magnets lead to the choice of the superconducting technology that allows very high density currents in the magnet with, ideally, no Joule heating. The coils of the magnets are wound with NbTi cables (7000 km in total), working in superfluid helium at 1.9 K. This will corresponds to an amount of 470 tons of NbTi and 1500 tons of copper.

The requirements on the control of field quality of the main optics elements (dipoles, quadrupoles) that stem from the demanded performance of the LHC beam are unprecedented in a superconducting accelerator of this size. The field errors, usually 4 order of magnitude smaller than the main field (dipolar or quadrupolar), have to be corrected better than 10 ppm to assure that stable beams run as long as possible on the circular orbit (for several hundreds of millions of turns), in order to increase the number of collisions between the counter-rotating beams. Because of this, the LHC will be equipped with several families of high-order multipole magnets that will be powered to correct the field errors in the main ring magnets as well as in the interaction region magnets. About 7000 corrector magnets will be grouped in various families that will control the orbit (dipoles), tune (quadrupoles), chromaticity (sextupoles), and higher order non-linearities (octupoles, decapoles and dodecapoles).

Clearly, the correction scheme based on the corrector magnets can be effective only if the errors are known to the desired accuracy. This is the main motivation of the large effort that has been devoted to the measurement and characterization of all the magnets that will compose the accelerator. From the point of view of instrumentation and test engineering, the most challenging developments are the new measurement systems that have been developed to collect data for the acceptance, sorting and, eventually, modelling of the field errors in the LHC superconducting magnets.

The measurement challenges are several. An ideal measurement system for field mapping would have an accuracy of 10 ppm or better both for the measurement of the main field as well as

on the field errors, expressed as higher order terms in a multipole expansion. This is difficult as the error terms are smaller than the dominating main field by 4 order of magnitude, thus demanding a very large dynamic range. The field to be measured can change in time, e.g. when the magnets are powered following the LHC acceleration cycle with a ramp rate of  $7 \text{ mTs}^{-1}$  (corresponding to 10 A/s). Also for this reason, it is desirable to have a short measurement time (fractions of s) to resolve fast dynamic and transient phenomena. For specific field properties, and in particular for the field polarity, strength and direction, the measurement system should deliver values with very high reliability. In fact, an error in the field polarity of a main magnet would induce faults ranging from minor control errors to potentially catastrophic beam loss. Finally, instrument robustness and stability are mandatory to limit the maintenance and calibration requirements.

No instrument is available to date to perform all above tasks with the required accuracy and reliability. In practice, different instruments are used to deliver partial information at different levels of accuracy and reliability [2]. The measurement methods most widely used for field mapping of the LHC magnets are rotating coils, well adapted to the measurement of integral steady-state or slow varying fields, and Hall plates, providing a fast sample of local field values. The typical instrument capabilities can be represented graphically as shown in Fig. 1, that reports indicative ranges for the measurement accuracy (expressed as error on the measured field) vs. the sampling time (expressed as the time interval needed to complete a measurement).

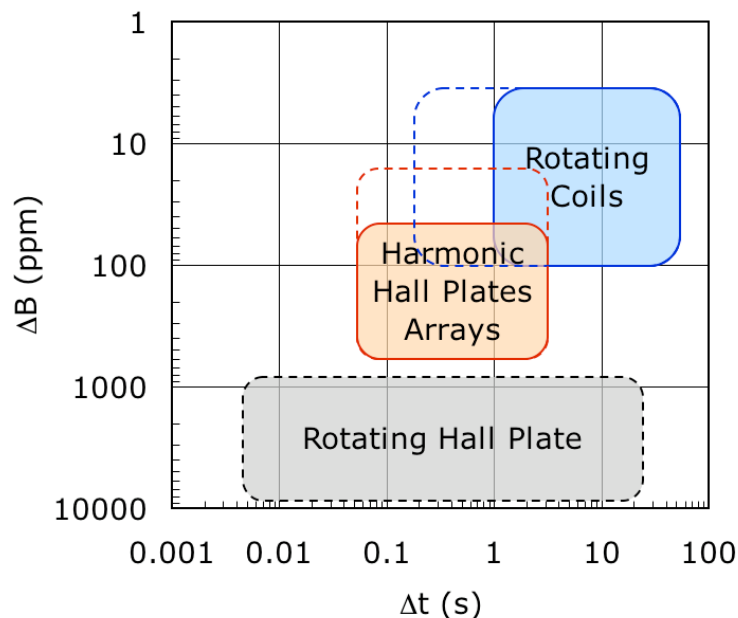


**Figure 1: Comparison of the typical ranges of accuracy and time resolution for measurement systems based on rotating coils and Hall plates. In dashed lines the result of the developments described in this thesis .**

Rotating coils are mainly used for the measurement of the integrated field and higher order harmonics. The harmonics are obtained through Fast Fourier Analysis on the flux samples collected during a complete coil turn. The flux samples are obtained by means of integration of the voltage picked-up by the coil, using the digital integrators developed at CERN about 15 years ago and based on the principle of voltage-frequency conversion and counting [3]. The integration is performed in the angular domain using the pulses coming from an incremental encoder that acts as a trigger. Rotating coils can reach overall accuracy of the order of 10 ppm, and the measurement time is of the order of few s. The main source of errors in the measurement comes from the precise calibration of the chain of coil-amplifier-integrator. Furthermore, when the field is not static, the Fourier series is no longer representative of the true expansion of the field, as the flux is no longer a periodic function of the rotation angle.

The integrator is the focal point of this *high accuracy* measurement method. Since few years it has become clear that the resolution of the current integrator is only marginally enough for present measurements, especially to analyse the fast flux variations expected during the LHC acceleration, and surely insufficient for the measurement of rapidly pulsed synchrotrons that are considered as future accelerators. For this reason several major laboratories have started active R&D aiming at a new integrator. Work at Fermi National Accelerator Laboratory (Batavia, IL, USA) focussed on a solution based on the chain of an ADC and DSP to perform the integration in the numeric domain, aiming at an improvement of the resolution. This development is based on a series of commercial acquisition and data processing cards that result in a complex final configuration [4]. Besides, this development did not tackle the question of the uncertainty on the trigger detection. At the Centre d'Etudes Nucleaires in Saclay (F) a digital integrator development was pursued since 1999 [5]. In this solution the voltage signal is sampled by an ADC with 16 bit-resolution and maximum sampling rate of 100 kHz. The sampled points are then integrated by a numeric board. The first release was based on a LabView<sup>TM</sup> software running on a PXI platform. Unfortunately, this development came to an end before reaching maturity.

A first part of the thesis is devoted to the conceptual design, performance analysis and demonstration of a new integrator based on ADC sampling and a DSP integrator, that also includes a suitable trigger response. The aim is to increase the integration resolution and speed so to extend the range of rotating coils measurements to fractions of s, without loss of accuracy, as shown in Fig. 1. At this speed it will be possible to perform dynamic measurements of magnets ramped. In these conditions the standard FFT is no longer appropriate, and the treatment of the non-periodic signal accumulated during one or more rotations of a coil in a varying field to reconstruct the instantaneous value of the harmonics is discussed. Two algorithms will be presented. The first one

applies quadrature detection and short time Fourier transform (STFT) to the acquired magnetic flux samples in a combined way. The second approach extrapolates magnetic flux samples over three complete coil turns, thus giving the possibility of reconstructing the magnetic flux at any given time instant. Both the proposals are suitable for operation in real time, and can be implemented in firmware of the DSP on-board the integrator, thus providing a very compact and attractive solution.

Hall plates can be used to sample the field at a small location in the magnet (typically  $0.1 \times 0.1 \text{ mm}^2$ ). At CERN, harmonic arrays of Hall plates have been used to measure specific harmonics of importance for accelerator operation, such as the normal sextupole and decapole [6]. These systems are affected by errors of the order of 50 ppm or larger, and hence only have *medium accuracy* with respect to rotating coils, but deliver results at much higher frequency, up to typically 10 Hz, as shown in Fig. 1. The main error source comes from the non-linearity of the Hall plate (0.2 % or worse in the range of interest), and the stability of the chain formed by the Hall-plates, the analog conditioners, the amplifiers and the data acquisition. Initial measurements carried out with a prototype acquisition systems showed scarce system repeatability, thus resulting in the need of frequent calibration. Moreover, instability of the analog compensation and amplification cards resulted in high measurement uncertainty.

To address these problems, a full metrological characterization of the existing probe was performed. This allowed discovering and characterizing all the possible uncertainty sources and, most important, the instability of the compensation cards responsible for the frequent instrument calibrations. As it will be shown, the instrument was improved by using an automated calibration procedure (taking the rotating coils as reference instrument) on newly developed compensation and amplification boards that can achieve higher long-term stability. Finally, digital bucking, namely the compensation of the main field after the sampling of each Hall plate signal by means of numerical sum, was explored as a mean to extend the measurement accuracy to 20 ppm, as shown in Fig. 1. An implementation of this approach, based on 18 bit AD converter, over-sampling and dithering techniques as well as compensation of the Hall plates non linearity in real time, is discussed in detail.

The accuracy of both rotating coils and Hall plate arrays in determining the *strength, direction* and higher order *errors* of a given magnetic field is relatively good. In spite of this, none of the different versions of these instruments can be reliably used to verify without doubt the polarity of a given magnet. The reasons are several, from the long cabling chain between the probes and the acquisition, with several interconnection, to the presence of amplification stages, or ambiguity in orientation that have no effect on the measured values apart for the sign.

On the other hand, magnetic field polarity is possibly the most important magnetic property to be verified in the LHC magnets [7]. Polarity inversions can happen at the level of a single winding, but much more frequently these take place at the level of the interconnections within the cold mass (bus routing from the magnet to the current leads) or, possibly, at the interconnection between magnets at installation. None of these faults can be easily mended once the cryostat is closed, and hence particular care is asked in the verification of the field polarity. In practice, all magnets need to be verified before they are lowered for installation in the tunnel housing the accelerator. This is a tantalizing task, to be performed on several thousands of magnets, that has been delegated to the operators that perform the electrical verification of the magnets in the absence of experts in field mapping technology.

Such a measurement only require *low accuracy* (typically 0.1 % to 1 % is more than sufficient), and is not time critical (a measurement over few s is acceptable). A suitable technique for the above requirements is to use a rotating Hall plate to sample the field on a circle, and analyse the result in Fourier series to determine the order and polarity of the main field component. A polarity checker that can perform this measurement was designed and produced at CERN based on a development initially performed at Brookhaven National Laboratory (Upton, NY, USA). The working principle of this novel device will be described, the signal conditioning and acquisition chain, demonstrating how the characteristics of Fig. 1 have been achieved in an instrument that is robust and easy to use.

Indeed, the difficulty in this case, originated from the fact that the consequences of a measurement failure are potentially harmful to the performance of the accelerator, and the associated risk cannot be tolerated. At the same time, the level of experience of the measurement operator is not necessarily high, which means that the measurement system must provide for its own diagnostic. This implies that the measurement is focused on robustness, at the expense of accuracy. The demands on the polarity checker to those on the two other systems discussed above are compared in Fig. 2, by plotting the requested accuracy vs. the ratio of perceived risk and operator experience. In the case of rotating coils the risk is limited, as accelerator control is based on average field properties over the ring, while operators on dedicated test stations for field mapping are relatively experienced. In other words the demands on the system are high in term of accuracy, but the operators assist in achieving this result. For the harmonic Hall plate arrays the measurement is objectively delicate, but the consequences of a measurement fault are minor, as this instrument is mostly used for special studies. Measurements are always performed in the presence of experts, thus resulting in a low risk/experience ratio.

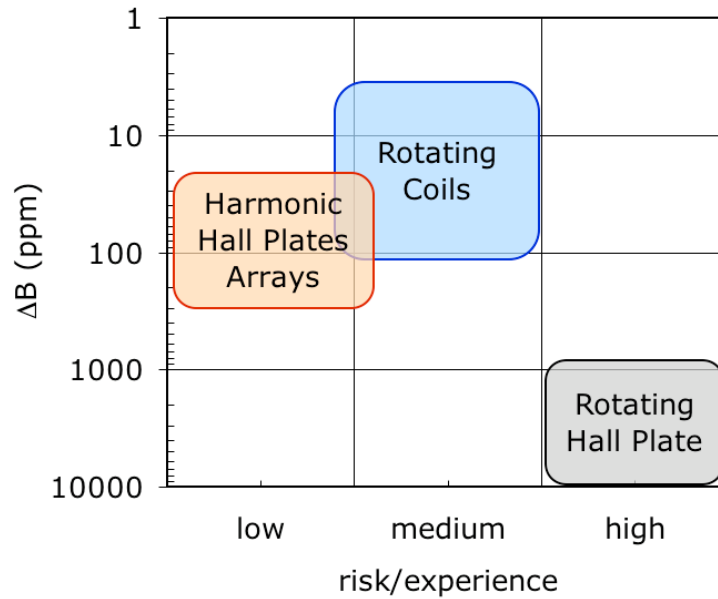


**Figure 2: Scatter plot of accuracy requirements vs. the ratio of perceived risk and operator experience for the three measurements systems discussed in this thesis.**

The common denominator of the developments discussed in this thesis is the use of modern digital acquisition and signal processing techniques to extend the reach of existing techniques (e.g. rotating coils or Hall plates array) or to devise new instruments (the polarity checker based on rotating Hall plate). Like the techniques, discussed here, can be extended over the whole range of accuracy (from 1 % to 1 ppm), time scale (from few ms to tens of s) and reliability (from expert driven instruments to virtually error-free measurements) will be shown.

In Chapter I a summary of the LHC project is presented, with particular attention devoted to the magnets function and the description of the field errors. Chapter II gives the status of the art of the measurement systems, discussing their use as well as their drawbacks. In Chapter III the design of a new digital integrator that allows to reach *high accuracy* at much improved speed if compared to the existing electronics is discussed. The algorithms to deal with fast measurement of ramped fields are discussed in Chapter IV as a complement to the fast digital integrator. Chapter V deals with the characterization and improvements introduced on the Hall probe arrays, the *medium accuracy* system. Finally, in Chapter VI the polarity checker is described, at the end of *low accuracy* but high reliability.

## ***References***

- [1] D I Kazakov. Beyond the standard model (in search of supersymmetry). In N Ellis and J March-Russell, editors, 2000 European School of High-Energy Physics, Caramulo, Portugal, pages 125–198. CERN, 2000.
- [2] L. Walckiers, L. Bottura, M. Buzio, P. Schnizer and N. Smirnov, “*Sensitivity and accuracy of the systems for the magnetic measurements of the LHC magnets at CERN*”, Seventh European Particle Accelerator Conference (EPAC 2000) 26-30 June 2000, Vienna, Austria
- [3] P. Galbraith, “*Precision electronics (integrators) for field measurements*”, CERN , EDMS N. 021120
- [4] R. Carcagno, J. Di Marco, S. Kotelnikov, M. Lamm, A. Makulski, V. Maroussov, R. Nehring, J. Nogiec, D. Orris, O. Poukhov, F. Prakoshin, P. Schalabach, J.C: Tompkins, and G.V. Velez, “*A fast continuous magnetic field measurement system based on digital signal processor*”, *19<sup>th</sup> Magnet Technology*, October 2005
- [5] C. Evesque, “*A new challenge in magnet axis transfer*”, *IMMW11 Brookhaven National Laboratory*, September 1999
- [6] M. Haverkamp, “*Decay and Snapback in the superconducting Accelerator Magnets for the large Hadron Collider*”, PHD Thesis, University of Twente, 2002.
- [7] P. Proudlock, “*LHC Magnet Polarities*”, Engineering specification LHC-DC-ES-0001, version 2.2, EDMS 90041

# **Chapter I - THE LARGE HADRON COLLIDER**

## ***1.1 - The LHC Project***

Located at Geneva in Switzerland, the European Organization for Nuclear Research was founded in 1953 (under the name of CERN) following a recommendation of the UNESCO Meeting in Florence 1950. The motivation for this project, in the wake of the World War, was to prove that European countries could cooperate, in a field as sensitive such as nuclear physics, in order to advance fundamental science. Starting from the early



**Figure I-1 Overview of the Geneva area with a drawn of the two circular accelerators: Super Proton Synchrotron (SPS 7 Km) and the larger Large Hadron Collider (LHC 27 Km).**

stage of the Proton Synchrotron (PS) accelerator, subsequent projects enhanced the scientific complex with more machines. The SPS (Super Proton Synchrotron) machine provided the energy to discover the weak force particles  $W^+, W^-, Z_0$  resulting in the 1984 Nobel prize attributed to Carlo Rubbia and Simon Van de Meer. On the way to higher energies the LEP (Large Electron Positron collider) was built, providing high precision values for the aforementioned particles already during start up. On the quest for higher energy the LHC (Large Hadron Collider) is being currently constructed.

The LHC machine will accelerate and collide 7 TeV proton beams but also heavier ions up to lead. It will be installed in a 27 Km long underground tunnel (see Fig. I-1) that has been housing the Large Electron-Positron collider (LEP) until 2000.

Two counter-rotating proton beams will collide at a nominal center-of-mass energy of 14 TeV achieving a nominal luminosity of  $10^{34} \text{ cm}^{-2} \text{ s}^{-1}$  in order to study the interaction of the basic constituent of the matter in the TeV energy range. The collider will allow also experiments with lead nuclei that will reach collision energies up to 1150 TeV and luminosities up to  $10^{27} \text{ cm}^{-2} \text{ s}^{-1}$  [1].

Fig. I-2 shows the chain of the CERN accelerators. Bunches of about  $10^{11}$  particles are prepared in the Booster and the PS, and are accelerated up to the injection energy of the SPS (26 GeV). The beam will then be injected from the SPS into the LHC at the insertion points at the energy of 450 GeV.

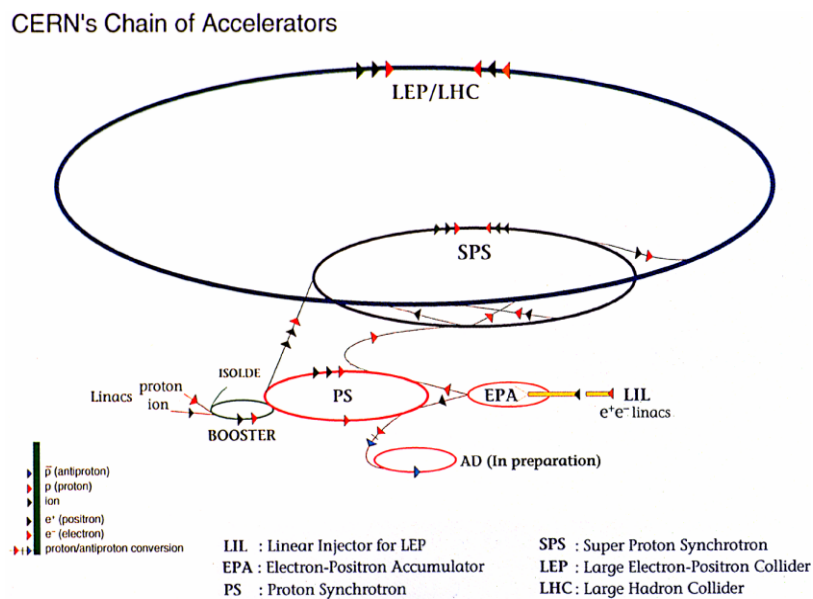


**Figure I-2 The CERN accelerators structure from the beam production through different acceleration steps up to the largest accelerator the LHC.**

With the LHC the aim is to continue to push our understanding of the fundamental structure of the universe. The results from the LHC might shed light on: Dark energy, Dark matter, Extra dimensions, Higgs boson, Supersymmetry [2].

## ***I.2 - Particle Circular Accelerators***

In general particle accelerators are machines that accelerate charged particles to high kinetic energies by applying electro magnetic fields. A particle of charge  $q$  and momentum  $\vec{p}$  moving through an electromagnetic field is submitted to the Coulomb and Lorentz's forces expressed by:

$$\vec{F} = \frac{d\vec{p}}{dt} = q(\vec{E} + \vec{v} \wedge \vec{B}) \quad \text{(Eq. I-1)}$$

where  $\vec{F}$  is the electro magnetic force exerted by the electric field  $\vec{E}$  and the magnetic field  $\vec{B}$  on a particle of velocity  $\vec{v}$  [3]. The electric field  $\vec{E}$  and magnetic field  $\vec{B}$  change both the particle trajectory and the velocity so the trajectory and the energy can be modified.

According to (Eq. I-2), three fundamental elements are necessary to realize the particle accelerator:

- particle beams have to be accelerated. Radio Frequency cavities (RF) are installed in the arc in order to increase the particle energy at every turn;
- particles must be guided on the reference “circular” orbit; for this reason 1232 dipole field magnets will be installed in the arcs to bend the beam on the reference trajectory;
- particle beams must maintain during their revolution a proper intensity and size, i.e. they must be focused or defocused; for this reason 360 quadrupole magnets are used to focus or to defocus particles onto the reference orbit.

The bending dipole field intensity is imposed by the curvature of the orbit and by the particles energy. At the equilibrium the Lorentz and the centrifugal forces of the particle beam are equal in intensity and opposite in sign. In the LHC particle beams will be highly relativistic, practically circulating at the speed of light  $c$ . The equilibrium condition results in the following expression [4]:

$$|B| \cong \frac{E \cdot v}{\rho c^2 q} \cong \frac{E}{\rho c q} \quad (\text{Eq. I-3})$$

where  $E$  is the energy of particle of charge  $q$  and  $c$  is the speed of light.

Along the energy ramp, the equilibrium condition requires a sharply ramping magnetic field.

### ***I.3 - The LHC Dipole and Quadrupole Magnets***

A bending dipole field  $B$  of 8.33 T is required by a protons beam to reach the energy of 7 TeV on a circular trajectory with a curvature radius of 2803 m, for the LHC the orbit radius is constrained by the existing LEP tunnel. The LHC quadrupole magnets are designed for a gradient of  $223 \text{ Tm}^{-1}$  and a peak field of about 7 T. These high intensity magnetic fields can be efficiently and practically achieved with superconducting magnets only. The LHC will contain a total of 8.400 magnets, including the 1232 (15 m long) dipoles (Fig. I-4 (a)), 360 (3.25 m long) quadrupoles (Fig. I-4 (b)) and the various families of corrector magnets up to dodecapole orders [1].

The high strength of magnetic field to be achieved in the LHC magnets lead to the choice of the superconducting technology that allows very high density currents to flow producing negligible joule heating. The coils of the magnets are wound with NbTi Rutherford cables (7000 km in total), working in superfluid helium at 1.9 K. This will



**Figure I-3** A LHC dipole magnet being transported to the test benches.

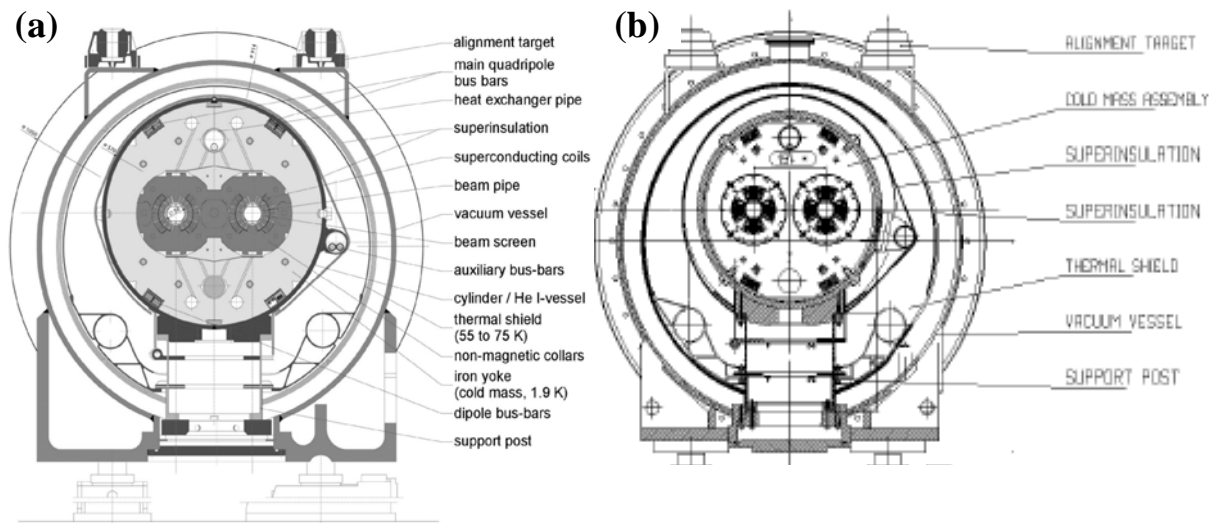


**Figure I-4 (a) The cross-sections of the LHC main dipole and (b) main quadrupole, with their cryostats and overall mechanical structure.**

correspond to an amount of 470 tons of NbTi and 1500 Tons of copper.

As shown in Fig. I-4 (a), the LHC bending dipoles feature a compact two-in-one design with the two apertures featuring a common force retaining steel collar, a single flux return iron yoke and a single cryostat. On the other hand, the quadrupoles, as shown in Fig. I-4 (b), have two separate force retaining collars.

### *1.3.1 - The superconducting cables*

The main dipole and quadrupole cables feature a geometry called “Rutherford type”: they are manufactured by flattening hollow tubular multistrand cables, compacted by rolling. Each strand consists of approximately 15000 NbTi filaments (8900 inner, 6520 outer) twisted together and embedded in a copper matrix for inner coil and by 7000 filaments in outer coil. The filament size is of 7  $\mu\text{m}$  for the inner

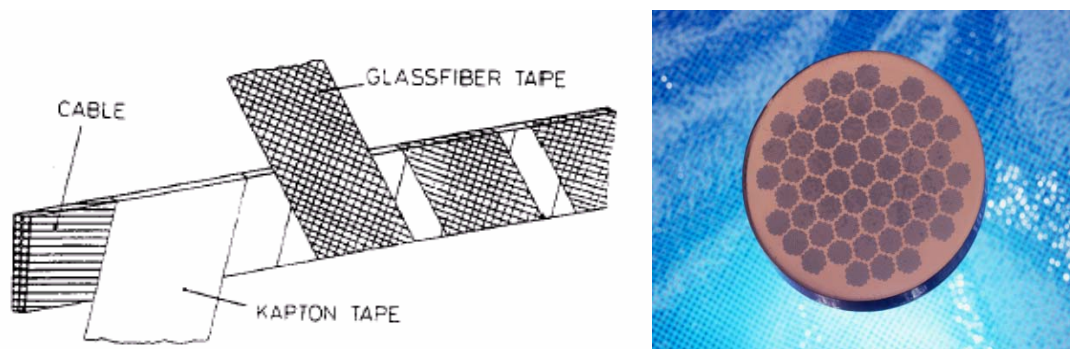


**Figure I-5 On the left, Rutherford cable with Kapton and glass-fibre epoxy insulation. On the right, the cross section of an LHC dipole strand.**

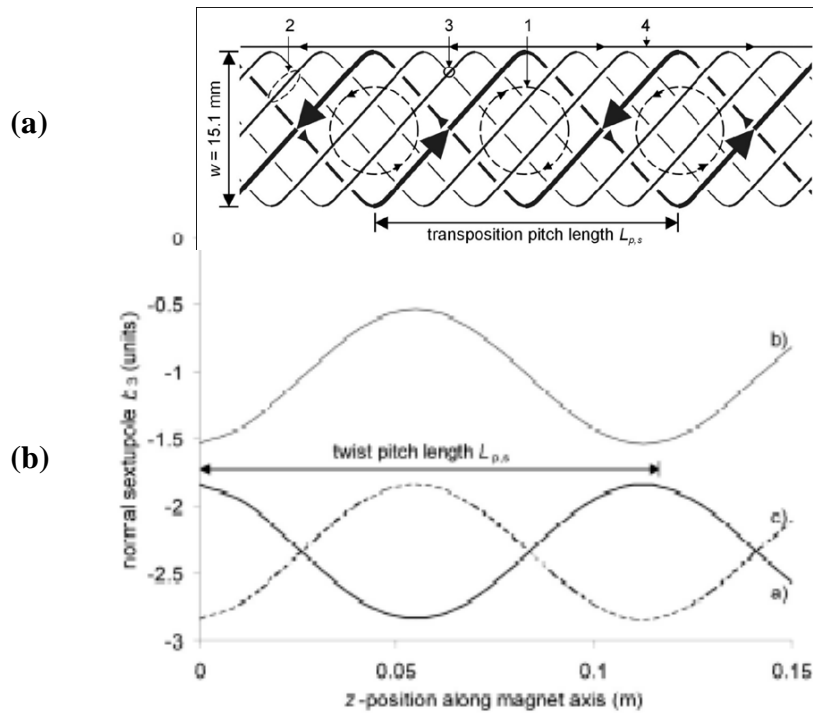


**Figure I-6 (a) A schematic view of the paths followed by the strands in a Rutherford cable. (b) The longitudinal “periodic field pattern” of the  $b_3$  field component resulting from the currents loops shown in (a).**

layer strand and  $6 \mu\text{m}$  in the outer layer strand. The main reasons for the subdivision into small filaments are: 1) the cryogenic stabilization (elimination of the so-called “flux jump” instability); 2) the reduction of the flux pumping effects. A cable insulation composed of polyimide layers wrapped around the cable is provided to withstand the voltage between the turns and is sufficiently porous to let the superfluid helium carry away the heat.

In the field sweep regime, the induced currents diffuse into the cable following a zigzag path along the strands as shown in Fig. I-6 (a). In the beam pipe these currents imbalances results in an observable spatially periodic field pattern along the magnet axis. Such pattern is observed in all field components and has a sinusoidal shape. The sinusoid wavelength of the pattern is equal to the Rutherford type cable transposition pitch length [9].

## I.4 - Multipoles and Field quality

In storage rings like the LHC stable beams have to run as long as possible on the circular orbit (for several hundreds of millions of turns), in order to increase the number of collisions between the counter-rotating beams. This imposes strong constraints on the tolerable field perturbations along the trajectory. Deviations from the dipole and quadrupole fields, even if short in both space and time, can induce instabilities which reduce the beam life-time. Higher-order multipoles correctors are required to compensate the unavoidable imperfections of dipole and quadrupole magnets.

Ideally, a pure  $n$ -pole field could be produced by a current flowing along an infinitely thin cylindrical shell, with a cosine like distribution,

$$I(\theta) = I_0 \cos(n\theta) \quad (\text{Eq. I-4})$$

where  $\theta$  is the azimuthal angle [5]. Fig. I-7 shows schematically the current distributions that produce pure dipole, quadrupole and sextupole fields.

The current distribution that can be practically achieved is only an approximation of the ideal one that would produce a perfect multipole field magnet.

The LHC dipoles are 15 meters long with a beam aperture of 50 mm in diameter, allowing the possibility to consider the coils as infinitely long and to evaluate the magnetic field in the  $x$ - $y$  complex plane neglecting the  $z$  component. This 2-dimensional approximation is very convenient to describe  $\vec{B}$  in terms of a complex variable  $z$ . In the central part of the dipole taking into account the properties of the analytical functions, one can postulate that the magnetic field generated  $\vec{B}$  can be expanded in the complex plane in a power series as follows [6]:

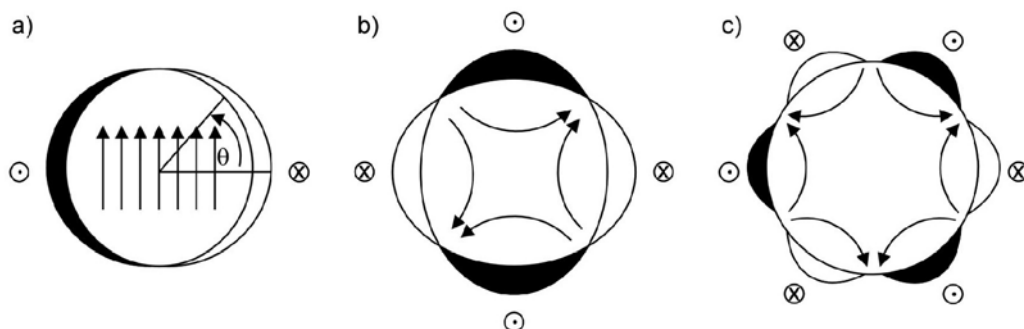


**Figure I-7** Generation of pure dipole (a), quadrupole (b) and sextupole (c) fields by  $\cos(n\theta)$  current distributions with  $n=1, 2$  and  $3$  respectively.

$$B(z) = B_1 \sum_{n=1}^{\infty} \frac{C_n R_{ref}^{n-1}}{B_1} \left( \frac{z}{R_{ref}} \right)^{n-1} = B_1 \sum_{n=1}^{\infty} c_n \left( \frac{z}{R_{ref}} \right)^{n-1} \cdot 10^{-4} \quad (\text{Eq. I-5})$$

$C_n$  is in units of T\*m<sup>1-n</sup> while  $c_n$  given by  $c_n = C_n \frac{R_{ref}^{n-1}}{B_1}$  are the multipoles normalized respect to the main dipole field and referred to a reference radius  $R_{ref} = 17$  mm [4]. In this way all the series coefficients  $c_n$  result dimensionless and are expressed in so called units of the main field at the reference radius; they are then multiplied by the scaling factor  $10^4$  that is the order of the ratio between the main field and the field errors.

In the complex plane the  $C_n$  coefficient can be decomposed in its normal and skew term as follow:

$$C_n = B_n + iA_n \quad (\text{Eq. I-6})$$

Using the decomposition above and applying the scaling factor to the normal and skew field components deduced from Eq. 1-5 one can express the field components in units of the main field  $B_1$  as follow:

$$\begin{aligned} a_n &= A_n \frac{R_{ref}^{n-1}}{B_1} \cdot 10^4 \\ b_n &= B_n \frac{R_{ref}^{n-1}}{B_1} \cdot 10^4 \end{aligned} \quad (\text{Eq. I-7})$$

The existence of non-zero  $b_n$  and/or  $a_n$  coefficients reflects the fact that the magnetic

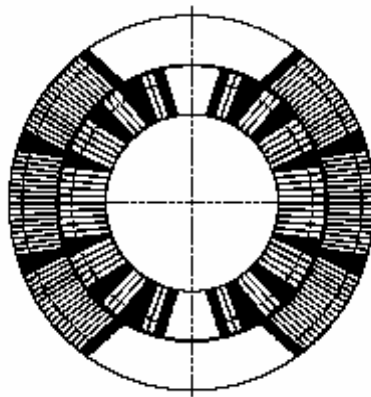


**Figure I-8 Approximation of a  $\cos(\theta)$  distribution with current blocks in the LHC dipole.**

field generated by the superconducting coil in a dipole is not a pure dipole and is affected by higher order of multipoles (quadrupole, sextupole, etc.). The multipole components

	<b>Commissioning</b>	<b>First Year</b>	<b>Nominal</b>
<b>b1 (units)</b>	$\pm 2$	$< \pm 1$	$\pm 1$
<b>b2 MB (units)</b>	$\pm 0.2$	$\pm 0.03$	$\pm 0.01$
<b>b2 MQ (units)</b>	$\pm 4$	$\pm 0.75$	$\pm 0.25$
<b>b3 (units)</b>	$\pm 0.5$	$\pm 0.15$	$\pm 0.02$

**Table I-1 Tolerances for the LHC operation for depole (MB) and quadrupoles (MA).**

are generated by the difference between the ideal current distribution of Eq. 1-3 and the actual current distribution in the coil. All undesired multipole components other than the main field are referred as *field errors*.

### ***1.5 - Harmonics tolerances from the beam dynamics***

Stability requirements for the beam motion impose stringent constraints to the quality of the magnetic field of the LHC magnets. The multipoles of order higher than three affect the size of the dynamic aperture. The sextupole, the decapole and the 14<sup>th</sup> pole components are among the most critical multipole field harmonics to control in order to insure a long beam life-time. These constraints have been expressed into a set a maximum field imperfections (tolerances on the multipoles) to be achieved at operation and summarized in field quality errors tables [8]. In the following we will recall the major tolerances on multipoles stemming from beam dynamics requirements.

### ***1.6 - Field error sources in LHC dipoles***

In addition to the errors associated with the geometry approximation of the superconducting coils, field errors in superconducting magnets can have origins that depend on the different elements and materials used. In superconducting magnets we can distinguish two classes of errors that affect the field quality: errors that are static and are constant in time and errors that are dynamic and change with time. The various components of the field errors are identified and quantified from magnetic measurements on the LHC dipoles in order to understand how to correct them during the operation of the machine.

### I.6.1 - Static errors

For steady state operation, the three main sources of magnetic field errors are:

- **Coil geometry errors.** They are originated by the differences between the real coil shape and the ideal current distribution producing a perfect dipole field. This error is proportional to the transport current flowing through the coils. To minimize this reproducible contribution, mechanic placement of cables must be very accurate in the manufacturing and also during magnet excitation, typically to within 25  $\mu\text{m}$ .
- **Iron yoke saturation.** The iron yoke gets gradually saturated about 2 T. For this reason, the field level in the yoke is not linearly proportional to the excitation current. Saturation effects result in a reduction of the transfer function (the field generated per unit current) of approximately 60 units in dipole and 14 in quadrupole, as well as harmonic errors. This effect is amplified by the cross talk between the two apertures, consequence of the two-in one design of the dipole cross section. Saturation effects are controlled by the optimization of the yoke and the insert geometry.
- **Persistent currents.** They are originating from the contribution of the magnetization of the superconducting filament when the field is applied. These persistent currents are long lasting and are induced in the superconducting filaments as a response to an external magnetic field. They appear at a first approximation as a trapped magnetization and they give rise to the hysteretic behavior of the field. An example of this phenomenon is underlined by the typical magnetic measurement of the sextupole component in a LHC dipole magnet, as shown in Fig. I-9 when the current

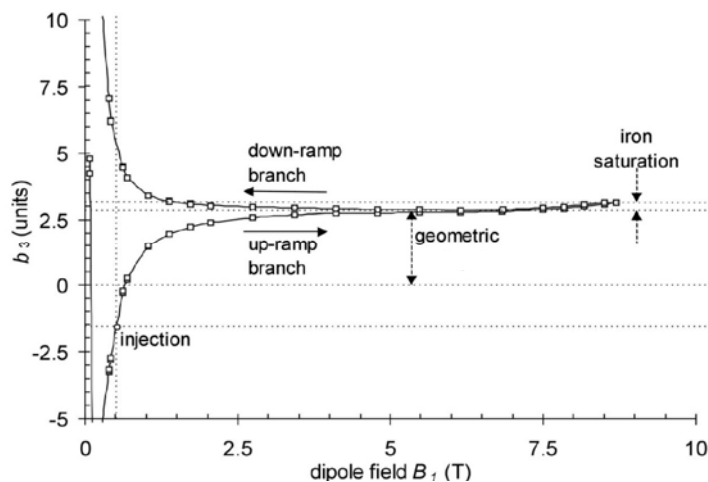


Figure I-9 Normal sextupole hysteresis cycle measured in LHC dipole model at different current levels in steady-state conditions. The currents were reached with stepwise ramp-up and ramp-down; the arrows mark the ramp directions.

is ramped until the nominal LHC operation level and then decreased back to zero. In absence of persistent currents, the hysteretic behavior would be absent. Only a transition to the normal state (i.e. a quench of the superconductor) can completely erase persistent currents flowing through filaments. As a consequence, to perform comparable magnetic measurements, a quench and the same current load cycle has to be applied to all magnets before starting with an equal current load ramp-up and down cycle. The reference cycle for operation is shown in Fig. I-10.

### *I.6.2 - Dynamic errors*

Additional dynamic field contributions i.e. imperfections linked with variation in time of the magnetization affect the field quality inside the dipole. All dynamic effects induce additional allowed or non-allowed harmonics. The major sources of this field distortion are the following.

- **Coupling currents.** A varying field applied to a Rutherford cable generates eddy currents that couple electromagnetically the strands (see Fig. I-10). These eddy currents are referred to as inter-strand coupling currents and their intensity is inversely proportional to the inter-strand resistance  $R_c$  at the strand crossing point and proportional to the ramp rate  $dB/dt$ .  $R_c$  is controlled during the cable production with a specified minimum of  $20 \mu\Omega$ . Coupling currents induce loss, a field advance during the ramp (the field is larger in the magnet bore than expected) and allowed and non allowed multipoles. With respect to persistent currents, the time constant of coupling currents is extremely small, on the order of 100ms;

- Decay and snap-back.** The decay refers to as a drift with time of the magnetization created by persistent currents, when the current of the magnet is held constant. When the current in the magnet is increased again the field bounces back (snaps back) to its pre-decay level. The field decay effect was observed first during the preliminary operation of the Tevatron collider where a measure of the chromaticity pointed out the evidence of a large drift in all allowed field components during long constant current periods [9]. Later direct measurements of sextupole harmonics confirmed that the normal  $b_3$  decays during a constant current period but when the current is ramped up again, after the current plateau, the sextupole returns to its original value (Fig. I-11). The decay of the magnetization is characterized by a drift of the magnetic field with typical time scales in the order of several minutes to several hours, when the current is held constant, for example during the injection plateau (0.54 T) in a representative cycle that will be applied in the machine. This decay of the multipoles is followed by a snap back to their initial value as soon as the current increases by 15 or 30 A (10-20 mT of field change). The snap-back phenomenon occurs during a typical time period of 50-80 s. The decay and the snap-back in the LHC dipoles are measured at 1.9 K after on going the same pre-cycle conditions. The duration of the injection plateau is fixed at 1000 s as a reference.

Measurements were also performed on 15 m long dipoles with changing the current level of pre-cycle fixed duration plateau. The higher is the field reached during the pre-cycle the stronger is the drift observed on the multipoles  $b_3$  and  $b_5$ . The same

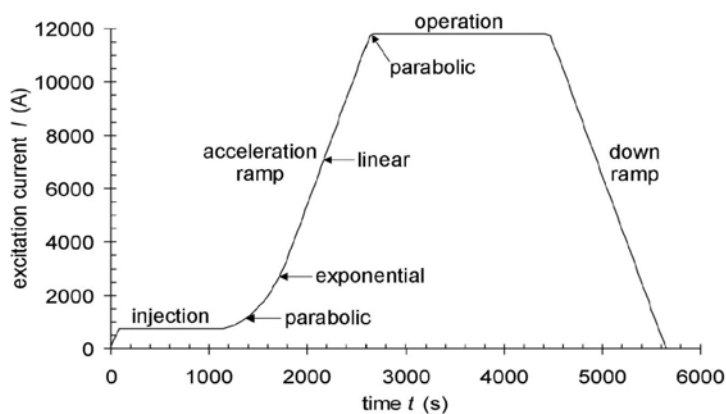


**Figure I-10** The LHC current level cycle. During injection the LHC main ring will accept particles from the SPS, then a ramp-up during particle acceleration is needed to achieve the 7 TeV beam energy. At last the current is decreased back to zero.



that change over time and which depend on the history on the magnet operation require a new correction for each operation cycle of the machine and a real-time modification of the corrector powering during the operation.

In other words the high order correctors connected in series per arc and per aperture represent the actuator of the correction system whilst the controller output is the current law to download in each actuator power converter. Since the load high inductance the updating frequency of the current is about 2 Hz.

In principle if the field model for each multipole is known and provide an estimation of the errors behavior as function of the machine operative conditions with the desired accuracy no feedback would be required and the current law would be obtained simply from the transfer function of the actuator magnets.

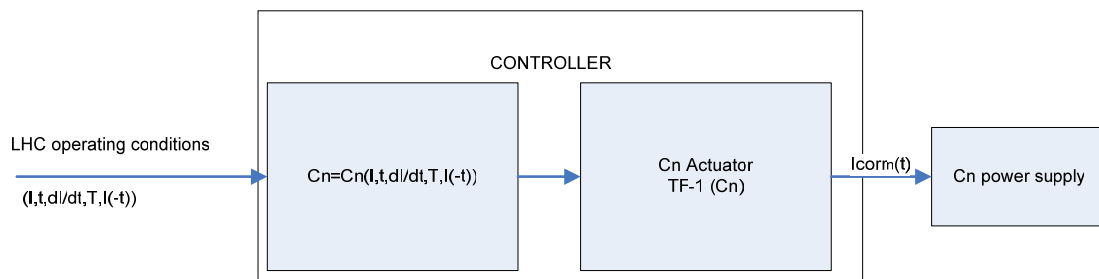


**Figure I-12: Principle of the LHC multipoles errors correction without feedback**

The field model is expressed in the form:

$$C_n = C_n \left( t, I, \frac{dI}{dt}, T, I(-t) \right) \quad (\text{Eq. I-8})$$

in fact every field harmonics depends from the following variables:

- time  $t$ ,
- magnet operating current  $I$ ,
- magnet ramp-rate  $dI/dt$ ,
- magnet temperature  $T$ ,
- magnet powering history  $I(-t)$  (the superconducting magnets have memory).

Up to now an intensive field quality characterization of the LHC dipoles and quadrupoles has been carrying out supplying the magnets in standard operative

conditions (i.e LHC machine cycle). Special measurements to study the higher field harmonics behavior as function of the powering history are performed and will continue for all the 2006.

Many efforts have been done and are in progress to establish from all the data accumulated an accurate model for all the field harmonics (in particular for b1,b3 and b5 that are the main causes of the beam quality degradation) by means of simple fitting of experimental data or establishment of scaling laws .

### ***1.8 - The reference magnetic system project***

Modeling alone may not suffice to predict and hence satisfy the strict requirements on the multipoles errors, because of the following aspects:

- a maximum of 30% of the overall dipole population will be tested at cold (i.e. at nominal temperature of 1.9 K and up to the nominal current of 11850A) and 100% at warm (i.e. room temperature). The multipoles values at cold of the remaining 70% will be obtained by means of warm-cold correlations that are affected from uncertainty;
- the magnets are not characterized by a good stability over the time: the coil geometry was observed to change during the magnet life on the effect of the Lorentz's force. As a result, the geometric multipoles change over cycles. On few magnets tested a systematic effect was observed only on the allowed multipoles [10];
- the sample used to determine the snapback model for b3-b5 multipoles is based only on a limited number of magnets (maximum 20 magnets over the overall population of 1232 dipole);
- the field model has been establishing taking into account standard machine operational conditions, i.e. LHC standard cycle and only modifications of this latter (flat top current and flat top time). If in the future the machine operational power cycle had to change, the model couldn't foresee anymore the multipoles behavior.

Therefore, the model may need to be supplemented by additional informations.

Although direct diagnostics on the beam is the ideal mean to collect the information required on the field errors, a number of considerations make a feed-back system solely based on beam feed-back far from ideal. In particular:

- given an energy ramp, the required bandwidth depends on the magnitude of the error that requires correction. As an example a beam-based correction of the sextupole change in the main dipole may result in unreasonable demands on the bandwidth for the chromaticity measurement (10 Hz and higher);
- some beam measurements are destructive;
- some of the parameters cannot be determined easily from beam measurements, e.g. dynamic aperture that may be affected by high order multipoles such as normal decapole in the main bending dipoles.

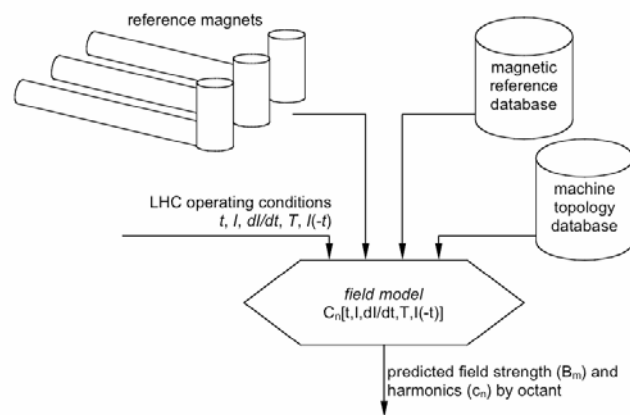


**Figure I-13: Reference Magnetic System concept**

Because of the above arguments, it is desirable to devise a method to bridge the gap between the magnet field errors as obtained from the production and installation and the requirements for operation. A Reference Magnetic System (RMS) was designed for this purpose.

The RMS concept is shown in Fig. I-13. The complement to the model is represented by the on-line reference magnets. These are magnets properly chosen to represent the average behavior of the accelerator magnets and driven by individual power converters with the same powering law of the rest of the machine i.e. having the same magnetic history. These magnets will be equipped with suitable magnetic measurements systems that will provide in real time information about their field quality. The key point is the so called “scaling law”, namely, the law that permits to correlate the harmonics behavior in

the reference magnets with the average per arc. For b1, b3 and b5 components of the LHC dipoles it has been proved that the decay and snapback model is scaled of a pure proportional coefficient between different magnets [11]. The analysis was achieved taking into account a significant sample of LHC dipoles but measurements of decay and snapback performed on Tevatron dipoles (different from the LHC dipoles both in superconducting cable and in coils) showed the same results [12]. This support the idea that the correlation found has some fundamental origin, and can thus be used for a robust prediction.

The function of the reference magnets is to provide only relative changes with respect to the expected behavior, while the software interpolator remains the main element for control. The feed-forward control implemented for instance on the b3 multipole is depicted in Fig. I-14: for a given operating conditions the b3 value for a specific sector is determined using the field model established from the series magnetic measurements and stored in the Magnetic Reference Database. The on-line measurement of b3 from a particular reference magnet is compared with the model estimate of the b3 for the same magnet. The difference from the measured value and the estimation gives the model error; this difference, properly scaled using the information stored in the Machine Topology Database, is used to correct the model result.

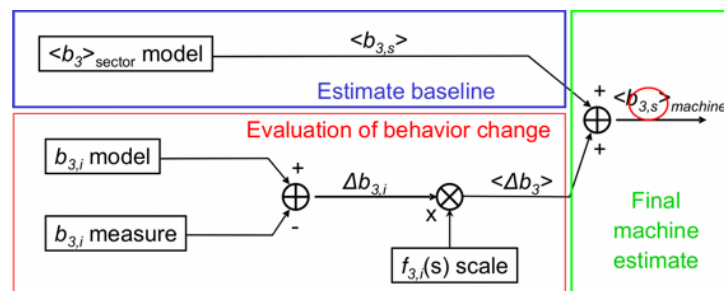


**Figure I-14: Feed-forward control on the b3 harmonic**

## ***I.9 - References***

- [1] O. Bruning et al., “*LHC Design Report*”, Volume 1 The Main Ring, CERN-2004-003-V-1, 2004.
- [2] <http://public.web.cern.ch/Public/Accelerators/welcome.html>
- [3] Feynman, Leighton, Sands “*Lectures on Physics*” Volume II, Addison-Wesley Publishing Company 1964.
- [4] H. Wiedemann, “*Particle accelerator physics I*”, Springer-Verlag, Berlin, 1993.
- [5] Mess, Schmuser, Wolff “*Superconducting accelerator magnets*”, World Scientific, Singapore, 1996.
- [6] A. K. Jain, “*Basic theory of magnets*”, CAS CERN Accelerator School on Measurement and Alignment of Accelerator and Detector Magnets, *CERN Yellow Report* 98-05, (1998).
- [7] H. Bruck, et al., “*Observation of a periodic field pattern in the persistent-current fields of the superconducting HERA magnets*”, proceedings IEEE Particle Accelerator Conference, 2149-51, San Francisco, USA, 1991.
- [8] S. Fartoukh and O. Bruning, “*Field quality specification for the LHC main dipole magnets*”, *CERN LHC-Project-Report* 501, 2001.
- [9] D.A. Finley et al. “*Time dependent Chromaticity Changes in the Tevatron*”, 12<sup>th</sup> Particle Accelerator Conference (1987), Washington DC, March 1987.
- [10] L. Bottura et al., “*A strategy for sampling the field quality of the LHC dipoles*”, 9<sup>th</sup> European Particle Accelerator Conference, Lucern, 2004.
- [11] L. Bottura et al., “*A scaling law for predicting the snap-back in superconducting accelerator magnets*”, 9<sup>th</sup> European Particle Accelerator Conference, Lucern, 2004.
- [12] G. Velev, et al., “*Measurements of sextupole decay and snapback in Tevatron dipole magnets*”, 9<sup>th</sup> Europ. Part. Accel. Conf., Lucerne, 2004.

## **Chapter II - STATE OF THE ART**

### ***II.1 - Outline***

In this chapter, the state of the art in the three measurement fields discussed in this thesis (harmonic coils, harmonic Hall probe array and multipole polarity verification) is presented including the description of the measurement principles, performances and their current limitations.

In section 2 rotating coils systems are discussed first, pointing out the limitations of both hardware and software related to measurement time reduction. On the hardware side, the main limitation is represented by the resolution of the current PDI integrators, based on the voltage-frequency conversion principle. A detailed state of the art on integrator devices used in other laboratories and characterized by higher resolution is hence done. On the software side, the current analysis procedure works well only for measurements in stationary conditions, whilst with varying magnetic fields, produces errors increasing as the current ramp rate increases. Two proposals of new analysis algorithms present in literature are summarized, highlighting their advantages and limitations.

In section [3] systems based on arrangements of fixed Hall plates measurement probe developed at CERN to measure at high speed the b3 and b5 harmonics is fully detailed. The requirements of the measurement instrument based on this probe are specified as well as the measurement problems discovered with the first measurements carried out with this sensor.

Finally, in section 3, the problem of the polarity test of all the LHC magnets is presented. The idea to use a system based on a rotating hall plate to determine the polarity of all the LHC magnet types, at warm conditions and with no errors is anticipated.

## II.2 - HIGH ACCURACY SYSTEMS BASED ON ROTATING COILS

Rotating coil systems are one of the most successful methods in the measurement of field and strength harmonics for accelerator magnets. Devised since 1954 [2], the method has become now widely used for magnets with cylindrical bores, in both stationary and time-varying fields.

With careful calibration, these systems deliver the field harmonics with a resolution that can reach a few ppm and a measurement uncertainty in the range of 10-100 ppm. In addition the speed of the coils can arrive at maximum value of 1 turn/s to avoid mechanical vibrations that can give problems on the measurement accuracy.

### II.2.1 - The measurement principle: The Faraday-Lenz's law

The principle of the measurement is based on Lenz's law: when a conductor loop moves with respect to a magnetic field, a flux variation occurs and a voltage is induced proportional to the time variation of the flux.

In Fig. II-1 a cylindrical surface parallel to the axis of the magnet  $z_m$  and uniform in the axial direction is considered.  $\Gamma$  designates the arc at the intersection between  $\Sigma$  and the xy plane.  $z_1$  and  $z_2$  determine the positions of the ends in the complex plane. The magnetic flux  $\Phi$  through this surface is defined by:

$$\Phi = \iint_{\Sigma} \vec{B} d\vec{\sigma}, \quad (\text{Eq. II-1})$$

with  $d\vec{\sigma}$  the surface element vector.

Since the surface is parallel to the axis of the magnet, and since  $\vec{B}$  and  $\Sigma$  are uniform along the magnet's axis:

$$\Phi = L \int_{\Gamma} \vec{B} (\vec{z}_m \times d\vec{\gamma}), \quad (\text{Eq. II-2})$$

with L the length of the surface along the  $z_m$  axis and  $d\vec{\gamma}$  the arc element vector.

Now the coordinates of  $d\vec{\gamma}$  are set to  $(dx, dy, 0)$ . The coordinates of  $(\vec{z}_m \times d\vec{\gamma})$  are  $(-dy, dx, 0)$ .

Using the two dimensional expression of the  $\vec{B}$  the flux is given by:

$$\Phi = L \text{Re} \left[ \int_{\Gamma} B_y dx - B_x dy \right] \quad (\text{Eq. II-3})$$

In complex notation it is expressed by:

$$\Phi = L \operatorname{Re} \left[ \int_{z_1}^{z_2} B(z) dz \right] \quad (\text{Eq. II-4})$$

Introducing the definition of the complex potential [1] and using the multipoles expansion series (I-1) the flux is expressed in terms of field harmonics as:

$$\Phi = L \operatorname{Re} \left[ \sum_{n=1}^{\infty} \frac{1}{n} C_n \frac{z_2^n - z_1^n}{R_{\operatorname{Ref}}^{n-1}} \right] \quad (\text{Eq. II-5})$$

Now it is assumed that the surface  $\Sigma$  represents the surface for all turns of a pick up coil rotating around the axis  $z_m$  (i.e. the windings are infinitely thin). The angle  $\theta'$  describes a rotation of the surface around the axis  $z_m$ .  $z_2$  and  $z_1$  are the positions of the extremities of the arc  $\Gamma$  at  $\theta'=0$ . So for any angle  $\theta'$  the location of the ends  $z_{1\theta'}$  and  $z_{2\theta'}$  is described by

$$z_{1\theta'} = z_1 \exp(i\theta') \quad \text{and} \quad z_{2\theta'} = z_2 \exp(i\theta') \quad (\text{Eq. II-6})$$

Using the equation (II-5) and (II-6) the flux  $\Phi$  seen by a rotating coil is

$$\Phi(\theta') = \operatorname{Re} \left[ \sum_{n=1}^{\infty} K_n C_n \exp(in\theta') \right], \quad (\text{Eq. II-7})$$

with  $K_n$  the coil's sensitivity to the  $n^{\text{th}}$  multipole:

$$K_n = \left( \frac{NwLR_{\operatorname{ref}}}{n} \right) \left[ \left( \frac{z_2}{R_{\operatorname{ref}}} \right)^n - \left( \frac{z_1}{R_{\operatorname{ref}}} \right)^n \right], \quad (\text{Eq. II-8})$$

In the equation (II-8)  $Nw$  represents the number of the coil turns, so that  $K_n$  only depends on the coil geometry.

The voltage induced by a flux change is given by Faraday's law:

$$V = -\frac{d\phi}{dt}, \quad (\text{Eq. II-9})$$

A change of flux inside the coil is achieved either by varying the magnetic field (i.e. varying the magnet current) or by rotating the coil inside the magnetic field. Here the second method, called rotating coil method, is described. The angular dependence of the flux on the angular position of the coil is shown in equation (II-7).

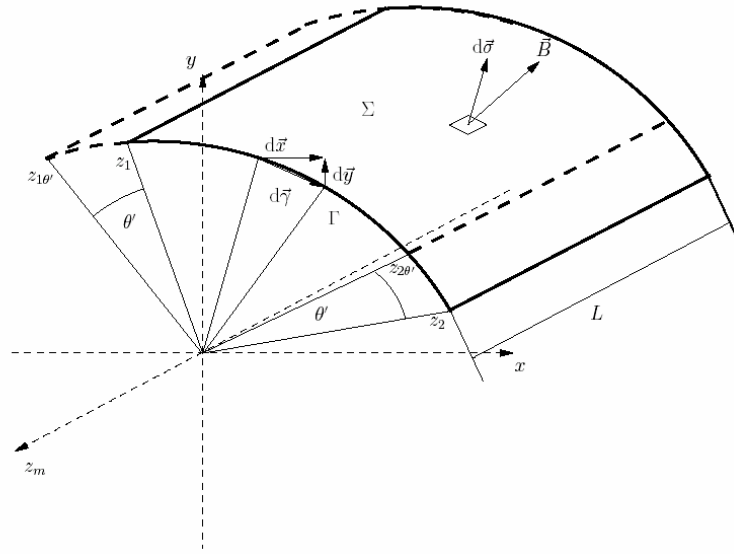


**Figure II-1: Magnetic flux through a cylindrical surface.**

In the following the magnetic field is considered to be independent from time, so that the field harmonics  $\mathbf{C}_n$  are assumed constant. Faraday's law gives the voltage versus time. To calculate the multipoles  $\mathbf{C}_n$  the flux versus angle is needed.

Therefore the measurement is performed in the following way:

- the coil is turned by a motor;
- the voltage induced in the coil is fed to an integrator;
- the integrator is read out by a controller;
- an angular encoder triggers this readout to ensure equidistant readouts. This is needed by the *standard analysis* which is based on a Fourier transform.

In the following this procedure is described mathematically. It is assumed that the  $Nw$  turn pick up coil is rotating around the  $z$ -axis with angular velocity  $\dot{\theta}(t)$ . Then the angle  $\theta'$  at a given time  $t$  equals  $\theta(t)$  and the angular speed equals its first derivative:

$$\theta' = \dot{\theta}(t) \text{ and } \frac{d\theta(t)}{dt} = \dot{\theta}(t). \quad (\text{Eq. II-10})$$

In the ideal case

$$\theta' = \omega \cdot t \text{ and } \frac{d\theta(t)}{dt} = \omega, \quad (\text{Eq. II-11})$$

with  $\omega$  the ideal (i.e. constant) angular velocity.

Faraday's law (II-9) applied to equation (II-7) gives:

$$V(t) = -\dot{\theta}(t) \operatorname{Re} \left[ \sum_{n=1}^{\infty} nKnCn \exp(in\theta(t)) \right].$$

(Eq. II-12)

The voltage is then integrated using an integrator :

$$\phi(t) = -\int_0^t V(t') dt', \quad (\text{Eq. II-13})$$

assuming that the integration starts at  $t = 0$ .

The angular encoder triggers the readout of the integrator to ensure equally spaced angular steps. Since  $\theta(t)$  gives the position of the coil versus time, its inverse function  $t = \theta^{-1}(\theta')$  describes the time at which an angle was reached. Thus the flux  $\Phi_i$  given by the integrator for an angular interval  $\theta'_i - \theta'_0$  as:

$$\phi_i = -\int_{\theta^{-1}(\theta'_0)}^{\theta^{-1}(\theta'_i)} V(t) dt. \quad (\text{Eq. II-14})$$

$\theta'_0$  is the angle at which the integration started and  $\theta'_i$  :

$$\theta'_i = \frac{2\pi}{P} i \quad i=1\dots P, \quad (\text{Eq. II-15})$$

with P the number of readings per revolution. The flux  $\Phi_i$  can be further written as

$$\phi_i = -\int_{t_0}^{t_i} V(t) dt = \int_{\theta_0}^{\theta_i} \frac{1}{\dot{\theta}} V(\theta) d\theta. \quad (\text{Eq. II-16})$$

$\Phi_i$  corresponds to the value of the integral at  $t_i$ . Comparing the last term of the above statement to Equation (II-12) it is evident that  $\Phi_i$  is speed independent. A discrete Fourier transform is applied to the total readout  $\Phi = \{\Phi_i \mid i = 1 \dots P\}$  of the integrator

$$\psi = \text{DFT} [\Phi], \quad (\text{Eq. II-17})$$

with  $\psi$  the spectrum of the flux and DFT the discrete Fourier transform. It can be showed [2] that the multipoles  $C_n$  are given by:

$$C_n = \frac{1}{Kn} \psi_n. \quad (\text{Eq. II-18})$$

## II.2.2 - Experimental Setup

The rotating coil shafts are inserted into the anti-cryostat in the two magnet apertures (Fig. II-2). The twin-rotating unit simultaneously drives the two shafts. The voltage signals from the coils are amplified in a mobile rack. The data acquisition and a first harmonic analysis are carried out in electronic racks using the data treatment explained earlier.

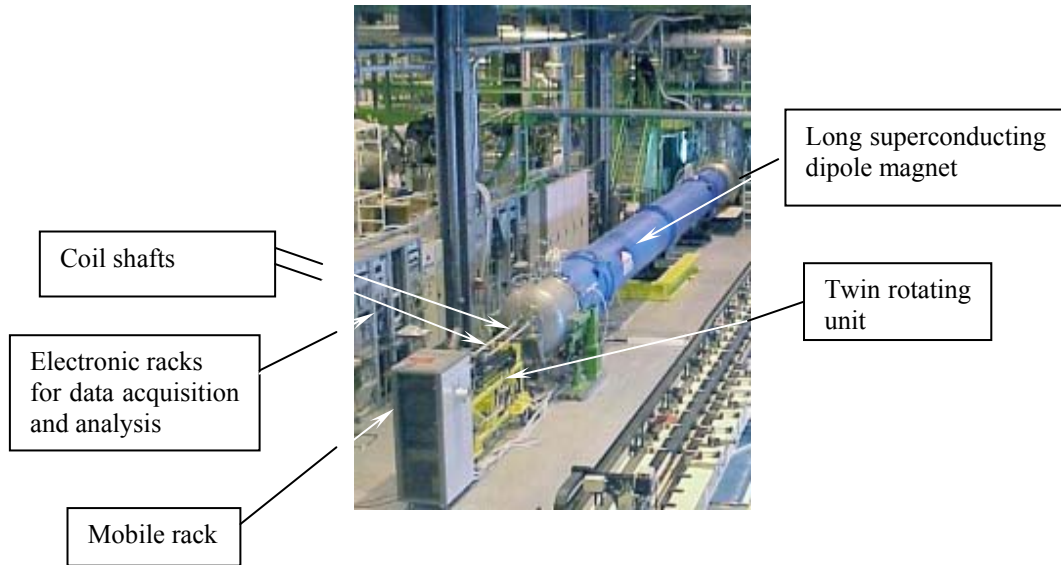


**Figure II-2: Rotating coil test set-up in a long dipole magnet in the SM18 laboratory**

### II.2.2.1 - The coils

The measurement of the magnetic field is realised using tangential rotating coils mounted on a 16-m long ceramic shaft. The shaft is obtained by assembling thirteen modules of approximately 1.25m lengths each [3]. This covers the 15m length of the LHC dipole and the adjacent corrector magnets. All modules are identical to allow interchange of position and easy management spares. The module cross-section is shown in Fig.1. Ceramic ( $\text{Al}_2\text{O}_3$ ) is the material used for the support [4]. The ceramic has a high rigidity and geometric stability both mandatory for proper calibration of the coil sensitivity. In addition this material is non-magnetic and non-conducting, thus can turn freely in a magnetic field without perturbing it. The support has a simple geometry, i.e. a hollow cylinder equipped with tangential coils. Each coil can be calibrated individually and matched to other coils with the same cross-section to achieve the highest possible dipole compensation ratio. To simplify the setup and ensure better accuracy, the LHC dipoles are therefore equipped with an anticryostat (a warm bore) with a 40mm inner diameter. This imposes a maximum outer diameter of 36mm to the rotating coil, to leave enough clearance for installation and operation.

Each module is made up of three coils: two tangential coils and one centred. A single coil is insufficient to measure the small multipole field components of high order ( $b_3, b_5, b_7$  and  $b_9$ ) in the presence of the large dipole background field. This is the reason for using an analog bucking: a configuration of two coils with equal width and equal number of turns connected electrically in series with opposite polarity, the central coil and one tangential coil (a second tangential coil is used as a spare). The dipole contribution to the "compensated signal"  $V_{comp} = V_{central} - V_{tangential}$  vanishes. The dipole field, "absolute signal" is from  $V_{tangential}$  only.

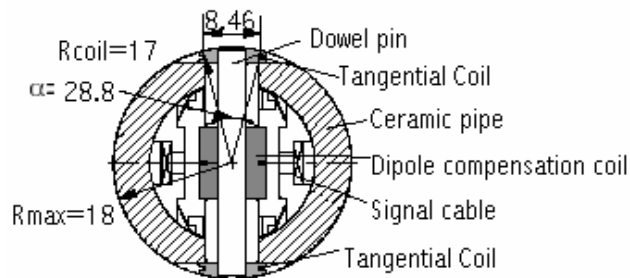


**Figure II-3: Cross-section module showing details of support and coils.**

The sensitivity of a tangential coil to a harmonic of order  $n$  depends strongly on the opening angle  $\alpha$  of the coil. In particular the sensitivity of the coil is zero when the harmonic order is equal to a critical value  $n = 2\pi/\alpha$ . The opening angle is a geometrical quantity defined by the coil rotation radius and the width of the coil (Fig.II-3). The coil rotation radius is maximised to increase the sensitivity to higher order harmonics. This radius is limited to about 17mm by the space available in the anticryostat. The nominal opening angle is  $28.8^\circ$  [5], that corresponds to zero sensitivity to the harmonic of order 12.5.

As shown in Fig.2, each coil module is completed at one end with a ceramic (SiN) flange (h) that houses an integrated ceramic ball bearing (a) in a brass cage equipped with beryllium-copper rollers (b). The rollers allow moving the shaft inside the warm bore. At the other end a small Ti-

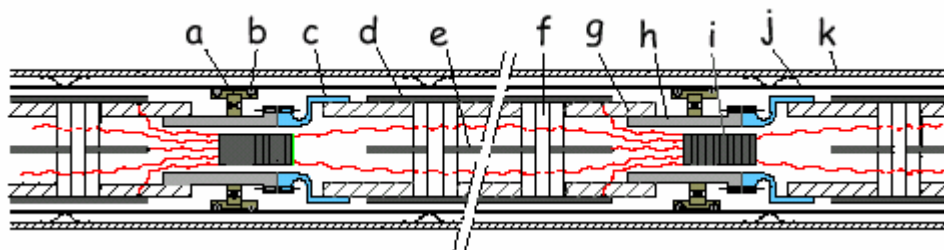


**Figure II-4: Schematic assembly of a module showing the main components: (a) ball bearing, (b) brass cage with roller, (c) Ti-bellow, (d) tangential coil, (e) central coil, (f) dowel pin, (g) ceramic support, (h) SiN flange, (i) cable connector, (j) anticryostat, (k) cold bore.**

bellows is glued on the module (c). The titanium bellows has a flange mating with the opposite ceramic support, so that the modules can be mechanically assembled. The function of the bellows is to accommodate the curvature of the dipole cold bore (k) (0.4mrad at each junction) as well as the anticryostat (j) centring errors in vertical and horizontal direction.

#### II.2.2.2 - Twin rotating units

A Twin Rotating Unit (TRU) shown in Fig.II-5 drives the two coil shafts. The nominal rotation speed is 1Hz with variations smaller than 3% [3]. The acquisition software remotely controls the operation of the unit. An angular encoder gives the angular position of the shaft with 4096 counts per revolution plus a “zero” pulse on a separate channel. The encoder housing is rigidly connected to an electronic inclinometer, giving an absolute reference for the orientation of the encoder “zero”. Furthermore the TRU side of the shaft is provided with a reference surface, aligned with the reference surface on the coil shaft.



Figure II-5: Twin rotating unit.

Each measurement cycle consists of three turns in alternating direction. The first turn is for accelerating the shaft in order to get the right constant rotation speed. The read-out is executed during the second turn with constant rotation speed. The last turn is for decelerating the shaft so as to change the rotation direction. This mode is called *washing machine* mode [6]. The final measurement results are obtained from the average of the forward and backward revolutions

#### II.2.2.3 - PDI Integrators

Digital integrators have been the basic electronic tool for magnetic measurements at CERN since the 80's. The CERN Portable Digital Integrator (PDI model AT 680-2030-050) first designed mostly realised by P. Galbraith [7], has been in use for now over 20 years. The CERN integrator

principle has been perfected and commercialised by Metrolab in its gain-programmable PDI-5025 model [8].

In this integrator the voltage from the induction coil  $V_{in}$  is sent, after conditioning and amplification, to a Voltage-to-Frequency Converter (VFC) whose output is a square signal with frequency  $f$  proportional to the VFC input voltage. This signal is then entered in a counter that accumulates the number  $n$  of square pulses during a measurement period  $\Delta t$  starting at  $t_{start}$  and ending at  $t_{end}$ . The frequency  $f$  of the square signal is equal by definition to the time derivative of the number of pulses  $dn/dt$ , and the output of the counter is, apart for the amplifier gain  $g$  and a proportionality constant  $K_{VFC}$ , a digital measurement of the integral of the input voltage:

$$n = \int_{t_{start}}^{t_{end}} f dt = g K_{VFC} \int_{t_{start}}^{t_{end}} V_{in} dt \quad (\text{Eq. II-19})$$

The flux increment  $F$  is then obtained as:

$$F = \frac{n}{g K_{VFC}} \quad (\text{Eq. II-20})$$

The digital integrator achieves high accuracy thanks to the conversion to frequency domain. The limiting elements in this concept are the stability and linearity of the VFC, and the resolution of counting operation that depends on the maximum operation frequency of the VFC. Hybrid technology VFC's have linearity and stability of better than a few ppm over the whole range of input voltage. The typical maximum frequency of operation is 1 MHz. In order to make the circuit practical some additional features are added to the basic scheme described above. Commercial VFC circuits work only with single polarity voltage, e.g. 0 to 10 V, while the signal from an induction coil can have both polarities. The dual polarity capability is restored by shifting the input voltage by a precise and stable reference  $V_{ref}$  whose effect is to place the input zero exactly in the middle of the VFC range. This offset is then eliminated after counting, subtracting the counts from a reference source  $f_{ref}$  oscillating at exactly half of the maximum frequency of the VFC. Another technical detail that allows to avoid dead times during the transfer of the result from the buffer of the counter to the downstream circuitry is to use two parallel counters working in alternance. This technique is very effective and results in the cancellation of cumulative errors: a count lost due to the trigger detection uncertainty is recovered in the next flux variation measurement.

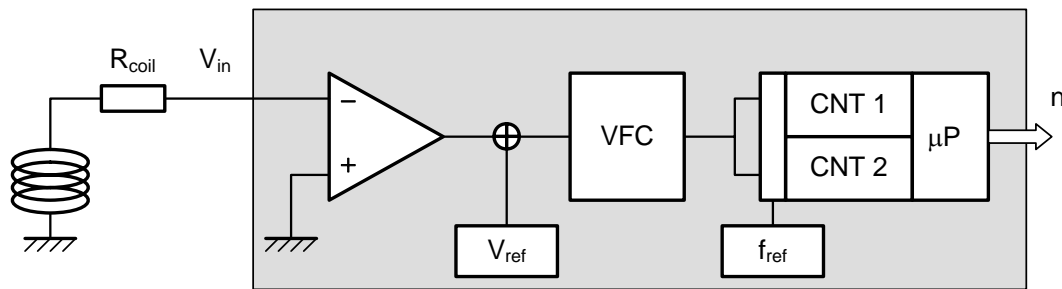


**Figure II-6: Principle of the digital integrator based on voltage-to-frequency conversion**

#### II.2.2.4 - Data Acquisition system

The voltages induced from coil sections are readout at the same time by the PDI integrators triggered by the angular encoder. The integrated voltages are equal to the flux changes through the measuring coil for all angular steps, and rotating velocity variations during the measurements are

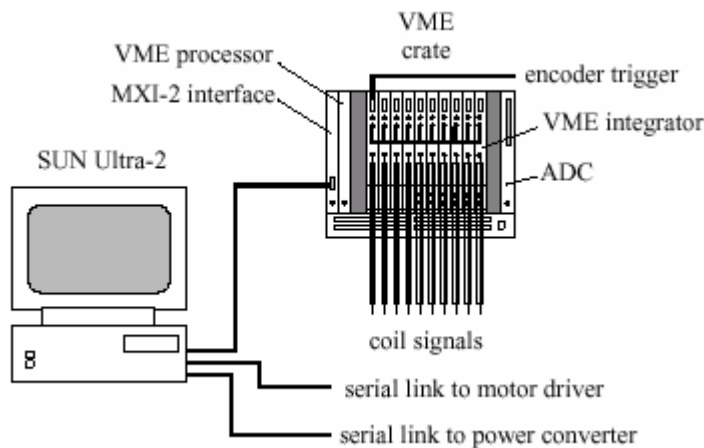


**Figure II-7: Block diagram of the rotating coils DAQ system.**

compensated up to the first order. A real-time processor configures the integrators and reads the integrated voltages. Integrators and processor are mounted on a VME-bus (Versa Module Europa, IEEE 1014-1987 standard) [9]. Overall control of the power supply, of the precision current reading, of the motor rotating the shaft and of the integrators is achieved using a LabVIEW software [10] running on a SUN Ultra-2 workstation. Fig. II-7 shows the block diagram of the DAQ system.

Flux increments  $\Delta\Phi_i$  are therefore available at each angular interval and express the magnetic flux change over an angular step (integral of coil voltage). The integrator provides also the time interval between the two pulses. The raw data are the stored flux increments and the time intervals. The value of the flux  $\Phi_k$  for an angle  $\theta_k$  is the sum over the flux increments  $\Delta\Phi_i$ ,  $i \leq k$ . Each  $\Delta\Phi_i$  is

the average of measurements obtained during a backward and forward rotation. The averaging over forward and backward rotation cancels the systematic offset in the angular encoder and symmetric torsion effects.

### *II.2.3 - The new measurement requirements*

Finally, at present, the typical measurement time of this system is about the 15 seconds (in the washing mode, 3 turns in each opposite direction are performed in order to reach a constant speed of the coil before doing the acquisition).

If for the usual measurements on dipoles and quadrupoles this time can be considered acceptable, now the measurement speed has become a critical point.

The rotating coils system will be used also for the potential Reference Magnets System on-line [11]. For this application the field harmonics coming from the reference magnets (3 dipoles and 1 quadrupole) shall be delivered in a time dictated from the control frequency of the LHC corrector magnets. Since this frequency is around 2 Hz, in order to use the experimental data together with the field model to provide the expected current law to download in the LHC spool pieces, the measurement time of the reference magnets field harmonics has to be around one hundred ms.

The dynamic effects in superconducting magnets as the snapback in the dipoles during the current injection is a fast phenomena (the full duration is about 60 seconds). For a correct observation a measurement time of the field harmonics maximum of few hundredths of milliseconds is required.

Therefore, the rotating coils system will be used for measurements of fast pulsed magnets such as prototypes for FAIR at GSI or for the upgrade of the CERN injector chain characterized by very high ramp rates.

Mechanical improvements to the current system in order to reach continuous coils rotation at speed of some Hz, by themselves, don't assure the satisfaction of the new requirements. The following limitations have to be taken into account:

- the PDI integrators are characterized by a resolution that is not enough to resolve rapid flux variations in measurement at high ramp rates as well as small flux increments consequents to a higher trigger frequency;
- the standard analysis is based on the assumption that the field harmonics are constant during one complete coil turn. The error in the estimation of the field harmonics of varying magnetic fields increases with the current ramp rate.

### II.2.3.1 - The hardware limitations: PDI integrators

In the following section the operational limits for the digital integrator as used today at CERN for the measurement of the magnetic field are examined. The discussion is made in terms of the output of the integrator  $F$  (in [Vs]), as a function of the integration time  $\Delta t$  (in [s]).

#### *Input voltage limit*

Using standard instrumentation electronics, it is common to limit the input voltage to the analog-to-digital converter to a signal in the range of few V. This is the range of the VFC used in the present integrator version, which has a 0...10 V input range. equivalent, in bi-polar mode, to a  $|V_{max}| = 5$  V maximum voltage input. The maximum flux that can be integrated is then:

$$F_{max} = V_{max} \Delta t \quad \text{(Eq. II-21)}$$

This is a straight line with slope 1 in a log-log plot of  $F$  vs.  $\Delta t$ , passing through the point (5 Vs, 1s).

#### *Integrator noise*

The electronic noise generated by the input analog front-end can be assumed gaussian with a white spectrum, zero average and a standard deviation  $\sigma_{noise}$ ;

The white noise spectrum is shaped-filtered by a factor  $1/f$  in the ideal integrator, where  $f$  is the frequency of the signal. Hence, the high frequency components in the noise are reduced with respect to the low frequency components. At the same time the integration time  $\Delta t$  acts as a time window on the input noise of the integrator. As shown in the next chapter the noise at the integrator output is given by:

$$\sigma_y = \sqrt{\Delta t} \cdot \sigma_{noise} \quad \text{(Eq. II-22)}$$

Then, the standard deviation at the output of the ideal integrator is the product of the standard deviation of the input noise and the integration time. Therefore, the integration noise increases with integration time.

Instead of the noise standard deviation, it is common to refer to the peak-peak noise level that can be found in amplifier's datasheets. In Table 1 the values experimented on the analog front-end of the PDI integrators are shown:

G=1	10 $\mu$ V
G=10	1 $\mu$ V
G=100	0.3 $\mu$ V

**Table II-I: Input voltage noise (peak-peak)**

### *Integration Offset*

The second limit due to input analog electronics is the offset at the integrator input. It produces a drift of the integrator that is proportional to the integration time:

$$F_{offset} = V_{offset} \Delta t \quad (\text{Eq. II-23})$$

In the log-log plot of  $F$  vs.  $\Delta t$ , the above relation is a straight line with slope 1 passing through the point ( $V_{offset}$  Vs, 1s), where  $V_{offset}$  is typically 7  $\mu$ V.

### *Resolution*

The resolution of the integrator system is defined as the minimum flux variation appreciable in the output. The minimum flux value measurable is obtained considering only one pulse of the VFC output counted, so from the Equation (II-20) for  $n$  equal to 1 it follows:

$$F_{min} = \frac{1}{ki} \quad (\text{Eq. II-24})$$

The worst resolution is obtained for unit gain of the input amplifier unit, given by the inverse of the transfer function of the VFC used. The integrators currently used at CERN have a VFC characterized by a maximum frequency of 500 kHz at 10 V then:

$$F_{min} = 2 \cdot 10^{-5} \text{ Vs for } G=1$$

and is a constant, independent of the integration time.

In the log-log plot of  $F$  vs.  $\Delta t$ , the above relation is a horizontal line. It must be noted that the digital resolution imposes a hard limit on the integral, as any flux increment below this value is

effectively *lost*. It is hence mandatory that the operation is adapted so that the input signal is several times larger than the resolution.

*Minimum integration time*

The minimum integration interval is limited by the VFC maximum frequency. In fact, under the assumption that the integration trigger is synchronized with the VFC clock, the minimum interval time is equal to the minimum VFC period that is,  $2 \cdot 10^{-6}$  s.

The above limits are shown in Fig. II-9, obtained for the case of an input gain of 1 (as used for absolute coil signals). In the plot are also reported the operating points for typical rotating coil systems presently used at CERN (blue squares), as well as the projected operating points for fast systems adapted to the harmonic measurements in pulsed magnets.

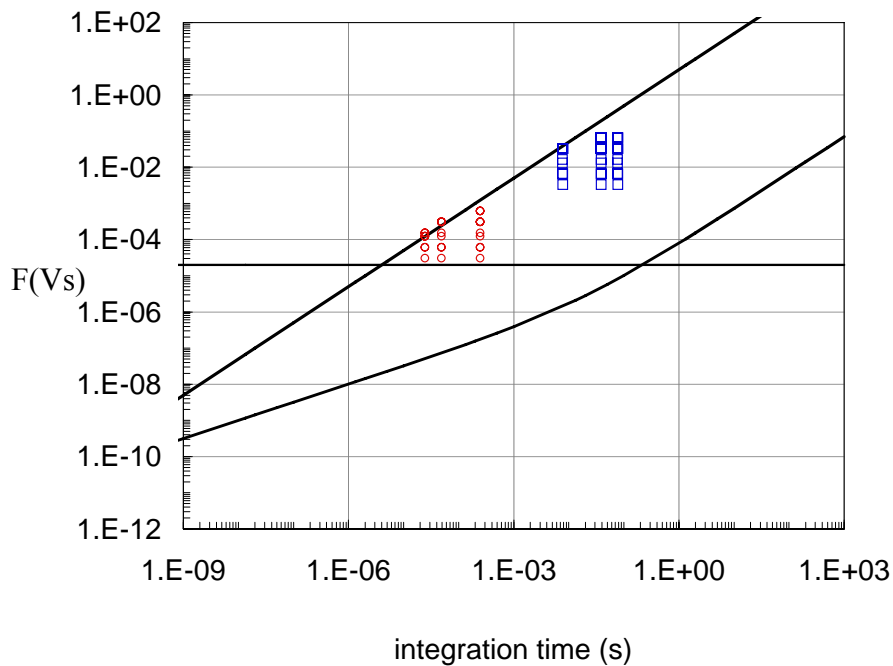


**Figure II-8: Operating limits of the PDI integrators**

It is evident from the plots reported that the integrators are suitable for the present measurements (trigger frequency in the range of few 10's to few 100's Hz), with two orders of magnitude margin with respect to the digital resolution and well above the analog noise limits. An increase of a factor 100 on the acquisition speed (trigger frequency in the range of few 1000's to few 10000's Hz), will result in a drastic reduction of the working space.

This is in fact the main reason why the realisation of a digital integrator based on an alternative design is needed.

### II.2.3.2 - The standard analysis limitations

The standard analysis operates with success only in stationary conditions and it exploits the nice property of harmonic coefficients  $C_n$  to be a linear function of the discrete-time Fourier transform (DFT) of the acquired flux samples. In the presence of non-stationary magnetic fields (due, for instance, to LHC current ramps), the standard procedure does not work properly.

Inaccuracy is principally due to the spectrum spread related to the variation of the fundamental harmonic coefficient in a single coil turn. Hardware solutions such as analog bucking or increasing coil rotation speed are insufficient to completely eliminate the problem.

### II.2.4 - New integrators: State of the art

The main laboratories involved in magnetic measurement and the technologies used for voltage integration are resumed in the Tab. II-II.

<b>Laboratories</b>	<b>Technology for magnetic measurement</b>
<b>Fermi LAB</b>	<i>Architecture based on the chain ADC-DSP is being developed</i>
<b>CEA SACLAY</b>	<i>Architecture based on the Analog digital conversion; developing of the test method with a PXI rack</i>
<b>Los Alamos National Laboratory</b>	<i>Metrolab Instrument (PDI)</i>
<b>Japan Atomic Energy Research Institute</b>	<i>3 Voltage-to-Frequency at different full scale + Counters; DSP chooses the best measurement</i>
<b>Shangay National Synchrotron Radiation Center</b>	<i>Metrolab Instrument (PDI)</i>
<b>Stanford Linear Accelerator Center (SLAC)</b>	<i>Metrolab Instrument (PDI)</i>

**Table II-II: Digital integrator solutions used in the main laboratories**

#### II.2.4.1 - FERMILAB

A voltage integrator based on the chain of a Programmable Gain Amplifier (PGA), an analog-digital converter (ADC), and a Digital Signal Processor (DSP) has being developed for the measurement of the magnetic field by the rotating coil system. The ADC is the Pentek model 6102 and the DSP is the Pentek model 4288. The Pentek 6102 is an ADC with 16-bit resolution and a maximum sampling rate of 250 kHz. The Pentek 4288 is a DSP at 40 MHz with a computing power up to 120 MFLOPS. The communication is performed through a proprietary high speed mezzanine

bus, Intel's Modular Interface eXtension (MIX). The coil signal is sampled at 40-50 kHz and then integrated. The flux values are transferred to the VME accessible memory for reading by the control VME PPC computer. The performances in terms of trigger frequency, resolution in Vs and accuracy are not clearly mentioned [12].

#### **II.2.4.2 - CEA SACLAY**

In 1999 the CEA has patented a new integrator device. The voltage signal is sampled by an ADC, 16 bit-resolution and maximum sampling rate of 100 kHz and then the data are managed by a numeric board. The first release is based on a PXI platform; CEA is looking for an industrial partnership for further developments [13].

#### **II.2.4.3 - Los Alamos National Laboratory**

For the determination of the multipole content of the magnetic field at the rotation speed of 14 turns/min the Metrolab voltage integrator has been used. The voltage integrator has been connected to a Macintosh computer via a GPIB interface [14].

#### **II.2.4.4 - Japan Atomic Energy Research Institute**

A new integrator with high input voltage has been developed. This integrator uses Voltage to frequency converters (VFC) combined with up-down counters (VFC-UDC). To reduce errors due to VFCs input saturation, the new digital integrator is composed of three VFC-UDC units in parallel with different input ranges and a DSP that selects the best integrated output at a sampling frequency of 10 kHz, according to input level. Linearity errors of the VFC: 0.002% of full scale  $\pm 10$  V; dead band 0.02 mV [15].

#### **II.2.4.5 - Shangay National Synchrotron Radiation Centre**

A rotating coil magnetic measurement system has been built at SSRC to measure the quadrupole and sextupole magnet prototype of its accelerator. Metrolab PDI-5025 is used to integrate the flux linkage; the data in ASCII format are then transferred to the PC via GPIB [16].

#### **II.2.4.6 - Commercial Measurement Instruments**

In the following the instruments found on the market to perform the integration of an input voltage are reported.

##### *Metrolab PDI 5025*

The Metrolab Instrument PDI 5025 is very diffused in accelerator research laboratories. This integrator is based on the Portable Digital integrator developed at the CERN, using a chain of a

VFC and two up-down counters. It is built by Metrolab Instrument SA, Geneva, Switzerland. The main electrical features can be found in [17].

*Wenking EVI 95*

Wenking *EVI 95* is a long term integrator. An analog circuit integrates the input signal up to a precisely set voltage level detected by a discriminator circuit. At this discrimination level the integrating capacitor is discharged to zero immediately and charged again. The number of discharges is counted by a dual six decade counter, separately for each polarity. The instrument is capable to integrate over a time period from less than 1 s to more than 10000 hours. The main features of this instrument are shown in the Tab. III [18].

Output range	1 Vs, 2 Vs, 5 Vs up to 1000 Vs
Input offset current	$< 10^{-12}$ A at 25 °C
Short-term offset voltage drift	$< 2 \mu\text{Vh}^{-1}$ and $10 \mu\text{V}^{\circ}\text{C}^{-1}$
Long-term offset voltage drift	$< 20 \mu\text{V}$ per 100 hours
Accuracy of range resistors	0.1% (1 Vs to 10 Vs), 0.25% (20 Vs to 200 Vs), 1% above.

**Table II-III: Wenking, model EVI 95 main feature**

*RDM-Apps VII0F*

This instrument presents a low pass active filter, with an adjustable cut-off frequency, adjustable time constant by potentiometer or digitally. The main features are resumed in Tab. IV [19].

Input voltage range	$\pm 10$ V
Minimum time constant	0.01 s
Maximum time constant	10 s
Accuracy (10 °C to 40 °C)	$\pm 0.2$
Offset voltage drift	$\pm 20$

**Table II-IV: RDM-Apps VII0F main features.**

### *A square root voltage-to-frequency converter*

This instrument has been published at the IEEE transactions on instrumentation and measurement. It is a clock-controlled voltage-to-frequency converter in which the output is proportional to the square root of the input voltage. It is based on the working principle of the double ramp converter; indeed it presents the big advantages of such converter, as the independence from analog front end circuit parameters (resistors and capacitors), reaching an accuracy of about 0.02 % of full scale for the voltage input range from 1 mV to 10 V if it is built with 18 V CMOS components and auto-zero amplifier (very low offset). This instrument cannot work at high frequency because of the limitations of the double ramp converter [20].

### *II.2.4.7 - Discussion*

The main accelerator laboratories use the Metrolab PDI 5025 or they are developing new fully digital instruments. In particular, Fermi Lab is oriented towards a solution based on the chain of an ADC and DSP to perform the integration in the numeric domain; the solution is partly based on commercial solution. No technique to improve the integration accuracy aimed at reducing the effect of the uncertainty on the trigger detection has been described in the literature. The measurement instruments present on the market, apart for the Metrolab PDI (based on CERN experience), do not assure high accuracy; the maximum accuracy (0.02% of full scale) is reached by the voltage-to-frequency converter presented at the IEEE [20] but it is based on the scheme of the double ramp converter, which cannot assure high trigger frequency.

### *II.2.5 - New analysis algorithms: State of the art*

Some efforts to improve analysis algorithms to reduce the error in the harmonics estimation during measurement in a varying magnetic field are present in literature. A. Jain at Brookhaven National Laboratory proposed an iterative algorithm to correct the averaged field coefficients measured at each coil turn [21]. The analysis is based on the definition of a  $C_{avg}(n)$  that is the n-th harmonic strength corresponding to the average current over one coil turn. The instantaneous harmonic value  $C_n(t)$  is expressed as  $\frac{C_{avg}(n)}{I_{avg}} I(t)$  as well as  $\frac{\partial C_n(t)}{\partial t} = \frac{C_{avg}(n)}{I_{avg}} R(t)$  where  $R(t)$  is the current ramp rate. By knowing the magnet supply current, i.e., the average current as well as the ramp rate every coil turn, thanks to an iterative procedure the  $C_{avg}(n)$  value are estimated. It was proved that for polynomial current ramps, convergence is reached in three or four iterations.

A preliminary investigation of the error produced by the standard analysis for measurements with high ramp rates was carried out by T.Ogitzu [22]. A method based on the 2D fit of the flux surface as a function of the time and the coil angular position acquired on many coil turns was proposed. The basic idea is to recover, by means of interpolation, the flux samples related to a complete coil at the same time instant (during the acquisition consecutive flux samples are taken at different times, depending on the coil speed). In this way, in post processing, the standard analysis is applied at different sections of the flux surface, each one related to a different time, delivering the field coefficients at the given time [23].

The algorithms already present in literature have several drawbacks such as the need for information about magnet current, or they cannot be implemented in Real-Time, as they resume post processing large amounts of data.

### ***II.3 - Systems based on fixed hall plates***

A different kind of measurement devices with good time and spatial resolution is needed to better resolve in time the snapback evolution and to observe the spatially periodic field pattern during the decay. A sensor with a high acquisition frequency and that can give local measurements along a periodic field pattern of approximately 125 mm was developed at CERN [24, 25, 26]. The idea was to use rings of Hall probes for magnetic measurements. The device was derived from an old prototype version that includes only two  $b_3$  sensors. Details and results obtained from the first Hall probe sensor can be found in [27]. The new device contains six sextupole sensor rings placed over a length of 125 mm and two decapole sensor rings displaced at half cable twist pitch (55 mm).

Rotating coils technique has the advantage to give in a single measurement cycle all the field harmonics. With Hall probes a limited number of components depending on the geometry of the sensor are measured. In this case the sensor was planned to measure the first two allowed harmonics after the dipolar one: the sextupole and the decapole components.

The  $b_3$ - $b_5$  sensor developed at CERN allows measurements of the decay and snapback at a higher acquisition frequency (3-10 Hz) resolving properly the snap back phenomenon in time. Moreover Hall plates are small (active region  $0.1 \times 0.1 \text{ mm}^2$ ) and so they give point-like measurements that allow the local characterization of the field component along a cable twist pitch.

In principle, it is possible to measure any  $m$ -th order harmonic of the field using an appropriate arrangement of Hall plates. The voltage signal of a single probe provides local information on the average value of the total field over the active surface of the probe; the resolution of high order harmonics requires a particular disposition of a set of probes. Such a disposition for magnetic

measurements is well known and has been used by Bruck on the HERA superconducting magnets to measure the time variation and the longitudinal periodicity of the sextupole field component [28].

### II.3.1 - The measurement principle

To measure the  $m$ -th order harmonic of the magnetic field inside the magnet bore, one can use  $m$  Hall probes connected in series and placed tangentially to a ring at a radial distance  $R$  and at the azimuthal angles  $2\pi m^{-1}$ . Such placement allows the compensation of all the lower order components giving a signal proportional to the  $m$ -th order harmonic only. The measured signal for the field component of order  $m$  can be maximized if all Hall plates are placed in the poles of the  $2m$ -pole field.

The magnetic field  $B$  inside the magnet bore is considered in the 2-dimensions approximation. For convenience a cylindrical coordinate system is used. Every point inside the magnet cross section can be identified by a radius  $\rho$  and an angle  $\theta$  (measured starting from the horizontal axis). Inside the magnet bore the magnetic field can be expressed in its radial and tangential components; each component can be expanded in series as follows [29]:

$$\begin{aligned}
 B_r &= \sum_{n=1}^{\infty} \left( \frac{r}{R_{ref}} \right)^{n-1} [B_n \sin(n\theta) + A_n \cos(n\theta)] \\
 B_\theta &= \sum_{n=1}^{\infty} \left( \frac{r}{R_{ref}} \right)^{n-1} [B_n \cos(n\theta) - A_n \sin(n\theta)]
 \end{aligned}
 \tag{Eq. II-25}$$

where  $B_n$  and  $A_n$  are the normal and the skew multipoles of order  $n$  as defined in Eq.I-5.

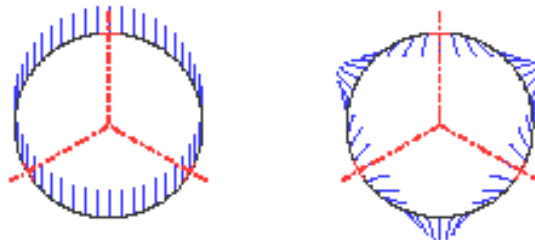


**Figure II-9: Working principle of the sextupole probe. The field vectors are shown for a dipole (left) and for a sextupole (right).**

Consider a circle of radius  $R$ , centered in the origin of the cylindrical coordinate system. On this circle the magnetic field associated with a multipole of order  $n$  is a rotating vector of constant

module with an angular rotation frequency equal to the order of the multipole. As shown in Fig. II-10, a disposition of  $m$  Hall plates placed on the circle at equispaced angular intervals, measure the radial component of the total field at these positions.

If  $\varphi$  indicates the angle corresponding to the first probe, and  $\theta_j$  ( $j=1$  to  $m$ ) the angle corresponding to a generic probe [30]:

$$\theta_j = \varphi + j \frac{2\pi}{m} \quad (\text{Eq. II-26})$$

The sum signal  $S$  coming from  $m$  probes placed as described above is given by the following formula:

$$\begin{aligned} S &= \sum_{j=1}^m \sum_{n=1}^{\infty} \left( \frac{R}{R_{ref}} \right)^{n-1} [B_n \sin(n\theta_j) + A_n \cos(n\theta_j)] = \\ &= \sum_{n=1}^{\infty} \left( \frac{R}{R_{ref}} \right)^{n-1} \left\{ B_n \sum_{j=1}^m \left[ \sin \left( n\varphi + n j \frac{2\pi}{m} \right) \right] + A_n \sum_{j=1}^m \left[ \cos \left( n\varphi + n j \frac{2\pi}{m} \right) \right] \right\} \end{aligned} \quad (\text{Eq. II-27})$$

Considering the complex representation of the sine, and expressing the finite sum of sine waves on the right hand side of Eq. 3-3, we obtain:

$$\sum_{j=1}^m \left[ \sin \left( n\varphi + n j \frac{2\pi}{m} \right) \right] = \sum_{j=1}^m \left[ \text{Im} e^{i \left( n\varphi + n j \frac{2\pi}{m} \right)} \right] = \text{Im} \sum_{j=1}^m \left[ e^{i \left( n\varphi + n j \frac{2\pi}{m} \right)} \right] \quad (\text{Eq. II-28})$$

At this point two cases have to be distinguished:

- the ratio between the harmonics order  $n$  and the number of probes  $m$  is integer and equal to  $k$
- the ratio between the harmonics order  $n$  and the number of probes  $m$  is not integer

In the case (a) the sum in Eq. II-28 can be expressed as follows:

$$\text{Im} \sum_{j=1}^m \left[ e^{i \left( n\varphi + n j \frac{2\pi}{m} \right)} \right] = \text{Im} \sum_{j=1}^m \left[ e^{i (n\varphi + jk2\pi)} \right] \quad (\text{Eq. II-29})$$

As  $jk$  is an integer number, the complex numbers which are summed in the right hand side of Eq. II-29 have a phase shift multiple of  $2\pi$ , which means that they all have the same phase.

The sum in Eq. II-29 can be then expressed as follows:

$$\text{Im} \sum_{j=1}^m \left[ e^{i (n\varphi + jk2\pi)} \right] = m \text{Im} e^{in\varphi} = m \sin(n\varphi) \quad (\text{Eq. II-30})$$

In the case (b), the sum in Eq.II-28 can be written in the following form:

$$\text{Im} \sum_{j=1}^m \left[ e^{i \left( n\varphi + n j \frac{2\pi}{m} \right)} \right] = e^{in} \text{Im} \sum_{j=1}^m \left[ e^{i \left( \varphi + j \frac{2\pi}{m} \right)} \right] \quad (\text{Eq. II-31})$$

The complex numbers in the sum at the right hand side of Eq. II-31 have the same module (equal to 1), and, independently of  $m$ , their phase shift is such that their sum is always equal to zero.

The same kind of demonstration can be followed for the sum of cosines at the right hand side of Eq. II-27, so that finally the following expression for the sum signal  $S$  according to the ratio  $\frac{n}{m}$  is obtained :

$$S = \begin{cases} \sum_{n=1}^{\infty} \left( \frac{R}{R_{ref}} \right)^{n-1} [m B_n \sin(n\varphi) + m A_n \cos(n\varphi)] & \text{for } \frac{n}{m} = k \text{ with } k \text{ integer} \\ 0 & \text{for } \frac{n}{m} \text{ not integer} \end{cases} \quad (\text{Eq. II-32})$$

The only harmonics that contribute to the sum signal are the normal and skew multipoles of order multiple of the number of probes,  $km$ . Thus with this configuration the dipole field is suppressed and information about the  $m$ -th component and higher multipoles are obtained. Furthermore the signal generated by the normal  $m$ -th multipole can be maximized if the first sampling point is set at an angle  $\varphi = 90^\circ$  as in Fig. II-11. In this particular case:

$$\sin(n\varphi) = \begin{cases} \sin\left(\frac{n\pi}{2}\right) = (-1)^{\frac{n-1}{2}} & \text{for } n \text{ odd } \quad n = 1, 3, 5, \dots \\ 0 & \text{for } n \text{ even } \quad n = 2, 4, 6, \dots \end{cases} \quad (\text{Eq. II-33})$$

$$\cos(n\varphi) = \begin{cases} 0 & \text{for } n \text{ odd } \quad n = 1, 3, 5, \dots \\ \cos\left(\frac{n\pi}{2}\right) = (-1)^{\frac{n}{2}} & \text{for } n \text{ even } \quad n = 2, 4, 6, \dots \end{cases} \quad (\text{Eq. II-34})$$

The consequence is that only the normal odd and the skew even multipole of  $m$  contribute to the sum signal  $S$ . Being  $k = \frac{n}{m}$ , if  $m$  is odd its multipole of order  $k$  ( $k = 1, 2, 3, \dots$ ) are alternatively even and odd so that the sum signal can be written as,

$$S = \sum_{k=1}^{\infty} \left( \frac{R}{R_{ref}} \right)^{(2k-1)m-1} (-1)^{\frac{(2k-1)m-1}{2}} m B_{(2k-1)m} + \sum_{k=1}^{\infty} \left( \frac{R}{R_{ref}} \right)^{2km} (-1)^{km} m A_{2km} \quad (\text{Eq. II-35})$$

For the probe realized at CERN the Hall plate sensors are of two types: a sextupolar and a decapolar ring with  $m=3$  and  $m=5$  probes, respectively (Fig. II-11). In these two particular cases the total sum signal is given by:

$$S_{sextupole} = \sum_{k=1}^{\infty} 3 \cdot \left( \frac{R}{R_{ref}} \right)^{3(2k-1)-1} B_{3(2k-1)} + \sum_{k=1}^{\infty} 3 \cdot \left( \frac{R}{R_{ref}} \right)^{6k-1} (-1)^k A_{6k} \quad (\text{Eq. II-36})$$

$$S_{decapole} = \sum_{k=1}^{\infty} 5 \cdot \left( \frac{R}{R_{ref}} \right)^{5(2k-1)-1} B_{5(2k-1)} + \sum_{k=1}^{\infty} 5 \cdot \left( \frac{R}{R_{ref}} \right)^{10k} (-1)^{5k} A_{10k} \quad (\text{Eq. II-37})$$

Note that in the sum only odd normal multipoles and even skew multipoles enter. The sextupole signal is so proportional to the odd normal multipoles  $B_3, B_9, B_{15}$  and higher order and to the even skew  $A_6, A_{12}, A_{18}$  and higher order. The decapole signal is proportional to the odd normal components  $B_5, B_{15}, B_{25}$  and higher order and to the even skew  $A_{10}, A_{20}, A_{30}$  and higher order. The formula can be simplified recalling that, in a *normal* dipole magnet, odd normal harmonics are allowed by symmetry, but they strongly decrease in amplitude with increasing order. On the other hand the even skew multipoles are not allowed by the symmetry. Thus, for a magnet with good construction quality, they are expected to be close to zero. Hence in the first approximation placing the probes at a radius  $R$  close to the reference radius, we can neglect the coefficients corresponding to the harmonics with an higher order than  $m=3$  and  $m=5$ , Eq. II-36 and Eq. II-37 can be simplified as follows.

$$S_{sextupole-ring} \approx 3 \cdot \left( \frac{R}{R_{ref}} \right)^2 B_3 \quad (\text{Eq. II-38})$$

$$S_{decapole-ring} \approx 5 \cdot \left( \frac{R}{R_{ref}} \right)^4 B_5$$

In first approximation, the signals coming from the arrangement of the sensors in the rings (Fig. II-11) are proportional to the normal sextupole and decapole harmonic, respectively. The dipole field component is completely compensated by the symmetry. Note that in the case of the decapole geometry also the sextupole harmonic is compensated by the Hall probe arrangement.

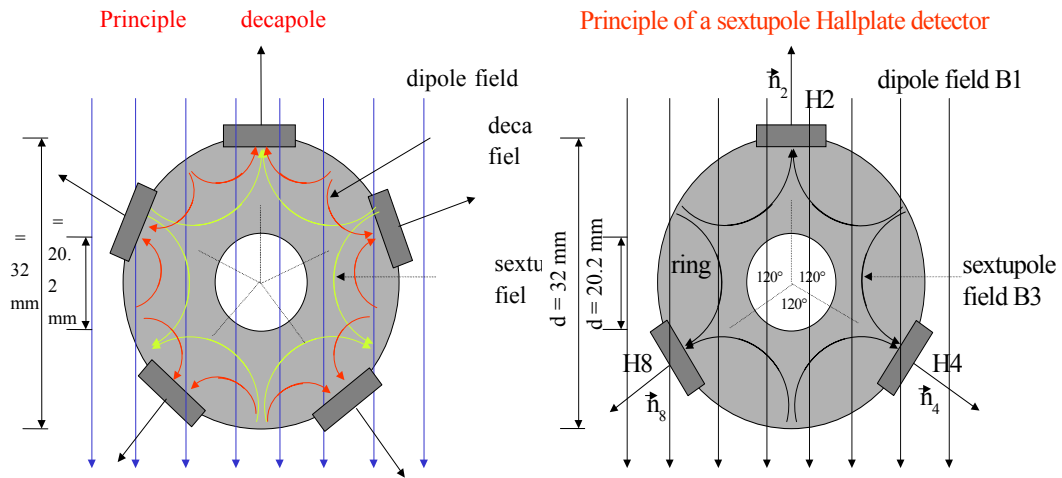


**Figure II-10: Sketches of sensors used to measure the decapole (left) and the sextupole (right).**

### II.3.2 - The measurement probe developed at CERN

The Hall probe based sensor consists of six rings for the sextupole measurements and two rings for the decapole. The detector is based on the following components:

- the *support shaft* is the piece that supports the eight sensor rings;
- the *shaft* corresponds to the 300 mm aluminium piece supporting the connector;
- the term *extension shaft* describes the 1 m long aluminium modules (four in total) that allow a modulation of the length of the device.

The *support shaft* is made of Ti6Al4V alloy to avoid mechanical misalignments of the rings (Fig. II-11). The choice of the material was important, the material had to be non-magnetic and with a high electrical resistivity to avoid perturbations of the magnetic field, both in the steady state and during ramps. At the same time a good thermal conductivity was desirable, in order to stabilize the temperature of the Hall plates on each ring. The titanium alloy was chosen due to its high electrical resistivity ( $\rho \approx 1.7 \mu\Omega m$ ) and adequate thermal conductivity ( $k \approx 7 Wm / K$ ). The alloy also has a very small paramagnetic behavior ( $\mu_r \approx 1.0002$ ). The support shaft is 300 mm long, has a diameter of 33 mm, a hole of 15 mm diameter is carved inside it in order to minimize the quantity of Ti6Al4V. The front end of the shaft is equipped with ball bearing and rollers in order to translate and rotate the device inside the warm bore of the magnet.

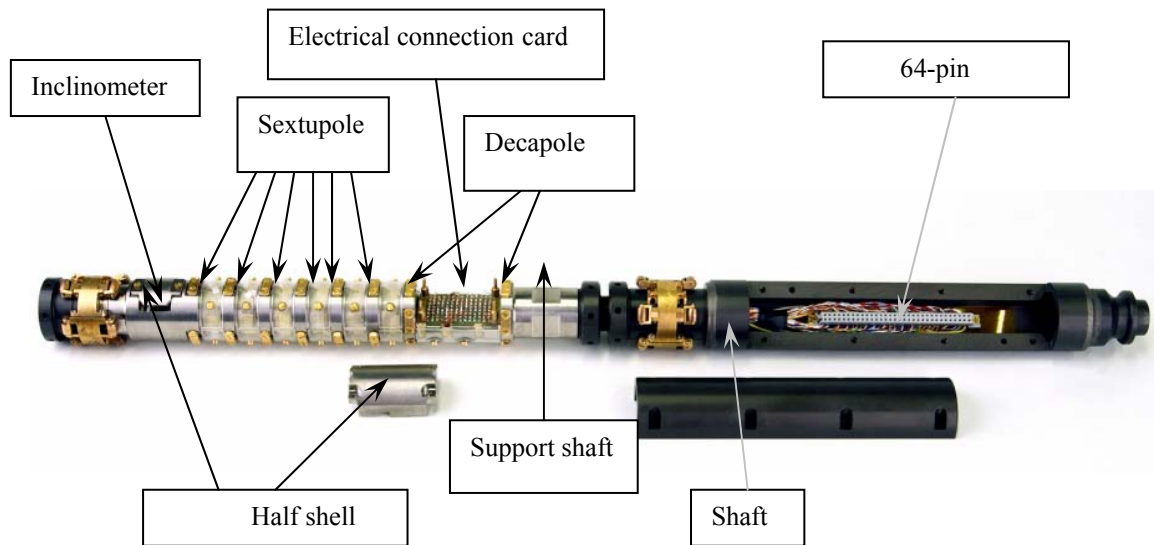


**Figure II-11: The hall probe based sextupole and decapole sensor.**

The device includes the eight rings and contains two flat surfaces: one for the electrical connection card (with a depth of 15 mm) and the other for the inclinometer (with a depth of 19.5 mm). The inclinometer provides an absolute reference for the angular position of the shaft with respect to gravity. The six  $b_3$  sensors are placed at a distance of 19.2 mm in order to cover a wavelength of the cable twist pitch. The two  $b_5$  rings are spaced by approximately half a pattern wavelength (57.5 mm). Hall plates are mounted as shown in Fig. II-10 into grooves on the rings at angular spacing of  $120^\circ$  and  $72^\circ$ , for the sextupole and decapole respectively. The angular tolerance on the positioning is  $\pm 1^\circ$ . The size of the Hall plate housing is 3.3x6x0.8 mm. The *shaft* (Fig. II-11 on the right) contains a 64-pin connector and also has a ball bearing with rollers. Wires are directed to a flat connector with sixty-four connections located in the shaft. The eight sensors are connected in series. To protect the connector against magnetic interferences and to restore the dimensional stability a cover is placed on the connector.

One purpose of the device is to measure the spatial variation of the sextupole and of the decapole along the magnet length. Moreover four *extension shafts* of 1 m each long were added. The four tubes can extend the detector length up to approximately 5 m. The extension devices allow measurements of the harmonics in the magnet straight part avoiding the end effects. The detector with this configuration is carried by ball bearings and rollers. This allows translations of up to 150 mm and rotations up to a few degrees inside the anti-cryostat.

### *II.3.2.1 - Characteristics of the Hall Probe*

The Hall plates used are provided by AREPOC, a company in Bratislava, Slovakia. The Hall plates are of the type HHP-NU, made up of InSb and unpackaged. The probes typically have sensitivities around 220 mV/T at the excitation current of 50 mA. The active area of each Hall plate



**Figure II-12 Axial unpackaged Hall Plates from AREPOC, type HHP-NU used in the existing Hall detector.**

is approximately 0.01 mm<sup>2</sup> (Fig. II-12) and is connected with very thin and fragile wires. They all lay on a ceramic support corresponding to an overall area of 20 mm<sup>2</sup>. The small temperature coefficient of about 10<sup>-4</sup> K<sup>-1</sup> guarantees insensitivity against gradients or variations of the temperature. Non-linearities are smaller than 0.2% in a field range between 0 and 1 T. This grants a linear behaviour of the compensated signal in a limited range around the field level during injection.

### *II.3.2.2 - Cabling and Acquisition*

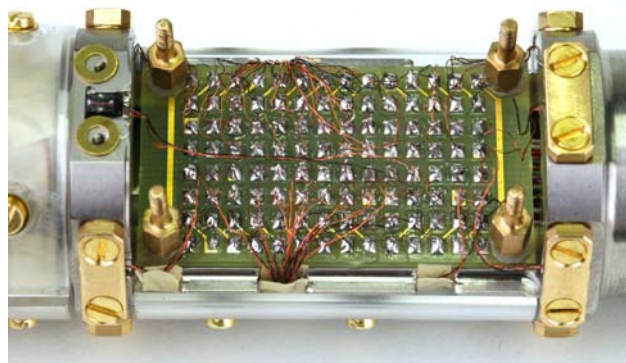


**Figure II-13: The electronic connection card containing 112 points of plugs.**

The Hall plate signal wires (112 in total with a diameter of 0.1 mm) are transported over the surface of the support through rails and grooves machined in the rings. They are soldered to an electronic

connection card containing 112 points of plugs and located between the two decapole rings. The Hall plate wires join the three wires from the inclinometer and then are directed to a flat 64-pin connector located in the 300 mm long aluminium piece (Fig. II-13).

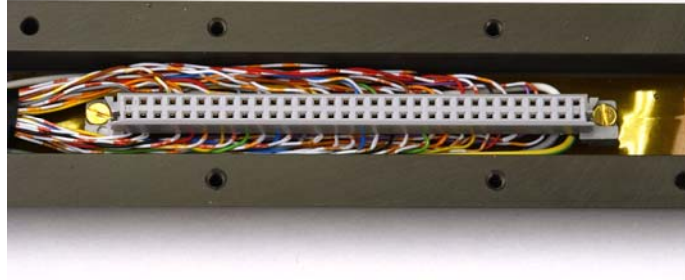


**Figure II-14: The flat 64-pin connector located in the 300 mm long aluminium shaft.**

### *II.3.3 - The measurement problem*

The measurement target of the probe developed is the decay and in particular the snapback phenomena of the b3 and b5 field components. The snapback is characterized by duration of some tenths of a second, so a sampling frequency of 10 Hz is required in order to have enough experimental points to characterize the phenomenon.

The b3 decay amplitude is typically 2 units with a standard deviation of 0.5 units (0.8 units for b5 decay) hence imposing a minimum resolution of 0.1 units to permit b3 modelling. This resolution represents a considerable challenge especially because it is  $10^5$  orders of magnitude smaller than the superimposed main dipole field.

The compensation of the main dipolar field is carried out using an analog bucking solution; bucking cards were built to sum the signals coming for the hall plates of the same ring. On the same card, compensation, at the first order, of the differences in sensitivity and offset between the hall plates is performed through input amplifiers with adaptable gain and offset (see Chapter V for details).

Measurements with this new probe and the analog bucking cards were already carried out on few LHC dipoles. They gave important inputs for the modelling of the decay and snapback phenomena [31], but pointed out some measurement problems:

- the analog bucking doesn't cancel completely the main dipolar field. A residual uncompensated contribution is always present mainly due to the hall plate non linearity and the misalignment errors of the hall plates;

- the bucking cards are not characterized by long term stability so frequent calibrations are needed. On the other side the behaviour on the short term (2000 s, namely the measurement duration) was never investigated.

Concluding, the only way to validate measurements carried out acquiring the bucked signals was a tedious calibration performed by comparison with data provided by the rotating coils system concerned the same measurement.

#### ***II.4 - System based on rotating hall plates***

Magnetic field polarity is possibly the most important magnetic property to be verified in the LHC magnets [32]. This is especially important in superconducting magnets, that cannot be accessed in operating conditions (as opposed to normal conducting magnets) and are often composed of several magnetic elements assembled in a single cold mass. One such example is the LHC Short Straight Section that contains the main quadrupole (MQ), the package with the orbit corrector and the lattice sextupole (MSCB), and a MQT/MQS/MO corrector package that depends on the specific assembly.

Polarity inversions can happen at the level of a single winding, but much more frequently these take place at the level of the interconnections within the cold mass (bus routing from the magnet to the current leads) or, possibly, at the interconnection between magnets at installation. None of these faults can be easily mended once the cryostat is closed, and hence particular care is asked in the verification of the field polarity.

The measurement of polarity is trivial only apparently. In principle all the systems used for routine measurements of strength and field quality, as an example, the harmonic coil systems provide also the information about the field polarity; this depends however on a high number of parameters (i.e. direction of coil rotation, sense of insertion into the magnet, polarity of dozens of cables and connectors, sign conventions used in various coefficients and subroutines within the analysis software) and is therefore not always reliable.

The polarity test requires an instrument that is robust, easy to use, capable to indicate the polarity of any magnet type (in agreement with a defined convention), working at room temperature to intercept errors before the costly cryogenic tests.

A *polarity tester* is a relatively straightforward device for a dipole field, a Gaussmeter or a compass needle can be enough to verify the field generated by a superconducting dipole, even when powered in warm conditions at  $10^{-3}$  of its nominal field. For higher order magnets the field

generated in warm conditions powering at currents that can be sustained long enough can be very small, comparable to the residual magnetization of the iron yoke of the magnet itself. Furthermore access to the magnet bore is difficult, sometimes meters inside the cold mass, and precise positioning of a field measurement sensor (e.g. a Hall plate) or observation of an orientation (e.g. a needle) is delicate.

For the above reasons a polarity tester adapted to the field levels of the LHC magnet assemblies was devised. The basic idea is to use a single Hall plate as the field measurement sensor, and rotate this sensor over a turn to map the angular dependence of the field. This angle-dependent signal is analyzed in Fourier series to extract the field harmonics. The measurement target is the field polarity but all the main characteristics of the magnet under test can be obtained: main harmonic order, transfer function (TF), magnet type (normal or skew) and field direction with respect to gravity.

## II.5 - References

- [1] A. Devred, M. Traveria, “*Magnetic Field and Flux of Particle Accelerator Magnets In Complex Formalism*”, CRYOMAG/94-08.
- [2] Luca Bottura, “*Standard Analysis Procedures for Field Quality Measurement of the LHC Magnets Part I: Harmonics Standard Analysis*”, CERN Engineering Specification, EDMS N. 313621.
- [3] J. Billan, L. Bottura, M. Buzio, G. D’Angelo, G. Deferne, O. Dunkel, P. Legrand, A. Rijllart, A. Siemko, P. Sievers, S. Schloss, L. Walckiers, “*Twin Rotating Coils for Cold Magnetic Measurements of 15m Long LHC Dipoles*”, LHC Project Report 361, CERN, 1 Dec.1999.
- [4] LHC-MTA team, “*User Manual for Magnetic Measurements of Main Dipole at MB Test Station (SM18)*”, No. Volume-4(A) MM UM, CERN, 19 Mar. 2001.
- [5] F. Bodry, “*LHC Power Converters. Performance Requirements*”, Proceedings of the LHC Workshop, CERN-SL-2001-003 DI, pp. 250-255, 15-19 Jan. 2001, Chamonix, France .
- [6] L. Bottura, “*Standard Analysis Procedures for Field Quality Measurement of the LHC Magnets – Part II: Transfer Functions and Parameterisation*”, MTA-IN-98-027, 22 Jun. 1998.
- [7] P. Galbraith, “*Precision electronics (integrators) for field measurements*”, CERN , EDMS N. 021120.
- [8] [http://www.metrolab.ch/5025/5025\\_General.html](http://www.metrolab.ch/5025/5025_General.html)
- [9] Z. Ang, I. Bejar, L. Bottura, D. Richter, M. Sheehan, L. Walckiers, R. Wolf, “*Measurement of AC Loss and Magnetic Field during Ramps in the LHC Model Dipoles*”, IEEE Transactions on Applied Superconductivity, Vol. 9, No. 2, pp. 742-745, Jun. 1999.
- [10] H. Reymond, L. Bottura, A. Raimondo, “*The Magnetic Measurement Software Ver. 6.0.0.*”, IAS-LS-00-02, 9 May 2000.
- [11] S. Amet, L. Bottura, L. Deniau, L. Walckiers, “*The Multipole factory: an Element of the LHC Control*”, IEEE Trans. Appl. Sup., 12 (2002) no. 1, pp.1417-1421.
- [12] R. Carcagno, J. Di Marco, S. Kotelnikov, M. Lamm, A. Makulski, V. Maroussov, R. Nehring, J. Nogiec, D. Orris, O. Poukhov, F. Prakoshin, P. Schalabach, J.C: Tompkins, and G.V. Velev, “*A fast continuous magnetic field measurement system based on digital signal processor*”, 19<sup>th</sup> Magnet Technology, October 2005.
- [13] C. Evesque, “*A new challenge in magnet axis transfer*”, IMMW11 Brookhaven National Laboratory, September 1999.

- [14] D.B.Barlow, “*Rotating Coil Measurements System for the APT/LEDA CCDTL Quadrupole Magnets*”, *IEEE Transactions on applied Superconductivity*, Vol. 10, N. 1, pp1447-1449, March 2000.
- [15] Y. Kawamata, I. Yonekawa, and K. Kurihara, “*Development of an intelligent digital integrator for long pulse operation in a Tokamak*”, *19<sup>th</sup> Symp. On Fusion Engineering*, pp 172-175, 21-25 January 2001.
- [16] J.D. Zhang, Z. Cao, F.L. Ren, Q.G. Zhou, L.H. Zhang, Y.Li, H.P. Yan, A.L. Zhang, and Y.B. Zhao, “*Design and Fabrication of a rotating coil magnetic measurement system*”, *Proceedings of the second Asian Particle Accelerator Conference, Beijing, China, 2001*.
- [17] [www.metrolab.ch/5025/5025\\_Specs.html](http://www.metrolab.ch/5025/5025_Specs.html)
- [18] [www.GMBH.com](http://www.GMBH.com)
- [19] [www.vi.rdm-apps.com](http://www.vi.rdm-apps.com)
- [20] F.N. Trofimenkoff, F. Sabouri, J. Quin, and W. haslett, “*A square voltage-to-frequency converter*”, *IEEE Transactions on instrumentation and measurement*, Vol. 46, N. 5, pp. 1908-1911, October 1997.
- [21] A. Jain, “*Recent Magnetic Measurement Activities at BNL*”, *Proceedings of the 11th International Magnet Measurement Workshop (IMMW-XI) Brookhaven National Laboratory, Upton, NY, September 21st-24th,1999*.
- [22] T. Ogitsu, “*Influence of Cable Eddy Currents on the Magnetic Field of Superconducting Particle Accelerator Magnets*”, *PhD Thesis, January 1994*.
- [23] Animesh Jain, John Escallier, George Ganetis, Wing Louie, Andrew Marone, Richard Thomas, Peter Wanderer, “*Measurements of the Field Quality in Superconducting Dipoles at High Ramp Rates*”, *19th International Conference on Magnet Technology Genova, Italy, September 19-23, 2005*.
- [24] L. Larsson, “*Sextupole snapback detector*”, *Master Thesis, Lulea University of Technology, May 2000*.
- [25] E. Benedico, “*A fast sextupole and decapole probe for chromaticity corrections*”, *Graduation Report, Universitat Politecnica de Catalunya, Spain, April 2002*.
- [26] T. Pieloni, et al. “*Field decay and snapback measurements using a fast Hall probe sensor*”, *IEEE Trans. Appl. Supercond.* 14, no.2, 1822-25, 2003.
- [27] M. Haverkamp, “*Decay and Snapback in the superconducting Accelerator Magnets for the large Hadron Collider*”, *PHD Thesis, University of Twente, 2002*.

- [28] H. Bruck, et al., “*Observation of a periodic field pattern in the persistent-current fields of the superconducting HERA magnets*”, proceedings IEEE Particle Accelerator Conference, 2149-51, San Francisco, USA, 1991.
- [29] A. K. Jain, “*Basic theory of magnets*”, CAS CERN Accelerator School on Measurement and Alignment of Accelerator and Detector Magnets, *CERN Yellow Report* 98-05, (1998).
- [30] M. Breschi et al., “*Fast measurements of field harmonics through a set of Hall probes*”, CERN Internal Note LHC-MTA-IN-2000-103.
- [31] L. Bottura, T. Pieloni, N. Sammut, “*Scaling Laws for the Field Quality at Injection in the LHC Dipoles*”, CERN-LHC-Project-Note-361.- 01 Dec 2004 .
- [32] P. Proudlock, “*LHC Magnet Polarities*”, Engineering specification LHC-DC-ES-0001, version 2.2, EDMS 90041.

## **Chapter III - HIGH ACCURACY**

### **SYSTEMS:THE NUMERICAL INTEGRATORS**

#### ***III.1 - Measurement problem***

The design of digital integrators is suitable for current measurement requirements: 10 to 100 ppm resolution with a trigger frequency in the range of few 10's up to few 100's Hz. This allows a two-orders of magnitude margin with respect to the digital resolution, well above the noise and drift limits associated with the analog electronics. Nevertheless, the development of rotating and fixed coil measurement systems planned for the near future, and, in particular, the rapid measurement of the LHC magnets to improve the characterization of the energy ramp, or the measurement of fast pulsed magnets such as prototypes for FAIR at GSI, or for the upgrade of the CERN injector chain, will demand an increase of the trigger frequency by a factor of 100 (trigger frequency in the range of few 1000's up to few 10000's Hz). Given the intrinsic limitations of the PDI design, this will result in a dramatic reduction of the margin with respect to the digital resolution.

In this chapter, an alternative design of digital integrator, based on an immediate signal digitalization and successive numerical integration, is described. The performance of the new solution (Fast Digital Integrator, FDI), as well as the improvements with respect to the PDI integrators, are highlighted. The architecture of the overall measurement system is defined by paying particular attention to the layout of the integrator board. With this aim, the design details of the analog front end for the offset and gain auto-calibration, as well as the programmable gain setting, are pointed out.

The concept was validated experimentally by emulating the proposed approach on a PXI platform. The metrological characterization is described. Flux measurements were carried out both by the prototype and by the PDI integrator as a reference, by highlighting the expected resolution limits.

Finally, preliminary test results of the new integrator analog front-end are illustrated.

### III.2 - Working principle of the proposed digital integrator

The block diagram of the proposed integrator is shown in Fig. III-1. The basic principle is to integrate the input signal  $V_{in}$  in the digital domain, immediately, without previous analog processing in order to reduce the impact of analog uncertainty sources.

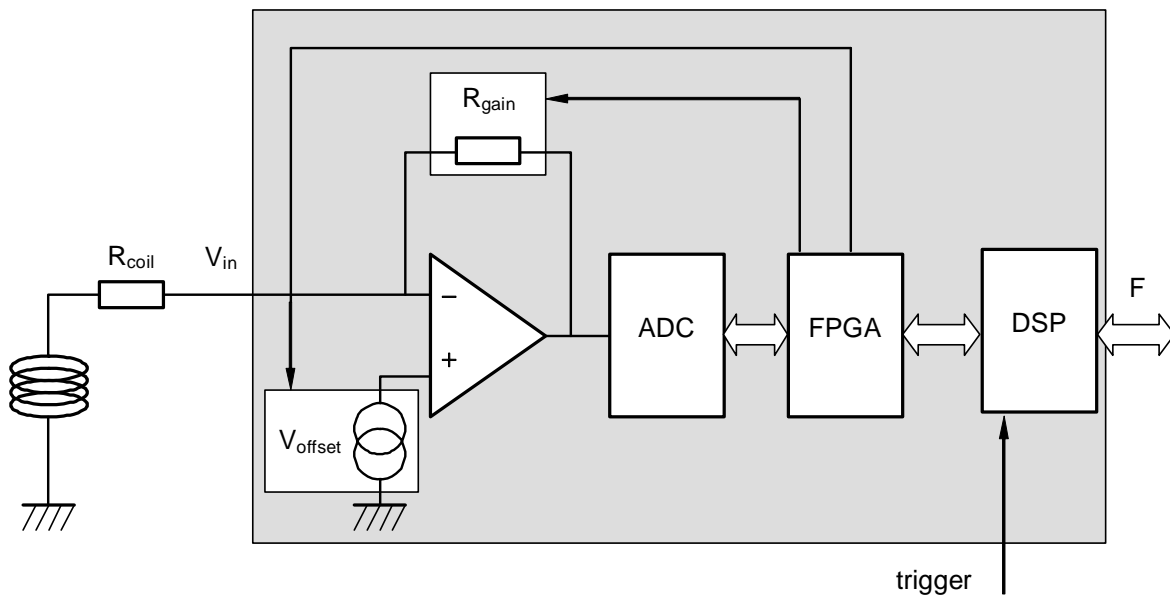


Figure III-1: Principle of the proposed digital integrator.

The input stage is a gain programmable amplifier, with automatic gain and offset calibration and adjustment. The gain and the voltage offset are controlled by a Field Programmable Gate Array (FPGA) performing the calibration, storing the calibration coefficients and applying them in measurements.

The input signal is digitized by an Analog-to-Digital Converter (ADC), with  $N_{resolution}$  bits, sampling at a rate  $f_{sampling}$ . The acquired signal is then input to a Digital Signal Processor (DSP) performing numerical integration when triggered from an external digital signal (e.g., pulses from

an angular encoder). The DSP manages the analog and digital I/O of the instrument, through the FPGA which plays as an I/O processor.

The integral result  $F$  is made available on a digital communication bus.

Main advantages are:

- the signal is sampled at a fixed rate, independently on the trigger frequency. As a result, the resolution of the digital integral is fixed, and, limited only by the sampling frequency  $f_{sampling}$  and the ADC resolution  $N_{resolution}$ ;
- the time integral can be performed with a variety of numerical algorithms that can be tested and uploaded on the DSP, easily without any change in the hardware. Filtering, decimation, or voltage acquisition can be performed on the board, once a suitable code is uploaded through the interface bus;
- analog electronics is fully programmable and can be calibrated on the field (e.g., before starting a measurement), in order to reduce long-term drifts in amplifier gain and offset;
- the on-board processor can be used in addition for reverse tasks, such as monitoring the physical coherence of the signals before, during, or after a measurement, thus providing a powerful mean to control errors.

### III.2.1 - System Resolution

The increment in flux resolution is given by the product of the ADC resolution,  $\varepsilon_{ADC}$  by the time resolution  $\varepsilon_{\Delta t}$ :

$$F_{\min} = \varepsilon_{ADC} \varepsilon_{\Delta t} \cdot \quad (\text{Eq. III-1})$$

The first term is obtained from the ADC voltage range and the number of bits as:

$$\varepsilon_{ADC} = \frac{V_{\max}}{2^{N_{resolution}} - 1}, \quad (\text{Eq. III-2})$$

while the second is given by the sampling frequency of the ADC directly:

$$\varepsilon_{\Delta t} = \frac{1}{f_{sampling}} \cdot \quad (\text{Eq. III-3}).$$

As an example, for an ADC with 18 bits of resolution, and a sampling rate of 625 kS/s, an  $F_{min}$  of  $3 \times 10^{-11}$  Vs is obtained. As for the case of the VFC-based integrator, this flux resolution is constant and independent on the integration time. This value is about 5 orders of magnitude higher than the PDI integrator resolution and represents one of the main advantages of this new approach.

Once the required time resolution becomes smaller than the sampling period, however, the ADC-DSP system loses track of changes in the signal and cannot integrate. Thus, operations are limited at trigger frequencies smaller than sampling rates.

### III.2.2 - Offset and gain calibration

Also digital integrator suffers the offset problem arising from the analog front-end. It depends mainly on the change of temperature and gain set of the input amplifier. Since the signal is sampled, immediately the drift voltage at the input of the ADC can be periodically monitored. The idea is to implement a periodic offset calibration procedure, by injecting a null signal at the integrator input. The measured value will be used for a first offset compensation in the integration process. In particular, in order to take into account noise on the input stage, the offset voltage is not evaluated by a simple sampling but by means of integration, in order to measure the actual drift on the integral, over a fix time interval.

Main requirement for the analog front-end design is high stability. The offset auto-calibration is performed before a measurement that can last even 20 minutes, thus a high offset short-term stability (less than 10 ppm) is required.

After the calibration, residual offset produces a drift proportional to the integration time:

$$F_{offset} = V_{offset} \Delta t . \quad (\text{Eq. III-4})$$

The same stability requirement has to be considered for the gain. Therefore, an automatic fine adjustment procedure is foreseen in order to set exactly the theoretical gain value.

### III.2.3 - Trigger uncertainty

An important uncertainty source in the integration process is the timing error on the encoder trigger pulses. The encoder pulses are first decimated by using a prescaler board to set the N value, namely the integration angular resolution, and then are sent to the DSP to drive the integration.

If  $f_{clock}$  is the clock frequency of the prescaler board, since the trigger pulses are obtained by a synchronous counter, the timing uncertainty on the trigger pulses can be estimated as:

$$\sigma_{trigger\_prescaler} = \frac{1}{f_{clock}} \cdot \quad \text{(Eq. III-5)}$$

The trigger is detected by the DSP by means of its interrupt response system. A jitter on the detection and the consequent delay in the response (interrupt response latency time) represents a further uncertainty source  $\pm\sigma_{interrupt\_DSP}$ .

The uncertainty on the integration due to the global trigger uncertainty can be expressed as:

$$\sigma F_{trigger} = V_{max} \cdot \sqrt{(\sigma_{trigger\_prescaler})^2 + (\sigma_{interrupt\_DSP})^2} \cdot \quad \text{(Eq. III-6)}$$

As an example, by taking into account a clock frequency of 100 MHz on the prescaler board and an interrupt latency time of 20 ns (a time reasonable for a DSP with 500 MHz clock), the consequent integration uncertainty is equal to  $\pm 2.2 \cdot 10^{-7}$  Vs.

It is worth to note that the encoder triggers mark both the start and the end of each integration.

The trigger uncertainty has to be some orders of magnitude lower than the sampling period in order to consider it negligible. In fact, the voltage is sampled in time domain and not in the angular domain (the encoder triggers are asynchronous with respect to the sampling frequency), thus the maximum error is given by the product of the maximum input voltage by the sampling period. As an example, for 800 kS/s sampling period and 10 V maximum input, this error is equal to 1.25 E-5 Vs. Without any further correction, the high potential resolution of this instrument is completely lost because of its last source of uncertainty. An high resolution interpolator is foreseen to reduce the instrument global uncertainty.

#### III.2.4 - Integration noise

In addition to the offset problem, the integrator is affected by noise, captured by the coil and/or generated by the amplifiers stage (electronic noise).

The electronic noise can be modelled as Gaussian with a white spectrum and a standard deviation  $\sigma_{noise}$ .

Such a noise is rejected in frequency by a factor  $1/f$  in an ideal integrator. Hence, higher frequency noise components are reduced with respect to lower ones. At the same time the integration time  $\Delta t$  acts as a time window on the input noise of the integrator.

By taking into account:

$$y(t) = \int_{t-\Delta t}^t x(\tau) d\tau \quad (\text{Eq. III-7})$$

$x(t)$  is the white noise in input to the integrator. It is a random signal WSS (wide sense stationary), therefore since white signal it is characterized by zero average and impulsive autocorrelation, namely Power Spectral Density constant:

$$X^2(f) = \sigma_{noise}^2 \quad (\text{PSD}) \quad (\text{Eq. III-8})$$

The power of this signal is infinite, since:

$$E[x^2] = \int_{-\infty}^{+\infty} X^2(f) df \quad (\text{Eq. III-9})$$

The integration process described by the equation 7 can be seen as the output of a system LTI (linear time invariant) characterized by impulsive response:

$$h(t) = 1(t) - 1(t - \Delta t) \quad (\text{Eq. III-10})$$

and transfer function:

$$|H(f)|^2 = \Delta t^2 \sin^2(f \cdot \Delta t) \quad (\text{Eq. III-11})$$

For a generic system LTI, if the signal input is WSS the output is a signal WSS as well.

The average of the integrator output signal is zero again since for a signal WSS, for definition, the statistical average of the temporal average evaluated over a finite time interval is equal to the statistical average of the signal whatever is the time interval; if the input signal statistical average is zero also the signal output will be characterized by zero average.

The power of the integrator output  $E[y^2]$  is evaluated by using the following relation:

$$E[y^2] = \int_{-\infty}^{+\infty} Y^2(f) df = \int_{-\infty}^{+\infty} |H(f)|^2 X^2(f) df \quad (\text{Eq. III-12})$$

Finally:

$$E[y^2] = \int_{-\infty}^{+\infty} Y^2(f)df = \int_{-\infty}^{+\infty} |H(f)|^2 X^2(f)df = \Delta t \cdot \sigma_{noise}^2 \quad (\text{Eq. III-13})$$

and then

$$\sigma_y = \sqrt{\Delta t} \cdot \sigma_{noise} \quad (\text{Eq. III-14})$$

Then, the standard deviation at the output of the ideal integrator is the product of the standard error on the average and the square root at integration time. Therefore, the integration noise increases according to integration time.

Instead of the noise standard deviation, in amplifier's datasheets, it is common to refer to the peak-to-peak noise level. According to the values experimented on the analog front-end of PDI integrator, the peak-to-peak noise level expected for the proposed integrator is:

G=1	10 $\mu\text{V}$
G=10	1 $\mu\text{V}$
G=100	0.3 $\mu\text{V}$

**Table III-1: Input voltage noise (peak-to-peak)**

### III.2.5 - Advantages

In Fig.III-2, the operating limits of the proposed DSP based-integrator and the PDI integrator are compared.

The amplifiers used in the proposed integrators are the same of the PDI integrator, thus the limits due to the peak-to-peak noise on the integrator output and to the offset are the same. In particular:

- the noise on the integrator output, given by Eq. III-14, in the log-log plot of  $F$  vs.  $\Delta t$ , is represented by the straight line with slope 1/2 passing through the point ( $\sigma_{noise}$  Vs, 1s), where  $\sigma_{noise}$  is typically 10  $\mu\text{V}$
- the offset limitation, expressed by Eq. III-6, in the log-log plot of  $F$  vs.  $\Delta t$ , is a straight line with slope 1, passing through the point ( $V_{offset}$  Vs, 1s), where  $V_{offset}$  is typically 70  $\mu\text{V}$ . This value can be considered as a residual offset after the auto-calibration procedure.

Such as in the PDI integrator, in the proposed integrator, there is a lower limit to the integration time; it is imposed, in principle, by the ADC sampling period ( $1.25 \mu\text{s}$  for an ADC with 800 KS/s sampling frequency).

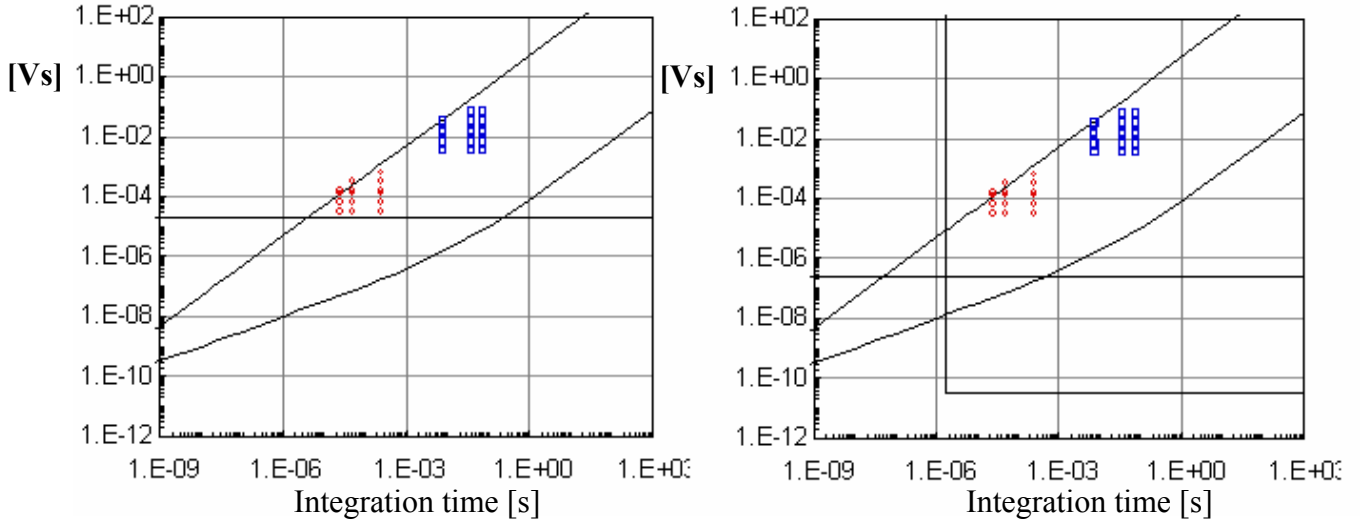


**Figure III-2: Comparison between operating limits for the proposed DSP-based integrator (on the right) and the PDI integrator (on the left), for an input gain of 1.**

Main advantage of the proposed integrator is that the resolution does not represent a limit: in fact, it is represented in the plot on the right by the horizontal line,  $3 \cdot 10^{-11}$  Vs. The actual limit is the integration uncertainty due to the timing trigger uncertainty; the value expressed by Eq. III-6 is depicted as the horizontal line,  $2.2 \cdot 10^{-7}$  Vs.

It is evident that the new approach is characterized by an expansion of the operating limits, now fully compatible with the expected working points at future fast rotating coil systems (red circles).

### ***III.3 - Experimental validation***

The advantage of the proposed approach, especially in term of increased resolution, was validated experimentally by implementing a one-channel numerical integrator, based on 18-bit ADC with 625 kS/s sampling frequency. As development platform, a PXI system National Instrument, equipped by a controller Pentium IV 2.4 GHz, operating system Pharlap RT, and LabView RT programming language, were used. On the system, two 18 bit DAQ cards 6289, each one characterized by 16 differential multiplexed input channels, and 625 kS/s maximum sampling frequency on single channel, are installed.

In this section, two different solutions are proposed:

- in the first, the encoder signal is treated as an interrupt signal on an input line of a DAQ card. Each time the interrupt service routine is waked up by the encoder signal rising edge, the integration result is stored and the integration process is reset. The current

result represents the flux increment corresponding to the angular position indicated by the encoder.

- In the second, both the signal to integrate and the encoder signal are simultaneously sampled by one channel of a DAQ card at the maximum sampling rate. The encoder pulses are recognized in RT, by using a robust rising edge detection algorithm.

A full characterization of both solutions were carried out. The results show that the second solution assures best performance and it was chosen to carry out comparative measurements of magnetic flux with the PDI integrator.

### *III.3.1 - Solution based on hardware interrupts for angular synchronization*

In Fig. III-3, the working principle of the PXI digital integrator based on interrupt is depicted.

The coil voltage to integrate is continuously acquired and the samples are stored in a circular buffer, dynamically allocated in the controller RAM. The voltage coil acquisition is triggered on the encoder zero signal so that the integration process (and then the flux obtained) starts on the zero of the angular reference system.

The integration process is synchronized on the pulses coming from the encoder via interrupt: the encoder signal is connected to a digital input line of the DAQ card, and for each rising edge, an interrupt service routine is executed. This mechanism is implemented in LabView 7.1™, thanks to the *Timed loop rising edges source* structure. At each rising edge, the following operations are carried out:

- Last samples are read from the circular buffer;
- The samples are integrated by a suitable algorithm (Simpson, Runge-Kutta, trapezoidal). The result represents the magnetic flux increments  $\Delta\Phi_k$  corresponding to the two consecutive angular positions (encoder pulses)  $\frac{2\pi}{N} \cdot (k-1)$  and  $\frac{2\pi}{N} \cdot k$ , where N is the angular resolution.
- The time difference between the actual and the previous interrupt detection is evaluated by using 1  $\mu$ s resolution RT clock of the system. This is just the  $tm_k$  value; namely, the time related to the k-th flux increment.

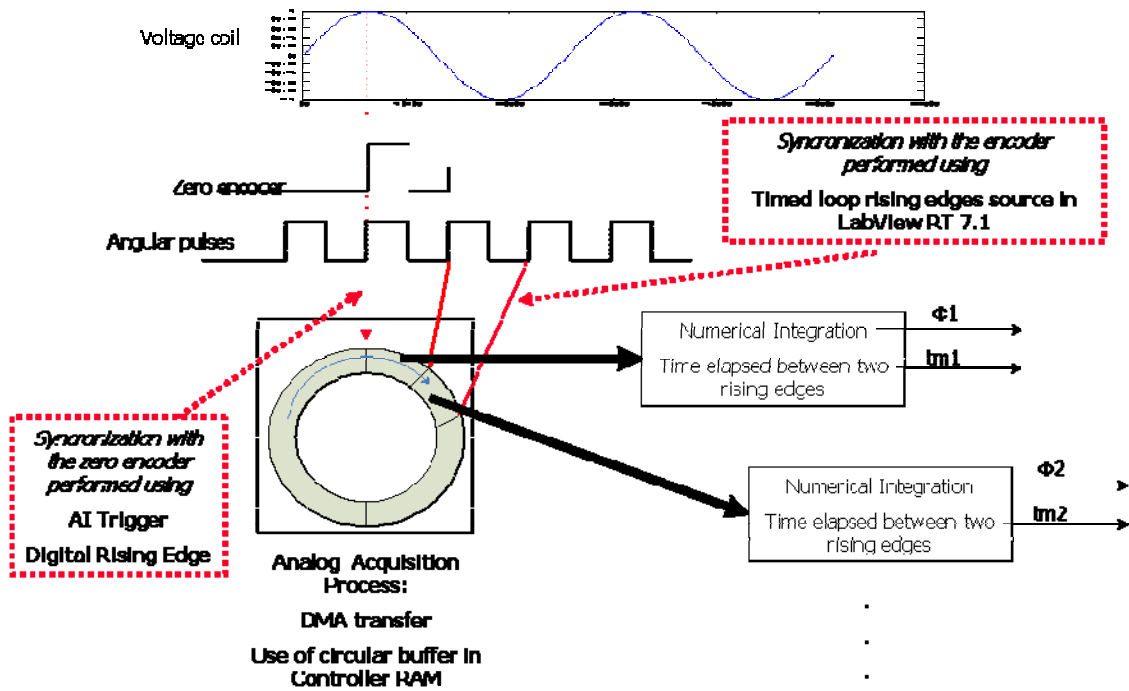


Figure III-3: Working principle of the PXI numerical integrator based on interrupt

The integration process is continuous, that is, once started, it will be stopped only by a specific user request. This means that this integrator, for concept, manages coil multiturns rotation. Data exchange with the host computer is organized in this way: at each coil turn, i.e. when a number  $N$  of flux increments was evaluated, the two arrays  $\Delta\Phi$  and  $\mathbf{t}_m$  of  $N$  rank are sent via TCP-IP to the host computer.

In Fig. III-3, the working principle of the proposed method is shown. Once the integration is launched, the DAQ card is prepared for the acquisition process that starts at the first encoder zero. For the controller, the coil voltage acquisition is a background process managed by DMA channels. The highest priority task is the integration process driven by the interrupt signal. At each encoder rising edge, it delivers a couple flux increment-time. This is stored in a RT FIFO (First In First Out) queue. The normal priority loop, NPL, is a task write at lower priority than the integration process; its duty is to check if in the RT FIFO, coil complete turn data are available and, in this case, send the two vector  $\Delta\Phi$  and  $\mathbf{t}_m$  to the host computer (Fig. III-4).

In Fig. III-5 the communication channels between the remote target and host computer are shown.

The channel from the host to the target represents commands and data sent by the user interface.

They can be so classified:

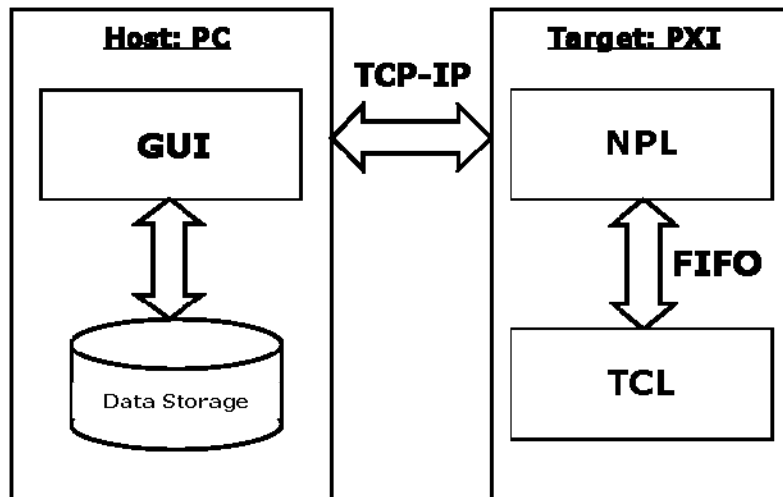


Figure III-4: Task hierarchy on the PXI target.

- Configuration data for the front end and the integration process. In particular settings for the coil voltage acquisition card (sampling frequency, input range, circular buffer length); the integration method and the samples number per turn;
- The Start and Stop Integration command;
- The Auto-Calibration command. Before starting the integration, an autocalibration procedure, aimed at evaluating the input offset, is foreseen. In absence of magnetic field, the coil voltage (that in theory should be zero) is sampled for a finite time and the DC value is computed; afterwards, taking into account this value as well as the  $tm_k$  value, a correction is applied after the  $\Delta\Phi_k$  evaluation

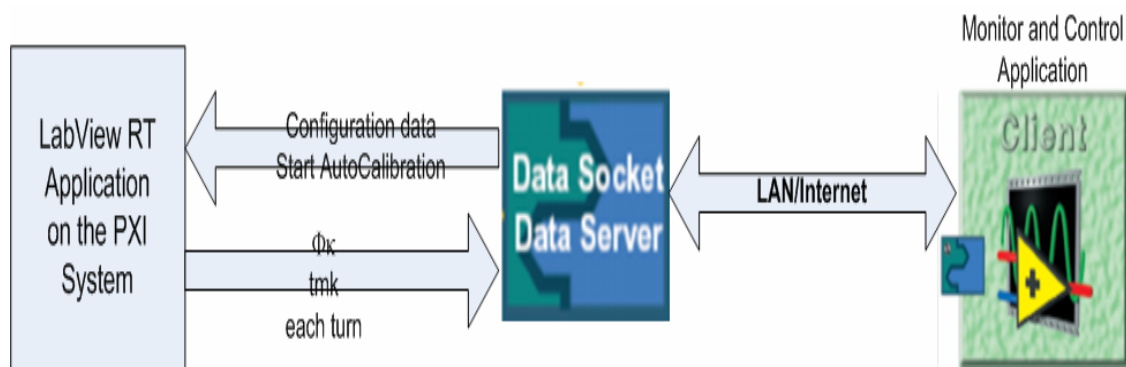


Figure III-5: Communication layout between remote target and host computer

The user interface running on the host computer is shown in Fig. III-6.

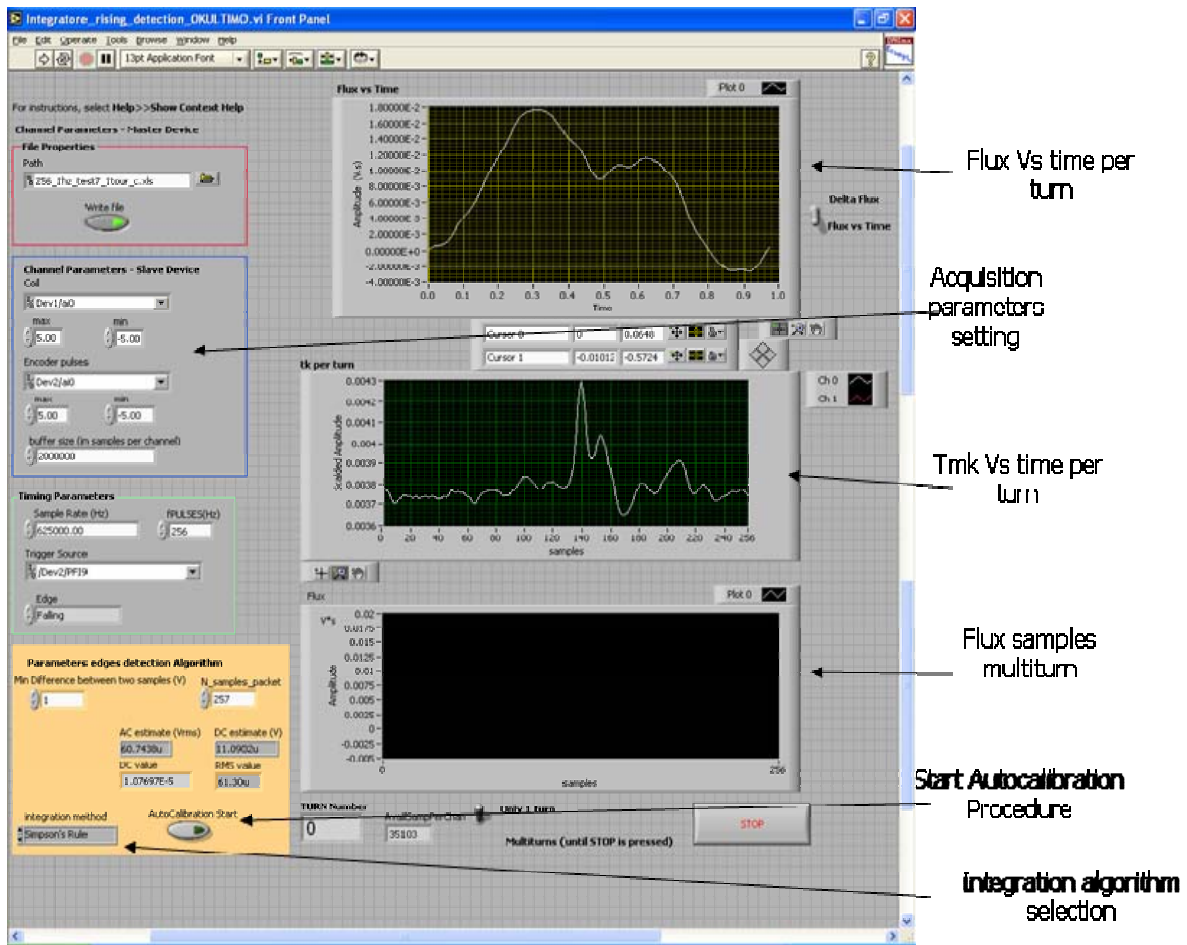


Figure III-6: PXI integrator User Interface

Its main functionalities are:

- visualization of the flux increments as well as the integration times at each coil turn;
- visualization of the magnetic flux versus the time for each coil turn;
- flux increments logging for multi-turns integrations;
- coil voltage acquisition setting;
- integration parameters setting;
- storing of the integration results.

### III.3.2 - PXI Integrator Solution 1: Metrological Characterization

The integrator was validate on a test bench based on a TTL generator and sinusoidal waveform generator to simulate, respectively, the encoder and the coil voltage to integrate, was arranged.

Possible uncertainty sources of the integration process were investigated. In the following, all the parameters measured as well as the measurement procedure are described.

### III.3.2.1 - Acquisition starting delay

The delay between the encoder rising edge and time starting of the coil voltage acquisition represents a key point for the rotating coil measurement system. It produces, in fact, a rotation of the measurement reference system with respect to the reference (i.e. the gravity) and a consequent error on the main field phase. Thus, it has to be negligible (under the zero encoder alignment accuracy) or at least well known.

It was measured by sampling a TTL signal at 250 Hz frequency at the maximum sampling rate (625 kS/s). The same signal triggered the analog acquisition. Different acquisitions (30) were carried out in order to evaluate the duration of signal first period. All the measurements were characterized by the same value (Fig. III-7) by negligible both the acquisition trigger jitter as well as the acquisition starting delay (much less than  $1.8 \mu\text{s}$  equivalent to a sampling period).

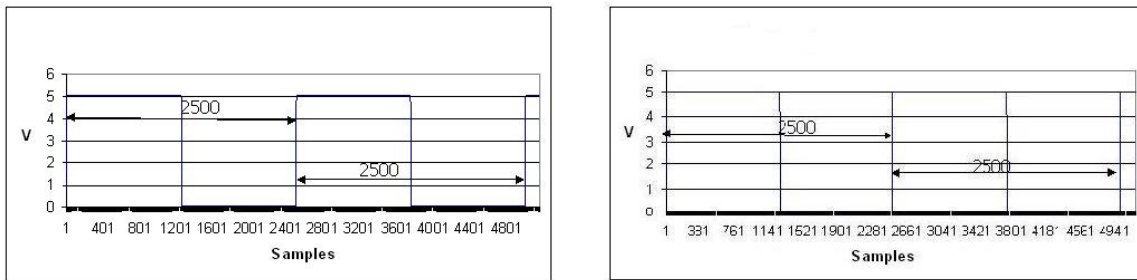


**Figure III-7: The TTL signal first period measured in different acquisitions was always 2500 samples long**

### III.3.2.2 - Timed loop starting delay

The encoder signal that ticks the angular positions is in phase with the encoder reference pulse. The correct working of the proposed integration algorithm is based on the lack at delay between the detection and the following response to the first encoder pulse. Thus, the acquisition process and the first flux increment integration have to start simultaneously so that the first delivered  $\Delta\Phi$  will be zero (since the first time that the timed loop will be waked up, the circular buffer is empty).

Several measurements are carried out in order to evaluate the synchronization between the acquisition and the integration. As in the previous test, a 250 Hz TTL signal was used as encoder signal simulator and sampled at 625 kS/s. The same signal was used both as acquisition trigger and sent to the interrupt line. Different acquisitions were performed and each acquisition was stopped

when the first encoder pulses rising edge was recognized. The pulses number acquired were measured.

Measurements show the lack of synchronization between the starting of the acquisition process and the starting of the rising edges detection. In fact, the acquisition process starts on the first TTL rising edge, the timed loop sometimes detects the second rising edge and other times the third one.

In order to synchronize the integration process and the encoder reference (trigger for the acquisition process):

- at the starting of the integration process the timed loop delay has to be measured ( $\Delta\Phi_1$  can be related to the second pulse);
- generally only after one complete coil turn the  $\Delta\Phi_k$  are equi-spaced and aligned with the encoder reference.

### III.3.2.3 - Interrupt response latency time

The interrupt response time is another important parameter to evaluate. In fact, this produces a systematic error on the flux increment evaluation.

The measurement procedure implemented is similar to the previous one, but in this case, the number of samples between the last rising edge and the samples array end is measured (Fig. III-8).

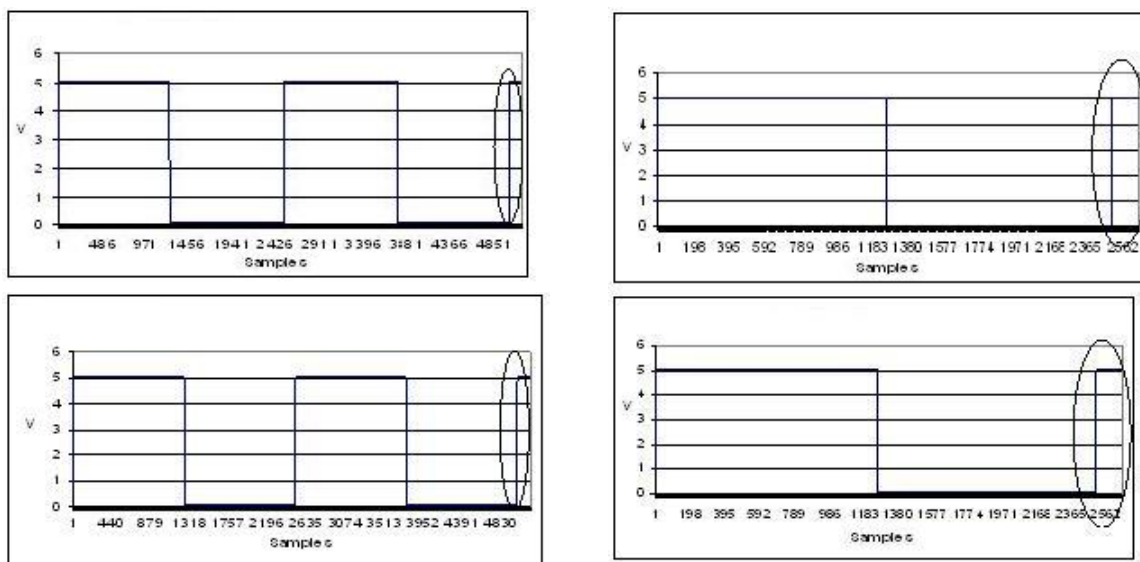


**Figure III-8: The interrupt response latency time in each acquisition was almost constant and equal to 150 samples (240  $\mu$ s with  $f_s=625$ KS/s)**

In all acquisitions (#30) the interrupt response latency time resulted approximately constant and equal to 150 samples (240  $\mu$ s with  $f_s=625$ kS/s).

In order to avoid a shift between the integrations in time and in angular domains a correction is applied to the integration process: during the sub-buffer read, when an encoder pulse is recognized, the last 150 samples have to be separated and taken into account in the next integration (added to the next samples array).

### III.3.2.4 - Timed loop jitter

By means of the previous measurements, initial delays and interrupt errors have been characterized and corrected. In order to evaluate random errors in the flux measurement, the jitter in the rising edge detection was assessed.

Again, a TTL signal was used as encoder pulses simulator and sent to the timed loop source.

The timed loop is implemented in LabView Real Time; each iteration of this loop is executed at period specified as time source. In this loop, the only operation performed was the evaluation of the time elapsed between two consecutive rising edge detections, using the LabView Real-Time clock 1  $\mu\text{s}$  resolution. In each test, a big amount of periods (10000) was measured and the  $tm_k$  dispersion was evaluated. Tests were performed with different input frequencies (250 Hz, 1kHz, 5kHz). Accurate period measurements that were performed by using the DAQ board 80 Mhz counter, were used as reference.

This test aimed at testing the TTL signal period stability. In fact, the measurements standard deviation is in agreement with the expected counting uncertainty (1 clock period at 80 MHz).

The same measurements carried out by using the interrupt system are characterized by a standard deviation one order of magnitude higher (0.44  $\mu\text{s}$ ). The maximum jitter in few cases reaches 4  $\mu\text{s}$ .

TTL reference signal frequency (Hz)	10000 consecutive period measurements with 80 Mhz counter		10000 consecutive period measurements with the Timed loop	
	$\mu$ ( $\mu\text{s}$ )	$\sigma$ ( $\mu\text{s}$ )	$\mu$ ( $\mu\text{s}$ )	$\sigma$ ( $\mu\text{s}$ )
<b>250</b>	4.00E+03	1.5E-02	4.0 E+03	4.4 E-01
<b>1000</b>	1.00E+03	1.27E-02	1.0 E+03	5.1 E-01
<b>5000</b>	2.00E+02	1.89E-02	199.996	6.7 E-01

Table III-2: Timed loop jitter characterization summary

In Tab. III-2, the results related to different frequency of the signal reference are summarized. The jitter error in the rising edges, detected via the hardware source timed loop, increases according to the TTL signal frequency. Anyway, even with a frequency of 5 kHz (equivalent to a coil turn rate of 20 Hz), the maximum jitter is less than 4  $\mu\text{s}$ , with 0.6  $\mu\text{s}$  standard deviation evaluated on 10000

periods (the same order of magnitude of the encoder accuracy). On the integration process (both  $\Delta\Phi_k$  and  $tm_k$  evaluation), the jitter error on the encoder pulses detection can be considered as negligible.

### III.3.2.5 - Integration process execution time

The proposed integrator can work only if the computation of  $\Delta\Phi_k$  and  $tm_k$  is performed before the next encoder pulse. The integration time imposes main limits to the:

- sampling rate; in fact, this determines the number of samples to integrate in the same time interval and, since integration algorithms have linear computational complexity, the integration time rises linearly with the points number:
- Maximum encoder frequency (hence coil speed and angular resolution); a higher encoder frequency means a shorter integration time interval, thus, less time to complete the integration;
- Maximum integration channels number. The DAQ card used can work in multiplexed mode with only 50 ns inter-channel delay; for instance, using 5 analog input channels for each cards, an acquisition, practically simultaneous, of 10 channels at 100 kS/s sampling rate is achievable.

The integration execution time on a 2500 samples array, corresponding to 625 kS/s and 250 Hz encoder frequency ( $N=256$  and coil rotation around 1 Hz) was evaluated using a Real Time (RT) timestamp (a 64 bit controller register). The trapezoidal integration algorithm was used. Many executions were considered in order to carry out a complete characterization of the execution time. Fig. III-9 shows the time execution statistics of the integration operation. .

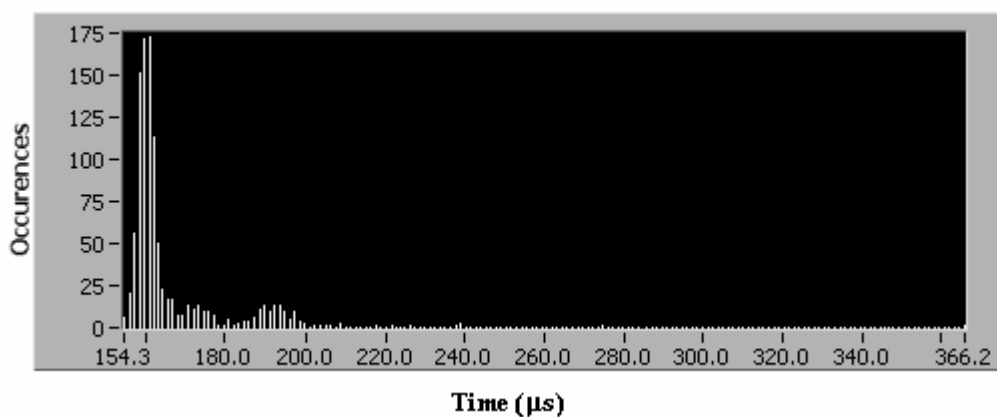


Figure III-9: Trapezoidal integration algorithm: execution time evaluation on 2500 points array- Distribution referred to 1000 executions

The measurement results are summarized in Tab III-3.

<i>Integration execution time tests results</i>	
<b>Mean (<math>\mu\text{s}</math>)</b>	166
<b>Maximum jitter (<math>\mu\text{s}</math>)</b>	201
<b>Standard deviation (<math>\mu\text{s}</math>)</b>	14

Table III-3: Integration execution time tests summary

The integration interval time is equal to 4000  $\mu\text{s}$  and the following operations have to be executed:

1. samples array reading from the circular buffer (execution time some tenths of  $\mu\text{s}$ );
2. integration;
3.  $t_{m_k}$  evaluation, time elapsed between two consecutive rising edges detection (execution time: few  $\mu\text{s}$ ).

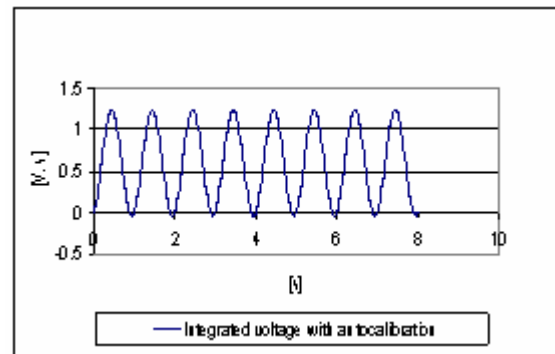
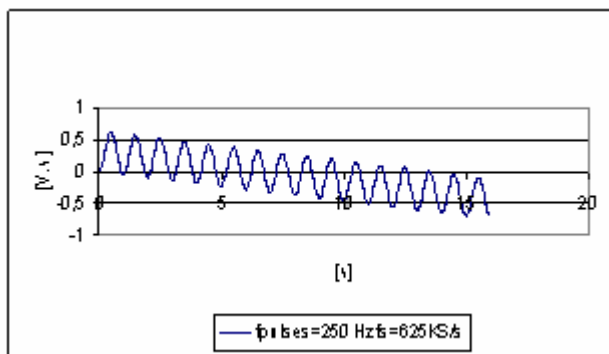
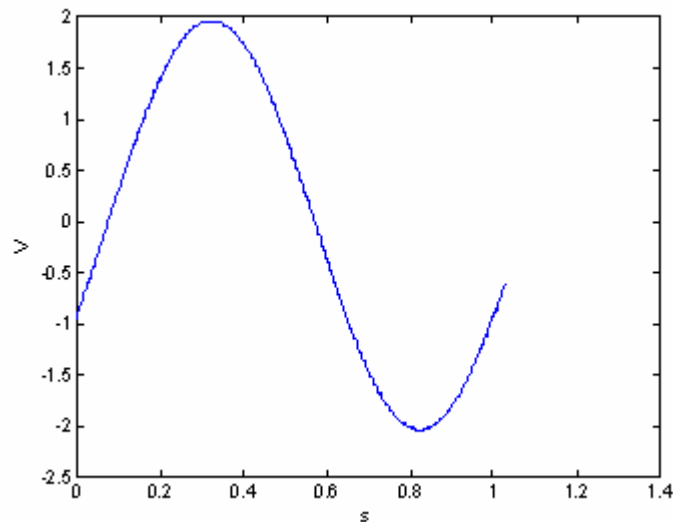


Figure III-10: Integrator autocalibration test: i)- The integrator input test signal, a sinusoidal signal  $A=2$  Vpp,  $f=1$  Hz (above) -The signal integrated over 8 s without offset correction (left) -The same integration performed with the autocalibration and the RT offset correction (right)

The computation process of the couple  $\Delta\Phi_k$  and  $tm_k$  needs only 1/20 of the full time slot available. This assures enough margin to have a higher encoder frequency or to perform an integration multi-channels.

### III.3.2.6 - Measurement examples and final considerations

A complete measurement campaign was carried out on the overall integrator by simulating different measurement conditions. The efficiency of the offset auto-calibration procedure and the measurement uncertainty  $tm_k$  were assessed.

Fig. III-10 shows the test of the input offset auto-calibration: a sinusoidal waveform with an amplitude of  $2 V_{pp}$  at frequency of 1 Hz is the input signal to simulate the output of the rotating coil(a). A TTL signal simulates an encoder 250 pulses per turn. A multiturn integration over 8 s time was performed without and with offset calibration. In the first case (a), the high drift is due to a 69 mV residual offset in the sinusoidal generator. Before starting the integration the input signal is sampled for 10 s at an integer multiple of the signal frequency, the DC component is evaluated and then corrected in real time at each integration (c).

In the same test conditions, the chart of  $tm_k$  measurements related to 4 coil turns is shown in Fig. III-11.

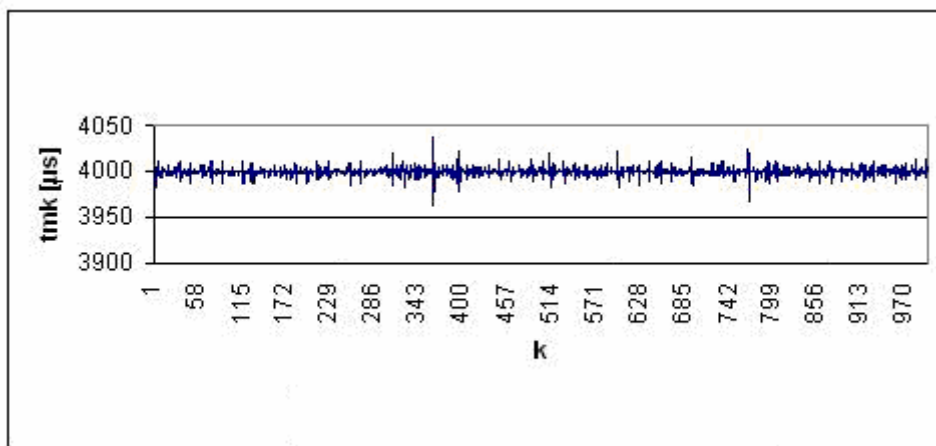


**Figure III-11: Tmk measurements of 4 coil turns integration**

By taking into account that the TTL signal used to simulate the encoder pulses is characterized by a frequency stability of 10 ppm, it is evident that the jitter error in the interrupt response reaches in some cases even 40  $\mu s$ . In the test, the standard deviation is 5.6  $\mu s$ . Further measurements were carried out at different sampling frequencies and TTL signal frequency in order to understand the origin of this uncertainty source, not in agreement with the previous characterization of the timed loop structure.

Tab III- 4 summarizes the results of these tests (2000 consecutive  $tm_k$  measurements carried out at different sampling rate and encoder signal frequency). The high jitter error in the pulses encoder detection, apparently, does not depend on the encoder signal frequency; on the other side, lower standard deviation was registered by decreasing the sampling rate. Timed loop uncertainty in the integrator implementation is principally related to the system (i.e. Operating system RT + DAQ card drivers).

The jitter error as reduced by means of a different implementation.

Test conditions		$tm_k$ measurements uncertainty	
Fs (kS/s)	F encoder (Hz)	$\mu$ [ $\mu$ s]	$\sigma$ [ $\mu$ s]
625	250	4000	5
625	500	2009	3
625	1000	1000	4
100	250	4000	2
200	250	4000	2

Table III-4:  $tm_k$  measurements uncertainty tests summary

### III.3.2 Solution based on encoder signal acquisition and rising edges detection

The further algorithm is based on the simultaneous sampling of both the signal to integrate and the encoder signal (Fig. III-12) The samples acquired are always transferred via DMA channels in a circular buffer dynamically allocated in the controller RAM.

Periodically, a fixed samples number is read from the buffer and the following operations are executed:

- on the encoder samples array a robust algorithm of rising edges detection is applied. It delivers an array containing the indexes corresponding to the starting and ending of each integration interval;
- for each index array element, a sub-array is extracted from the voltage input samples array. This is integrated and the result represents the corresponding flux increment;
- the difference between two consecutive elements of the indexes array multiplied for the sampling period gives the  $tm_k$  measurement;
- the residual elements in the arrays read from the circular buffer are merged to the next samples set.

The expected uncertainty in the  $tm_k$  evaluation is now equal to a sampling period ( $1.6 \mu s$  at the maximum sampling frequency). All the jitter problems are solved with this implementation. The only critical point is represented by the synchronization between the two channels acquisition. In order to assure a simultaneous sampling two channels on the two different DAQ cards was used. The two cards were synchronized by signals of the PXI trigger bus.

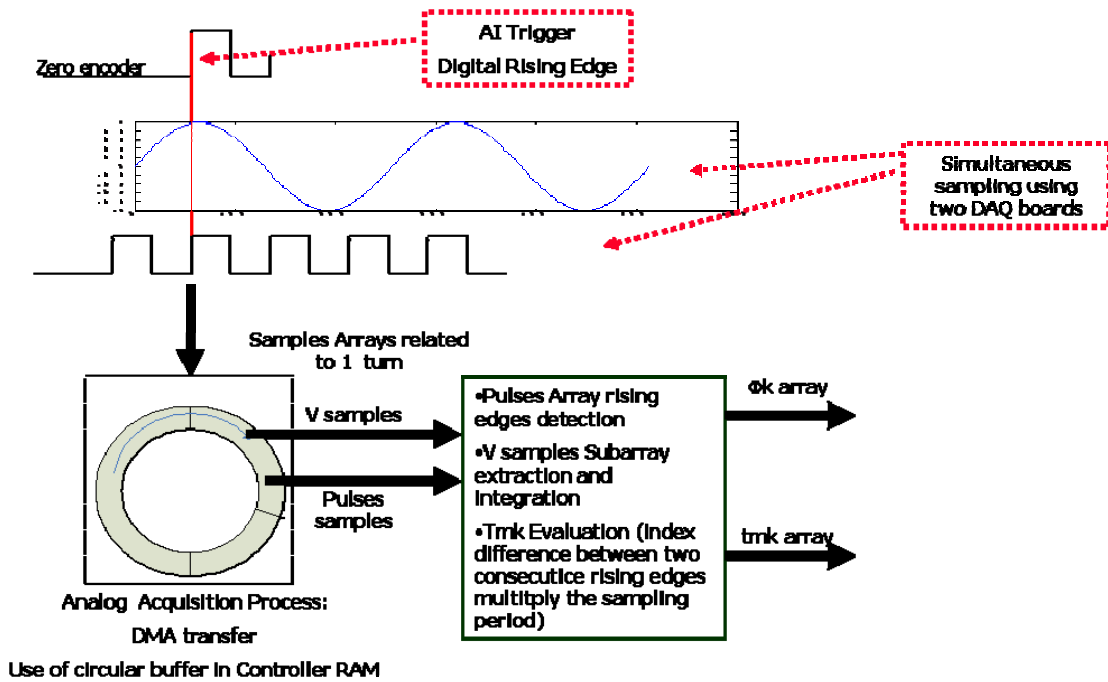


Figure III-12: Working principle of the PXI numerical integrator based on encoder signal sampling.

### III.3.2.7 - Interchannel delay evaluation

In order to check the synchronization between acquisition start and encoder signal, as well as the temporal shift in the two sampling, the same TTL signal was acquired on the two input channels. Its first rising edge is used as acquisition starting trigger.

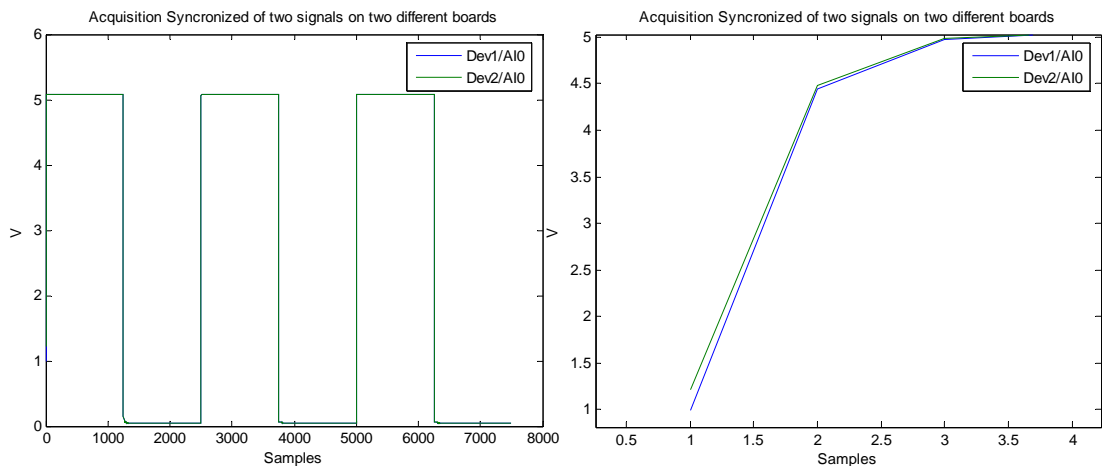


Figure III-13: Acquisition of the same TTL signal on the two input channels. On the right the perfect synchronization and the negligible interchannel delay is showed

In Fig. III-13, the test results are shown. No shift between the two signal acquisitions can be appreciated. It is reasonable to conclude that using signals of the trigger bus of the PXI backplane the acquisition of the two channels is practically simultaneous.

### III.3.2.8 - Measurement examples and final considerations

On this new integrator implementation the same measurements seen before has been carried out.

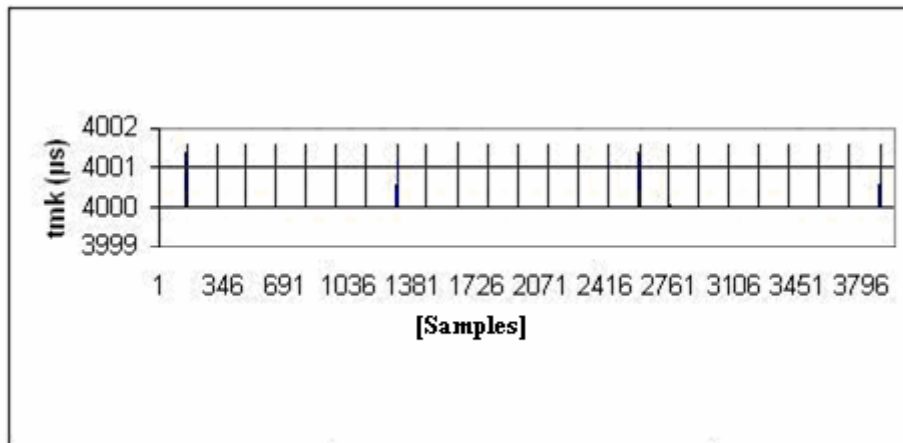


Figure III-14: Distribution of  $tm_k$  measurements performed with the new algorithm implemented

The measurement uncertainty in the  $tm_k$  measurements was in any condition equal to one sampling period ( $1.6 \mu s$  at the maximum sampling frequency).

Concluding, this implementation of numerical integrator has shown good results in terms of rising edges detection uncertainty and great robustness. The main technical data of this proof PXI integrator are summarized in Tab. III-5.

PXI integrator main data	
Input Voltage	$\pm 100 \text{ mV}$ to $\pm 10 \text{ V}$ ( $\pm 0.1, \pm 0.2, \pm 0.5, \pm 1, \pm 2, \pm 5, \pm 10$ )
Integration time	$>20 \mu s$
Minimum Resolution (Gain=1) (Vs)	$4.8 \cdot 10^{-11}$
$tm_k$ measurement accuracy (s)	$1.6 \mu s$
Integration accuracy (Vs)	$1.6 \cdot 10^{-5}$
Offset Autocalibration	Yes
Integration method	Trapezoid, Bode, Simpson

Table III-5: The proof PXI integrator-Main technical data

It is important to note that in spite of the high resolution (estimated as the product of the ADC resolution and the minimum sampling period) the integration accuracy is some order of magnitude higher. The value in the table is referred to the worst case of an input voltage equal to the full range multiplied by the sampling period that represents the uncertainty in the edge detection. This is the main uncertainty source in the integration process and has to be contained as much as possible in the proposed integrator based on the DSP.

### III.3.3 - Comparison with PDI integrators

Flux measurements on an LHC dipole supplied at warm were carried out by the PXI integrator developed and the PDI integrator, simultaneously. The experimental setup is shown in

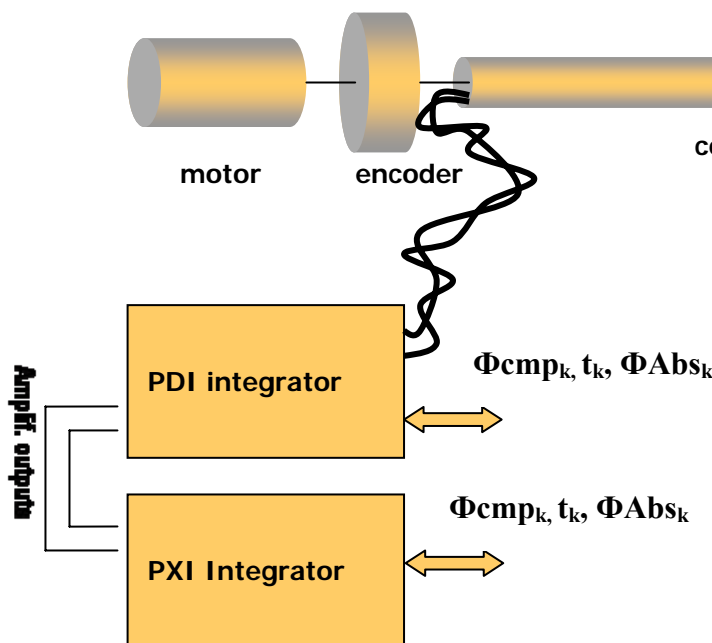


Figure III-15: Comparison between PDI integrator and PXI integrator- Experimental setup

The Fig. III-15. A coil of a length of 700 mm, coupled with an encoder, and equipped by slip rings, for continuous rotations, was used. The input signals to the PXI integrator concerning the absolute and the compensated coil come from the same PDI integrators amplifiers. For these measurements, owing to the extremely low level of the signal, they were set at 50 and 500 gain, for the signal absolute and compensated, respectively.

Tests were carried out at different coil speeds and supply current. The measurement settings are summarized in Tab.III-6.

Measurement Conditions	Test 1	Test 2	Test 3	Test 4
Rotation Speed (rad·s <sup>-1</sup> )	1.4393	3.1238	6.4605	6.4734
Absolute Integrator Gain	50	50	50	50
Compensated Integrator Gain	500	500	500	500
Number of points	256	256	256	512
Current (A)	10.001	10.002	5	5
Temperature (Degree)	22	22	22	22

Table III-6: Measurement setting comparison test.

In Fig.III-16 the input voltage, as well as its integral (the magnetic flux) measured (Test 1) by the PXI integrator over one coil turn, are shown.

The input voltage, the flux increments, and the flux samples over the time are shown both for

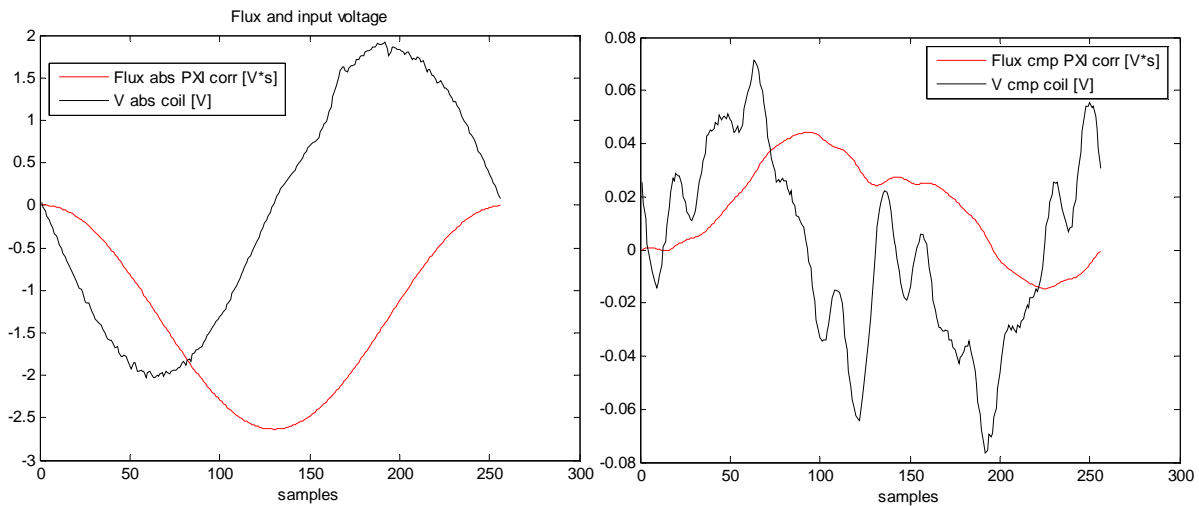
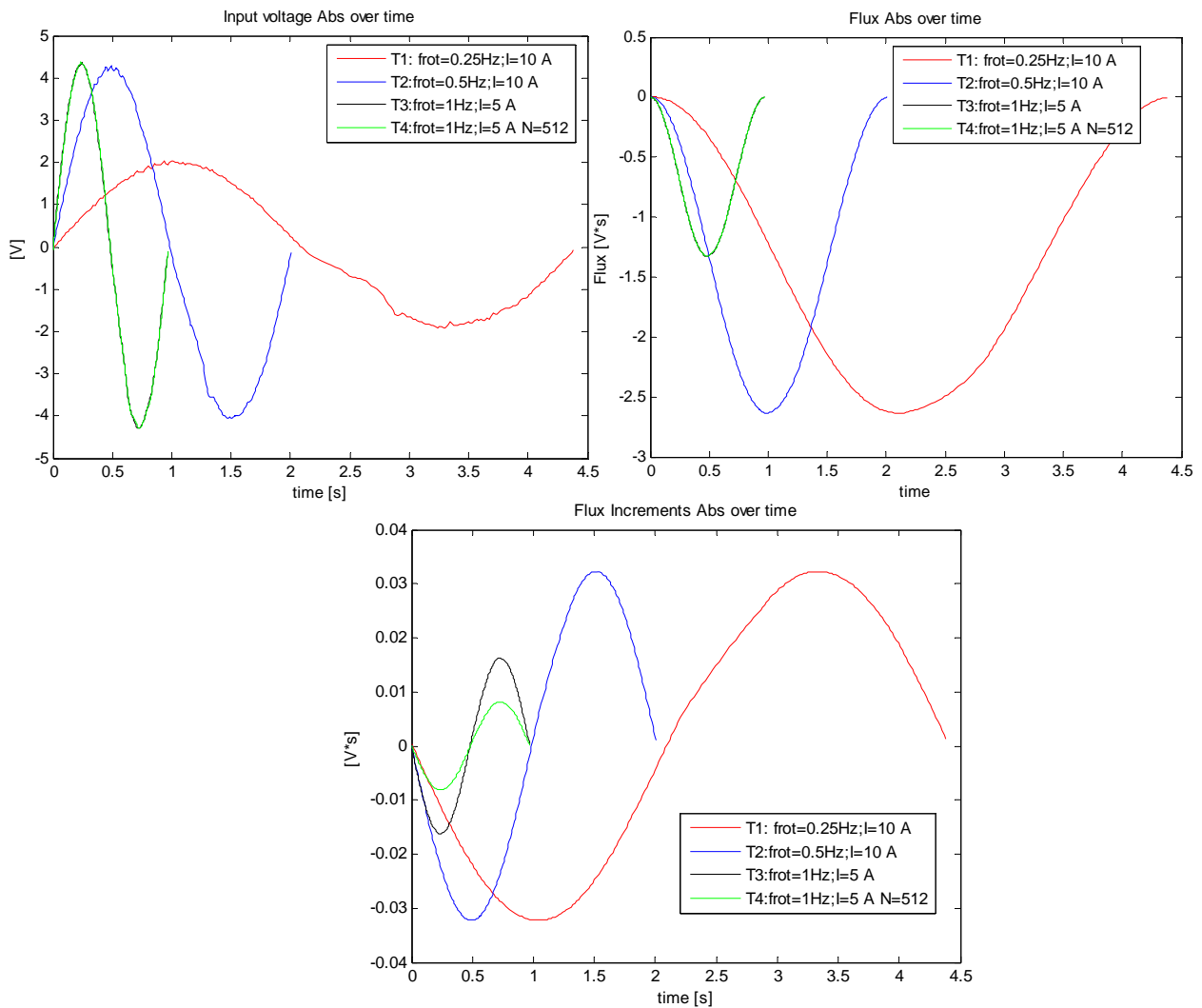


Figure III-16: Input voltage and flux integrated absolute (on the left) and compensated (on the right) for the test 1.

the absolute (Fig. III-16) and for the compensated measurements (Fig III-17). As expected, the input voltage increases according to the coil speed (in the test 3 and 4 the current is halved), while flux and its increments are about constant (if the coil speed increases, the voltage to integrate is higher, but the  $t_{m_k}$  become shorter). If, instead, the angular resolution doubles, each flux increment halves correspondingly (Test 3 and 4).

On the flux samples acquired both by the PDI and the PXI integrator an offset correction was applied in order to have comparable results. Since the measurement is in static conditions, a integer number of period of the sinusoidal waveform magnetic field is acquired after a complete turn coil;



**Figure III-17: Input voltage, Flux Increments and flux absolute at different coil speeds.**

thus, the overall integration offset can be evaluated as difference between the  $N^{\text{th}}$  and the first flux sample, (N is the number of flux measurements performed in one turn) from which, the input offset voltage is obtained; afterwards the offset correction is applied at each flux increment. An example of results of this procedure is shown in Fig. III-19.

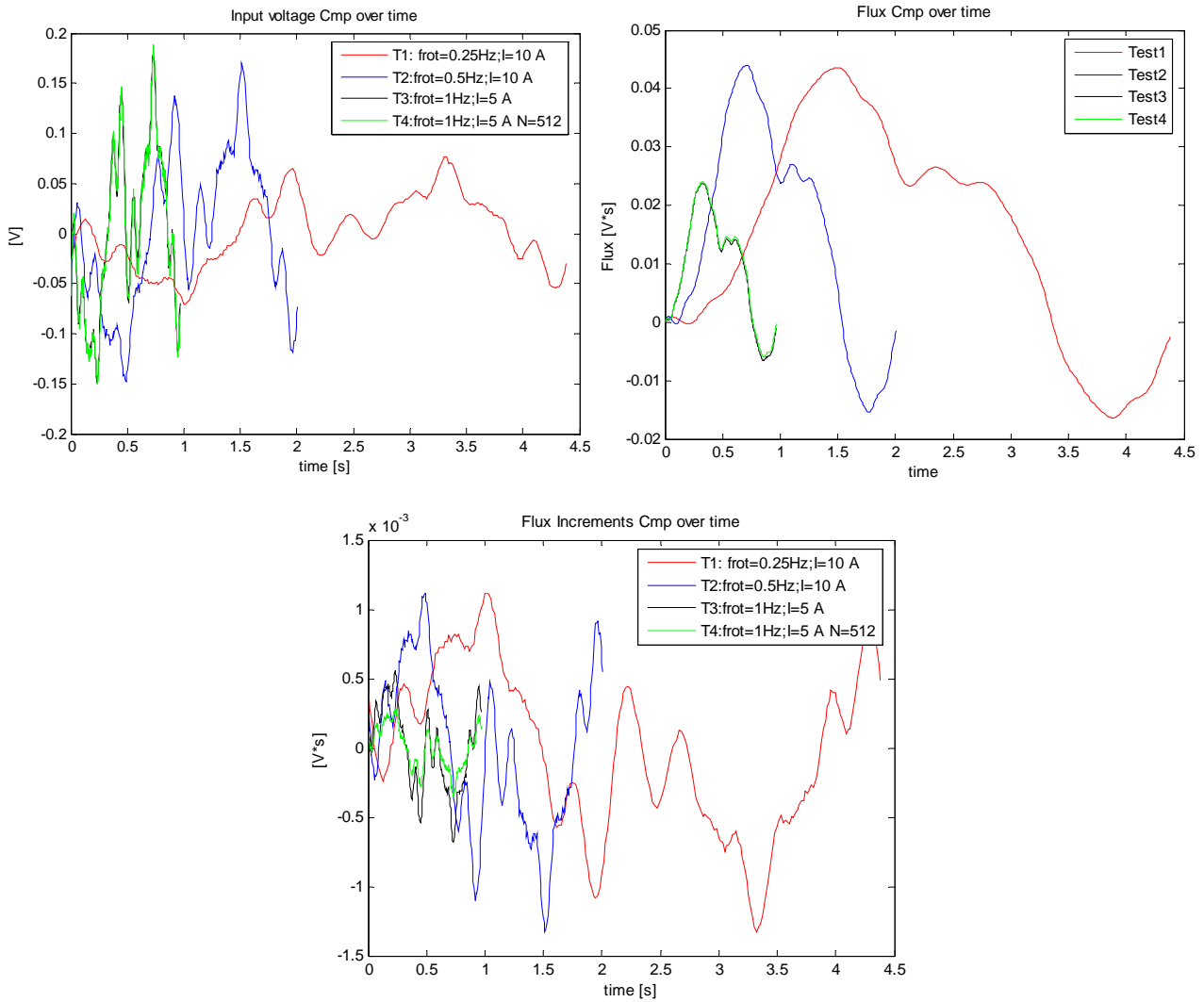


**Figure III-18: Input voltage, Flux Increments and flux compensated at different coil speeds**

In Fig. III-20 the compensated flux increments measured by PDI integrator and PXI at 1 Hz coil speed, and 512 points per turn, are compared. The resolution limits of the PDI integrator can be

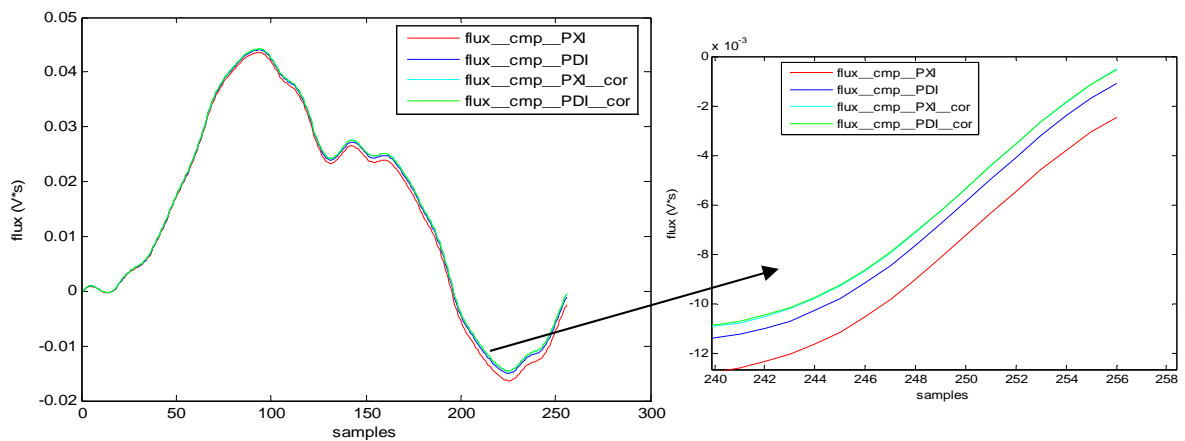


**Figure III-19: Compensated flux in test 1 measured by PDI and PXI integrator with and without offset correction**

argued by the higher quantization noise.

Tab.III-7 contains a set of flux increments around the zero crossing. Several values are under the PDI integrator resolution while, the PXI integrator appreciates even flux increments around  $10^{-7}$  Vs. In the same Tab., the different resolution in the  $tm_k$  evaluation are visible,  $1 \mu s$  for the PDI integrator and  $1.6 \mu s$  for the PXI system (with the algorithm based on the encoder signal sampling, the resolution is given by the sampling period).

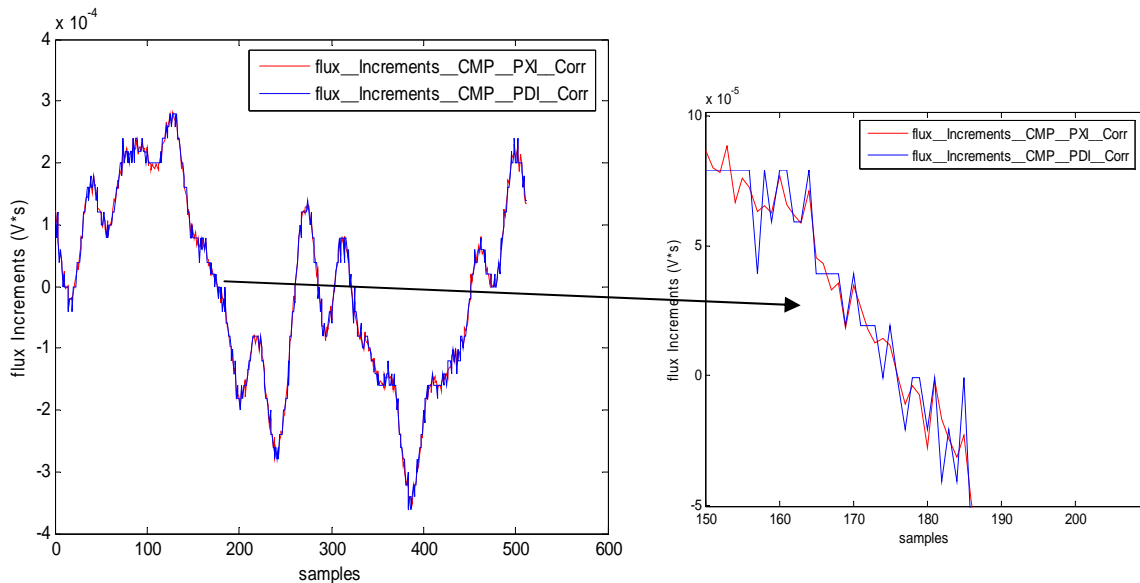


**Figure III-20: Test 4 compensated flux. On the right the PDI integrator resolution limit is evident.**

The flux increments residual as well as the differences between corresponding flux samples were evaluated for each test both for absolute and compensated measurements (Fig. III-21-22).

The residual flux increments is in agreement with the PDI integrator resolution, as a matter of fact its maximum value is just the PDI resolution ( $2 \cdot 10^{-5}$  Vs). However, strangely, the residual envelope follows the input signal (in the evaluation of the flux increments the sign inversion has not

FWDCmp	FWDCmp_PDI	TimeFWD_PXI	TimeFWD_PDI
4.1167E-05	4.0000E-05	1.8800E-03	1.8790E-03
2.8636E-05	4.0000E-05	1.8752E-03	1.8750E-03
9.9551E-06	0.0000E+00	1.8736E-03	1.8720E-03
2.4161E-05	2.0000E-05	1.8688E-03	1.8710E-03
5.9164E-06	0.0000E+00	1.8720E-03	1.8700E-03
-3.4007E-06	0.0000E+00	1.8688E-03	1.8690E-03
-2.5071E-06	0.0000E+00	1.8672E-03	1.8690E-03
5.4380E-07	0.0000E+00	1.8688E-03	1.8660E-03
-3.7308E-05	-4.0000E-05	1.8640E-03	1.8640E-03

**Table III-7: Comparison between compensated flux increments around the flux zero crossing measured respectively with PDI PXI and integrator in test 4.**

been applied); this behaviour is related both to the absolute and the compensated flux and increases according to the coil speed (because the input signal increases). As a consequence, the difference between the flux samples has a dipolar field trend for the absolute measurements. This produces a difference between the field multi-poles evaluated on the basis of the two flux vectors. Fig. III-23 shows this differences in the measurements carried out in Test1. In particular, the deviation of  $2 \cdot 10^{-8}$  T between the A1 harmonics is a direct consequence of the sinusoidal flux residual.

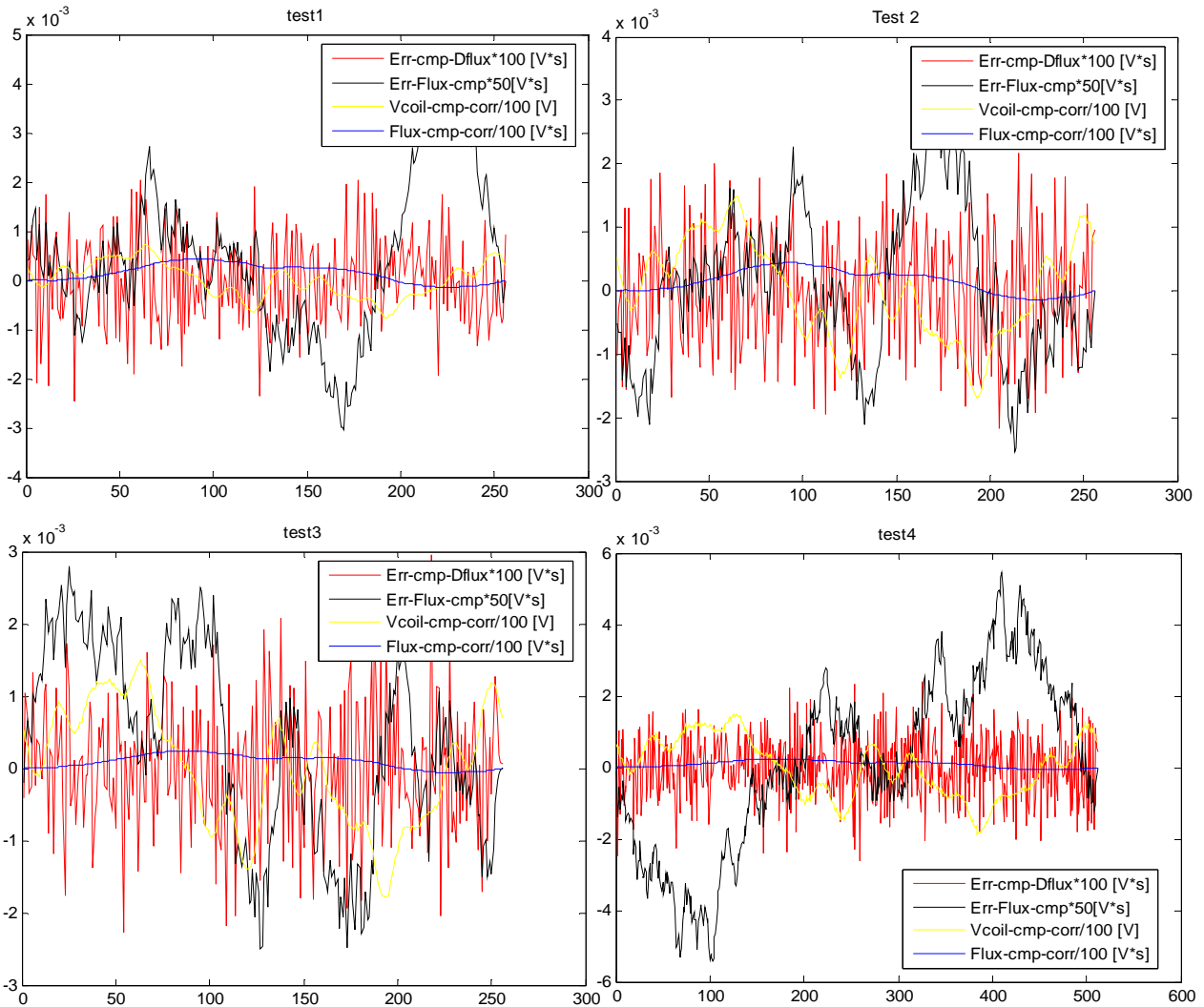


**Figure III-22: Comparison between the PDI and PXI integration in all the compensated measurements performed. On the same graph the differences between the flux samples and the respective flux increments as well as the input voltage and the flux are shown.**

The dipolar residual flux, evaluated as difference between the flux increments measured by the PDI and the flux increments measured by the PXI integrator ( $\Delta\Phi_{kPDI} - \Delta\Phi_{kPXI}$ ), is not constant as expected (difference of resolution). In fact it exhibits an alternating trend. This result can mean that the PDI integrator provides for each sample an extra-estimation of the flux increment with respect

to the PXI integrator. In order to understand if this phenomenon can be due to a wrong encoder pulses rising edges detection, in the PXI integrator, the difference between the time  $tm_k$ , measured by both integrator systems has been computed (Fig. III-24) for all the flux absolute measurements. The maximum difference registered is in agreement with the time measurement uncertainty of the two system ( $1 \mu s$  for PDI and  $1.6 \mu s$  for the PXI integrator). All the waveforms are correctly symmetric except the first graph, where a negative polarization is marked. This is sign of an extra estimation of the time intervals measured with the PXI system of 1 sampling period ( $1.6 \mu s$ ).

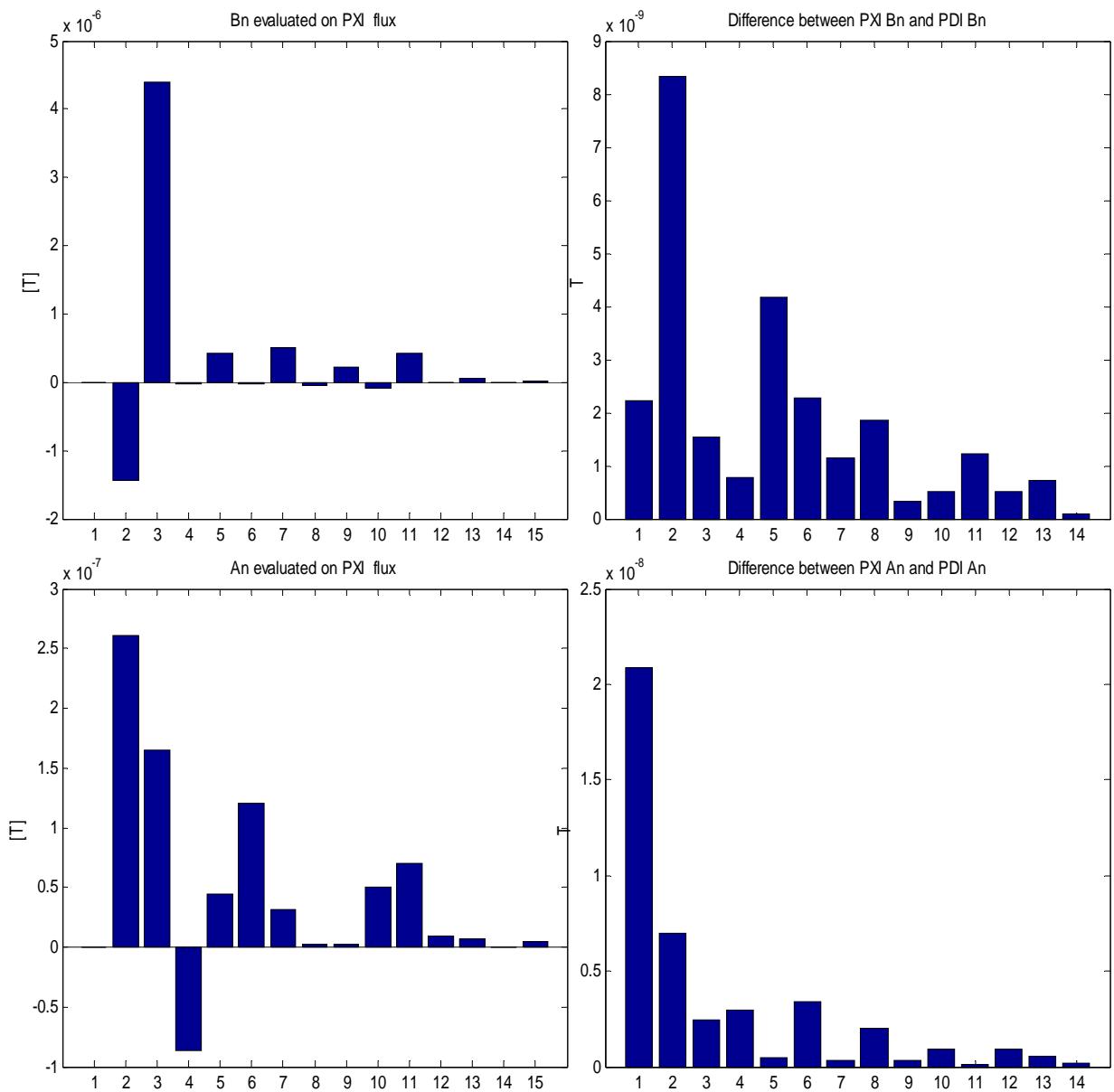


**Figure III-23: On the left multipoles values measured on the PXI flux samples. On the right the differences between the same multipoles measured using the PDI flux samples and the PXI. The main field B1 is equal to 7,0822 mT with 0.1889 mT A1. The measurement is related to the test1.**

This intuition is confirmed by the graphs in Fig. III-25, where the sum of the progressive time  $tm_k$  are depicted for all the absolute flux measurements done. The drifts show that the PXI system provides a  $tm_k$  measurement greater than the correspondent PDI integrator. By assuming that the surplus is equal to 1 sampling period ( $1.6 \mu s$ ) for each  $tm_k$ , on  $N$  measurements (with  $N$  is the number of the flux measurement in a coil turn) a maximum drift around  $400 \mu s$  is expected over one complete coil turn. All the graphs in Fig. III-25 are, meanly, just characterized by this maximum value.

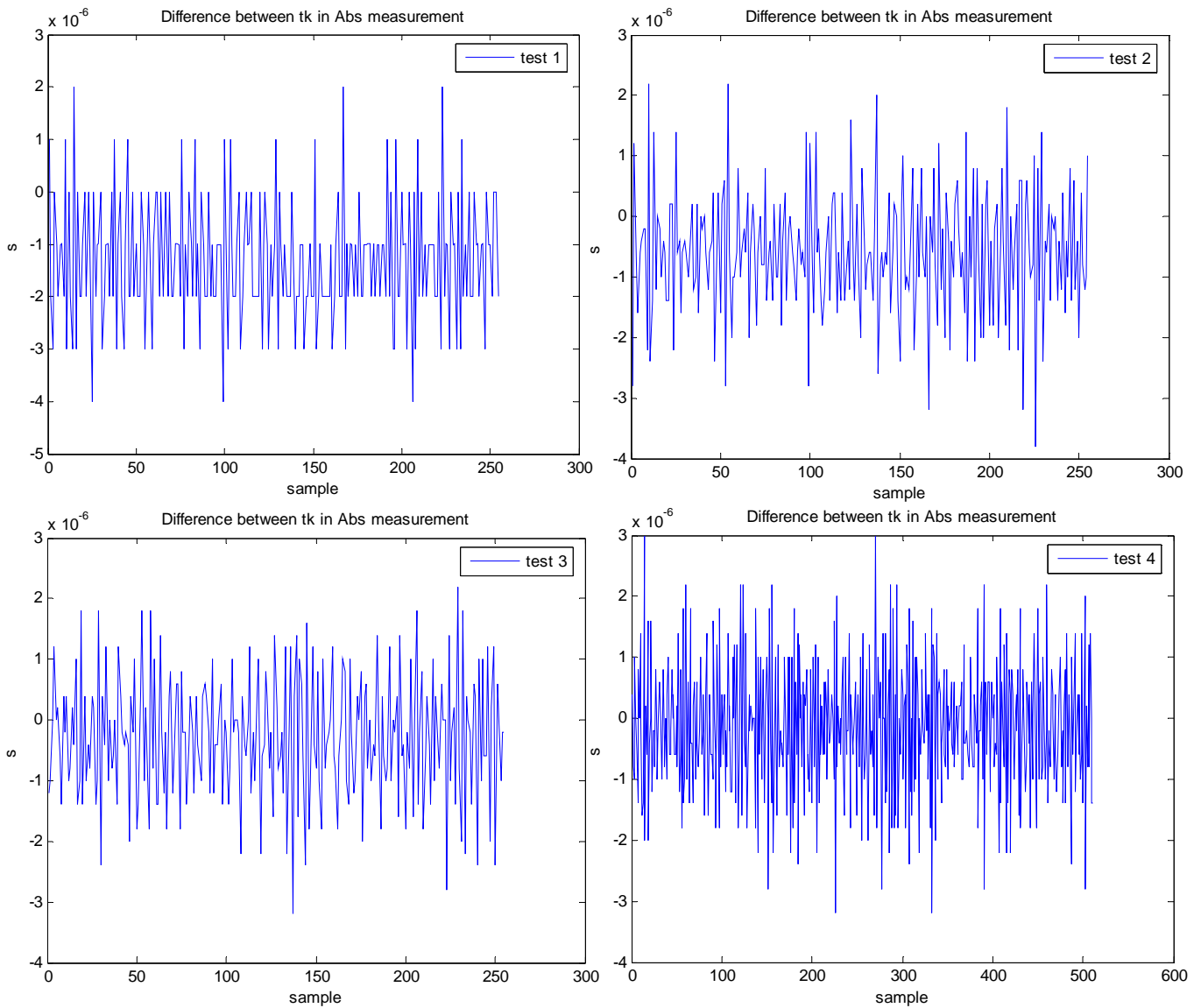


**Figure III-24: Differences between the  $tm_k$  measured respectively with the PDI and PXI integrator in all the absolute flux measurements performed**

With the PXI system, this extra-estimation of the time interval  $tm_k$  consequently leads to an extra-estimation of the  $\Delta\Phi_k$ , that is, in any case, lower than the product between the maximum input voltage and the sampling period. In fact, by taking into account 4 V as maximum input voltage

(correspondent to the maximum coil speed and absolute coil), the surplus on each flux increment can reach the value of  $8 \cdot 10^{-6}$  Vs, but, this value is still under the resolution of the PDI integrator.

Finally the PXI integrator is characterized by an error in the times and flux increments evaluation but this does not explain the trend of the flux residual; in fact the behaviour registered is exactly the opposite: the flux increments measured with the PDI integrator are, generally, greater than the one measured with the PXI. The only justification can be found in the difference between the theoretical  $K_{VFC}$  used in the conversion of the pulses counted in the PDI integrator and the real value that leads to an extra-estimation of the flux increments greater than the one introduced by the PXI system.

Concluding the PXI integrator was very useful to show:

- the limits in resolution of the PDI integrators when the angular resolution increases;
- the effect of the trigger uncertainty on the integration.

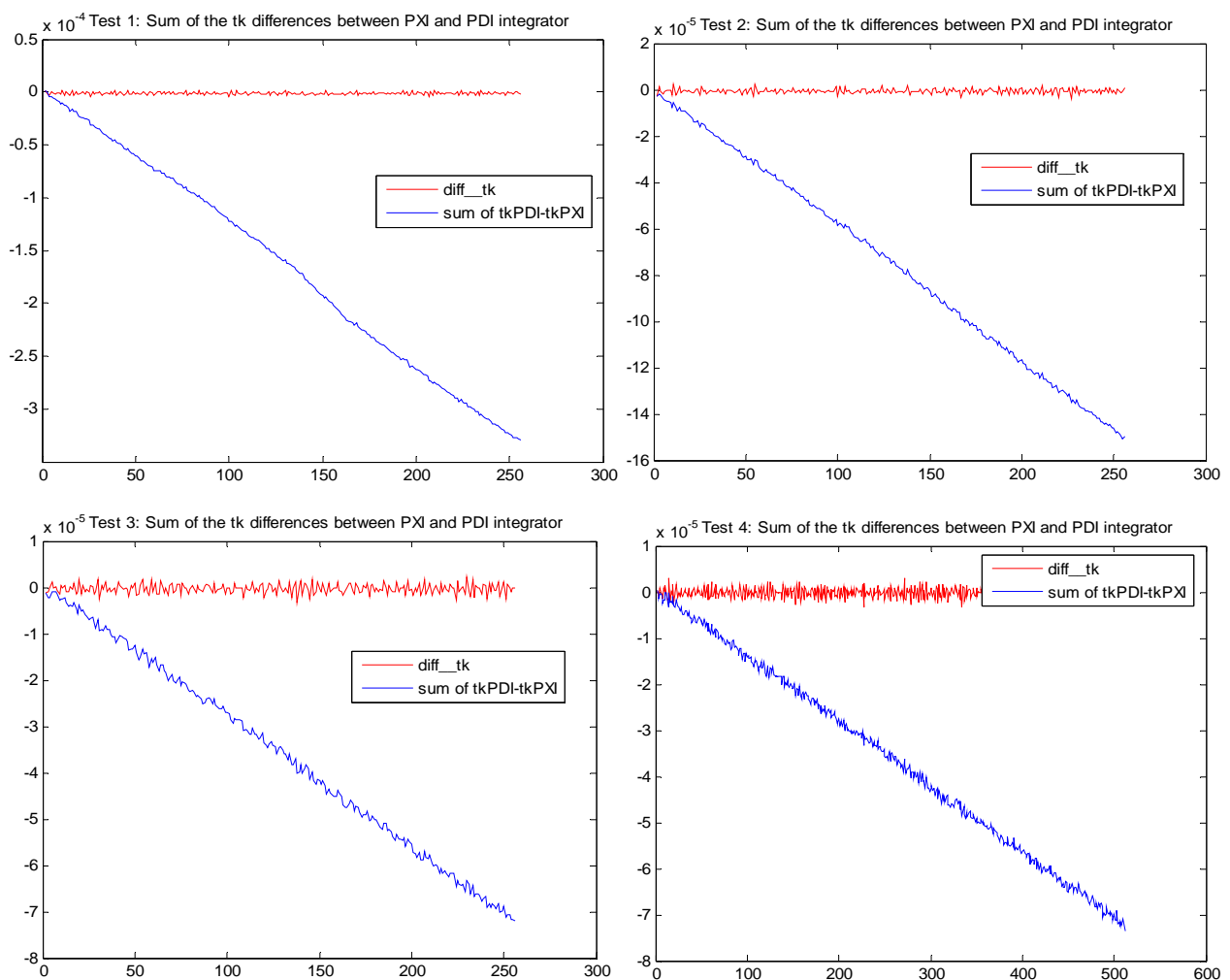


**Figure III-25: Sum of the differences between the tk measured respectively with the PDI and PXI integrator in all the absolute flux measurements performed**

### III.4 - Architecture Overview

The architecture of the new rotating coils measurement system is shown in Fig. III-26.

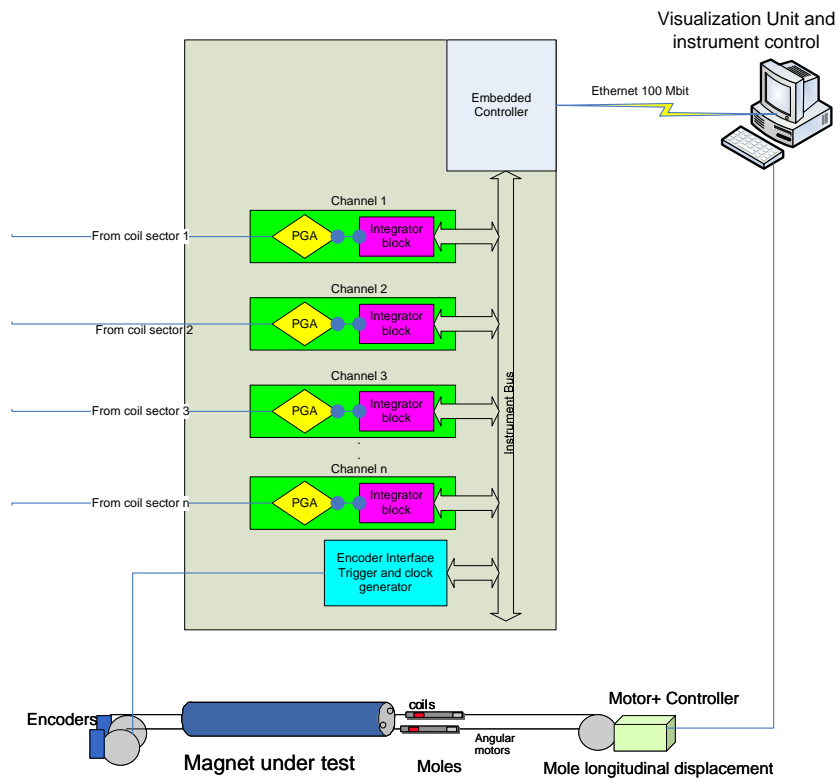


**Figure III-26: Architecture overview of the proposed instrument for the rotating coils measurements**

The integration of each coil sector is carried out by a Fast Digital Integrator (FDI). Provided that long coils for LHC dipole test are based on 13 sectors and that the two apertures of the magnet are tested simultaneously, the number of signals to be integrated is 56 (for each sector, the absolute and compensated signal). Hence, the same crate will host up to a maximum of 56 integrator boards.

An additional prescaler board is devoted to the decimation of the pulses coming from the encoder to obtain the requested angular resolution.

The boards communicate with the embedded controller via the instrument bus. The controller carries out the following tasks:

- By communication for exchange of information about the measurement (coil speed, magnetic field expected, spatial resolution and measurement duration):
  1. set the gain on each FDI board;
  2. initialize the FDI by sending the calibration command;
  3. program the prescaler board to obtain the requested angular resolution;
- measurements start and stop by sending the specific command to the integrators;

- application on measured data of the standard analysis or suitable algorithms , better, the new algorithms so that the measured field harmonics are delivered at fix time instants to the visualization unit via TCP connection (point to point);
- management of errors or exceptions upcoming from the integrators are handled.

Finally, through the visualization unit, the operator can set, start, and control a measurement. Field harmonics, as well as the supply current can be displayed in real time. This unit controls also other equipment involved in a rotating coils measurement.

#### III.4.1 - The new integrators boards: general layout

On the basis of the performance of PDI and according to the above analysis, the following design specifications are defined:

<b>Input Voltage</b>	$\pm 5 \text{ V}$
<b>Input Impedance</b>	1000 M $\Omega$ unbalanced, 2 M $\Omega$ balanced
<b>Input protection</b>	$\pm 50 \text{ V}$
<b>Gain selection</b>	0.1, 0.2, 0.4, 1, 2, 4,10, 20, 40, 100
<b>Gain non-linearity</b>	$\pm 10 \text{ ppm}$ of full range
<b>Gain stability</b>	100 ppm long term (1 day) 10 ppm short term (1 hour)
<b>Input voltage noise (peak-to peak)</b>	G=1 10 $\mu\text{V}$ G=10 1 $\mu\text{V}$ G=100 0.3 $\mu\text{V}$
<b>Input voltage offset</b>	G=1 70 $\mu\text{V}$ G=10 7 $\mu\text{V}$ G=100 1.5 $\mu\text{V}$
<b>Integrator resolution</b>	$3 \cdot 10^{-11} \text{ Vs}$
<b>Trigger</b>	external or internal up to tenth of kHz frequency.

**Table III-8: Design specification for the FDI integrator**

According to the requirements, of Tab.III-8, the architecture of the FDI was set up (Fig. III-27). In the following, the main components of the FDI architecture are analysed.

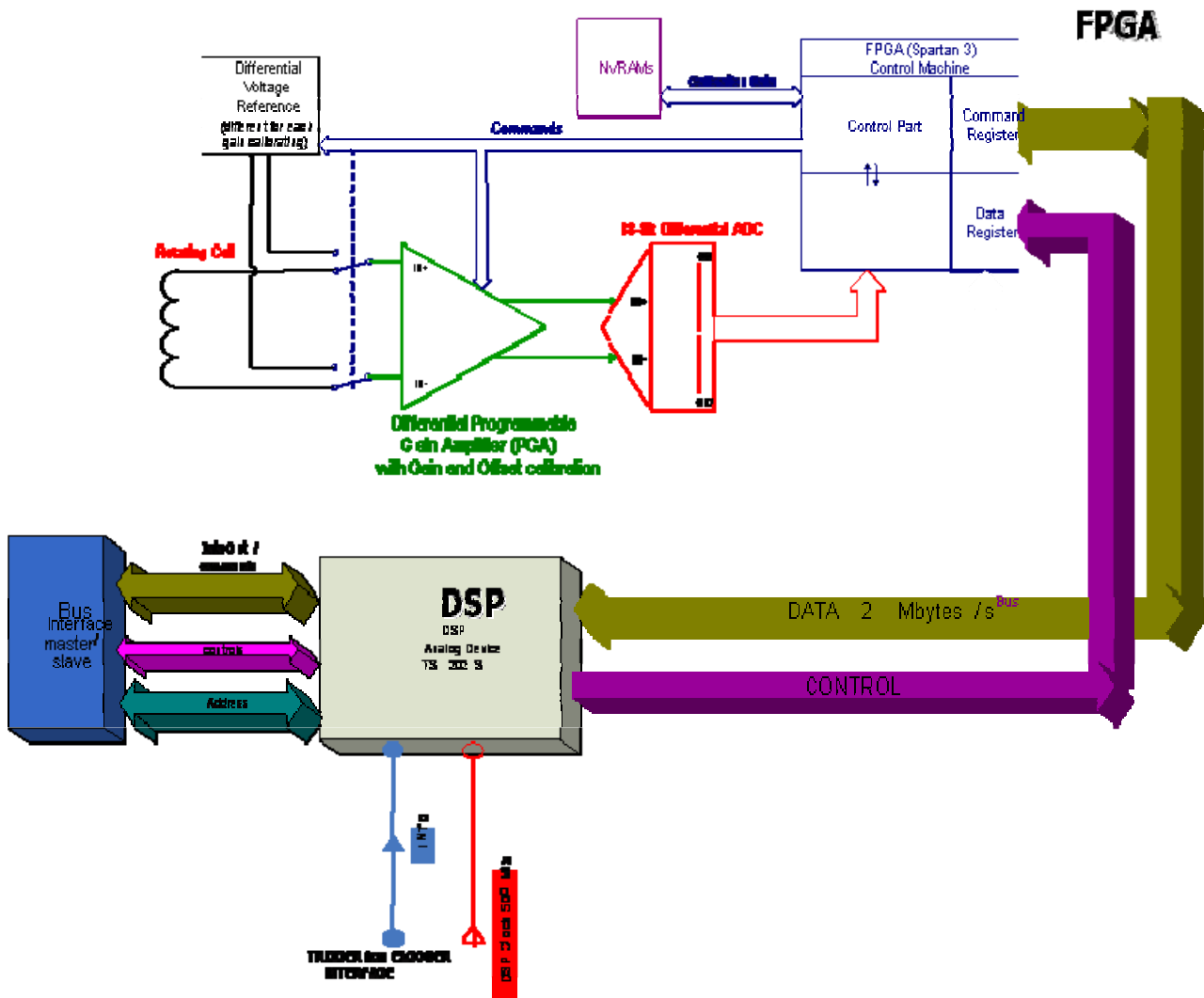


Figure III-27: Architecture of the new numerical integrator board

#### III.4.1.1 - Programmable gain amplifier

The programmable gain amplifier (PGA) of the analog front-end of the FDI is shown in the Fig. III-28; its design is based on the following key basic ideas:

- differential measurement chain: the input section, as well as, the ADC input, are fully differential in order to increase the CMRR;
- digital Kelvin resistive divider: the gain variation is obtained through a programmable Kelvin resistor, assuring high accuracy;
- FPGA control: at low-level a FPGA supervises PGA operations, self-calibration of the data acquisition chain, and interface with the board bus;
- dichotomic algorithm of self-calibration: the calibration of the analog front-end is carried out in real-time automatically, by means of a dichotomic algorithm running on the FPGA;

- real-time correction of systematic errors: by processing the samples out of the ADC converter, the FPGA establishes the correction of the input gain and of the voltage offset.

The core of the PGA is a Double Input Double Output (DIDO) structure in order to process the signal in differential mode and to change the gain by acting on only one resistor ( $R_{gi}$ ). PGA input, selected by the FPGA, are (i) the coil signal for the measurement operation, (ii) the voltage reference for the operation of the gain calibration, (iii) a short circuit for the operation of the offset compensation. The selection of the gain is done by means of a Kelvin divider structure (Fig. III-28). The amplification is carried in two sections: the pre-attenuation section is passive and two gain are selectable 1/10, and 1/20; the amplifier section allows to choose 8 different gains (2, 4, 5, 10, 20, 40, 50, 100) to be selected by means of the Kelvin divider resistor. The combined use of the pre-attenuation and of the active sections allow gains less than 1 to be achieved.

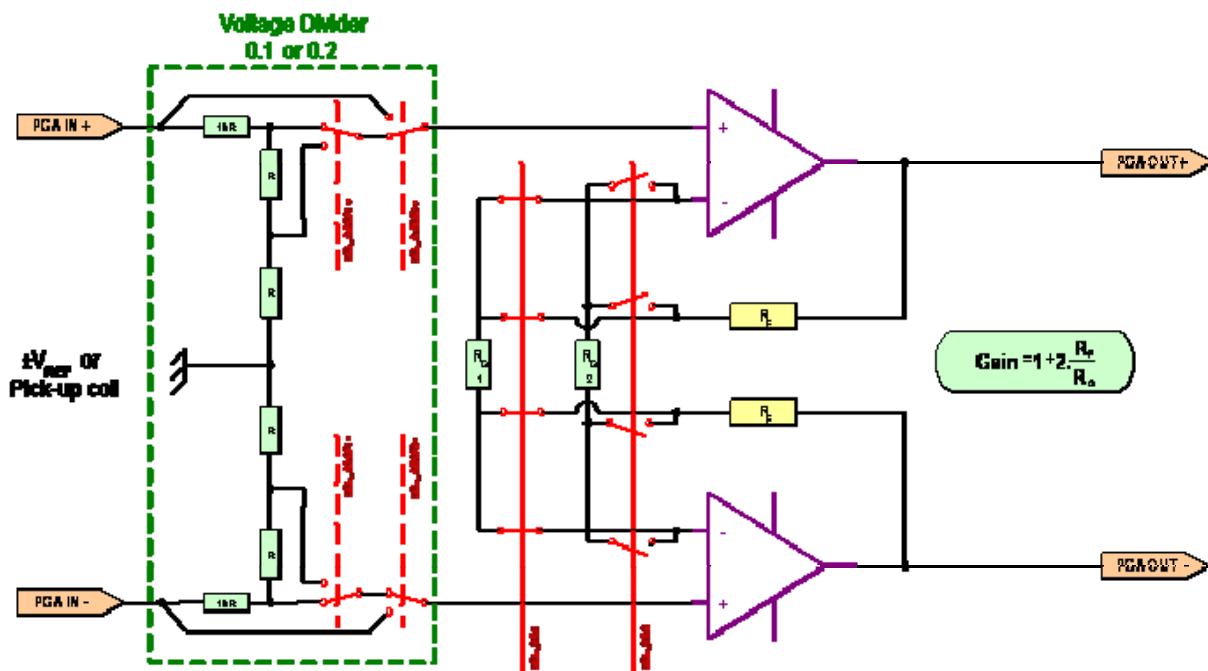


Figure III-28: Layout of the gain programmable amplifier.

The FPGA is in charge of calibrating offset and gain of the front-end section according to the following steps:

- offset calibration of PGA with input short circuit;
- gain calibration of PGA with Voltage Reference Generator (VRG) input;
- offset calibration with the coil signal.

The offset is compensated by summing the output voltage of a 16-bit Digital-to-Analog Converter (DAC) on the *Input +* of the coil signal; the calibration ends when the output of the ADC is null

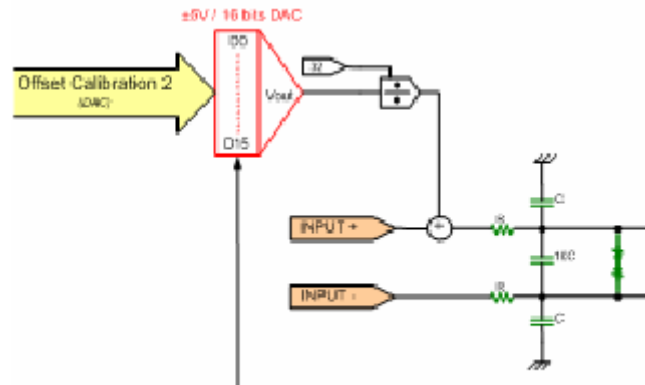


Figure III-29: The DAC based Offset calibration

(Fig. III-29).

The gain is calibrated by using as input the voltage output of the VRG selected according to the gain, thus the output of the PGA is at the full-scale (Fig. III-30). The gain is adjusted by a digital potentiometer acting on the feedback resistor  $R_f$  of the PGA (Figure III-31).

The data of offset and gain calibration are then stored in an NVRAM memory for in real time correction.

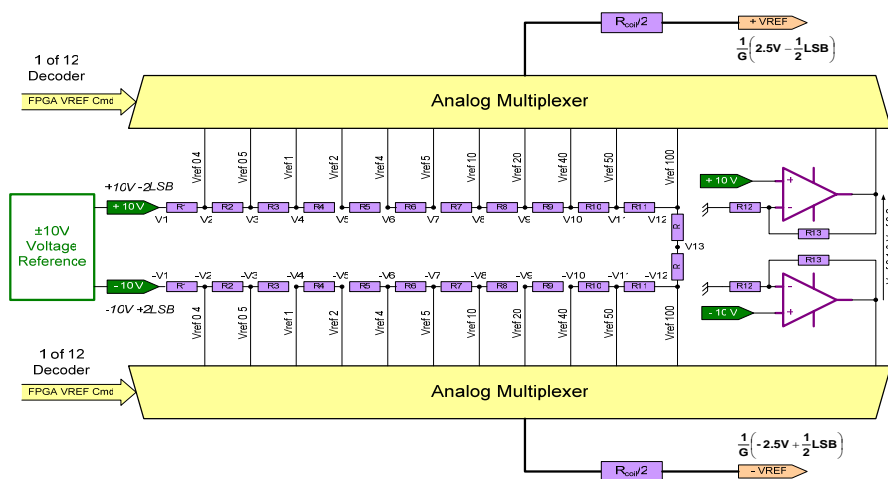


Figure III-30: Voltage reference generator.

### III.4.1.2 - ADC: AD7674

The AD7674 is an Analog Devices 18-bit, 800 kS/s, SAR, fully differential analog-to-digital converter operating on a single 5 V power supply. It includes a high-speed 18-bit sampling ADC,

an internal conversion clock, an internal reference buffer, error correction circuits, and both serial and parallel system interface ports.

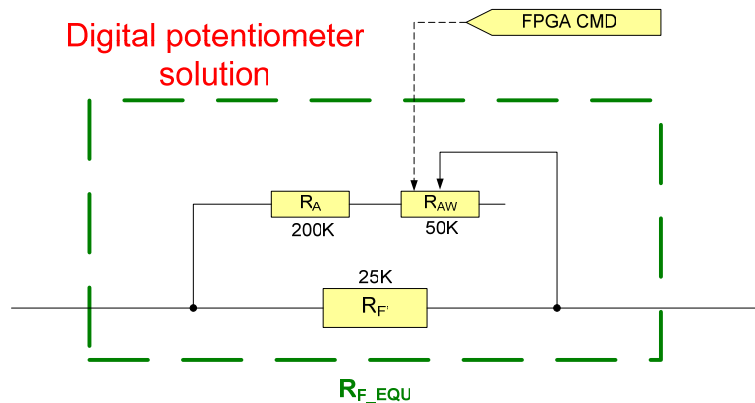


Figure III-31: Gain adjustment

The AD7674 is based on a charge redistribution DAC. Fig. III-32 shows the simplified schematic of the ADC. The capacitive DAC consists of two identical arrays of 18 binary weighted capacitors connected to the inputs.

During the acquisition phase, terminals of the array tied to the comparator's input are connected to AGND via SW+ and SW-. All independent switches are connected to the analog inputs. Thus, the capacitor arrays are used as sampling capacitors and acquire the analog signal on

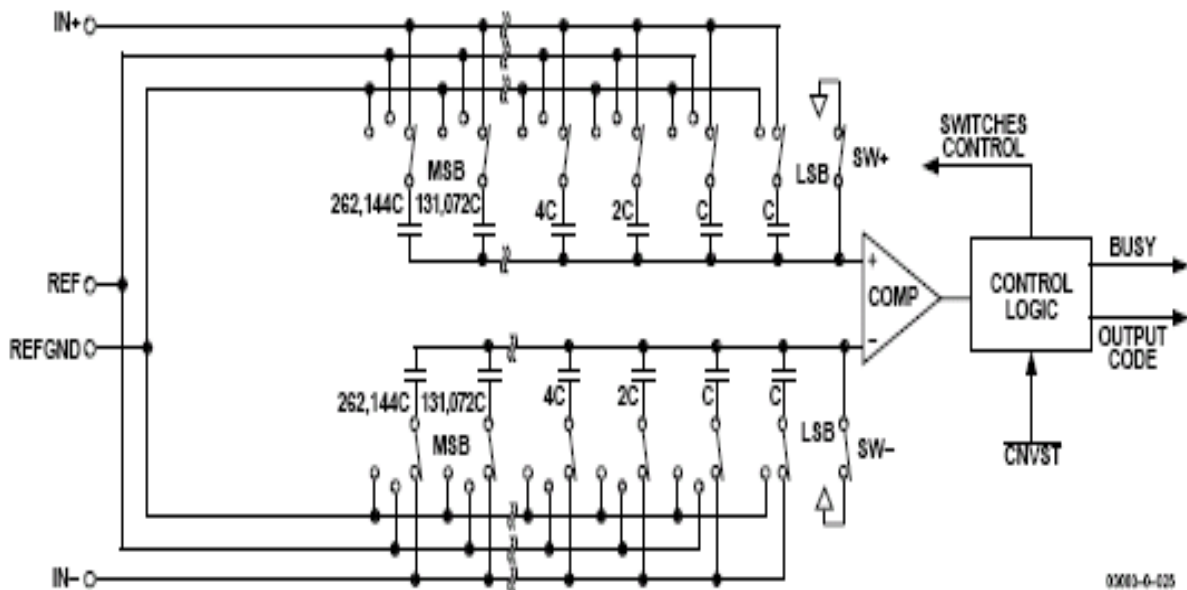


Figure III-32: Simplified schematic of the ADC 7674

the IN+ and IN– inputs. When the acquisition phase is complete and the CNVST input goes low, a conversion is initiated. When the conversion begins, SW+ and SW– are opened first. The two capacitor arrays are then disconnected from the inputs and connected to the REFGND input. Therefore, the differential voltage between the IN+ and IN– inputs captured at the end of the acquisition phase is applied to the comparator inputs, causing the comparator to become unbalanced. By switching each element of the capacitor array between REFGND and REF, the comparator input varies by binary weighted voltage steps ( $V_{REF}/2$ ,  $V_{REF}/4$ , ...  $V_{REF}/262144$ ). The control logic toggles these switches, starting with the MSB first, to bring the comparator back into a balanced condition. After completing this process, the control logic generates the ADC output code and brings the BUSY output low.

The AD7674 features three modes of operation: Warp, Normal, and Impulse. Each mode is more suited for specific applications.

Warp mode allows conversion rates up to 800 kS/s. However, in this mode and this mode only, the full specified accuracy is guaranteed only when the time between conversions does not exceed 1 ms. If the time between two consecutive conversions is longer than 1 ms (e.g., after power-up), the first conversion result should be ignored. This mode makes the AD7674 ideal for applications where a fast sample rate is required.

Normal mode is the fastest mode (666kSPS) without any limitation on the time between conversions. This mode makes the AD7674 ideal for asynchronous applications such as data acquisition systems, where both high accuracy and fast sample rate are required.

Impulse mode, the lowest power dissipation mode, allows power saving between conversions. The maximum throughput in this mode is 570 kSPS. When operating at 1 kSPS, for example, it typically consumes only 136  $\mu$ W. This feature makes the ADC 7674 ideal for battery powered applications.

The AD7674 allows the use of an external voltage reference either with or without the internal reference buffer. Using the internal reference buffer is recommended when sharing a common reference voltage between multiple ADCs is desired. However, the advantages of using the external reference voltage directly are:

- the SNR and dynamic range improvement (about 1.7 dB) resulting from the use of a reference voltage very close to the supply (5 V) instead of a typical 4.096 V reference when the internal buffer is used;
- the power saving when the internal reference buffer is powered down (PDBUF High).

### III.4.1.3 - FPGA control logic

The algorithms for the offset voltage compensation and for the gain calibration are dichotomic; the algorithm is implemented by means of three 16-bit registers A, B, and C; for the offset calibration at the first step, A contains the data 0, B contains the data 65535 ( $2^{16}-1$ ), and C is charged with the value  $(A+B/2)$ ; the machine measures the input voltage (the short circuit in the case of the first offset calibration or the signal from the immobile coil in the case of the second calibration) and a comparator between the output code of the ADC and the expected code (zero code) establishes which is the register (A or B) to upload with the old value of C. The algorithm ends in 16 steps (a 18-bit DAC is used for the offset compensation). An analogue procedure is implemented for the gain calibration; however, in this case, the initial value of A and B are 0 and 255 ( $2^8-1$ ) as the digital potentiometer acting on  $R_f$  is 8-bit; thus, the algorithm ends in 8 steps.

### III.4.1.4 - DSP unit

The DSP unit is the ADSP 21369 Shark Analog Device. The ADSP-21367/8/9 SHARC

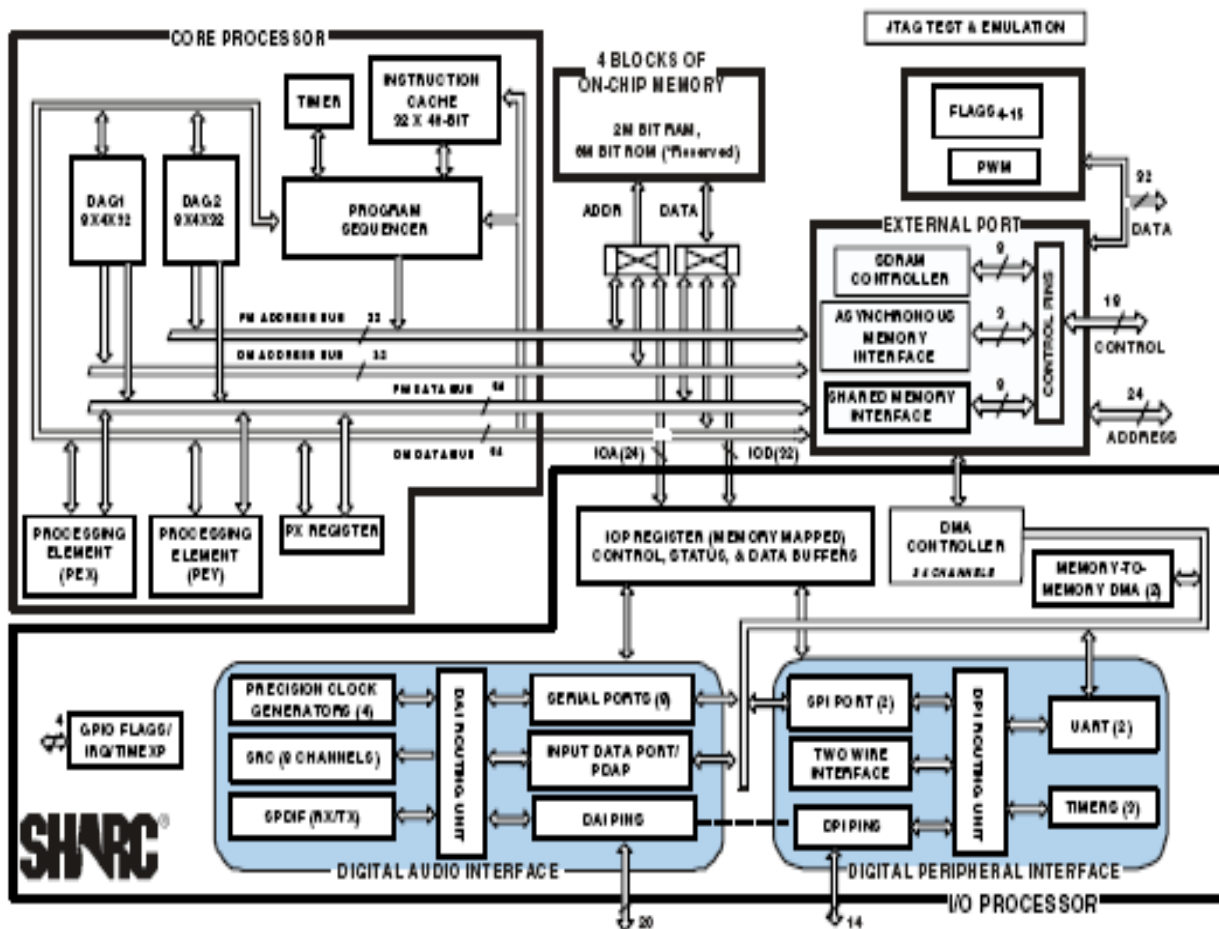


Figure III-33: The ADSP 21369's processor architecture.

processors are high performance 32-bit processors used for high quality audio, medical imaging, communications, military, test equipment, 3D graphics, speech recognition, motor control, imaging, and other applications. By adding on-chip SRAM, integrated I/O peripherals, and an additional processing element for single-instruction multiple-data (SIMD) support, this processor builds on the ADSP-21000 Family DSP core to form a complete system-on-a-chip.

A digital signal processor's data format determines its ability to handle signals of differing precision, dynamic range, and signal-to-noise ratios. Because floating-point DSP math reduces the need for scaling and the probability of overflow, using a floating-point processor can simplify algorithm and software development. The extent to which this is true depends on the floating-point processor's architecture. Consistency with IEEE workstation simulations and the elimination of scaling are clearly two ease-of-use advantages. High level language programmability, large address spaces, and wide dynamic range allow system development time to be spent on algorithms and signal processing concerns, rather than assembly language coding, code paging, and error handling. The ADSP-21367/8/9 processors is a highly integrated, 32-bit floating-point processor which provides all of these design advantages.

The SHARC processor architecture balances a high performance processor core with high performance program memory (PM) data memory (DM) and Input/Output (I/O) buses. In the core, every instruction can execute in a single cycle. The buses and instruction cache provide rapid, unimpeded data flow to the core to maintain the execution rate.

A detailed block diagram of the processor core and the I/O Processor (IOP) are shown in the Figure III-33. Together these figures illustrate the following architectural features:

- two processing elements (PE<sub>x</sub> and PE<sub>y</sub>), each containing 32-bit IEEE floating-point computation units-multiplier, arithmetic logic unit (ALU), shifter, and data register file;
- program sequencer with related instruction cache, interval timer, and data address generators (DAG1 and DAG2);
- an SDRAM controller that provides an interface to up to four separate banks of industry-standard SDRAM devices or DIMMs, at speeds up to fSCLK;
- up to 2M bits of SRAM and 6M bits of on-chip mask-programmable ROM;
- IOP with integrated direct memory access (DMA) controller, serial peripheral interface (SPI) compatible port, and serial ports (SPORTs) for point-to-point multiprocessor communications;
- a variety of audio centric peripheral modules including a Sony/Philips Digital Interface (S/PDIF), sample rate converter (SRC) and pulse width modulation (PWM);
- JTAG test access port for emulation.

Fig. III-33 also shows the three on-chip buses of the ADSP-21367/8/9 processors: the PM bus, DM bus, and I/O bus. The PM bus provides access to either instructions or data. During a single cycle, these buses let the processor access two data operands from memory, access an instruction (from the cache), and perform a DMA transfer.

#### **III.4.1.5 - Firmware**

The DSP is the heart of the board. It, in fact, realizes both the integration process and manages the communication with the FPGA logic control from a side and with the bus controller on the other side. In particular, the main steps of the firmware are:

##### *-Measurement setting-*

The DSP waits for setting commands to the PGA amplifier and measurement setting from the bus interfaces. These can be:

- setting of a given gain value,
- offset auto-calibration,
- gain adjustment,
- start/stop measurement,
- other measurement settings (coil speed, angular resolution, sensitivity coefficients of the coil connected to the specific integrator board).

Their execution is performed by means of writing the corresponding word in the FPGA control register, validated by the rising edge of the signal command. When the start command is received, the DSP goes before in the measurement preparation phase, and then the integration process starts as soon as the zero index from the encoder is received. During the measurement, all the commands coming from the bus are rejected for the stop.

##### *-Measurement initialization-*

Integrations in time and the in angular domains are synchronized via the DSP interrupt system. In particular, two interrupt channels are used: to the first one (higher priority) the encoder zero signal is connected to mark the measurement start, to the second one the trigger signals are sent (Fig. III-34).

When the command start is received, the following operations are carried out in order to prepare the measurement:

- the DMA channel used for data transferring from the ADC is initialized;
- the start command of the ADC sampling is sent to the FPGA and the data are transferred in block via the DMA channel. Data received are organized in the DSP

memory in a circular buffer. In this way, the data acquisition from the ADC can start before the coil is put in movement. The actual integration is triggered by the encoder zero signal;

- the hardware interrupt channels 0 is enabled;
- a command on the bus is sent to inform the embedded controller that the measurement initialization is terminated.

### *III.4.2 - Measurement execution*

Integration starts when the DSP receives on the interrupt channel at highest priority the rising edge of the encoder reference. The corresponding interrupt service routine carries out the following operations:

- the voltage samples circular buffer is empty by simply resetting the memory address pointer;
- a global timer is launched in order to measure the  $t_{m_k}$  (the time intervals between two consecutive encoder pulses);
- the interrupt on the channel 1 is enabled. In this way, the DSP is ready to response to the first encoder pulse, just after the reference tick;
- the interrupt on the channel 0 is disabled because the integration process is initialized only on the first coil turn;

The firmware for the evaluation of the flux increments  $\Delta\Phi_k$  and of the correspondent  $t_{m_k}$  is implemented in the channel 1 interrupt service routine. Main tasks are:

- reading of the last voltage samples available in the circular buffer;
- integration of the voltage samples array using an efficient integration algorithm;
- evaluation of the current  $t_{m_k}$  value by means of subtraction between the current global timer value and the value stored in the previous call of the same routine;
- storage in memory of the couple  $\Delta\Phi_k$ ,  $t_{m_k}$  in an array containing the flux increments related to the current coil turn.

Finally, the main program running on the DSP is devoted to data control and communication.

In particular:

- the evaluated interval times are compared to the expected value obtained by the information about the coil speed and the angular resolution set. If the evaluated  $t_{m_k}$  differs more than a threshold set, possible problems in the coil motorization block occur;

in this case, a command error is sent to the embedded controller and the measurement can be stopped;

- the number of couples  $\Delta\Phi_k$ ,  $tm_k$  measured is checked. If a complete coil turn is carried out (number of flux increments equal to the angular resolution set) the whole data block is sent transferred on the board bus;
- further controls can be foreseen on the increments flux measured in order to detect problems on the coil interconnections or bad working of the analog front-end.

The analysis of the flux samples, as well as the execution of the new analysis approaches, described in the next chapter, aimed at reducing the error on the multipoles evaluation in measurement of varying magnetic fields, can be carried out directly on the DSP in the main routine. In fact, by taking into account a coil speed of even 3 Hz, the time available to calculate the field harmonics starting from the flux samples array currently measured is around 0.3 s (this is the time required to complete the next coil turn). Even if in this time slot, the interrupt service routine for next flux increments measurement has to be carried out N times, the DSP can assure the respect of these requirements.

### III.4.3 - The prescaler board

The prescaler has the main task to divide the pulses coming from the encoder (usually 1024) for a programmable factor, according to the required angular resolution.

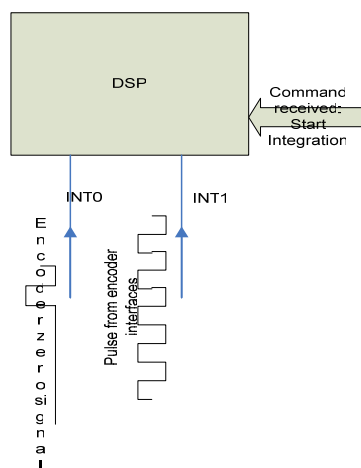


**Figure III-34: The DSP interrupt system used to synchronize the integration in time domain with the trigger coming from the encoder**

This board provides to all the integrator boards installed in the instrument both the trigger pulses and the zero reference signal. The card layout is shown in Fig. III-35. The signals coming from the encoder (the reference and the quadrature signals A and B) are before converted from

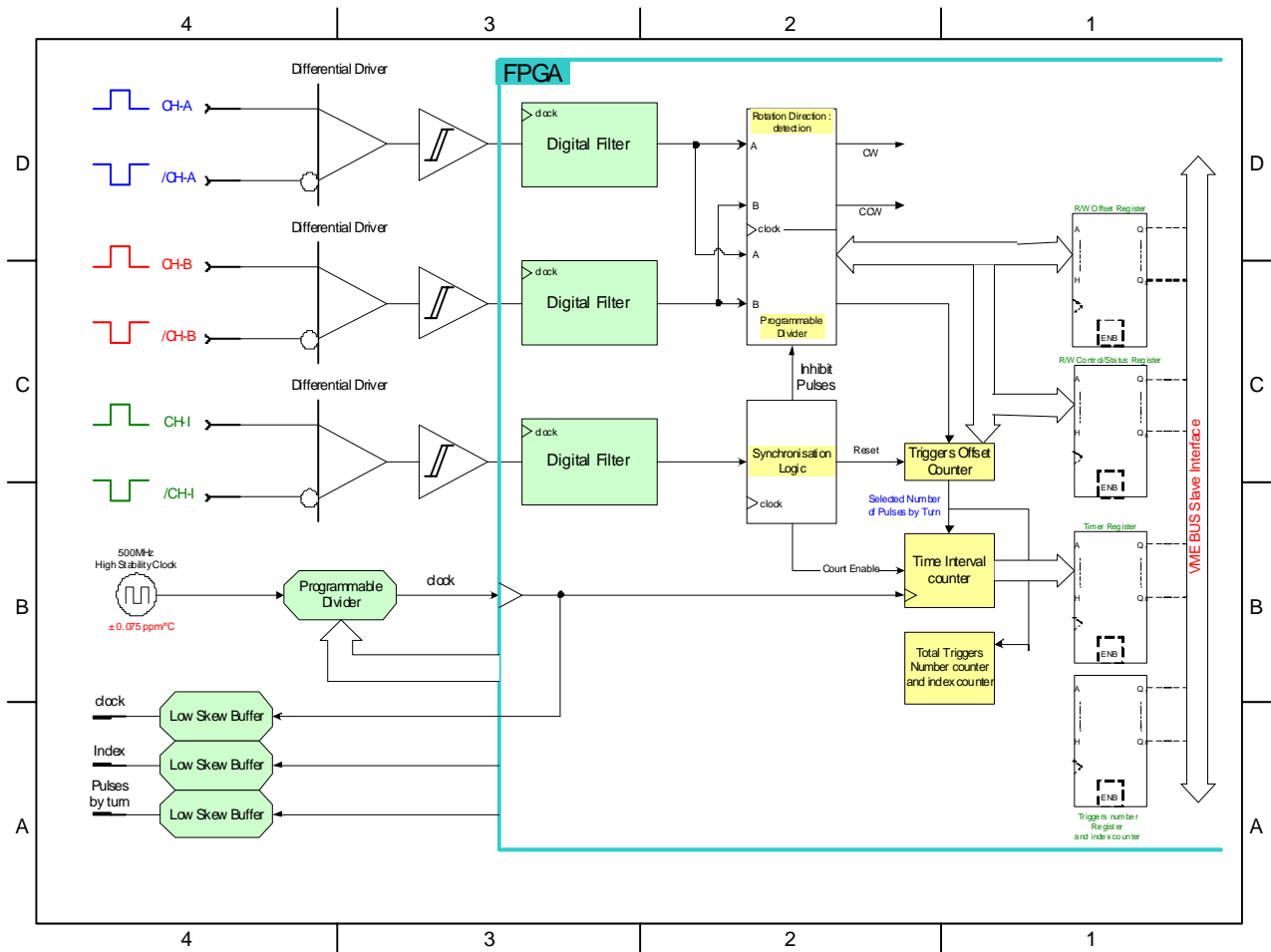


Figure III-35: Layout of the prescaler board

differential to single-ended mode by using standard RS-422 differential receivers. Then, two filtering stages are used to improve the noise rejection: the first, based on a Schimdt-trigger input buffer, the second, on digital filter aimed at reducing short noise spikes.

A synchronous programmable divider implemented on the FPGA is used to obtain the output signal to the requested frequency. The clock is derived by the DSP main clock (400 MHz) using a programmable prescaler. A 100 MHz value was considered acceptable to contain the trigger timing uncertainty.

An additional feature is the masking of the first encoder zero; in fact, this signal is used to start the integration process, thus, is delivered only to the second coil turn when the coil speed is become constant.

#### *III.4.4 - Consideration on the instrument bus and platform*

Particular attention was devoted to the instrument communication bus selection as well as the embedded controller and the operating system.

In the following the main criteria taken into account in the platform definition are discussed:

##### *- Required Bandwidth-*

In continuous flux measurement, if 10 Hz is the maximum coil speed, with an angular resolution of 1024 points per turn, the data flow sent on the bus towards the embedded controller is estimable in a hundredth of kbytes/s. Even if in the same crates are installed 26 integrator cards (for rotating coils measurement of a LHC dipole the signal coming from 13 coil sectors for each apertures have to be integrated) a bus band width of only 2 Mbytes/s is enough.

The situation is even better if the flux samples are analysed directly on the DSP of each board. In this case, in fact, each board will deliver only the fifteen complex field coefficients.

If the system has to work in sampling mode, namely each board is used as an independent DAQ card at the maximum frequency sampling of 800 kS/s, the instrument bus can become a limit to the maximum number of simultaneous acquisition channels.

##### *-Computational power required and temporal requirements-*

Main tasks of the embedded controller are the data communication management with each single integrator from one side, and the analysis and elaboration of each flux samples array on the other side. It delivers in real time at each coil turn, or even at higher speed (if extrapolation algorithms on the flux samples acquired are applied) the field harmonics.

The standard processors nowadays available on the market are properly tailored to this application. In despite of this, a real-time operating system has to be foreseen in order to satisfy the requirements on the measurement time and the instants at which the measurements results have to be delivered. This is an important prerequisite, for the use of the rotating coils system to monitor the reference magnets on-line (see appendix A).

##### *-Costs-*

The economic impact of the platform choice has not been neglected since a series production of 1000 integrator boards is foreseen.

*-Compatibility with CERN strategy-*

The use of CERN standard solution represents a big advantage both for the support availability and for the future maintainability. This is instead mandatory if the measurement system becomes part of the accelerator control system (i.e. RMS project in appendix A).

For instance, even if dated, the solution based on bus VME, power PC embedded controller (e.g. RIO 3 processor product by CES) and operating system LynxOs is become one of the main standard in the front-end platform.

***III.5 - Preliminary test results of the new integrator boards analogic front-end***

In Fig. III-36 the prototype of the analog front-end of the new integrator boards is shown

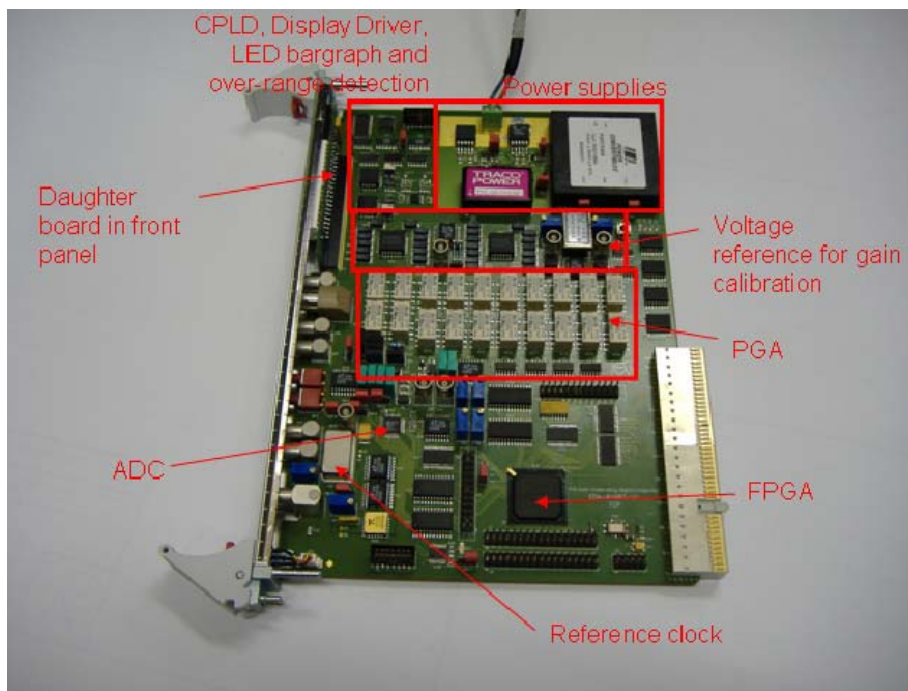


**Figure III-36: Analogic front-end prototype.**

Fig. III-38, the result of the stability test on the clock board is shown. The time window examined was 8 hours with a sampling period of 2 minutes. The clock stability is contained in 0.01

ppm.

In Fig. III-37, the result of the stability test on the gain of the programmable gain amplifier realized is showed. Over 8 hours working the gain was stable in 3 ppm

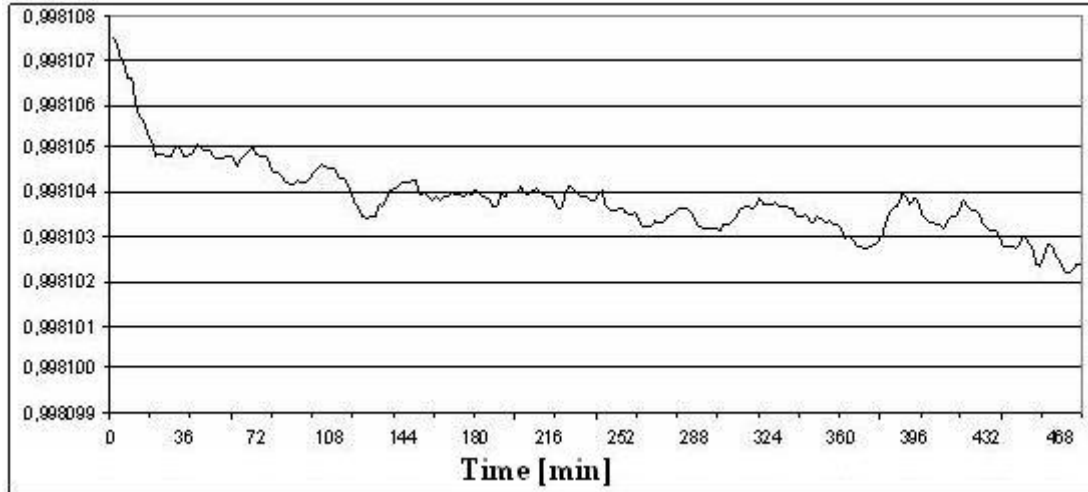


Figure III-37: PGA Gain stability test.

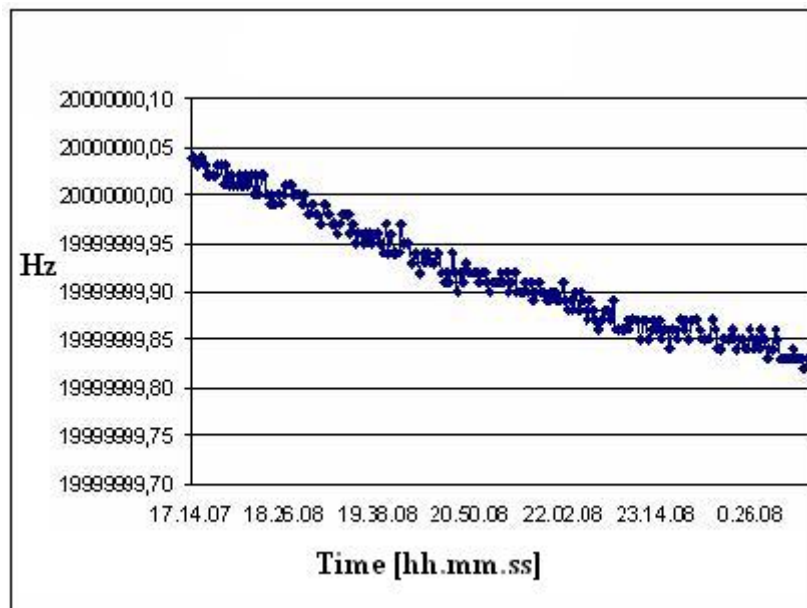


Figure III-38: Clock stability test.

# **Chapter IV - ROTATING COILS SYSTEM: THE NEW**

## **MEASUREMENT ALGORITHMS**

### ***IV.1 - Introduction***

The standard procedure for estimating magnetic harmonic coefficients exploits the Fast Fourier Transform (FFT) of the magnetic flux, acquired over one complete coil turn and assumed to be stationary. Such an assumption certainly holds for magnets measured along the loadline, i.e. through a powering cycle characterized by several plateaux, during which the magnetic flux is measured. For measurements carried out during a LHC cycle, where the supply current ramps up at  $10 \text{ As}^{-1}$ , the standard procedure provides only an approximation to harmonic coefficients over each coil turn. No possibility of tracking the instantaneous value of the coefficients is given.

In this chapter, this problem is first analyzed by applying the standard procedure to simulated magnetic fluxes for different current laws. In each condition, the difference between estimated and nominal mean values of harmonic coefficients, assumed as reference, is given. The results clearly highlight the need for new measurement approaches.

Then, starting from the assumption of a continuous coil rotation, two new digital signal-processing approaches are proposed. The first one applies quadrature detection and

short time Fourier transform (STFT) to the acquired magnetic flux samples in a combined way. The second approach interpolates magnetic flux samples over three complete coil turns, thus giving the possibility of reconstructing the magnetic flux over a complete coil turn at a given time instant. The performance of both approaches is assessed and compared.

#### ***IV.2 - The standard analysis***

The standard analysis, applied to the flux samples over one complete coil turn to obtain the field multipoles, is summarized in Fig. IV-1.

After suitable processing and normalization for the gain of the acquisition chain, each rotating coil measurement delivers the value of the magnetic flux  $\phi(\theta_p)$  as a function of the rotation angle  $\theta_p$  in a discrete series of points  $p$  for a total of  $P$  points. The sampling points  $\theta_p$  are equally spaced over the interval  $[0, 2\pi\left(\frac{P-1}{P}\right)]$ . By taking into account the magnetic field multipoles expansion, flux samples  $\phi_p$  can be written as [1]:

$$\Phi_p = \text{Re} \left\{ \sum_{n=1}^{\infty} \frac{K_n C_n}{R_{ref}^{n-1}} \exp(jn\theta_p) \right\} \quad (\text{Eq. IV-1})$$

where  $\text{Re}[\cdot]$  stands for real part operator,  $K_n$  is the  $n^{\text{th}}$  complex coil sensitivity-coefficient (described in chapter II), and  $R_{ref}$  is the reference radius, equal to 17 mm for the LHC machine.

Field multipoles are, in general, a function of the current level, powering history, ramp rate and time. At constant excitation, however, harmonic variations over the typical duration of a coil turn (1-10 s) are negligible [2].

Assuming constant  $C_n$ , the IV-1 is invertible [3]: by means of discrete Fourier Transform calculation on the measured flux samples vector, the field multipoles at the measurement current are recovered. In particular the DFT is defined as:

$$\Psi_m = \sum_{p=1}^P \phi_p e^{-2\pi i(m-1)\frac{(p-1)}{P}}, \quad m = 1..P \quad (\text{Eq. IV-2})$$

where  $\Psi_m$  is the  $m^{\text{th}}$  complex DFT coefficient. For an even number of points  $P$ , the value of coefficients  $C_n$  is:

$$C_n = B_n + jA_n \approx \frac{2}{P} \frac{R_r^{n-1}}{\kappa_n} \Psi_{n+1}, \quad n = 1 \dots \frac{P}{2} \quad (\text{Eq. IV-3})$$

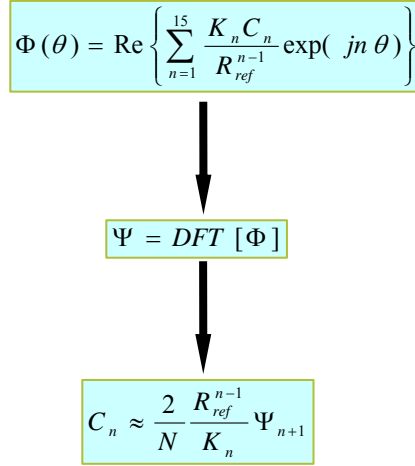


**Figure IV-1: Standard analysis representation.**

For varying magnetic fields, however, the coefficients obtained from Eq. IV-3 are significantly different from the mean value during a single coil turn. As an example, in measurements of LHC multipole magnets on current ramps (i.e. the LHC cycle), taking into account a continuous coil rotation, two effects have to be considered:

1. the magnetic flux due to the main component can be seen as an AM modulation of a sinusoidal carrier at frequency equal to the coil frequency rotation, where  $C_1(I(t))$  represents the modulating signal. The standard analysis provides an estimation of the average main harmonic coefficient over one turn with an error increasing according to the ramp rate [4];
2. for higher order multipoles, each one characterized by a variation law  $C_n(I(t))$ , the same effect have to be considered. In addition, interference due to the modulation produced by the dipolar field variation has to be taken into account. Considering for example main dipoles magnets, higher order multipoles are normally three or four order of magnitude smaller than the main component. In the analog bucked signal

the dipole is reduced by a factor which is typically between 200 and 4000, so in the most unfavourable case higher harmonics are just a factor 5 smaller than the main field. When the field is ramping, the side bands of the spectrum of the flux spread proportionally to the ramp rate and thus the interference between harmonics tends to increase. Assuming that harmonics ramp proportionally to the main field (i.e. considering only the geometrical field component, and neglecting second order effects linked to superconductor magnetization and iron saturation), the magnetic flux can be simulated taking into account:

$$\begin{aligned}
 B_1(\theta) &= \left(\varepsilon \frac{\theta}{2\pi} + 1\right), \\
 B_3 &= \frac{1}{5} \cdot \left(\varepsilon \frac{\theta}{2\pi} + 1\right); B_5 = \frac{1}{10} \cdot \left(\varepsilon \frac{\theta}{2\pi} + 1\right), \\
 B_2 &= 0; B_4 = 0.
 \end{aligned}
 \tag{Eq. IV-4}$$

Where:

$$\varepsilon = \frac{dI}{dt} \cdot \frac{\Delta T}{I_{\text{nominal}}} \cdot 2\pi$$

$\frac{dI}{dt}$  the current ramp rate

$\Delta T$  the time to complete a coil turn

$I_{\text{nominal}}$  the magnet nominal current (11850 A for the LHC dipoles)

The actual rotating coils speed (0.1 Hz) and the LHC cycle ramp rate of  $10 \text{ As}^{-1}$  implies a 0.1 % of B1 variation over 1 turn. The interference due to the main field variation on B3 and B5 is evident, even if in these condition is still possible to recover the higher order coefficients (Fig. IV-2 (a)). The higher is the ramp rate, the higher is the interference up to cover the same higher order multipoles. In Fig. IV-2 (b) a simulation related to a  $100 \text{ As}^{-1}$  ramp rate is shown. In this case the interference due to the main field variation covers the higher order multipoles.

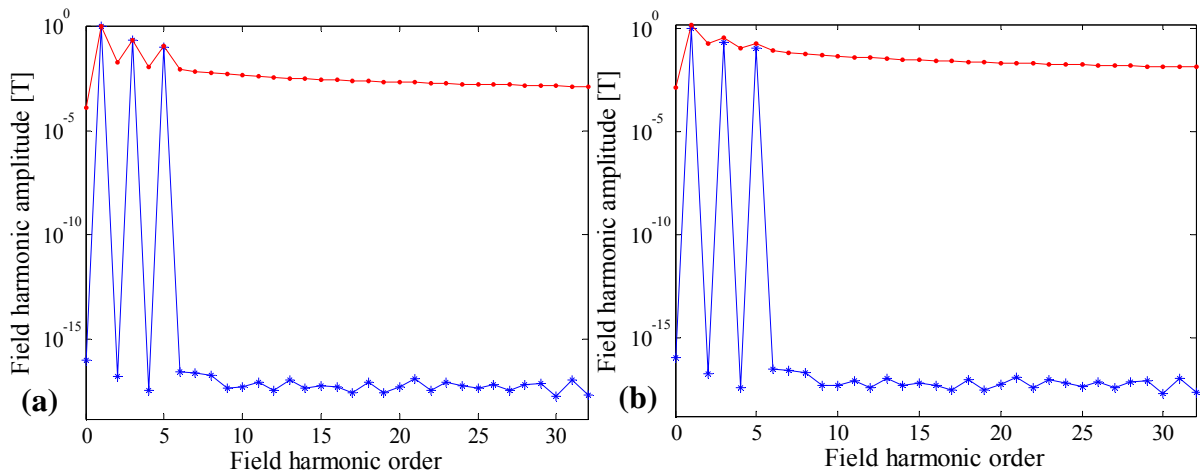


**Figure IV-2: Interference on higher order harmonics due to the main field modulation with coil rotating at 0.1 Hz: imposed (blu) and estimated (red) field harmonics (a) ramp rate  $10 \text{ A s}^{-1}$  (b) ramp rate  $100 \text{ A s}^{-1}$**

In principle, even if the coil speed is increased, the interference problem is not solved, because the dipolar flux modulation does not depend on the coil speed but only on the current ramp rate [5].

### *IV.3 - The rotating coil simulator*

A rotating coils simulator was implemented to characterize the standard analysis, as

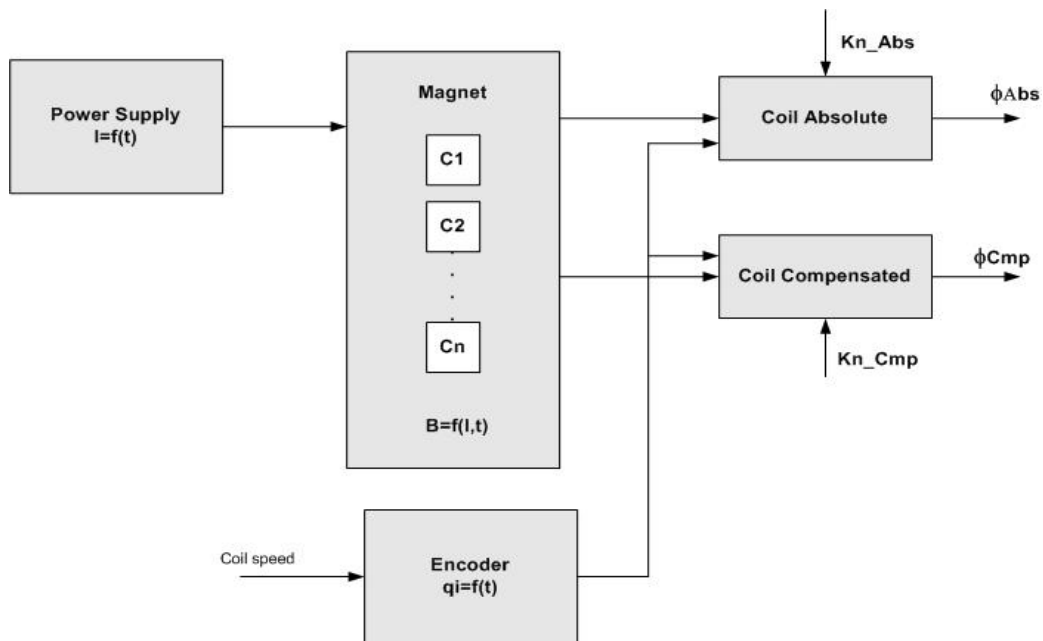


**Figure IV-3: Rotating coils simulator layout.**

well as to test the proposed method (Fig. IV-3).

This software provides continuous samples for both the absolute and the compensated flux of a coil, rotating inside an LHC magnet. To provide realistic results, the case of a 700mm long coil rotating inside a dipole actually having been tested, the n.1015, has been chosen. The time-histories of field harmonic coefficients are obtained by interpolating experimental data measured over a complete LHC cycle and the simulation can start and stop at any given time. All the other measurement system components (i.e. motor, shaft, encoder and integrators) are assumed ideal. This doesn't represent a limitation because the goals to reach are:

- a simulation of continuous flux samples as closer as possible to the real flux;
- a quality test of the analysis methods by evaluating the difference between the estimated and the expected coefficients for different measurement conditions of current ramps and ramp rates.

#### *IV.3.1 - The flux construction*

The harmonics up to the 15<sup>th</sup> order used to construct the magnetic flux are measured during an interval of 30 s, owing to the washing-machine mode of the actual rotating coils system (Table IV.1).

Time (s)	Current (A)	B1 (T)	b2 (units)	a2 (units)	b3 (units)	a3 (units)
1748	3897.644	-2.75434847	1.068254	3.048336	5.558452	0.1925704
1783	4240.284	-2.996486861	1.070478	3.054995	5.648487	0.1926493
1809	4497.11	-3.177901727	1.068484	3.059702	5.704516	0.1915331
1839	4801.898	-3.393265529	1.062627	3.06377	5.758517	0.1906177
1868	5093.931	-3.599547552	1.054003	3.067575	5.803007	0.1896843
1929	5701.661	-4.02885663	1.000404	3.072821	5.870846	0.1904032
1959	5997.335	-4.237693537	0.9549352	3.074682	5.893842	0.1894253
1992	6332.672	-4.474416246	0.8863236	3.07667	5.914308	0.1890658
2018	6597.064	-4.661059613	0.8219283	3.080657	5.928935	0.1881667

**Table IV-1: Some field harmonics measured on the 1015 LHC over the linear current ramp of the LHC cycle**

In simulation a typical coil rotation speed of 0.1 Hz was taken into account.

In order to obtain the values of each coefficient at every angular position (every  $10/N$  s with  $N$  the angular resolution used, usually 256 points per turn) an interpolation using as key the current was performed. In fact since the coil rotation is supposed ideal, the  $i$ -th angular position is given by:

$\theta_i = \omega \cdot t_i$  where  $\omega = 2\pi f_{rot}$ , is the coil angular speed and so known the current law for each instant time  $t_i$  is known the current value as well.

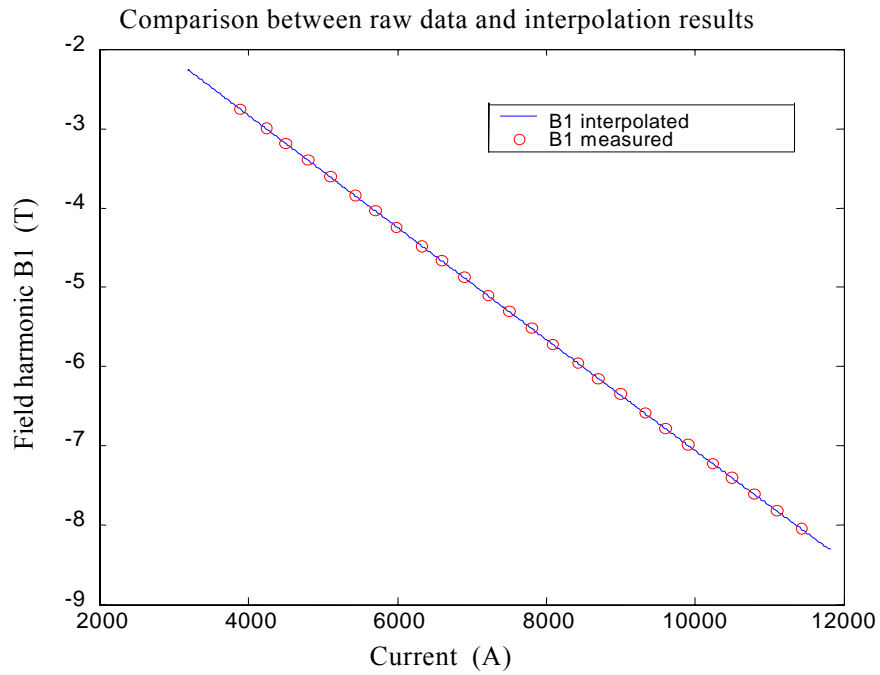


**Figure IV-4: Interpolation of the harmonic coefficient B1 on the linear current ramp at  $10 \text{ A s}^{-1}$  of the LHC cycle.**

On the injection plateau, where the current is constant for 1000s the time is used as interpolation key. For  $b_1, b_3$ , and  $b_5$  harmonics the decay and snapback model for this particular magnet was used [6].

At any coil turn, the flux samples are evaluated through the expression IV.1, by taking into account the samples in the interval  $\left[0 \dots \left(2\pi - \frac{2\pi}{N}\right)\right]$  to avoid spectral leakage.

### IV.3.2 - Current types

The current waveform used in the simulator is the LHC current cycle, i.e. (rising) Parabolic Exponential Linear (falling) Parabolic (PELP) [7].

The PELP shape of the current ramp brings all superconducting dipole magnets from a 0.537 T field up to the nominal value of 8.33 T, in 1500 s. It was computed in order to minimize the effects of the interstrand coupling currents (ISCCs) induced by the ramping [8].

In the following, details about each LHC cycle part are given.

#### IV.3.2.1 - Parabolic current ramp

The acceleration parabolic current ramp (see Fig. IV.14) is defined as follows:

$$I_a(t) = \frac{A}{2}(t - T_i)^2 + I_i \quad (\text{Eq. IV-5})$$

where:

- $A=9e^{-3} \text{ As}^{-2}$  acceleration during ramp up;
- $T_i=1000\text{s}$  initial time;
- $I_i=760 \text{ A}$  starting current;
- $1000\text{s} \leq t \leq 1325\text{s}$  parabolic current time interval.

### IV.3.3 - Exponential current ramp

It is defined by the following equation:

$$I_e = ae^{bt} \quad (\text{Eq. IV-6})$$

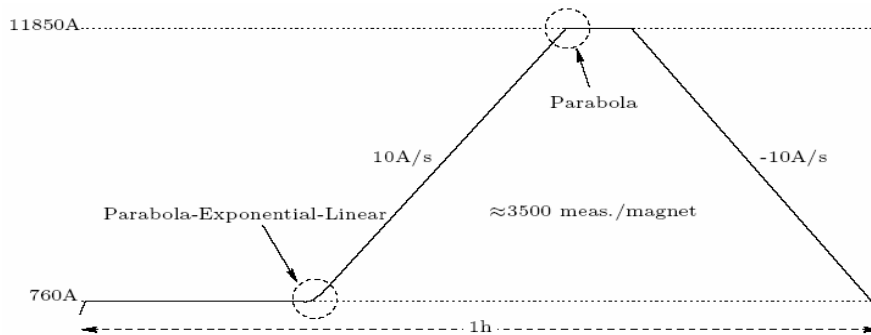


Figure IV-5: The normal LHC machine cycle (PELP).

where:

- $a=53.608907 \text{ A}$ ;
- $b=0.002368 \text{ s}^{-1}$ ;
- $1325s \leq t \leq 1724s$ .

#### ***IV.3.4 - Linear current ramp***

The ramp parameters, according to PELP LHC cycle, are defined in Tab.IV-2 :

Parameter	Value	Unit
Starting time	1724	s
Ending time	2588	s
Ramp rate	10	$\text{A s}^{-1}$

**Table IV-2: Main parameters of linear current ramp**

A plot of such a current ramp is given in Fig. IV-5.

For the linear ramp different ramp rates from  $10 \text{ A s}^{-1}$  up to  $100 \text{ A s}^{-1}$  are taken into account in order to simulate measurement conditions expected for future magnets prototypes.

#### ***IV.3.5 - The software implementation***

The rotating coil simulator was implemented in the Mathworks Matlab® environment (version 7.1). Matlab was preferred mainly to reduce the development time since it allows fast matricial calculations and is equipped with several useful analysis toolboxes.

In the simulator, the parameters to be set (Fig. IV-6) are:

- coil rotation frequency;
- type of current ramp;

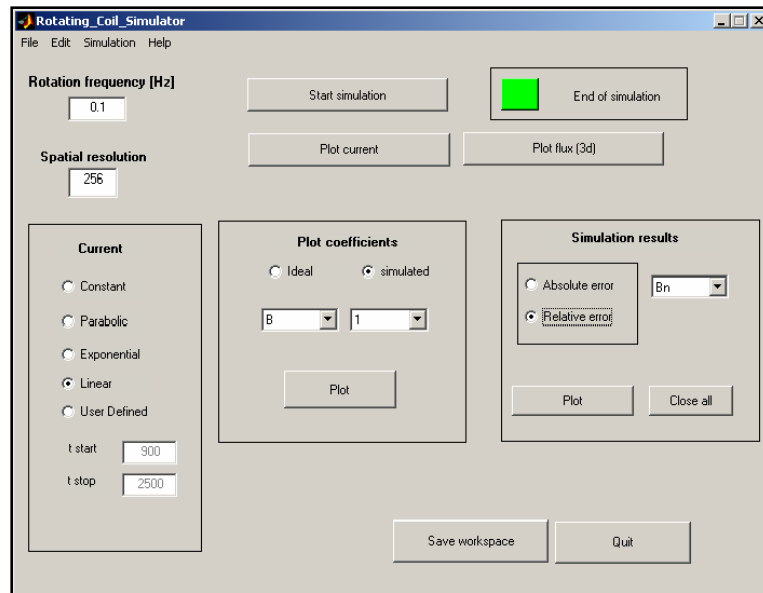


**Figure IV-6: Rotating coils simulator main panel**

- ramp rate.

On the flux samples (Fig. IV-7) generated on several turns according to the current ramp and the coil speed set, the performance of different analysis algorithms is assessed. In Figs IV-8, IV-9 and, IV-10, the plots of some expected instantaneous coefficients are

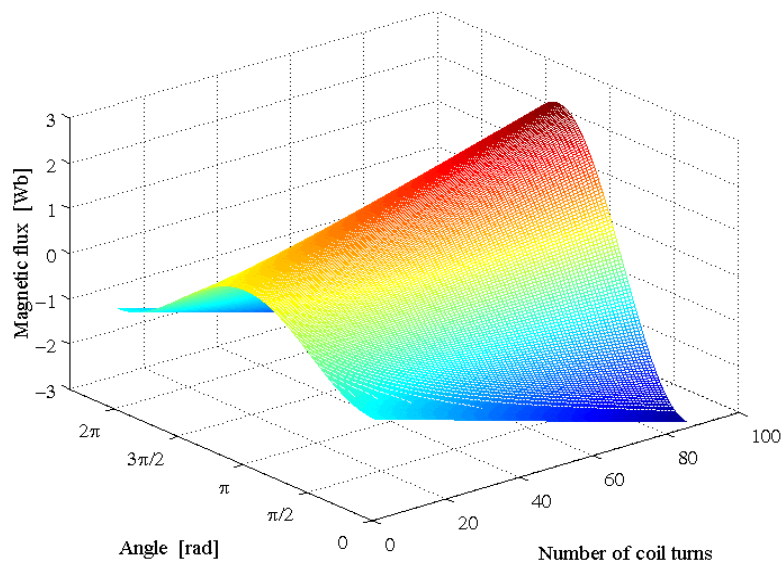


**Figure IV-7: Magnetic flux evolution for different angles and several turns of the coil rotating at 0.1Hz frequency. The current ramp is linear with  $10\text{A s}^{-1}$  ramp rate.**

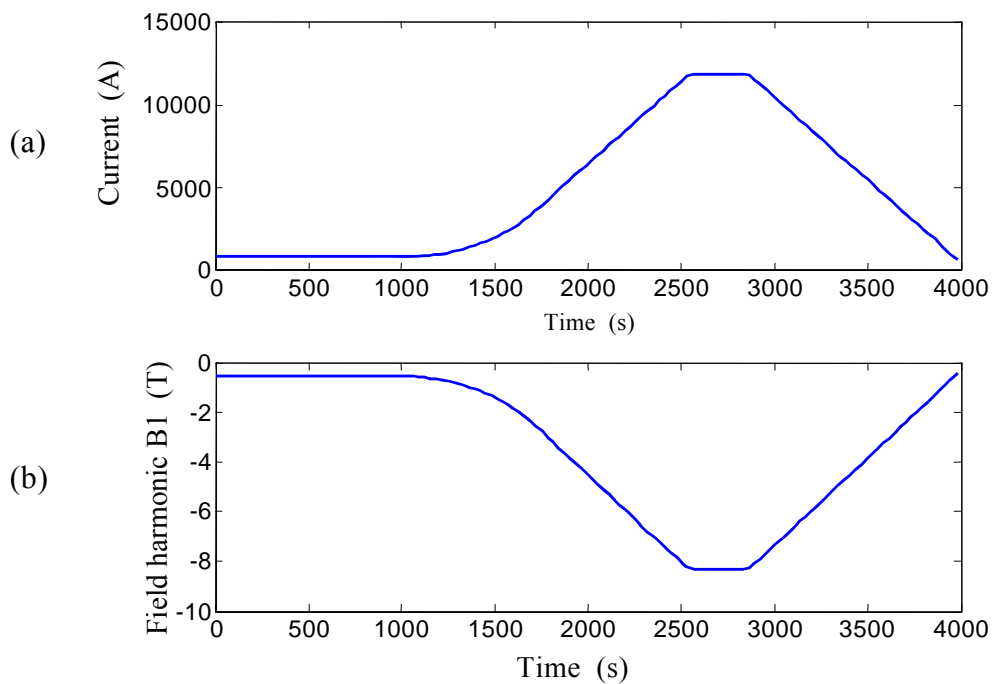


Figure IV-6: Harmonic coefficient B1 (a) and LHC current cycle (b) versus time.

shown.

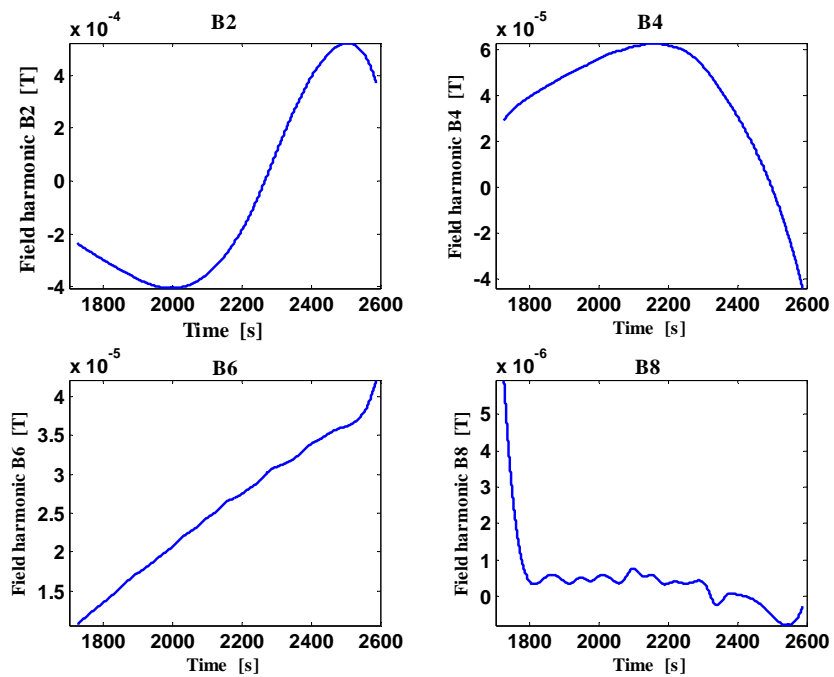
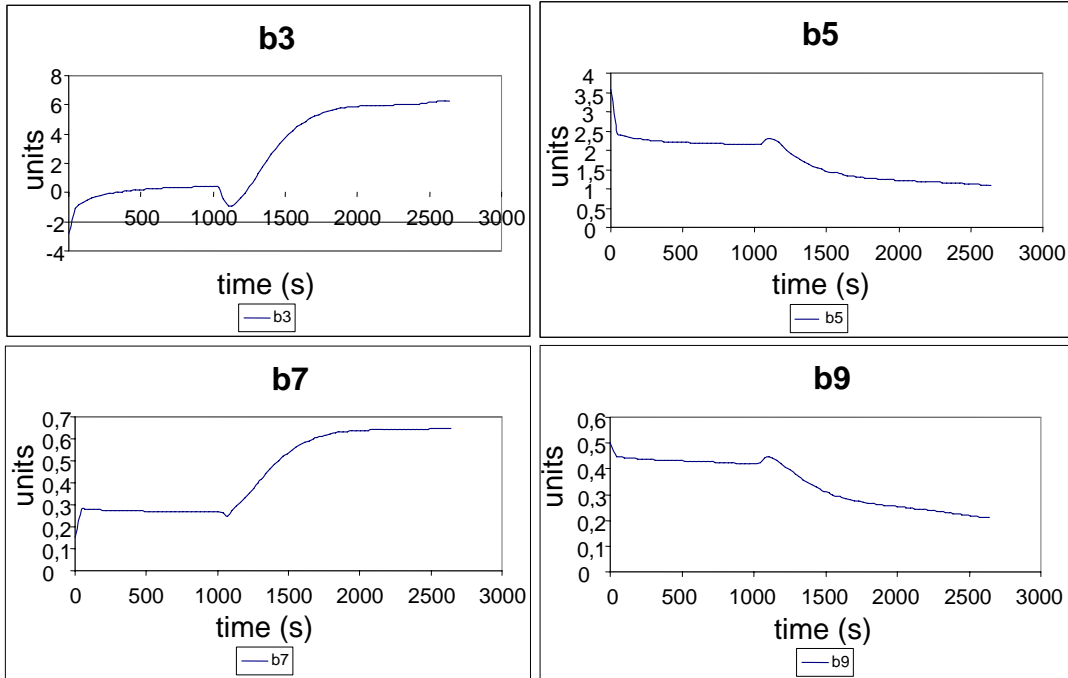


Figure IV-7: Even coefficients B2-B8 for a linear current ramp at 10A/s ramp rate starting from 1724 s.



**Figure IV-8: Coefficients b1,b3,b5,b7 for all the LHC cycle ramp up ( amplitude is expressed in unit in order to show the snapback phenomena at 1000 s).**

#### *IV.4 - Performance assessment of the standard analysis*

For each coil turn, the FFT on the N flux samples is computed to obtain the field harmonics coefficients. These are obtained by a sliding window FFT with N overlap factor (Fig. IV-11).

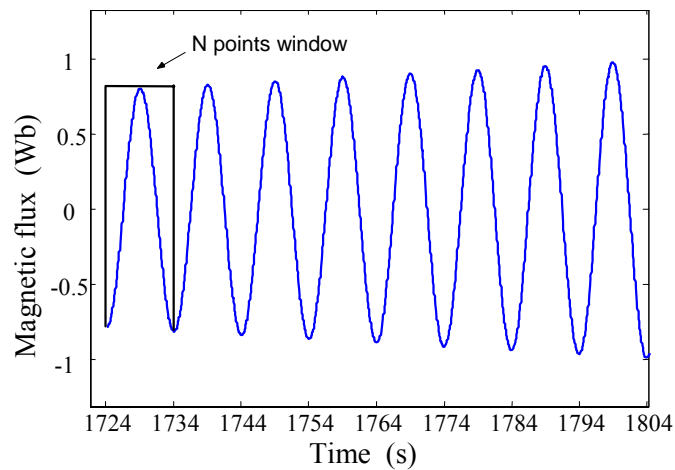


**Figure IV-9: The coil rotation period is 10s during a linear ramp with  $10 \text{ A s}^{-1}$  ramp rate.**

By iterating the procedure for the desired coil turns, the evolution of harmonic coefficients in a specific time (or current) interval can be estimated.

The procedure of characterization of the standard is shown in Fig. IV-12.

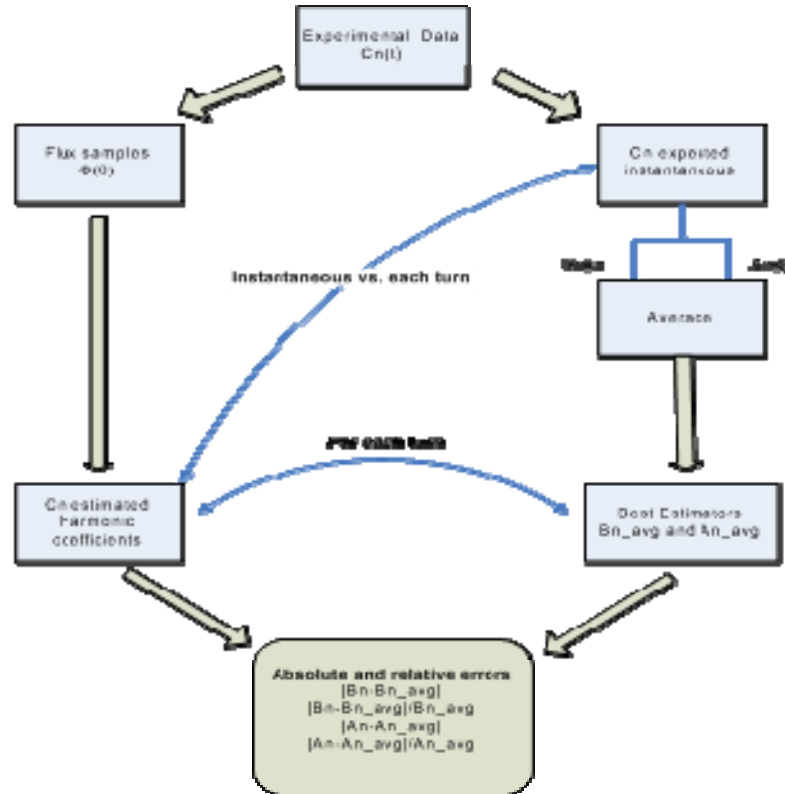
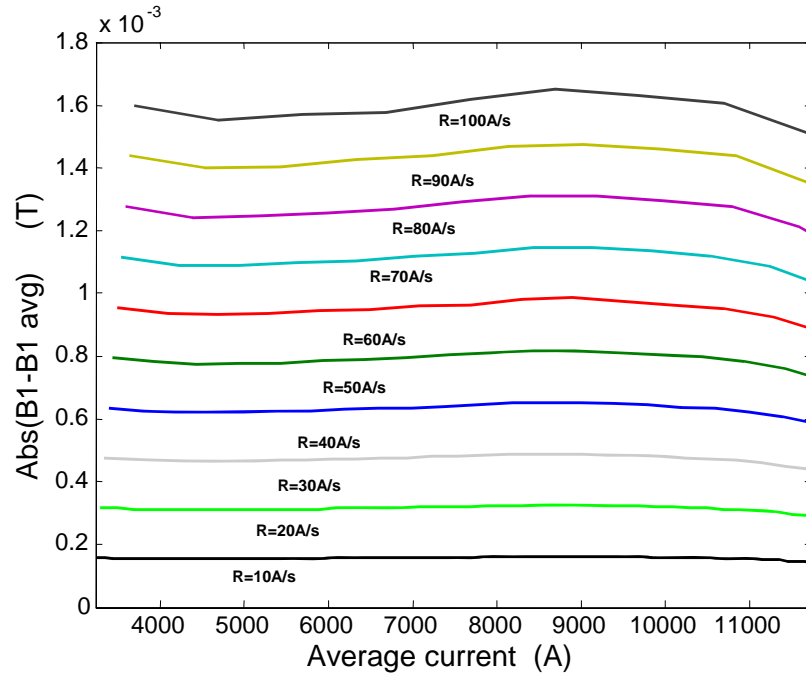


Figure IV-10: Standard analysis characterization data flow

The standard analysis delivers the field harmonic coefficients at each coil turn. The algorithm quality is assessed comparing each estimated coefficient with its *best estimator* represented, in this case, by the average of the instantaneous values (at the  $N$  angular positions) over the turn. The absolute error evaluated for each turn and in different simulated conditions characterizes the algorithm.

In Fig. IV-13 the absolute error for the  $B1$  coefficient for a 0.1 Hz coil frequency rotation over a linear ramp from 1000 up to 11000 A is shown. The ramp rate is varied from  $10 \text{ As}^{-1}$  up to  $100 \text{ As}^{-1}$ . The field transfer function is  $0.7 \text{ mTA}^{-1}$ , characteristic of the LHC dipoles. On the abscissa the average current over each turn is plotted instead of the time in order to compare the algorithm errors at different ramp rates. As expected, the

absolute error is constant at the different current values and at different ramp rates. On the LHC cycle linear ramp (the one at  $10 \text{ As}^{-1}$ ), the absolute error for the main harmonic field is less than  $2 \cdot 10^{-4} \text{ T}$  that is a significant value if compared with the B1 measurement uncertainty  $5 \cdot 10^{-5} \text{ T}$  (in stationary measurement conditions).



**Figure IV-11: Absolute error for coefficient B1 for a coil rotating at the frequency of 0.1 Hz during a linear current ramp. The ramp rate varies from  $10 \text{ As}^{-1}$  up to  $100 \text{ As}^{-1}$ .**

The absolute errors reach  $1.6 \cdot 10^{-3} \text{ T}$  for  $100 \text{ As}^{-1}$  ramp rate.

A comprehensive characterization of the standard analysis over the other ramp types was also carried out. The coil rotation frequency was set at 0.1 Hz, the minimum speed of the actual rotating coils measurement systems at high field. In the following, results related to (i) parabolic, and (ii) exponential current ramps simulations are shown.

#### IV.4.1 - Parabolic current ramp

The LHC cycle parabolic current ramp just after the injection plateau was taken into account.

In Fig.IV-14, the absolute error graphs for the first 4 normal coefficients show that the absolute error behaviour is linear.

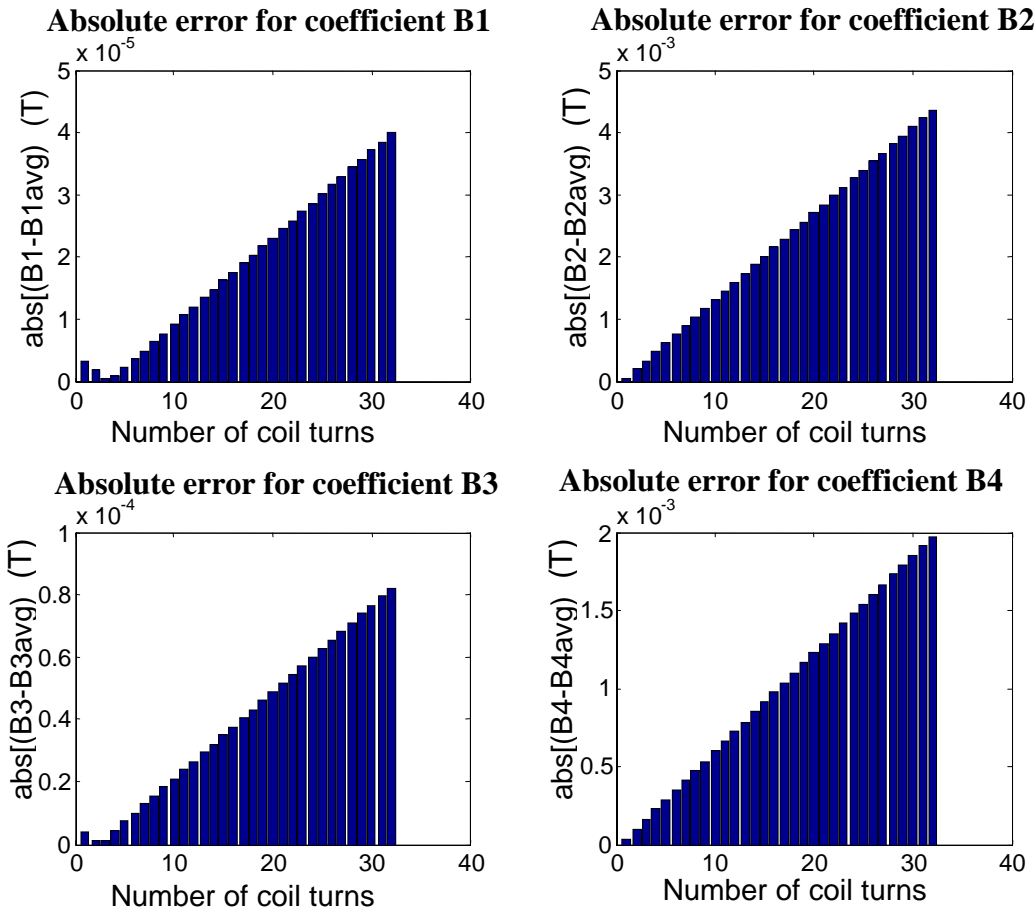


**Figure IV-12: Absolute errors on field harmonics B1-B4 for a parabolic current ramp. The coil rotates at 0.1 Hz frequency. The rotation starts from 1000 s**

#### IV.4.2 - Exponential current ramp

Fig. IV-15 show the absolute error graphs for the first 4 normal coefficients on the LHC exponential ramp. The absolute error behaviour is exponential (derivative of the current waveform).

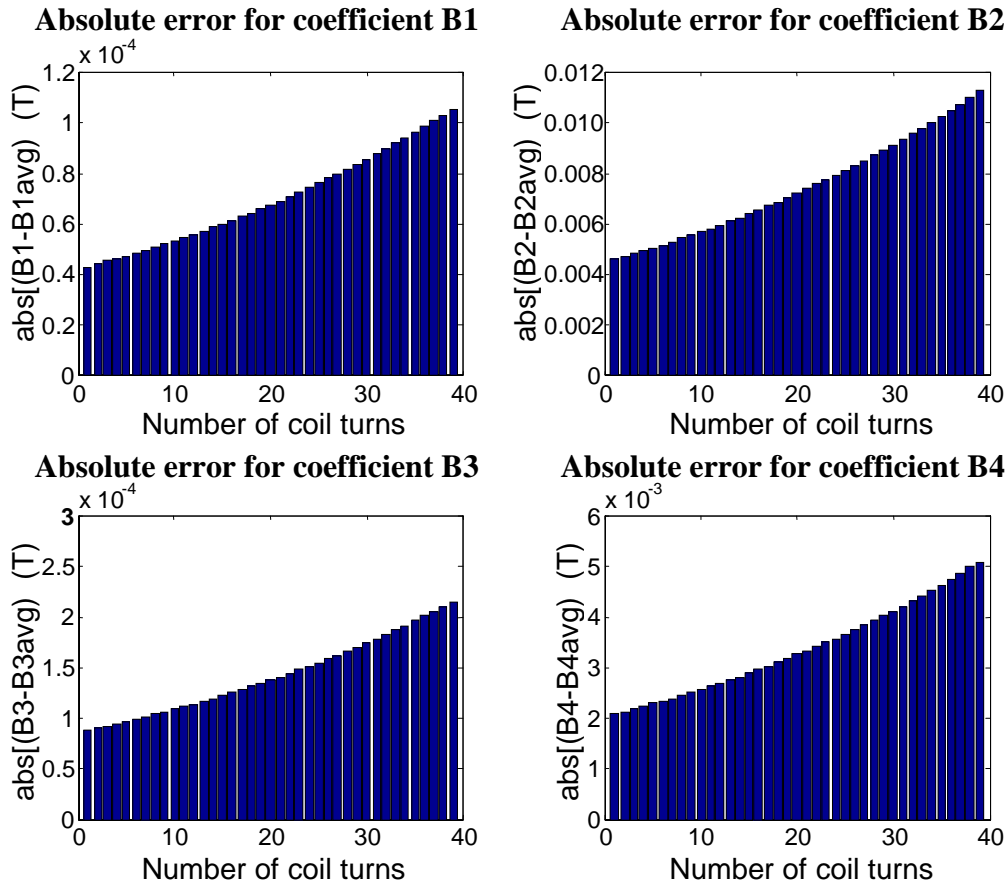


**Figure IV-13: Absolute errors for field harmonics B1-B4 during an exponential current ramp. The coil rotates at 0.1 Hz frequency and the rotation starts from 1325 s.**

#### *IV.4.3 - Discussion of results*

The standard analysis provides the estimate of the mean values of multipoles for each single coil turn. The estimation error depends on the current ramp type and on the ramp rate. In principle, if the field coefficient follows the current law, the simulation results show that the absolute error is proportional to the first derivative of the coefficient. For the dipole, the algorithm error on linear ramp is already significant at the nominal LHC cycle ramp rate. For the higher order harmonics, the relative errors are even greater than for the main field component, because their variation law is not linear.

### IV.5 - The method based on the flux demodulation

A method based on the combined use of quadrature demodulation and Short Time Fourier Transform (STFT) is proposed to improve coefficient estimates and obtain their instantaneous trend versus angular position.

In the following, the (i) demodulation of the main field harmonic, and (ii) the STFT to estimate the high order multipoles are detailed.

#### IV.5.1 - Demodulation of the main field harmonic

The starting point is the expression:

$$\Phi(\theta) = \text{Re} \left[ \sum_{n=1}^{15} K_n \exp(in\theta) C(n) \right] \quad (\text{Eq. IV-7})$$

In LHC superconducting dipoles the sum may be conveniently approximated by the

$$\Phi(\theta) \approx K_1 \cdot C(1) \cdot \exp(i\theta) \quad (\text{Eq. IV-8})$$

following expression:

This shows that the magnetic flux can be seen as a signal at a frequency equal to the coil rotation, amplitude modulated by the complex coefficient  $C_1$ .

The scheme used for magnetic flux demodulation is shown in Fig. IV-16.

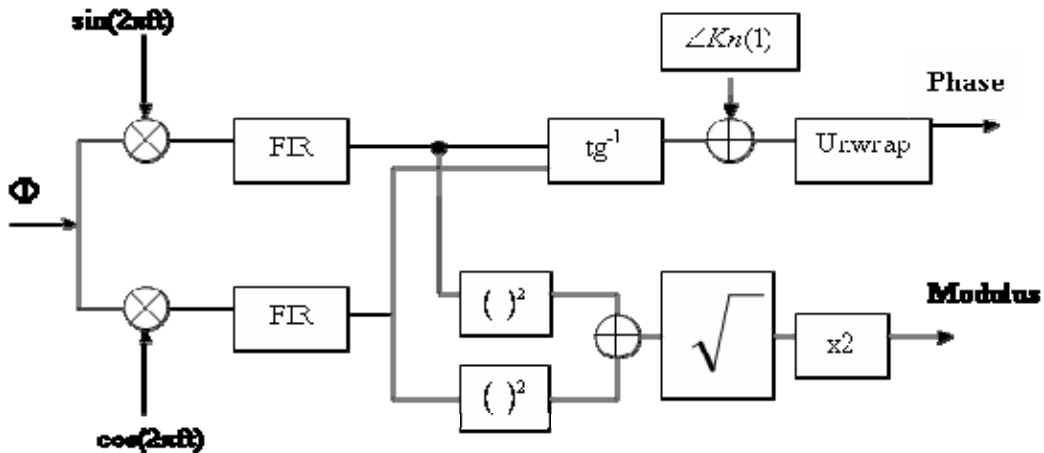
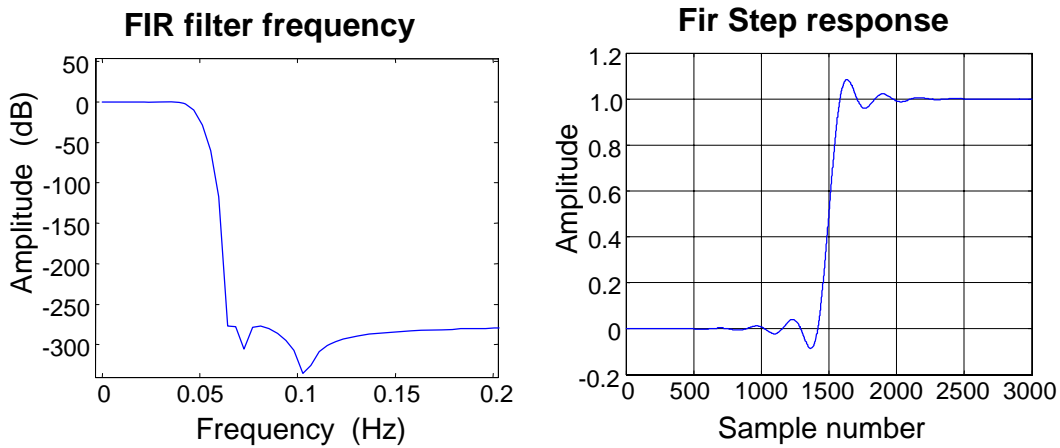


Figure IV-14: I-Q demodulation scheme.

FIR filters are used to cut the high frequency components of the output signals from multiplier. The carrier frequency is fixed in simulation at 0.1 Hz while the sampling rate is N times greater, where N=256 points. The filter used is the equi-ripple "remez" filter (Fig. IV-17). A 3000-taps, finite impulse response filter with a narrow bandwidth lower than 1/N in normalized frequency, high stop-band attenuation (higher than 80 dB), and linear phase response.



**Figure IV-15: FIR filter frequency and step response.**

The high filter length makes the filter very *slow*, characterized by very high settling times (a number of points at least equal to half filter length is needed to converge). The initial measurement delay time corresponds to 7 coil turns.

The output of the I-Q demodulator gives amplitude and phase of magnetic flux. From these two data, it is possible to obtain an estimate of main field harmonic by these relations:

$$\left\{ \begin{array}{l} |\Phi(t)| \approx |K_1 \cdot C_1(t)| = |K_1| \cdot |C_1(t)| \\ \angle \Phi(t) \approx \angle K_1 + \angle C_1(t) \end{array} \right. \Rightarrow \left\{ \begin{array}{l} |\tilde{C}_1(t)| \approx \frac{|\Phi(t)|}{|K_1|} \\ \angle \tilde{C}_1(t) \approx \angle \Phi(t) - \angle K_1 \end{array} \right. \quad \text{(Eq. IV-9)}$$

in which 'tilde' indicates the approximate C1 harmonic coefficient.

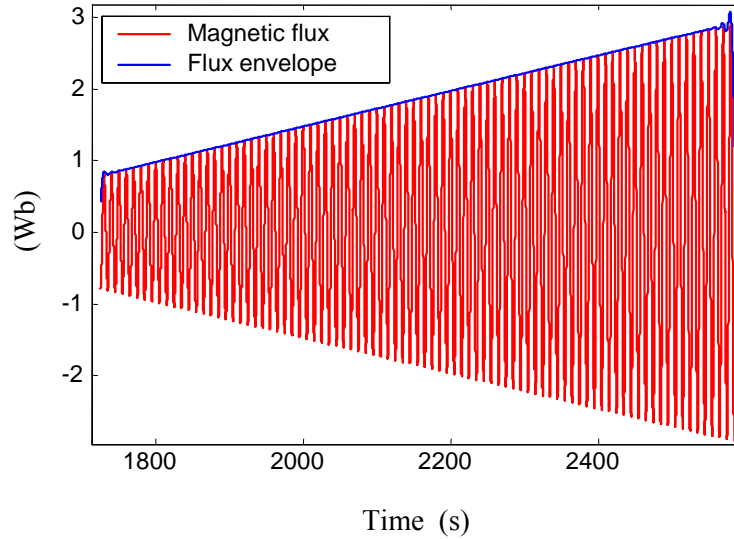


**Figure IV-16: Magnetic flux and its envelope obtained by demodulation. The current is a linear ramp starting from 1724 s and the coil rotation frequency is 0.1 Hz.**

The main field harmonic is obtained from the following equation:

$$B_1(t) = \text{Re}(\tilde{C}_1(t)) = \text{Re}\left\{C_1(t)e^{j\angle C_1(t)}\right\} \quad \text{(Eq. IV-10)}$$

The accuracy of this estimate was proven by computing the difference between the

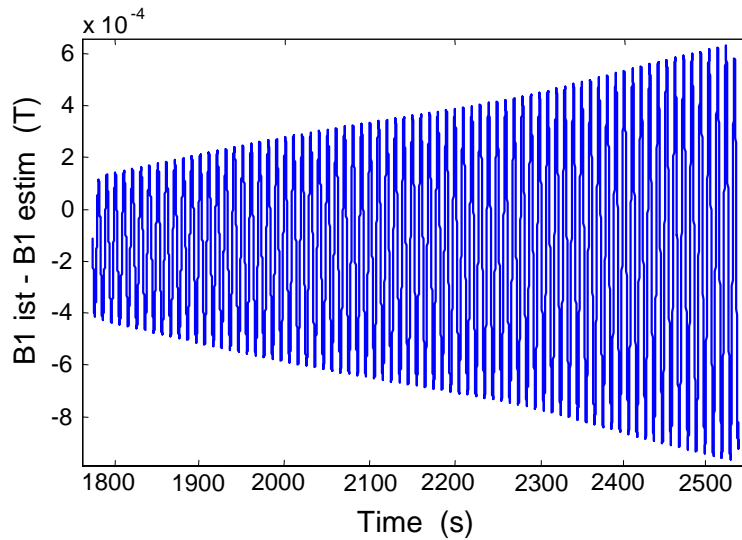


**Figure IV-17: Difference between estimated and instantaneous harmonic coefficient B1.**

instantaneous coefficient B1 and the estimated one (Fig. IV-19).

The main field harmonic, obtained by demodulation, is aligned with the results of standard analysis, according to which an absolute error of about  $10^{-4}$  was achieved

#### IV.5.2 - The higher-order multipoles estimation by STFT

A method to correct the interference due to the main harmonic modulation and the STFT can be combined to improve the higher order coefficients estimate as well as to obtain their instantaneous tracking. According to the method flow diagram shown in Fig. IV-20, the samples  $\psi_c(\theta)$  provided by analog bucking system (compensated flux samples) are firstly processed through the standard quadrature demodulation scheme.

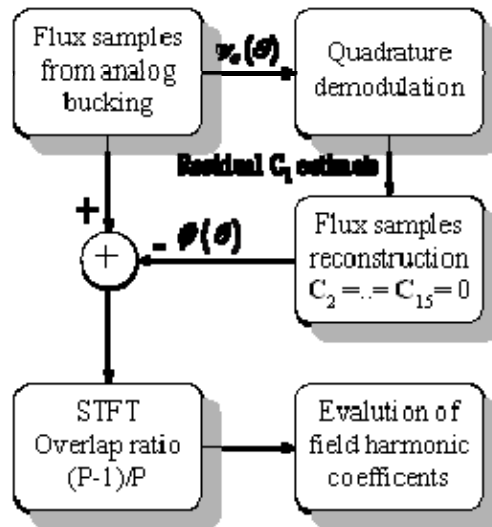


**Figure IV-18: Flow diagram of the method based on quadrature demodulation and STFT.**

Straightforward calculations allow modulus and phase of fundamental coefficient  $\tilde{C}_1$  to be estimated (the main field is evaluated from the compensated flux). Thus, samples of compensated magnetic flux  $\tilde{\psi}(\theta)$  can be generated through the Eq. IV-1, by assuming  $C_1 = \tilde{C}_1$ , and  $C_n = 0$ ,  $n = 2, \dots, \frac{P}{2}$ . The obtained time series is subtracted from the flux samples  $\psi_c(\theta)$  in order to perform further digital bucking. The STFT is then applied on

the results obtained in the previous steps; in particular, an implementation based on sliding window FFT was adopted to assure a suitably low processing time. Moreover, an overlap ratio equal to  $\left(\frac{P-1}{P}\right)$  was adopted to also recover the tracking of the coefficients, attained from STFT results through Eq. IV.3.

In Fig. IV-21, the B3 and B5 coefficients relative to the LHC cycle linear ramp at  $10 \text{ As}^{-1}$  are evaluated with the method proposed. In the same graphs, the results obtained by using only the STFT are also shown. For comparison fluctuations of B3 and B5 harmonics have been attenuated by means of the compensation of B1 demodulated term. Compensated coefficients present, indeed, a residue oscillation, but the error between instantaneous (expected) coefficients is lower than in standard analysis. The start-up transitory of about 6 turns, which corresponds to 60 s for a coil rotating with 0.1Hz frequency, does not represent a problem as there is an interval of seven hours between two consecutive LHC cycles.

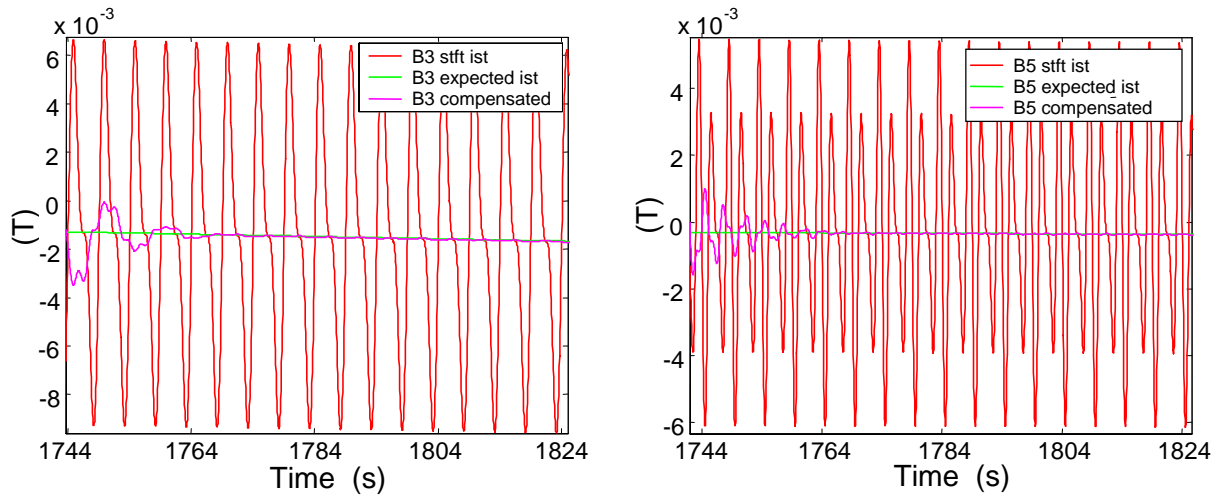


**Figure IV-19: B3 and B5 compensated by demodulation and instantaneous coefficient evaluated with STFT for a coil rotating at 10s period starting from 1724 s.**

## IV.6 - The method based on the extrapolation and interpolation of magnetic flux samples

Another proposal, performing better even in presence of high ramp rates, is based on a simple interpolation of the magnetic flux samples stored over more coil turns. The key idea underlying the method is illustrated in Fig. IV-22. Since the magnetic flux samples are acquired at different angular positions, they can be represented as  $P$ -points curves in a three-dimensional time-angle-flux space. When a single coil turn is completed, the angular position  $\theta$  wraps back to 0, while the time  $t$  keeps being updated. A suitable number of completed turns is retained, the surface  $\psi(t, \theta)$  can be interpolated with high precision by means of straightforward regression algorithms based on a polynomial fitting model.

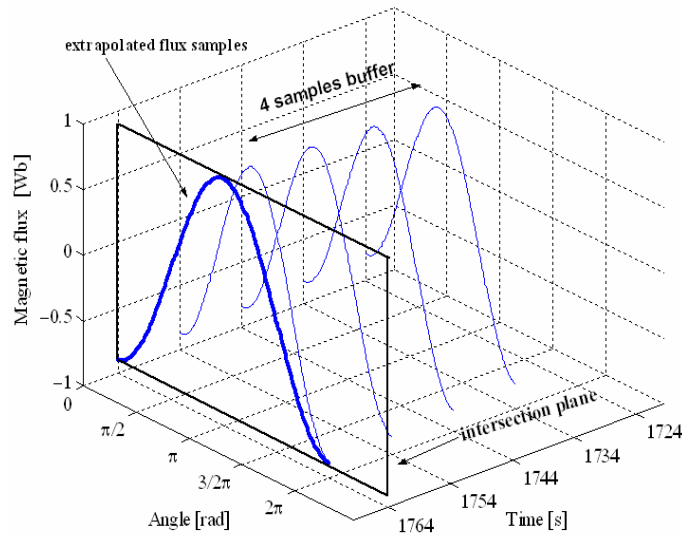


**Figure IV-20: Representation of the extrapolation-based method**

Simulation results show that the best trade-off between accuracy and computational load is obtained by choosing the order of the polynomial equal to 3. As an example, Fig. IV-23 shows a set of  $P$ -extrapolated flux samples, all related to the same time instant,  $t^*$ , and different values of angular position. The obtained samples can be considered as generated by a constant current equal to the actual current at time  $t^*$ . The standard

Fourier analysis can then be applied on the set of extrapolated flux samples characterized by the same time instant.

Deeper insight of the method can be attained by analyzing Fig. IV-23, that shows a projection of the acquired flux samples (blue lines) on the time-angle plane. For each

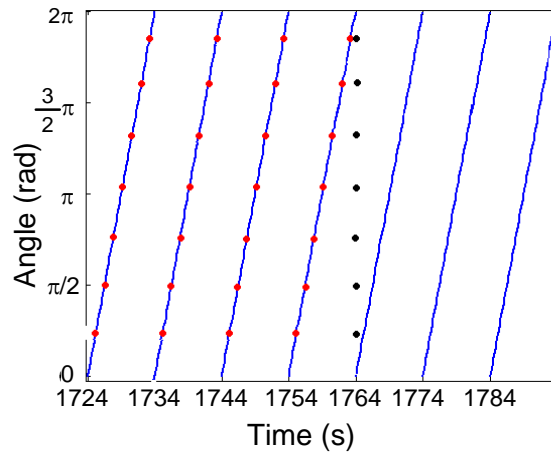


**Figure IV-21: Flux extrapolated at 1764 s .**

angular position, the flux samples acquired in the last four coil turns (red dots) are used to interpolate (or extrapolate) the flux samples related different angular positions at any given fixed time (black dots).

This procedure is repeated each time stop by using a FIFO buffer of length  $4 \times N$ . After an initial transient based on 4 coil turns, the magnetic flux samples vector relative to the time  $t^*$  is extrapolated, and the application of the standard analysis on this vector provides the field harmonics relative to the time  $t^*$ .

In this way, the measurement frequency can be increased at will, within computing power limit, but independently of the coil rotating speed, simply by choosing the desired  $t^*$  at each step.

In Fig. IV-24 to IV-26 the absolute errors between the estimated coefficients B1, B2, and B3 evaluated by the extrapolation method on the LHC cycle linear ramp (starting at 1724 s) and the corresponding instantaneous values are shown. It is worth to note that the reference values are now the instantaneous values of the field coefficients and not the average values over one coil turn, because, the key point of this method is just the estimation of the harmonics instantaneous values.

For all the three field coefficients the absolute error over all the ramp is smaller by one order of magnitude, with respect to the standard analysis.

### Absolute error for field harmonic B1

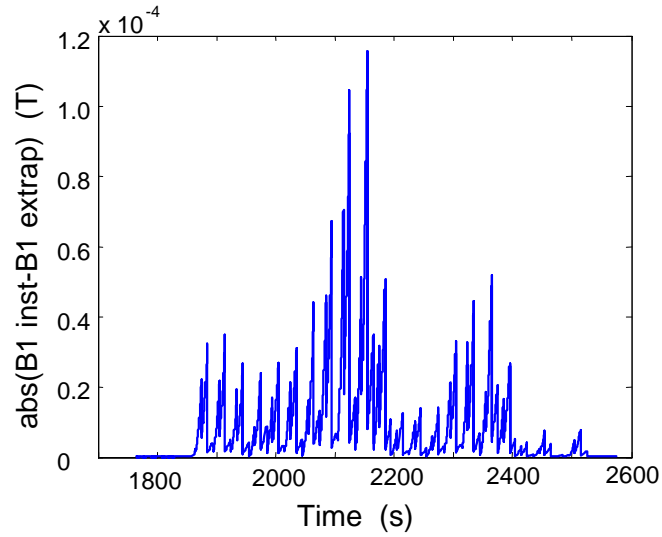


Figure IV-22: Absolute error for the main field harmonic B1 using cubic extrapolation on the LHC ramp.

### Absolute error for field harmonic B2

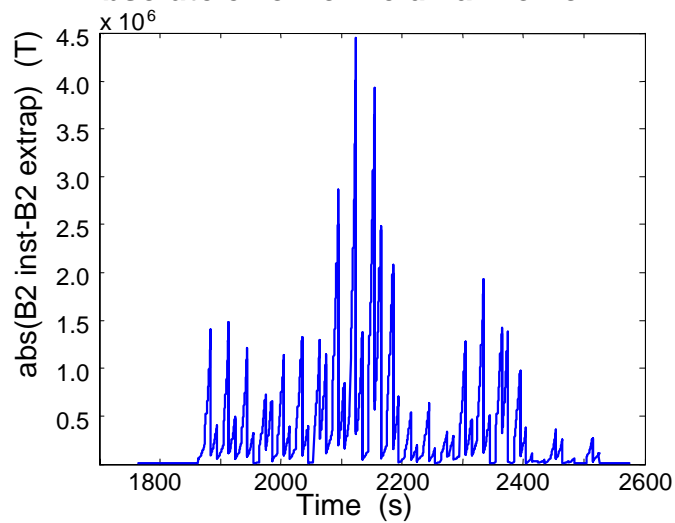
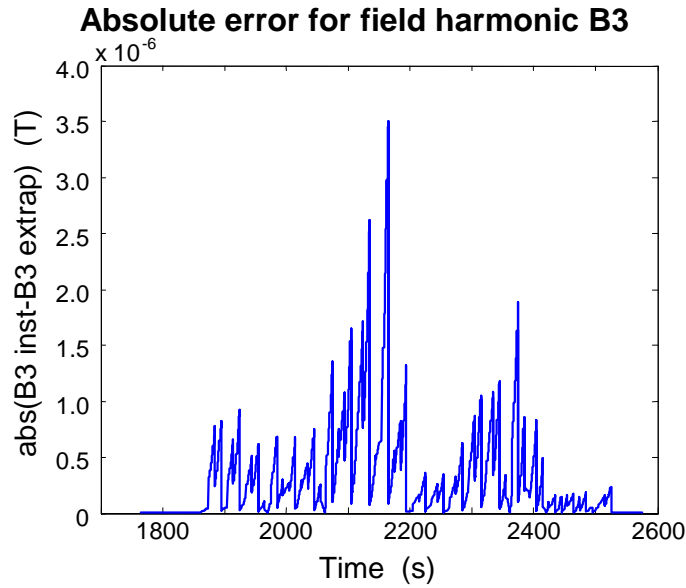


Figure IV-23: Absolute error for the harmonic B2 during the LHC linear current ramp.



**Figure IV-24: Absolute error for the harmonic B3 during the LHC linear current ramp.**

### ***IV.7 - Comparison of the different methods***

In this section the above proposed methods of analysis examined are compared with reference to the Standard analysis by assessing the RMS error:

$$RMS \text{ relative error} = \sqrt{\frac{1}{M} \sum_{n=1}^M \left[ \frac{(X_n - \bar{X}_n)}{\bar{X}_n} \right]^2} \quad \text{(Eq. IV-11)}$$

$$RMS \text{ absolute error} = \sqrt{\frac{1}{M} \sum_{n=1}^M [(X_n - \bar{X}_n)]^2} \quad \text{(Eq. IV-12)}$$

where:

- M indicates the number of harmonics measurements samples during a current ramp; for the standard analysis coincides with the number of coil turns during a current ramp;

- $X_n$  are the harmonic coefficients and  $\bar{X}_n$  are the best estimators. For the standard analysis the best estimators are the mean values of instantaneous coefficients (obtained fitting the raw data) for each coil turn; for the other two methods, the estimated harmonic coefficients are directly compared on the instantaneous ones.

The comparison was carried out for different current ramps: linear, parabolic, exponential.

#### IV.7.1 - Linear current ramp

A linear current ramp, with ramp rate varying between  $10 \text{ As}^{-1}$  and  $50 \text{ As}^{-1}$  was considered. In the comparison coil rotation frequency is set to 0.1 Hz.

Absolute errors for the field harmonics B1, B3, B5, and B7, relative to the different method, are shown in Fig. IV-27 and Fig. IV-28.

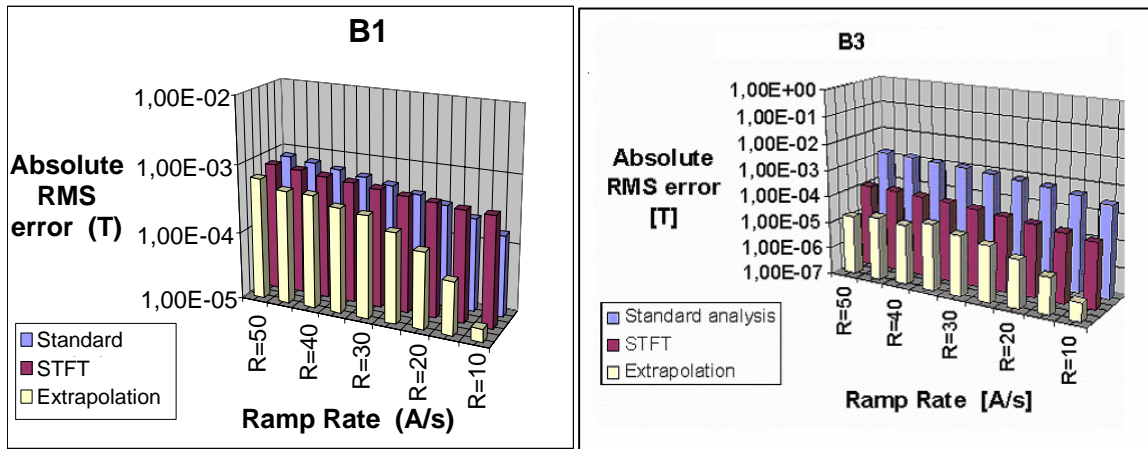


**Figure IV-25: Comparison of absolute RMS error for field harmonics B1 (left) and B3 (right) using different analysis procedures. The coil rotates at 0.1 Hz frequency**

The extrapolation method provides the best results for each ramp rate. For the main field (B1), the demodulation gives errors slightly above those obtained by the standard analysis, but the difference is evident only at  $10 \text{ As}^{-1}$  ramp rate. For high order harmonic coefficients the difference among the three methods is about one order of magnitude.

Extrapolation gives an error of about  $10^{-5}$  T, while STFT and standard analysis,  $10^{-4}$  and  $10^{-3}$  T, respectively.

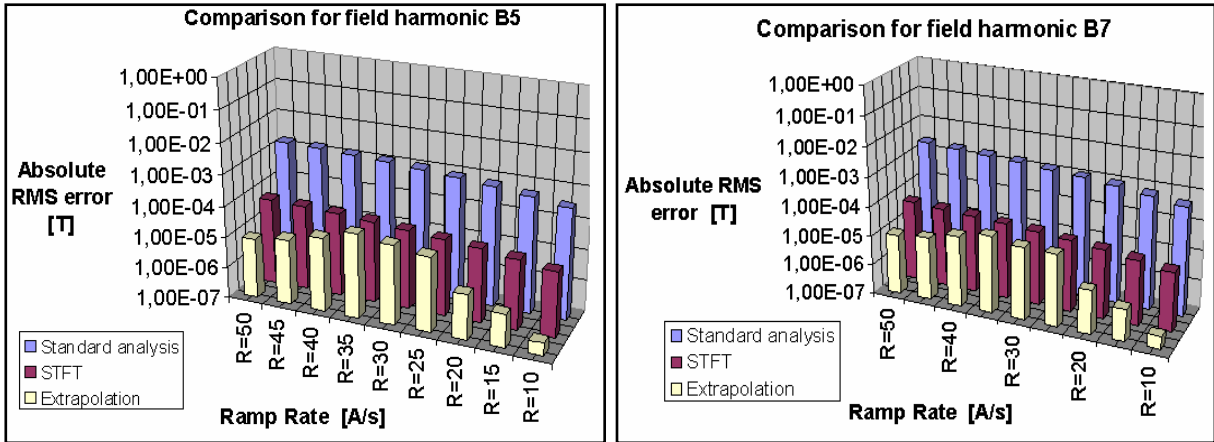


Figure IV-26: Comparison of absolute RMS error for field harmonics B5 (left) and B7 (right) using different analysis procedures. The coil rotates at 0.1 Hz frequency

#### IV.7.2 - Parabolic current ramp

Even in the most unfavorable case (parabolic ramp), the method based on extrapolation proves to be the most accurate for all coefficients (Fig. IV-29), while STFT performs better than standard analysis except for the main harmonic.

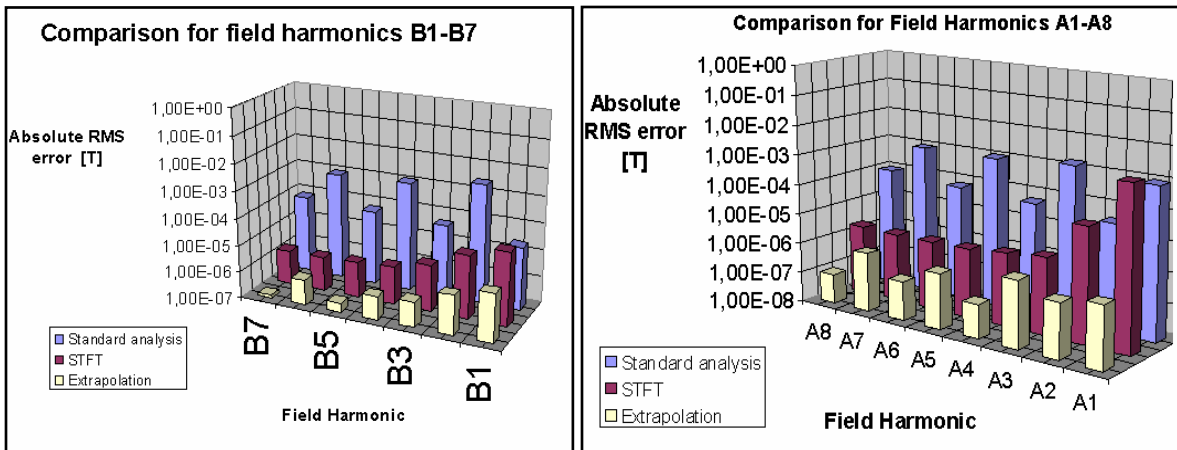


Figure IV-27: Comparison of absolute RMS errors on harmonic coefficients B1-B7 and A2-A8 for a parabolic current ramp. Coil rotation frequency is 0.1 Hz.

#### IV.7.3 - Exponential current ramp

Fig. IV-30 shows absolute errors on an exponential current ramp (according to PELP parameters) for all the field harmonics up to 8<sup>th</sup> order.

The extrapolation method is characterized by absolute RMS errors for all the harmonics two orders of magnitude lower than other two methods.

The STFT method is more accurate than standard analysis in estimating harmonic coefficients A2-A8. Only for harmonic coefficient A2 the results are comparable.

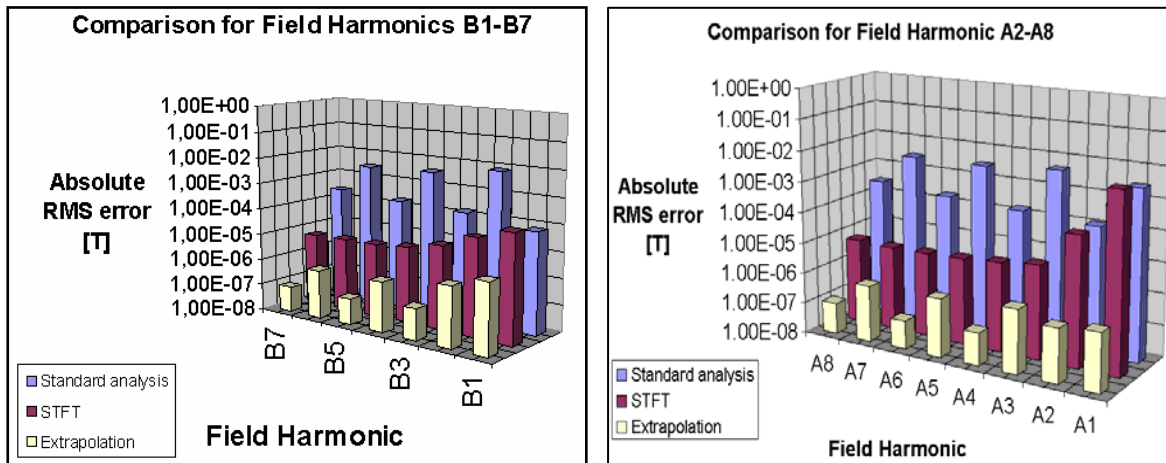


**Figure IV-28: Comparison of relative RMS errors on harmonic coefficients B1-B7 and A2-A8 for a parabolic current ramp. Coil rotation frequency is 0.1 Hz.**

#### IV.7.4 - Discussion

The standard analysis method with continuous coil rotation in a field following the time evolution of a nominal LHC cycle was fully characterized. Its limitations and the errors were highlighted for different ramp rates.

Without doubts, the algorithm based on the extrapolation of the flux samples, in despite of its simplicity, provides the best results consistently for all harmonics and all kinds of ramp. The method based on demodulation provides the instantaneous main field harmonic B1 with an accuracy slightly above standard analysis. The STFT method, with correction by demodulation and successive subtraction of coefficient B1, provides instantaneous higher order coefficients with accuracy much better than the standard

analysis. This can be considered a great approach to compensate the inefficiency of the analog bucking.

For the implementation on DSP of the new integrator cards the algorithm based on the extrapolation is certainly the best candidate.

#### ***IV.8 - Experimental Validation***

A resistive reference dipole of 1 T, at 300 A of nominal current, was first characterized using the DIMM rotating coil system [9]. The field multipoles were measured at 10 A steps, in stationary conditions. The DIMM was developed for magnetic measurement of LHC dipole and it is characterized by one rotating coil of 700 mm long working in the classical washing machine mode. The analog bucking technique is used to compensate the main field in the flux measurement for higher order multipoles evaluation. Two PDI integrator cards are used to obtain both the absolute flux and the one compensated. The standard analysis is applied on the flux samples acquired on a single turn in order to provide the field harmonics at the set current. The instrument software performs further corrections on the experimental data in order to compensate measurement errors arising both from the mechanics and the electronics side, i.e.:

- offset compensation: since the current is kept constant during the measurement, the difference between the 257<sup>th</sup> flux sample and the first one represents the integrator offset during the measurement time. Known the time to complete one coil turn the integrator input voltage offset is evaluated so that the offset compensation is applied at each flux increment;
- average between the flux samples backward and forward to balance mechanical imperfections in the coil rotation;
- feed-down, technique aimed at correcting mechanical misalignments of the coil axis by means of application of symmetry relations on the field harmonics [10].

The plot of the main field vs. the current is shown in Fig. IV-31.

Continuously rotating coil measurements of main and compensated flux were repeated on the same magnet with the PXI integrator, described in the previous chapter, with a linear current ramp at different ramp rates and coil speeds.

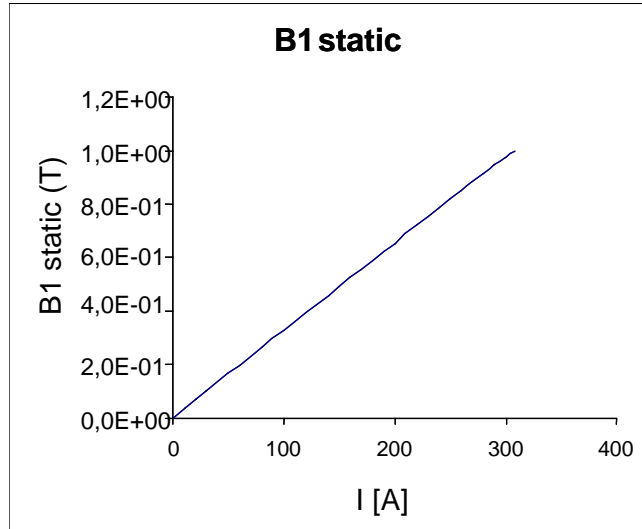


**Figure IV-29: Resistive reference dipole mapping of the B1**

For a resistive magnet, time and history-dependent effects are negligible for higher order multipoles. This means that, field harmonics measurements performed in stationary or dynamic should give the same results. The standard analysis was applied first at each coil turn to the continuous flux samples delivered from the PXI integrator.

In Fig. IV-32 the absolute differences between B1 values measured on different ramp rates and at different coil speeds and the B1 value corresponding to the same current value but measured in static conditions are shown. For the B1 the higher absolute errors as higher is the ramp rate depend also on the effect of the Eddy's currents. In fig. IV-33 the B3 plots measured in different dynamic conditions as well as on a loadline are shown. By analyzing this plot two important results have to be pointed out:

- the higher ramp rate gives the higher absolute error;
- in measurement of varying magnetic field using the standard approach, higher coil speeds only improve temporal resolution (instrument throughput) but the harmonics delivered are affected always by the same error.

Even for low ramp rate, the absolute error is very high since on the raw data obtained with the PXI integrator only the standard analysis was applied without no errors compensation instead, performed by the DIMM software.

Anyway as further proof applying the extrapolation algorithm on the raw data should be possible to show that the absolute error corresponding to different ramp rates becomes the same (or very close).

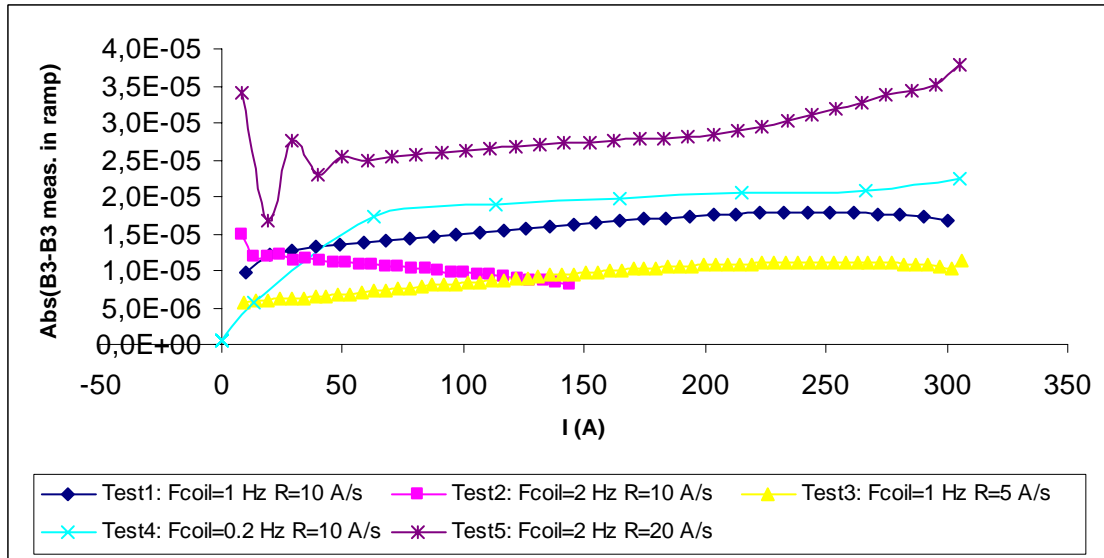


Figure IV-31: Absolute errors between B3 values measured at different current ramp rates and coil speeds and the B3 values at the same current measured in static conditions

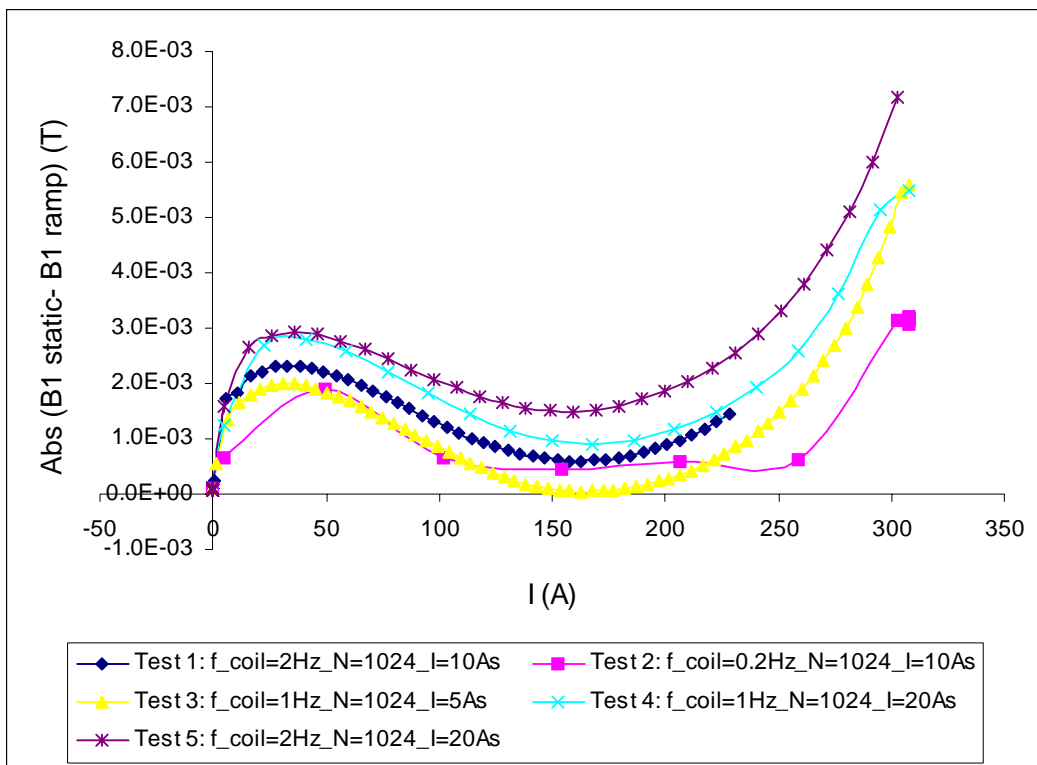
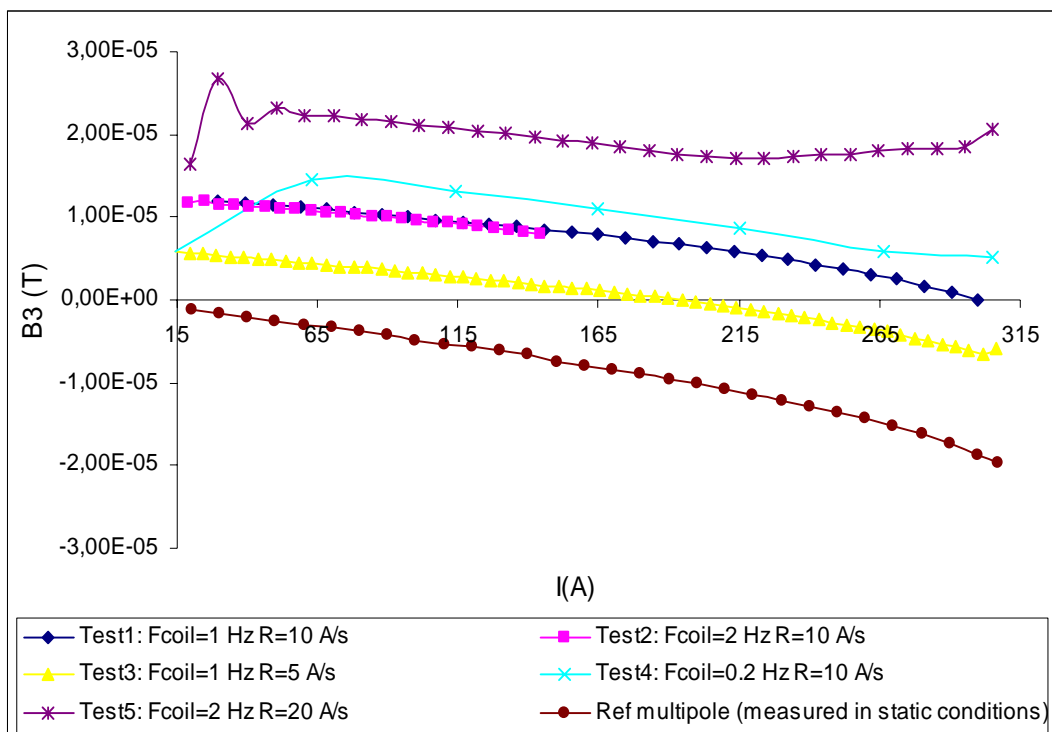


Figure IV-30: Absolute errors between B1 values measured at different current ramp rates and coil speeds and the B1 values at the same current value and measured in static conditions.



**Figure IV-32: B3 measured in static conditions and in dynamic at different ramp rates and coil speeds**

## ***IV.9 - References***

- [1] A. Devred, M. Traveria, “*Magnetic Field and Flux of Particle Accelerator Magnets In Complex Formalism*”, CRYOMAG/94-08.
- [2] M. Haverkamp, L. Bottura, et. Al. “*Long Term Dynamic Effects in Superconducting Dipole Magnets*”, LHC-MTA-IN-2001-163 2002-08-07.
- [3] L. Bottura, “*Standard Analysis Procedures for Field Quality Measurement of the LHC Magnets Part I: Harmonics*”, LHC Engineering specification, EDMS 313621.
- [4] A. Jain, “*Recent Magnetic Measurement Activities at BNL*”, Proceedings of the 11th International Magnet Measurement Workshop (IMMW-XI) Brookhaven National Laboratory, Upton, NY, September 21st-24th,1999.
- [5] A. Jain, “*Measurements of Field Harmonics at Very High Ramp Rates*”, Proceedings of the 14th International Magnet Measurement Workshop (IMMW-XIV), CERN, Geneve, CH, September 26th-29th,2005.
- [6] L. Bottura, T. Pieloni, N. Sammut, “*Scaling Laws for the Field Quality at Injection in the LHC Dipoles*”, LHC Project Note 361 2005-02-21.
- [7] L. Bottura, P. Burla, R. Wolf, “*LHC Main Dipoles Proposed baseline current ramping*” LHC project report 172, March 1998 .
- [8] A.P. Verweij, “*Electrodynamics of Superconducting cables in Accelerator Magnets*”, University of Twente, Nederlands 1995.
- [9] J. Billan ; J. García-Pérez, D. Giloteaux; A. Raimondo, V. Remondino, H. Reymond, A. Rijllart, “*Magnetic Measurement Systems for the LHC Dipole Assembly Companies*”, LHC-Project-Report-747, CERN 2004.

# Chapter V - THE SNAPBACK ANALYZER: AN INSTRUMENT

## TO MEASURE B<sub>3</sub> AND B<sub>5</sub> HARMONICS

### *V.1 - Introduction*

The 3<sup>rd</sup> and 5<sup>th</sup> order harmonics of the dipole field can be measured by using the Hall plate arrangement (Fig.V-1).

With this ideal geometry, the total signal S from the Hall plates at the first order is:

$$S_3 \approx 3 \left( \frac{R}{R_{ref}} \right)^2 B_3 ; S_5 \approx 5 \left( \frac{R}{R_{ref}} \right)^4 B_5 \quad (\text{Eq. V-1})$$

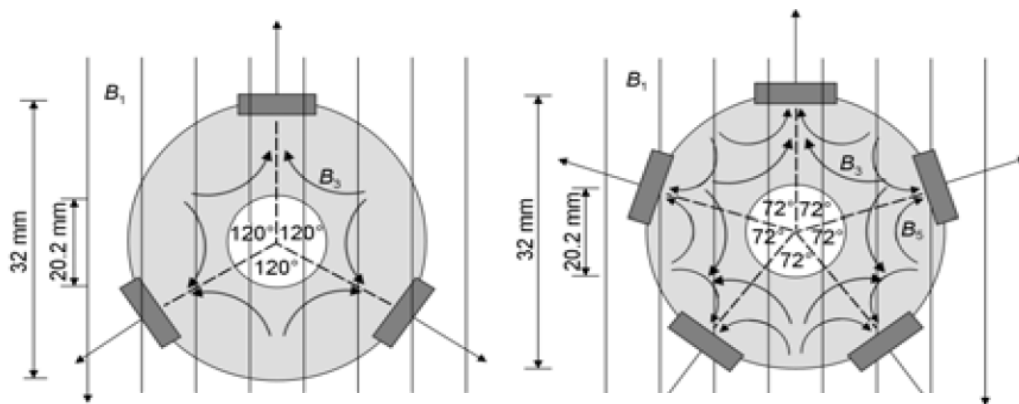
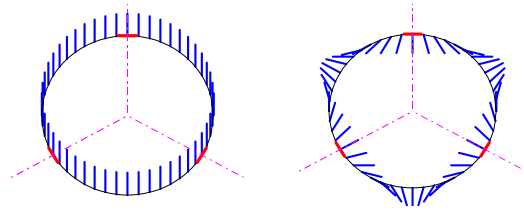


Figure V-1: Cross section of sextupole, left, and decapole ring, right (the dipole, sextupole and decapole field lines are also illustrated).

where  $R$  is the radius of the Hall plates,  $R_{ref}$  is the reference measurement radius ( $R_{ref} = 17\text{mm}$  for the LHC) and  $B_n$  is the absolute normal multipole component. As shown in Fig. V-2 (left), the dipole field component is completely compensated by the symmetry, if the signals of the Hall plates are summed together, and the total signal is proportional to the normal sextupole harmonic.



**Figure V-2: left) In a dipole field:  $\text{Sum} \propto B_1 - B_1/2 - B_1/2 = 0$   $\therefore$  Dipole field is bucked out. right) In a sextupole field:  $\text{Sum} \propto -B_3 - B_3 - B_3 = -3B_3$   $\therefore$  Sextupole field is isolated.**

The same principle is applied to the decapole harmonic.

In this chapter, the complete measurement system that delivers directly the  $b_3$  and  $b_5$  harmonics over the time, starting from the Hall plates voltage signals of the measurement probe (Fig. V-3), is described. The main feature of this instrument is to measure directly the decay and snapback waveforms used for modeling.

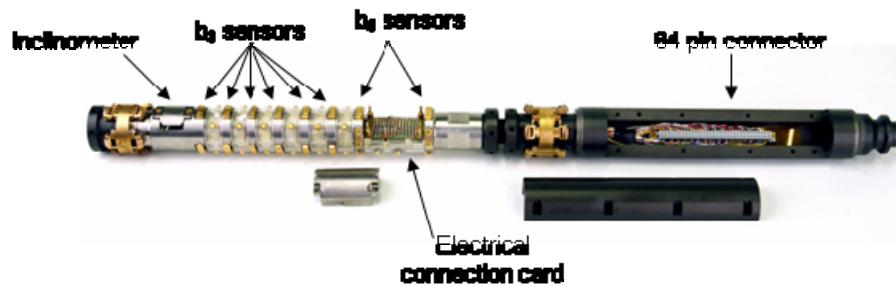


**Figure V-3: CERN probe to measure  $b_3$ - $b_5$ .**

In order to achieve the required resolution on the field harmonics and, since the  $b_3$  and  $b_5$  components are 4 orders of magnitude lower than the main dipolar field, an analog bucking was adopted. The signals of each ring (3 for the  $b_3$  rings and 5 for the  $b_5$  rings) are mixed in order to compensate the main field. The signal sum is then amplified and sampled. Details on the compensation cards developed as well as the data acquisition system used are given.

A full metrological characterization was carried out in order to discover and characterize all the possible uncertainty sources and, first of all, the unstability of the compensation cards responsible for the need of frequent instrument calibrations.

Test results suggested a calibration procedure, performed using the rotating coils as reference instrument, aimed at correcting errors in b3 and b5 harmonics up to the second order. This procedure was fully automated in the instrument software and represented the solution to the limited long-term stability of the used bucking cards. At the same time, according to the instrument characterization results, new compensation cards were developed in order to assure a higher long-term stability.

Digital bucking solution, namely the compensation of the main field after the sampling of each Hall plates signal by means of numerical sum, was also explored. The first b3 measurements proved the principle even if a 16-bit ADC was used. An implementation of this approach, based on a 18-bit AD converter, oversampling, and dithering techniques, as well as compensation of the Hall plates non linearity in real-time, is detailed.

## ***V.2 - The solution based on the analogic bucking***

### *V.2.1 - Hardware overview*

The instrument for the analysis of the snapback phenomenon can be decomposed in three main parts (Fig.V-4):

- the Hall plates probe;
- analog compensation cards;
- SCXI digital acquisition system.

The sensor is a project originally devised at CERN [1], already detailed in chapter 2.

The compensation cards correct the main dipolar field component and amplify the sum signal to adapt it to the input range of the data acquisition system. In the electronic rack in Fig. V-4, the conditioning module for the tilt sensor installed in the probe is also visible. This in fact, results indispensable to align the probe with respect the gravity before the measurement.

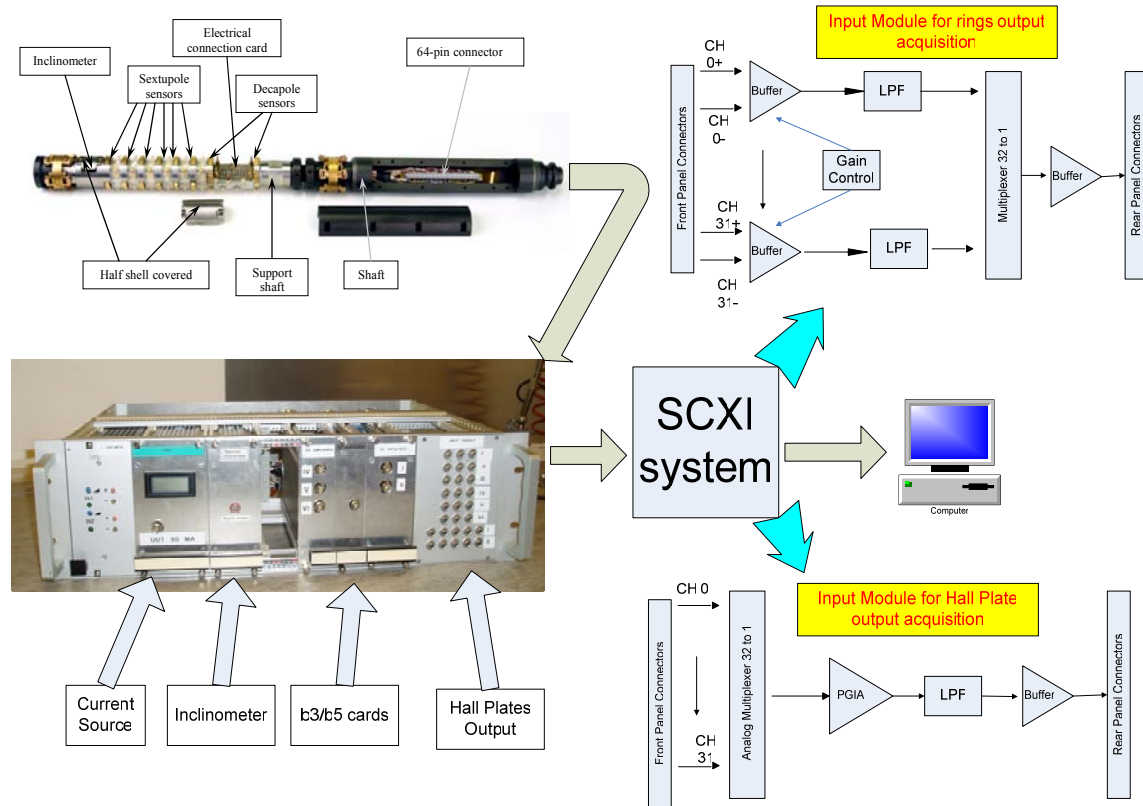


Figure V-4: b3-b5 analyzer-architecture layout.

The system named SCXI, is a commercial multi-channel data acquisition system from National Instruments. The selection criteria were:

- high number of channels to acquire; not only the sum signals by each ring are acquired but all the Hall plates outputs (28), in order to monitor in real time possible Hall plates faults and saturations;
- sufficient ADC resolution, in order to satisfy the requirement on the measurement resolution of b3 and b5 component. Since the signals proportional to b3 and b5 harmonics are characterized by slow variations (the snapback duration is about 60 s) a multiplexed architecture, based on a single ADC, was chosen (inter-channel delays are negligible);
- high capability of noise rejection obtained using programmable anti-aliasing filter on each single channel.

### V.2.1.1 - The compensation cards and the calibration in dipolar field

The decay/snapback emerges at low field, during the injection. Thus, the detector is designed to measure a dipolar field in the range from 0 to 1 T (at injection the value of the main field is 0.57 T). The Hall plate positioned on the top of the sensor is measuring the whole dipole field; in case of the sextupole ring, the other two Hall plates on the ring are measuring approximately half of the main component in opposite direction (they are at  $120^\circ$  from the dipole field). By considering that the sextupolar and decapolar component of the field are 4 orders of magnitude smaller than the dipolar field a high resolution is needed (at least 18 bits), in order to appreciate  $b_3$  and, in particular,  $b_5$ , by the signal coming out directly from the Hall plates. In particular, as the sensitivity of used Hall plates is 220 mV/T, the signals proportional to  $b_3$  and  $b_5$  field are in the order of 100  $\mu$ V, with an overlapped dipolar signal of 100 mV.



**Figure V-5: Compensation card for three sextupole rings.**

The geometrical configuration used in the Hall plates assures, in principle, the compensation of the dipolar field through simple sum of the signals belonging to the same ring. This is only an ideal case, but imperfections or systematic errors (Hall plates misalignments) of the sensor bring a residual dipolar component after the sum. One of the main causes of the compensation error is the difference in the Hall plates sensitivity.

The bucking cards are designed to analogically sum the signal coming from each Hall plate of a given ring by producing an amplified output signal proportional to the component of interest. The electronic circuit was designed in order to reduce the noise and to amplify the sensor signals before the acquisition in order to obtain a better resolution. Before the signals summation, a compensation of the sensitivity differences is carried out by adjusting the gain of the first stage amplifier. The compensation cards are two for the six sextupole sensors ring, and one, for the two decapoles rings. The electronic schematic for the sextupole compensation card is shown in Fig. V-6.

In the following, the different stages of a sextupole ring compensation circuit are detailed in order to highlight the signal treatment.

- *Pre-Amplification Stage.*

Before the signals from the three Hall plates of the sextupolar ring are connected to first amplification stage based on INA 128U instrumentation amplifier (IC1, IC2 and IC3 in Fig. V-6).

The input is in full differential mode, thus reducing the common mode voltage of each Hall plate signal (all the 28 Hall plates are connected in series).

The gain adjustment to compensate the sensitivity difference is performed by trimming the two potentiometers P1 and P2.

In particular, P2 (100  $\Omega$  value) allows a fine regulation of the gain. In this first stage, the output offset can be adjusted to compensate possible offset differences between the Hall plates.

- *The Mixer Stage.*

All signals output by the Hall plates mounted on one ring go through the pre-amplification stage first, and, then, to the mixer (or adder) stage. This is implemented with the amplifier OP 27GS (IC 13). The main characteristics of this stage are a unitary gain and regulation of the output offset (trimmer P28). Changing the output offset it is possible to adjust the bucking of the dipolar component at the injection.

- *Final stage*

Another INA 128U (IC 10 in Fig. V-6) is used to amplify the adder output signal before acquisition and to restore the correct polarity of the signal (the amplifier

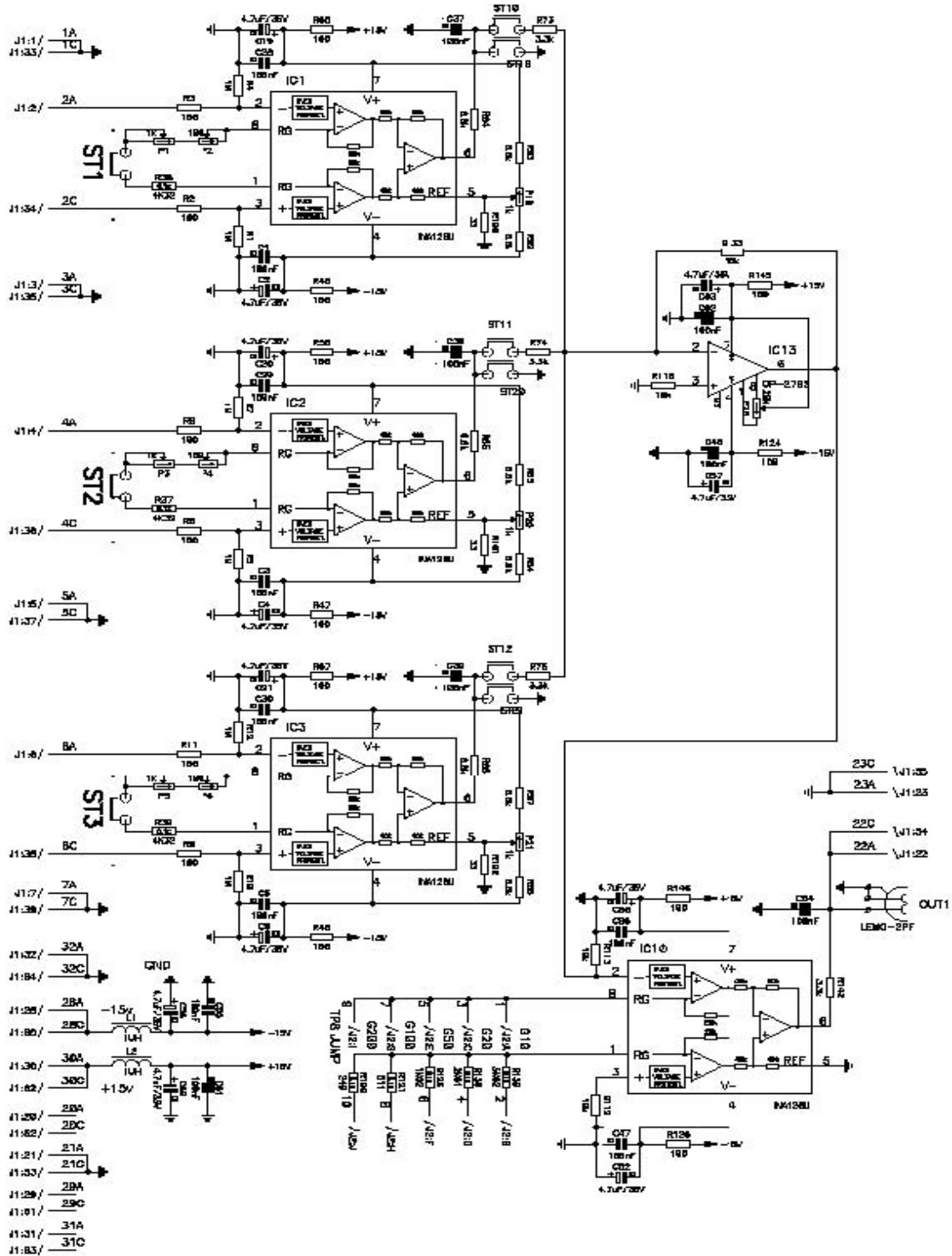


Figure V-6: A schematic draw of a sextupole compensation card.

inverts the signal sign). Five different gains (10, 20, 50, 100 and 200) can be selected by changing the jumper TP8.

The calibration procedure of the compensation cards is carried out inside a reference resistive dipole magnet (Alstom HB436/MCB22) permanently checked by a Nuclear Magnetic Resonance teslameter (PT2025 MetroLab) characterized by an accuracy of  $10^{-7}$  T. The voltages on the boards test points are measured using a  $7\frac{1}{2}$  digits integrating multimeter, with an estimated accuracy of  $\pm 1 \mu\text{V}$ .

The calibration proceeds as the following:

- *Hall plates offset correction* is carried out putting the probe in a no field chamber (in this way the effect of the earth magnetic field is removed and only the Hall plate intrinsic offset is taken into account) and by adjusting to zero the offset of each input stage;
- *Hall plates sensitivity differences correction*- The probe is inserted into the resistive reference magnet at the field of 0.537 T, corresponding to LHC injection conditions. The Hall plates are oriented one by one perpendicularly to the dipolar field (by using the inclinometer for top Hall plates, since the reference dipole is normal; for lateral Hall plates, the alignment is made by rotating the probe and by checking the signal maximum through the voltmeter) and the gain of the first input stage is adjusted to have the same voltage in output;
- *dipolar component compensation*- In the reference dipole at 0.537 T, the probe is aligned to the gravity (according to its correct working position) and the mixer offset is adjusted to null the output stage of the ring.

With this calibration, a correction at the first order of the differences of the Hall plates transfer function, as well as a rough compensation of the main dipolar field is achieved.

#### **V.2.1.2 - The SCXI Data Acquisition system**

The data acquisition system chosen for the Snapback analyzer is a National Instrument SCXI system connected to a DAQ card PCI 16 bit (model 6052 E) installed in a Personal Computer Windows Xp (Appendix B).

Thanks to the use of the analog bucking a 16-bit converter is enough to satisfy the resolution requirement on the b3 and b5 harmonics acquisition (0.1 unit). In fact, taking into account that decay and snapback measurements are carried out at injection plateau, at a dipolar field of 0.537 T, 0.1 unit on the higher harmonics correspond to  $0.5 \cdot 10^{-5}$  T; considering that the Hall plate sensitivity is around 220 mV/T and the compensation card output gain is around 110, 0.1 unit of field corresponds to about 100  $\mu$ V at the DAQ system input. Since the input range is selectable at 2 V, a 16-bit ADC implies a resolution on the compensated field harmonics of 0.03 unit.

Timing resolution constraints (10 Hz) are surely satisfied, since the system maximum sampling frequency is 2000 S/s; this guarantees even the use of a 100 oversampling factor in order to reduce the input noise.

#### *V.2.2 - The measurement uncertainty sources*

In an ideal configuration, the dipole field is erased by the sensor geometry; experimentally, owing to different error sources, an un-bucked component is always present.

In fact, taking note that the sextupolar and decapolar components of the field are four orders of magnitude below the main field, the compensation of the dipole field should be performed with an accuracy at least of  $\pm 100$  ppm on all the working range of the probe ( $0.537 \text{ T} < B_1 < 1 \text{ T}$ ). This means that the electronic stability, namely the variation of gains and offsets in any stages of the compensation cards should be contained in some tenths of ppm. The stability during the measurement time (usually 1 hour) is mandatory, but generally a medium term stability is requested in order to avoid frequent calibration procedures.

In addition, following factors have to be taken into account:

- temperature-dependent Hall plates drift;
- Hall plates angular misalignments; these are corrected, in principle, at a single working point (0.57 T) and not on all the measurement range;

- nonlinearity of the Hall plates transfer functions; the correction of sensitivity and offset differences carried out by the compensation cards assumes a linear behaviour of each Hall plate;
- absolute accuracy of the data acquisition system.

In the following, an analysis of these uncertainty sources is described, starting from the linearity and the stability of the compensation cards.

#### V.2.2.1 - Compensation Cards Characterization

The tests on the compensation cards can be divided in two categories: the ones aimed at characterizing the boards amplifiers and the ones aimed at testing the stability of amplifiers parameters.

The following tests belong to the first category:

1) Evaluation of the transfer functions for all the 28 input amplifiers. In particular, the following quantities were tested:

- the **differential gain** applying a test voltage in the range  $[-300\text{mV}, +300\text{mV}]$  with 25mV steps. Non linearity error has been evaluated on the obtained transfer function;
- the **common mode gain**, by applying on each input a common voltage into the range  $[-7.125, +7.125]$  with step of 250 mV. This parameter is very important because the twenty-eight Hall plates of the measurement probe are connected in series and the output of each one is given by a differential voltage (the useful signal) plus a common mode that depends on the position of the Hall plate in the series. The common mode voltage has to be rejected in the same way by all the input amplifiers to avoid a different offset on each output;
- the **offset**, evaluated as the intercept of the previous transfer function.

2) Evaluation of the transfer function for each overall compensation circuit (six for b3 rings and two for b5 rings). In particular, the following quantities were tested:

- the **gain**, by applying to all the compensation circuit inputs (three for b3 rings, and five for b5 rings) the same voltage with values into the range [-30 mV, +30 mV] by 1 mV of increasing step. By referring to Fig. V-6, calling  $G_i$  (with  $i=1$  to 3 for b3 circuits and  $i=1$  to 5 for b5 circuits) the input amplifiers gains,  $G_{adder}$  the adder gain (equal for each input channel) and  $G_{out}$  the output amplifier gain, the output voltage expected to measure is given by:

$$V_{out} = (G_{out} \cdot G_{adder} \cdot \sum_i G_i) \cdot V_{input} \quad (\text{Eq. V-2})$$

- the **offset** of the compensation chain, as a whole measured by setting to 0 all the circuit inputs.

The stability was measured after the electronic warm-up, during five hours working, with 5 minute of sampling time, the following quantities were monitored:

- the **overall gain** of each compensation circuit;
- the **offset** of each output channel (compensation circuits outputs);
- **Hall plates supply current**;

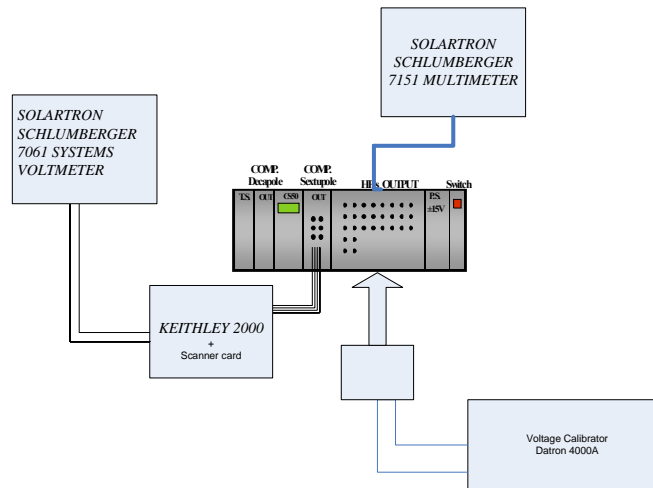


**Figure V-7: Compensation cards test bench**

- **voltage supply** of all the electronic boards;
- **temperature** inside the electronic rack.

In Fig. V-7, the test bench for the compensation cards is shown.

The voltage calibrator is characterized by  $\pm 0.34$  ppm of absolute accuracy on 1 V range (with the temperature correction). Output voltage was measured by a digital integrating voltmeter with a  $7\frac{1}{2}$  digits resolution ( $\pm 1.5$  ppm of absolute accuracy at 0.2 V range and  $\pm 5.4$  ppm on range 2 V). The Keithley 2000 equipped by a scanner card dispatches the 8 outputs of the compensation cards to the input of the voltmeter. Finally, another multimeter (SOLARTRON SCHLUMBERGER 7151) is used to measure the temperature inside the electronic rack with a resolution of 0.01 degree. All the instruments are driven via GPIB 488 by automatic measurement software developed in LabView™.

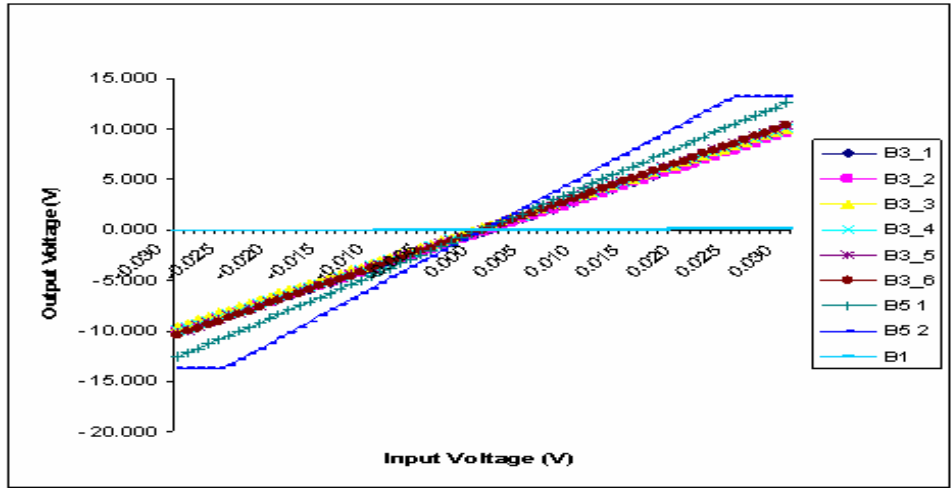


Figure V-8: Compensation circuits transfer functions.

The transfer functions for all the eight compensation circuits are shown in Fig.V-8.

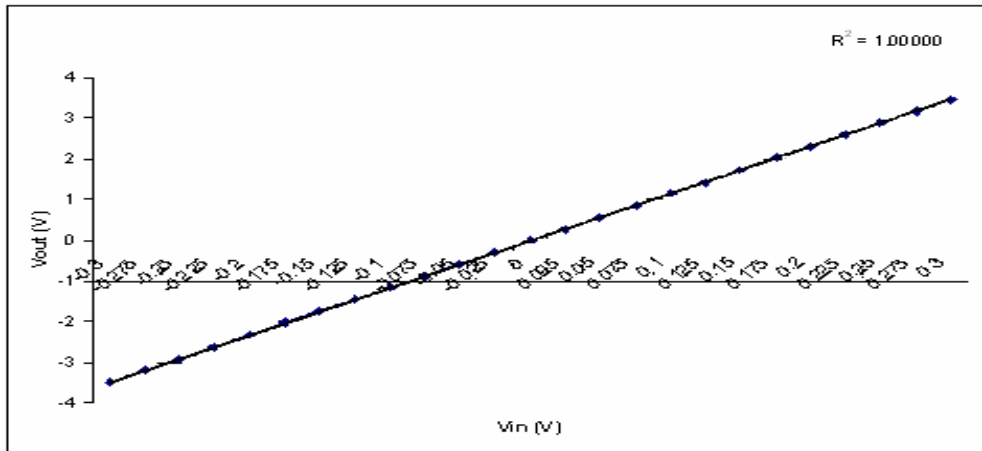
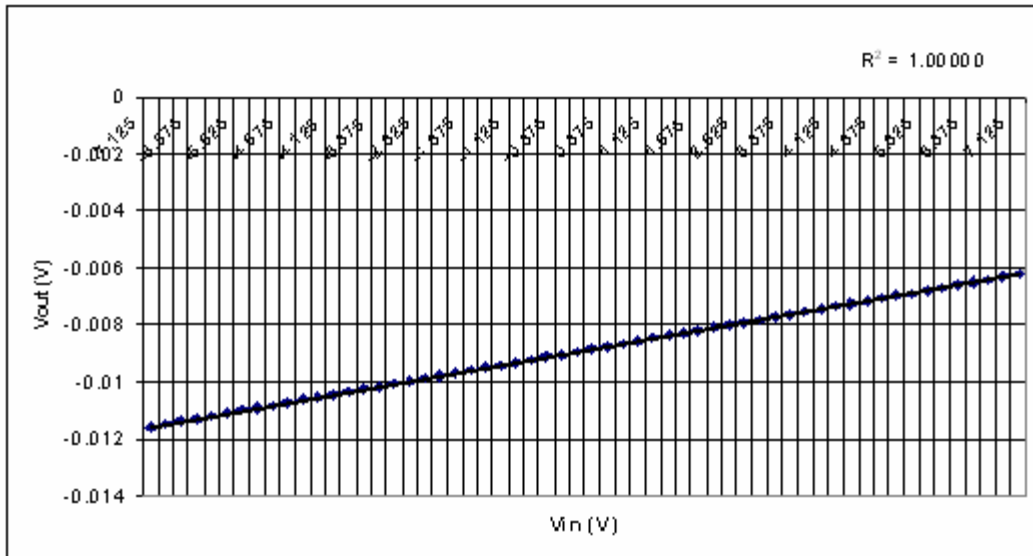


Figure V-9: Transfer function of the 1<sup>st</sup> input amplifier with a common mode input. The gain is 3.762E-4.

Owing to the mixer stage, since to each input channel is applied the same voltage, the maximum input is limited to 30 mV in order to avoid the saturation of the final



**Figure V-10: Transfer function of the 1<sup>st</sup> input amplifier connected in differential mode**

amplifier. The linearity is good on all the input range; this is principally the linearity of the output stage. In Fig. V-9, an example of transfer function of only an input amplifier (in particular the one connected to the fist Hall plate), is given.

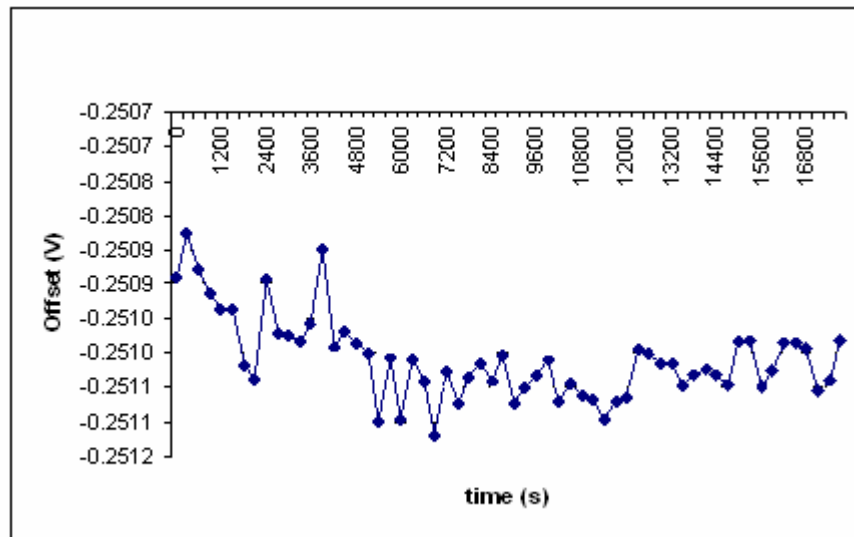


**Figure V-11: Offset variation on the output of the compensation circuit ring b3\_1.**

Again a good linearity over all the range  $\pm 300$  mV (220 mV in input correspond to 1 T dipolar field) is shown. In Fig. V-10, the transfer function of the same amplifier to a common mode input is shown. For all the input amplifiers, the common mode gain is around  $4 \cdot 10^{-4}$ . Since the Hall input resistance is about  $5 \Omega$  and the supply current is 50 mA the maximum common mode voltage (corresponding to the 28th Hall plate of the series) is around 7 V to which an output “error” voltage around 3 mV corresponds. Anyway this error for each input amplifier stage is corrected by means of the Hall plates offset correction procedure.

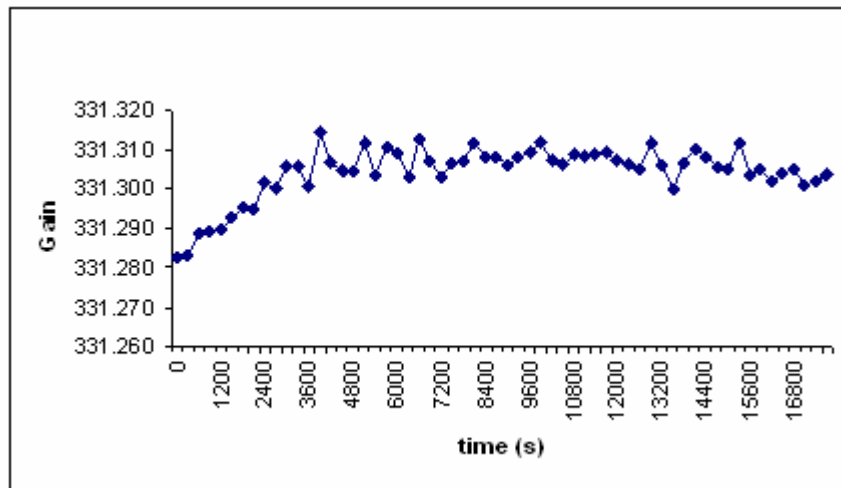


**Figure V-12: Gain variation of the compensation circuit ring b3\_1.**

As far as the stability tests are concerned, Fig. V-11 and V-12 show, as an example, typical gain and offset variation of the first ring b3 compensation circuit. The results for all the compensation circuits are summarized in Table 1. During 5h of working (after the warm-up), the spread of the offset at the output of the compensation circuits is not less than  $100 \mu\text{V}$ , while the global gain stability is better than 1%. Offset seems to increase with temperature (Fig. V-11), although its behaviour is often not well defined. The problem is that output offset depends on many causes, such as:

- offset and gain variation of the previous stages (mixer and input amplifiers);

- resistances variation on the boards as function of the temperature (in particular the regulation trimmer characterized by temperature coefficients around 1%);
- boards power supply instability;
- drift of each instrumentation amplifier.

	B3_1 Gain	B3_1 Off (uV)	B3_2 Gain	B3_2 Off (uV)	B3_3 Gain	B3_3 Off (uV)
$\mu$	331.3	-0.25101	326.0	-0.27801	324.8	0.22088
$\sigma$	6.9E-3	6.0E-5	6.5E-3	6.5E-5	5.8E-3	5.4E-5
	B3_4 Gain	B3_4 Off (uV)	B3_5 Gain	B3_5 Off (uV)	B3_6 Gain	B3_6 Off (uV)
$\mu$	333.9	0.04727	341.9	0.04935	345.8	-0.07680
$\sigma$	3.8E-3	4.3E-5	4.3E-3	8.2E-5	4.6E-3	9.4E-5
	B5_1 Gain	B5_1 Off (uV)	B5_2 Gain	B5_2 Off (uV)	B1 Gain	
$\mu$	418.8593	-0.001151	533.3542	-0.000510	4.649620	
$\sigma$	4.8E-3	5.6E-5	7.7E-3	7.3E-5	6.7E-5	

**Table 1: Summary of the stability tests on all the compensation circuits**

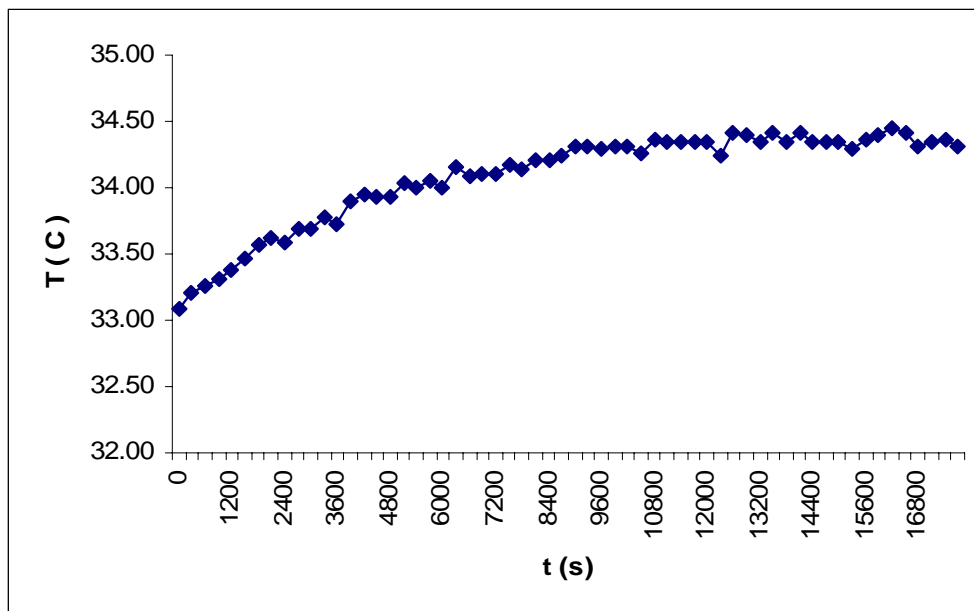


**Figure V-13: Temperature chart in the electronic rack during the stability test.**

During the measurement, also the Hall plates thermal drift has to be considered (the temperature stability factor for the Hall plates is 100 ppm/°C). Another important factor is the stability of the current generator used to supply the Hall plates series. Fig. V-14 shows the current chart over 5 hours working on a load resistance correspondent to the sum of the Hall plates input resistance at the injection field (the input resistance is function of the measured field). The current is stable at 10 ppm, value, this latter, is enough to consider negligible the effect on the Hall plates output.

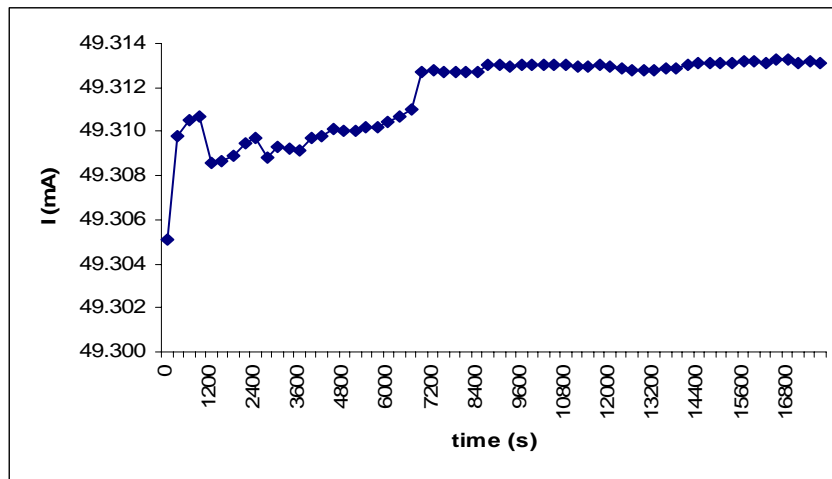


**Figure V-14: Hall plate current supply the stability test in 5 h working.**

By considering only the performance of the compensation cards, it can be concluded that, on the short term, the maximum gain variation produces errors on b3 and b5 signals of some hundredths of units (and then negligible), and the output offset instability up to

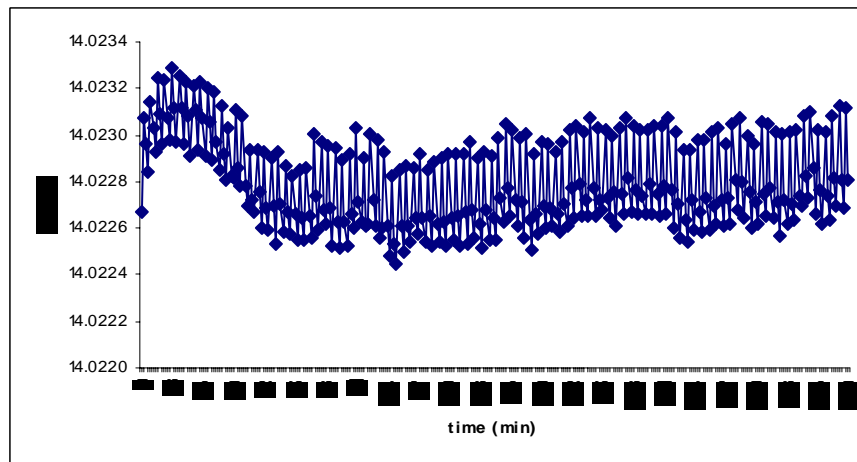


**Figure V-15: Supply voltage during 5 hours test.**

100  $\mu\text{V}$  is translated in measurement errors of 0.1 units (the same order of magnitude of the instrument resolution). In Fig. V-15 the chart of the supply voltage during the 5 hours of the test is shown.

### V.2.2.2 - Evaluation of the Hall plates transfer functions

The linearity of each Hall plate over all the measurement range was estimated by means of an automatic measurement bench. The field reference is provided by the resistive reference dipole used for the compensation cards calibration (1 T at 300 A nominal current) monitored by the Nuclear Magnetic Resonance teslameter (PT2025 MetroLab). The Hall plates output voltage is measured by using the same data acquisition system of the b3-b5 measurement with 16 bit resolution.

The measurement procedure was organised according to the following steps:

- each Hall plate under test is aligned to the gravity by using the probe inclinometer and/or checking when his maximum output voltage (the reference dipole) is normal;
- the magnetic field is changed in the range 0.3-1 T by steps of 0.05 T on 13 measurement points.

Fig. V-16 and V-17 show two measured transfer functions. A difference between the sensitivities around the 2 % is evident but, very strange, a sort of saturation, when the magnetic field approaches 1 T value, can be highlighted. As a consequence, a non linearity error of 1%, far from the 0.2% value specified in the technical data, arises.

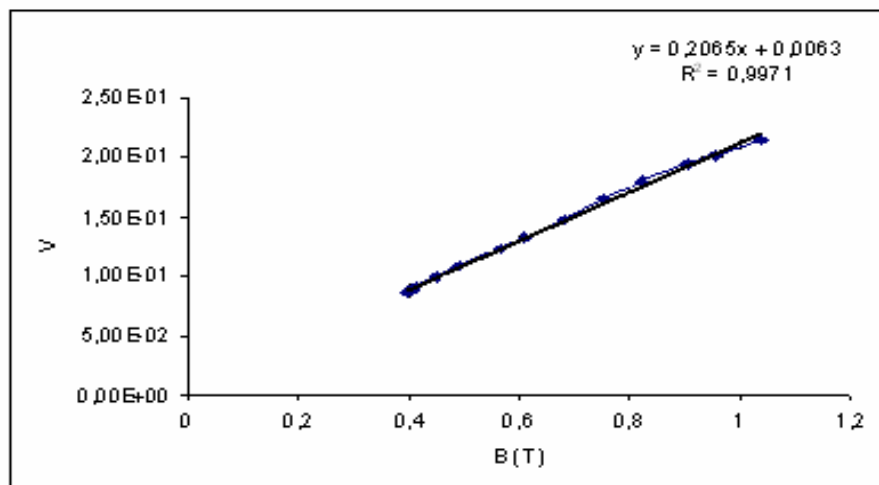
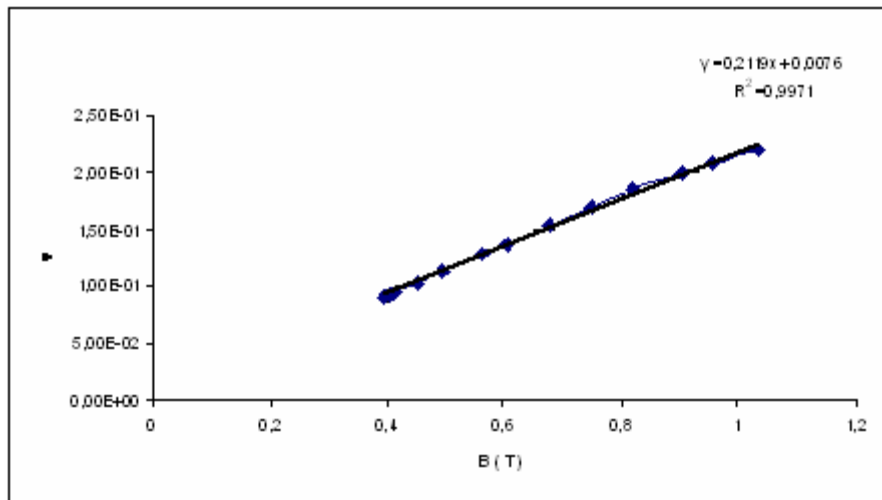


Figure V-16: First ring b3 Hall plate top transfer function



**Figure V-17: Second ring b3 Hall plate top transfer function**

Further investigations showed that the source is the current generator (Fig V-18). In fact, the Hall plates input resistance is function of the field, and, around 1 T, the resistance load reaches a value (around 150  $\Omega$ ) out of the generator working range.

Even after solving this problem, the measured Hall plates non linearity was not better than 0.2%.

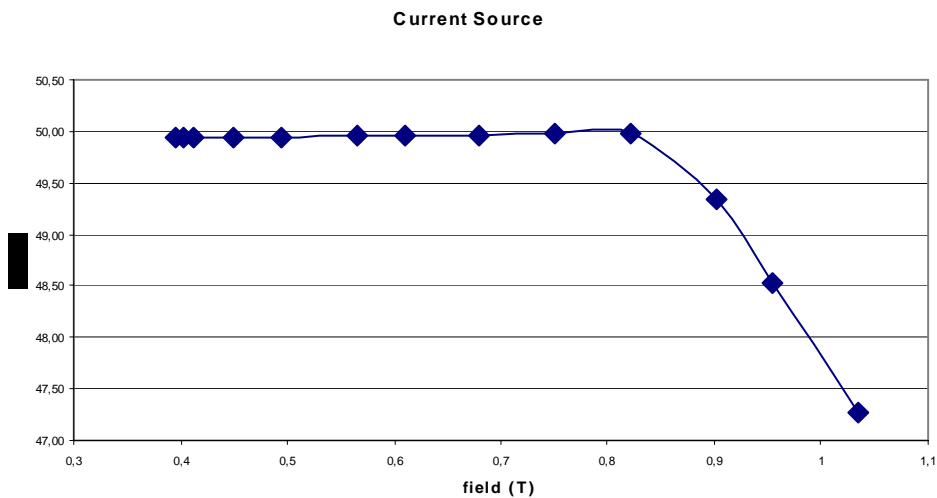


**Figure V-18: current source VS field.**

The misalignment angle of each Hall plate is evaluated by comparing the transfer function of the Hall plate aligned to the gravity with the one obtained with the same

Hall plate in the real mounting angle: as an example, the lateral Hall plates on the b3 rings are placed at a  $120^\circ$  angle with respect to the top Hall plate; if perfectly mounted, they have to measure half the main field when the correspondent top Hall plate is aligned to the gravity.

Possible differences are due to misalignment in the Hall plates mounting.

The performed measurement showed that this error is negligible with respect to the Hall plates non linearity.

### **V.2.2.3 - Discussions**

By the analogic bucking cards, the main dipolar field can not be compensated at 100 ppm, mainly owing to the Hall plates non-linearity (not better than 0.2 %) and to the instability of the compensation cards over the measurement time.

The b3 and b5 measurement will be affected by the following errors:

- an offset error due to a residual constant voltage in the compensation circuits or at the Hall plates drift;
- an error component proportional to the main field B1 due to the a residual uncompensated main field;
- an error component depending on the main field square caused by the Hall plates non linearity and the other errors of higher order.

The calibration procedure for correcting these errors is shown in the following section.

The measurement uncertainty can be assumed equal to 0.1 units as a result of the compensation boards offset instability over the measurement time.

The stability tests on the compensation boards showed no good stability at long term that implies frequent compensation cards calibrations. At the same time the analysis carried out have given inputs for improved analog cards (described afterwards):

- the offset regulation circuits of the amplifiers have to be independent from the supply voltage;
- the tuning trimmer has to be characterized by high temperature stability (0.1 ppm/ $^\circ\text{C}$ );

- chopped amplifier assures a lower offset drift (up to  $0.01 \mu\text{V } ^\circ\text{C}^{-1}$ ).

### V.2.3 - The off-line calibration

According to the results of the measurement system characterization, the signals acquired by the outputs of the compensation cards are processed by the following calibration formula:

$$b_n = \frac{K_n (V_n - V_{\text{offset}} - K_{\text{bucking}} B_1 - K_{\text{non-linear}} B_1^2)}{B_1} 10^4 \quad (\text{Eq. V-3})$$

where:

- $b_n$  is the normalized field harmonic of order n (sextupole for  $n=3$  or decapole for  $n=5$ );
- $V_n$  is the average voltage signal from the ring sensors; in particular, for b3 measurements the average of the 6 rings output is performed whilst for the b5 the signal average is evaluated on only two rings. As seen in chapter II, the six b3 rings are equi-spaced over the wavelength of the cable twist pitch and the two b5 rings are spaced by half a pattern wavelength approximately. They give information on the local variation of the field harmonic along a periodic field pattern. This variation is sinusoidal [2], the average computed over time on 6 (for b3) or 2 (for b5) points of this sinusoid represents respectively the b3 and b5 harmonics value as function of the time;
- $B_1$  is the dipole field;
- $V_{\text{offset}}$  is the residual electronic offset from the amplifiers;
- $K_n$  is the calibration factor for the voltage of the  $n^{\text{th}}$  plate sensor read-out (it depends on the Hall plates sensitivity factor and the gain set on the boards);
- $K_{\text{bucking}}$  is the dipole voltage bucking ratio;
- $K_{\text{non-linear}}$  is a second order correction for the Hall probes non linear sensitivity as a function of field.

The parameters  $V_{offset}$ ,  $K_{bucking}$ ,  $K_{non-linear}$  and  $K_n$  are obtained by an unconstrained optimization procedure aimed at minimizing the root mean square of the difference between Hall-plates reading and rotating coils results. The measurement carried out by the rotating coils on the same magnet under test over a load-line is hence used as reference. In particular, as an example, the ramp down curve of the pre-cycle measured by the Hall probe is compared with the load line ramp down measured by the rotating coil (Fig. V-19). The ramp up of the standard LHC cycle above 800A (to avoid the snapback data) of the Hall plates is compared with the ramp up of the load-line using rotating coils.

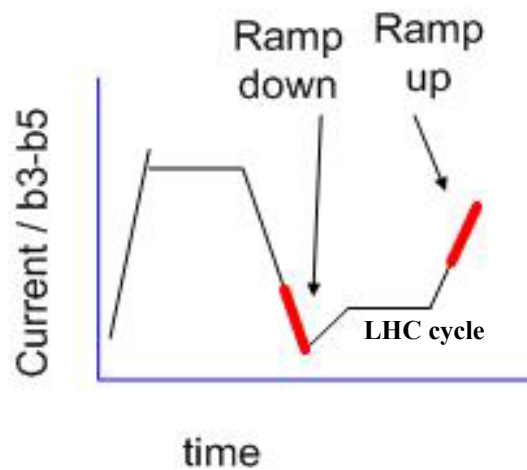


**Figure V-19: Indication of the rotating coils measurement data considered to calibrate the Hall probe measurement**

The rotating coils are used as reference because, in stationary measurements (on the loadline), guarantee a measurement accuracy of 0.01 unit on the b3 and b5 harmonics [3]. By considering in the calibration procedure a comparison between measurement data

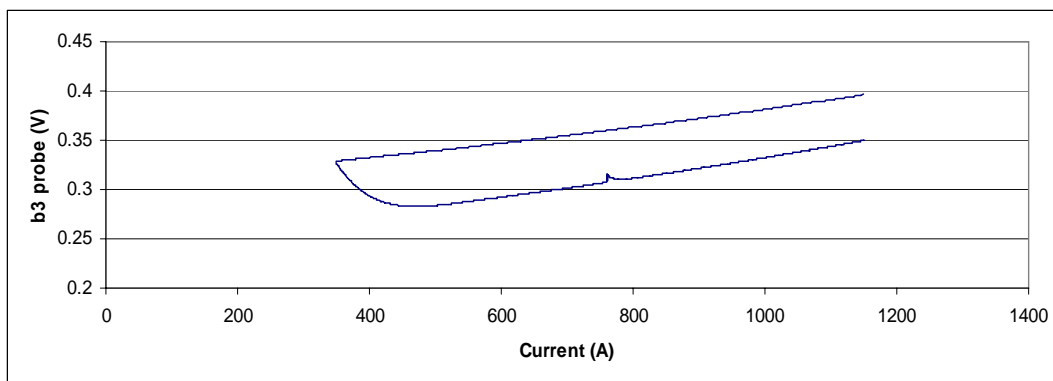


**Figure V-20:  $b_3$  hysteresis curve measured with the Hall probe with out calibration.**

before (Pre-cycle ramp down) and after the decay and snapback (the instrument measurement target) an offset or gain variation of the compensation cards during the measurement time (2000 s) is compensated.

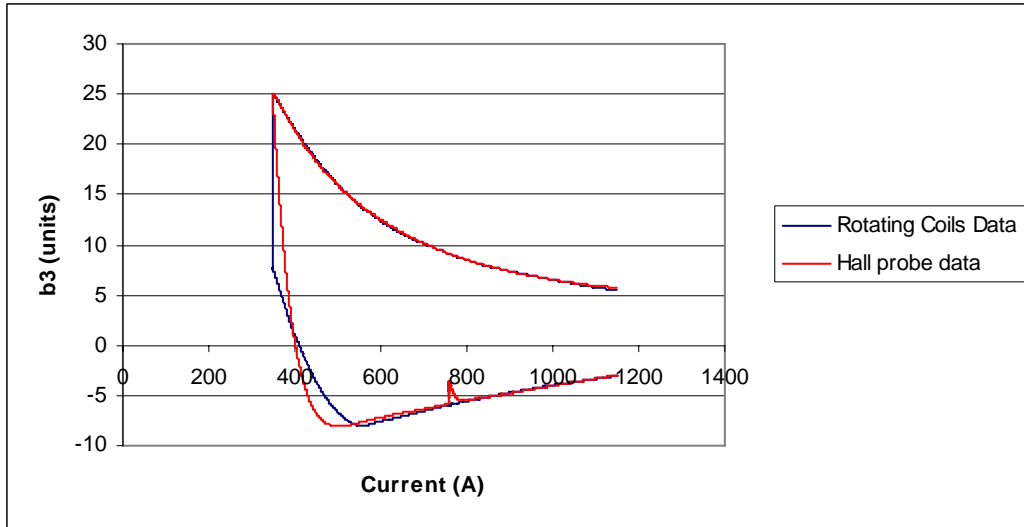


**Figure V-21: Rotating coils data (blue line) and Hall probe data (red line) after the calibration**

In Fig. V-20 and V-21, a measurement of a  $b_3$  hysteresis curve over an LHC cycle with 8 kA flat top carried out with the Hall probe is shown. In particular, Fig.V-20 shows the experimental data, whilst Fig V-21 shows the result of the calibration procedure.

#### V.2.4 - The software

The software aims at controlling the Snapback Analyzer system, and was completely developed in LabVIEW 6.1™.

The software can be decomposed in two main parts: the former devoted to the data acquisition (Appendix C), and the latter dedicated to the data calibration and data analysis.

Fig. V-22 shows the calibration and analysis software layout. The first step is the calibration; the software performs the average of the rings corresponding to the chosen field harmonic and extracts the current cycle data. The data of the measurement carried out by the rotating coils on the same magnet are loaded as well. A user interface permits to choose the ramp up and ramp down data to use in the calibration procedure. As seen,

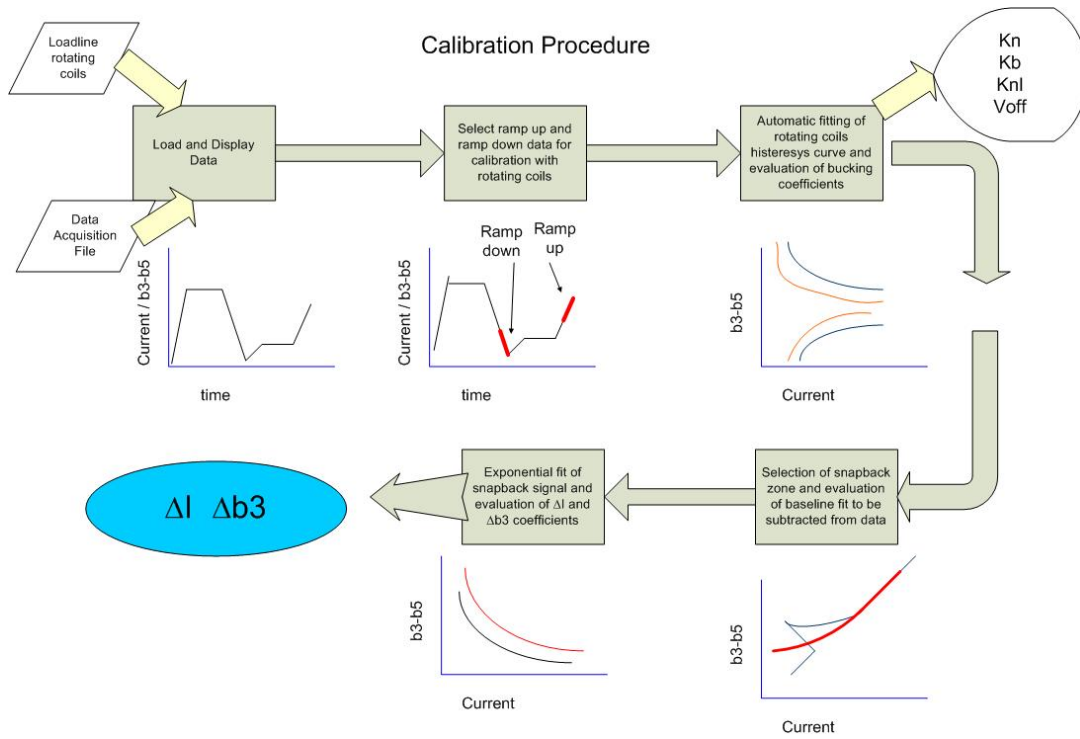


**Figure V-22: Calibration and data analysis software layout**

the choice is made considering values of current in the linearity range of the Hall plates and paying attention not to consider the snapback data. As a result of the calibration procedure, two curves are displayed (Fig. V-23): the rotating coils hysteresis curve and the one from the Hall plates converted with the Eq. V-3, using the four coefficients selectable in the bottom part of the panel. It is very difficult to converge especially because it has many solutions as well as local minima. Hence, the coefficient  $K_n$  is first approximated theoretically before trying to adjust all the other coefficients by using the following formulas:

$$K_3 = \frac{1}{3SG} \left( \frac{R_{ref}}{R} \right)^2 \quad \text{for } b_3 \text{ and} \quad \text{(Eq. V-4)}$$

$$K_5 = \frac{1}{5SG} \left( \frac{R_{ref}}{R} \right)^4 \quad \text{for } b_5 \quad \text{(Eq. V-5)}$$

where  $S$  is the sensitivity of the Hall plates ( $220 \times 10^{-3} \text{ mV T}^{-1}$ ),  $G$  is the amplifier gain (110),  $R_{\text{ref}}$  is the reference radius (17 mm) and  $R$  is the radius of the Hall plate rings (14.3 mm). The convergence of the minimization is favoured by the user by adjusting the calibration coefficients. Afterwards a script, that evaluates the minima for the square mean error depending from the 4 coefficients, is run in order to find the right values. The user panel shown in Fig.V-24 permits to select in all the calibrated hysteresis curve only the zone of interest (just before the injection plateau, when the decay is not yet started, until around 1150 A, or more exactly, until Hall plates still have a linear behaviour).

The measurement target is only the snapback phenomenon, therefore snapback data have to be isolated from *base-line* contribution, namely the value that the harmonic is supposed to have in a current cycle without any rest at the injection plateau. This is done subtracting the original harmonic hysteresis curve from the measured sextupolar ( $n=3$ ) and decapolar ( $n=5$ ) harmonics:

$$b_n^{\text{Snap-back}} = b_n^{\text{measured}} - b_n^{\text{base-line}} \quad (\text{Eq. V-6})$$

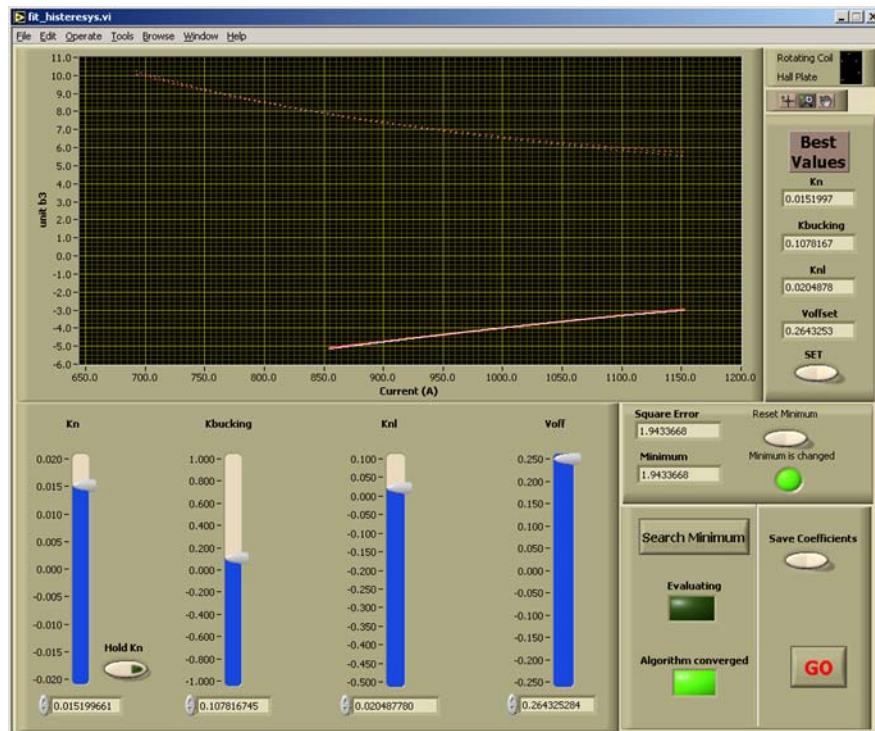
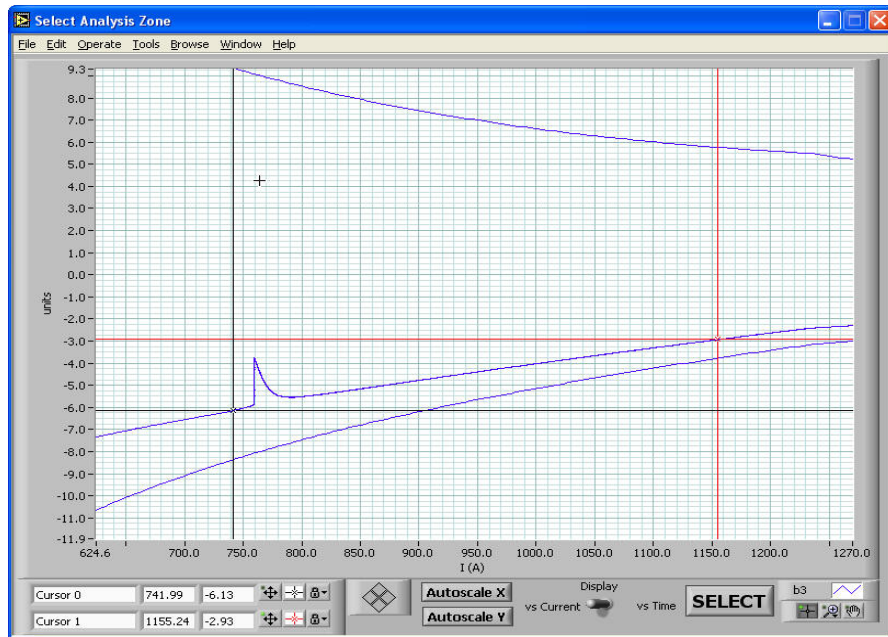


Figure V-23: hysteresis calibration panel

To this purpose, via a proper panel the base line data to fit are selected. Typically the zone ranges from 830 A to 1150 A, that is where the snapback phenomenon is ended and before going out from the probe measurement range. The fit algorithm can be chosen among different types: linear, 2<sup>nd</sup> order polynomial, 3<sup>rd</sup> order polynomial and a magnetization formula based on the analysis of the current in magnet strands [4], for which, to find the three parameters that characterize the fit formula, an automatic procedure to minimize the square mean error, as for the calibration procedure, was implemented.



**Figure V-24: Analysis zone selection panel**

Previously analysis of the snapback shape, to characterize in a mathematical form this phenomenon [5] showed that the snapback is modelled using a simple exponential form:

$$b_3^{snapback}(t) = \Delta b_3^{decay} e^{-\frac{I(t) - I_{injection}}{\Delta I}} \quad (\text{Eq. V-7})$$

Where  $b_3^{snapback}(t)$  is the sextupole change during the snapback,  $I(t)$  is the instantaneous value of the excitation current in the dipole magnet and  $I_{injection}$  is the

current injection value. The snapback initial amplitude due to the previous decay  $\Delta b_3^{decay}$  and the dipole current change  $\Delta I$  are the two fitting constants.

Therefore previously decay and snapback measurements proved that the exponential fitting parameters  $\Delta b_3$  and  $\Delta I$  related to measurements on different magnets are strongly dependent (are characterized by the same ratio) [6].

The final step of the analysis software is just the evaluation of the exponential fit on a snapback zone selected by the user. So that the instrument delivers the fit parameters  $\Delta b_n$  and  $\Delta I$ .

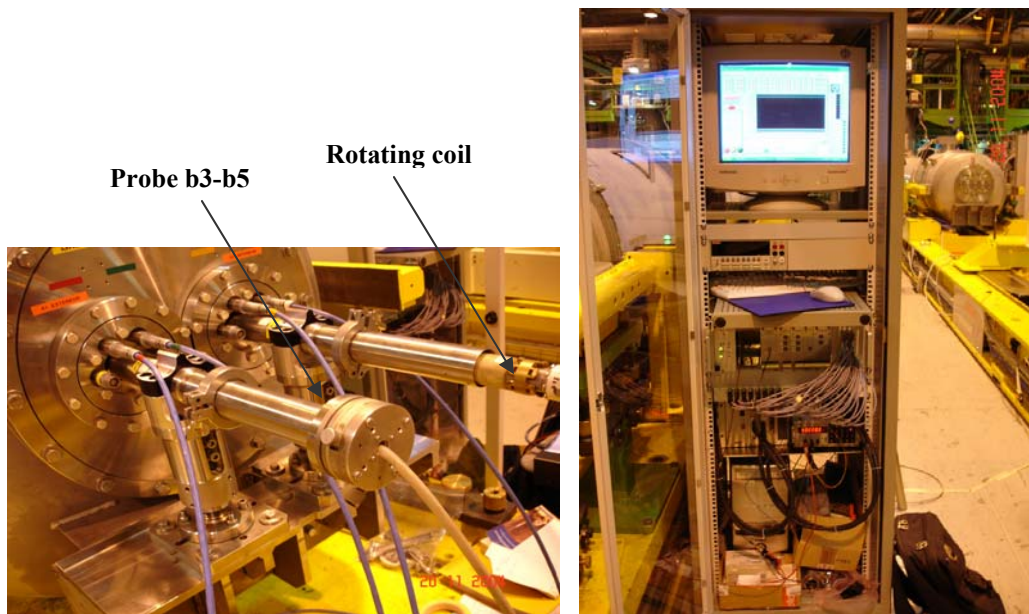


**Figure V-25: Probe installation in the dipole magnet and measurement rack.**

#### *V.2.5 - Measurements and results*

Cold measurements to test the Snapback Analyzer were performed on magnet 3164 and 2043 in SM18 facility [7]. Before starting the measurement with the Hall probe, a Load line cycle with rotating coils is performed in order to obtain the data necessary to reconstruct the field hysteresis cycle and, hence, to calibrate the probe after the measurement.

Test sequence includes different current cycles (different in the shape and in the maximum value) [8]. In fact the snapback parameters depend on the duration of the cycle and the maximum current [9].

Fig V-25 (left) shows details about the insertion of the measurement probe inside the magnetic bore and the alignment with the gravity. The b3-b5 probe is installed on the dipole left aperture on the right the rotating coil for the same measurement required for the calibration. The measurement equipment is showed on the right in the same figure.

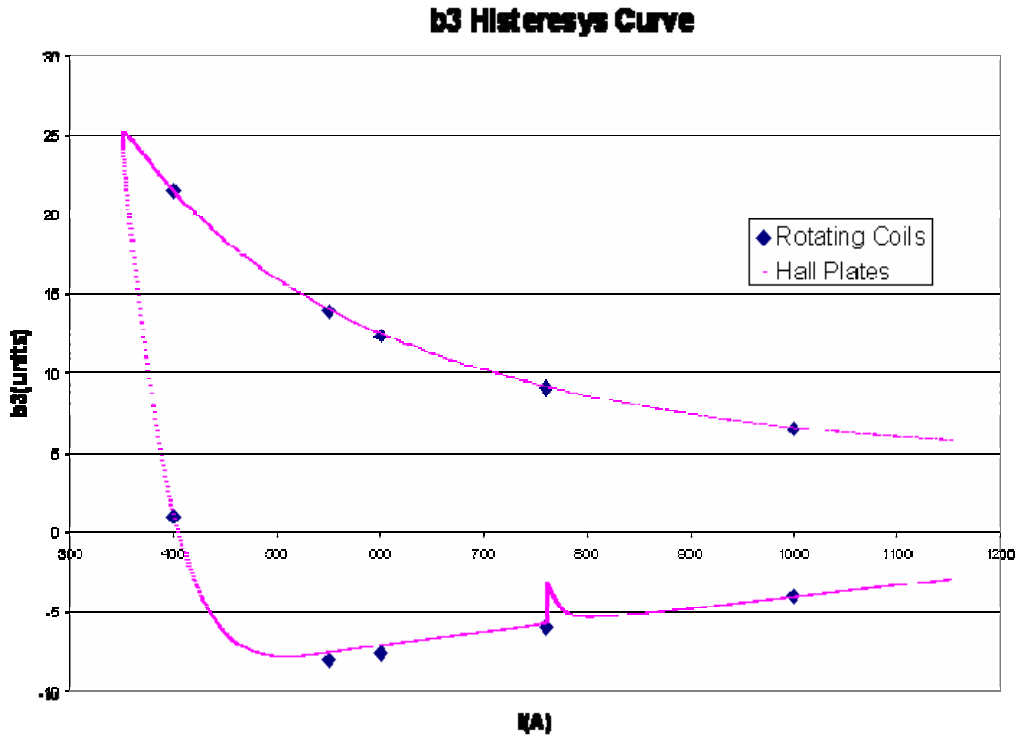


Figure V-26: comparison between rotating coils load line data (blue dots) and Hall probe data after calibration (purple line).

In Fig V-27 (top), the hysteresis curve calibration for the measurement on the LHC cycle performed on the magnet 3164 is shown.

In Fig.V-27 (bottom) a zoom on the only decay and snapback for the b3 measurement after calibration is shown. The time resolution is matched to the specification 0.1 s (10 points/s).

### b3 decay and snapback

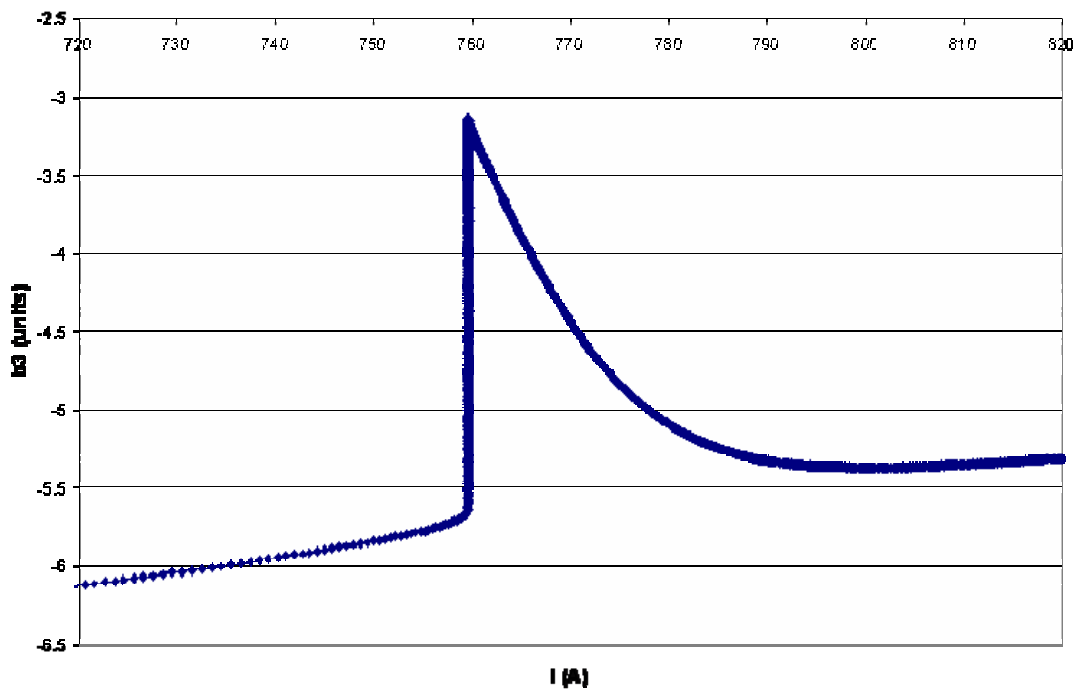
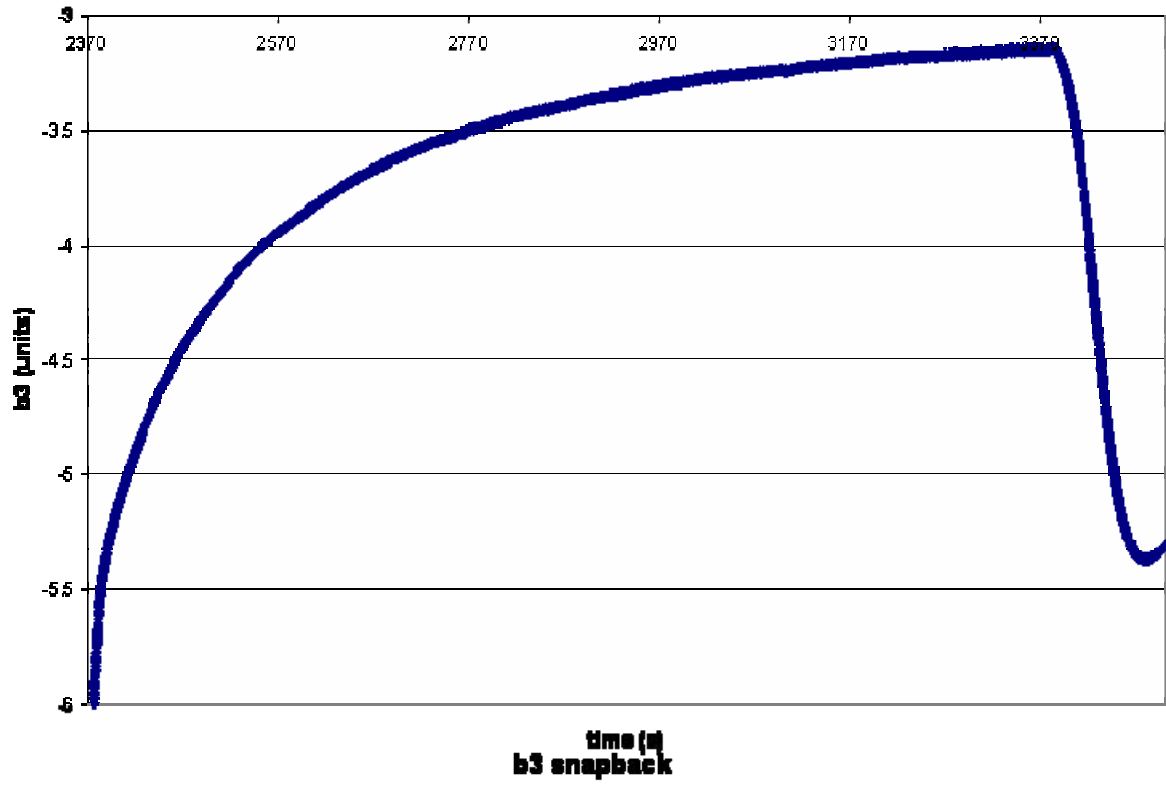
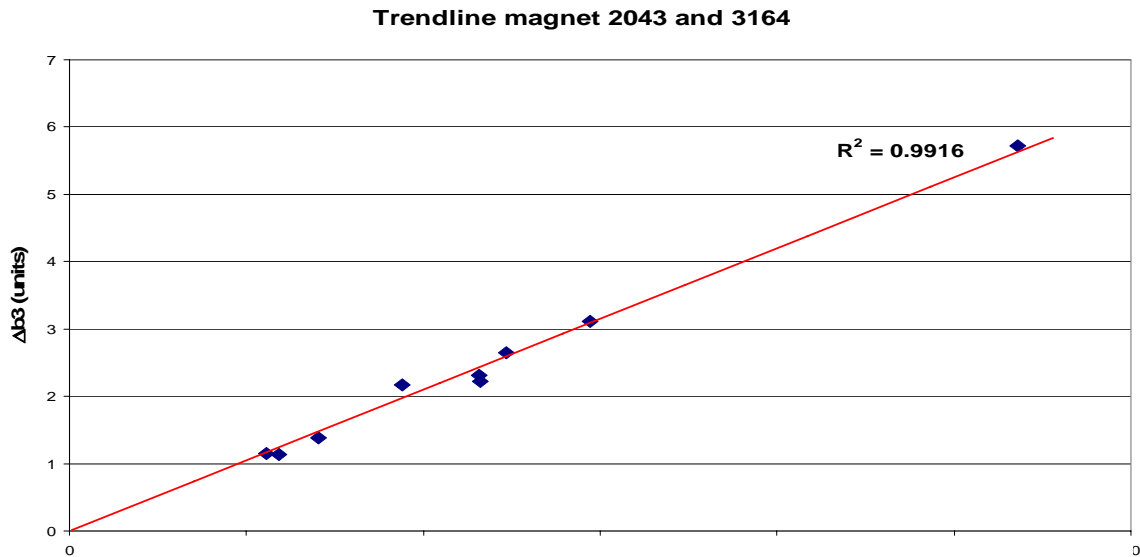


Figure V-27: Decay and Snapback of  $b_3$  (units) respect to time for Standard LHC cycle in magnet 3164.

the snapback parameters independently from the magnets under test, the good correlation in all the measurements carried out with the Snapback Analyzer on different current cycle and on the two magnets.



**Figure V-28: scatter plot for  $\Delta I$  vs  $\Delta b3$  for data obtained in measurement with magnets 3164 and 2043.**

#### V.2.6 - The new analogic bucking cards

The stability tests on the compensation cards showed a critical output offset variation, even on the short term, representing one of the main uncertainty sources of the analog bucking approach.

Accurate investigations suggested improvements to the old design in order to achieve a better stability even at long term.

The keywords of the new release can be summarized:

- use of chopped amplifiers (e.g. LT1150) in any stage characterized by very low offset drift (10 nV/°C) and small low-frequency noise. While these amplifiers achieved very low offset, low offset drift, and very high gain, they had limited bandwidth and required filtering to remove the large ripple voltages generated by chopping. Chopper stabilized amplifiers solved the bandwidth limitations by combining the chopper amplifier with a conventional wideband amplifier that remained in the signal path [10];

- all the resistors used as well as the regulation trimmer are characterized by high stability factor ( $1 \text{ ppm } ^\circ\text{C}^{-1}$ );
- all the circuits are closed in a metallic box kept at constant temperature ( $20 \text{ }^\circ\text{C}$ ) by means of warming up resistors supplied with a PWM current generator. The metallic box behaves even as shield against the EMC perturbations;
- the offset regulation of each input stage offset is performed using a dedicated voltage reference;
- all the offset and gain settings as well as the measurement points are placed on the front-end electronic rack for an easy calibration (Fig.V-29). This thanks particular attention devoted to the engineering process.

Fig. V-29 shows the electronic schematic of the new compensation card. The last amplifier stage has been eliminated, now on the mixer is possible to set the gain using a precision trimmer.

Tests carried out on this new board showed an excellent stability on the short term both for the gain and for the output offset. These parameters are now much more immune to the temperature variations thanks to the thermostatic boxes.

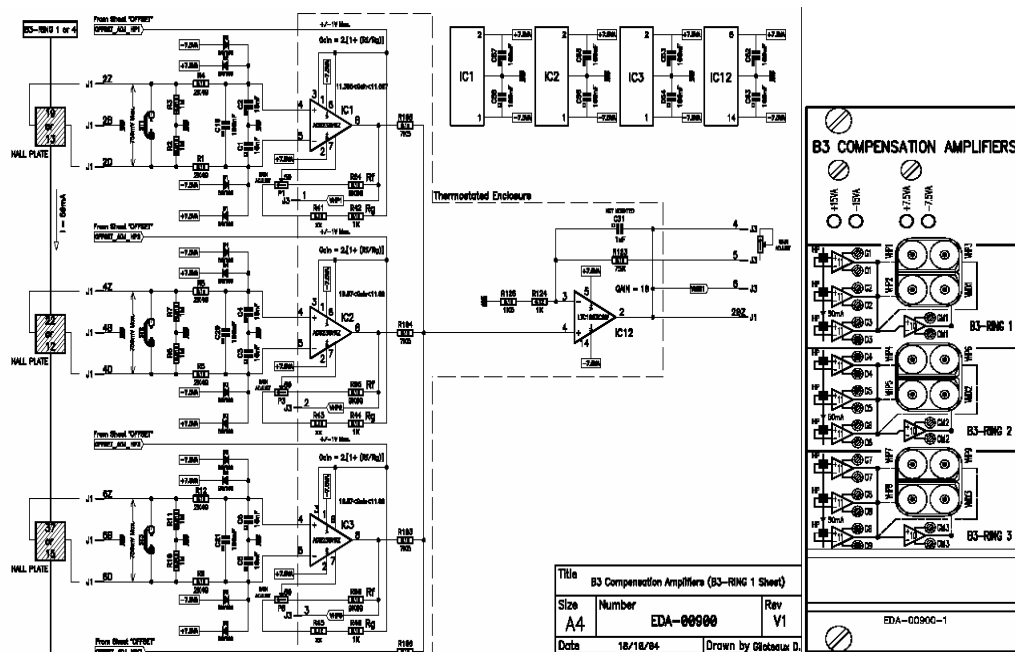


Figure V-29: Circuit layout of the new b3 compensation card and front panel.

### V.3 - The solution based on digital bucking

One of the main limitations of analogic bucking is the compensation for only first-order Hall plates nonlinearity producing a residual dipolar component even perfectly stable bucking cards.

In the following, a digital bucking approach is presented. The basic idea is to perform in real time the digital sum of the voltage samples from each Hall plate belonging to the same ring. In this case, by using the transfer function of each Hall plate, non linearity errors were compensated in real time. In order to reach the required resolution and to reduce the noise overlapped on the signal decimation with a high decimation factor was applied.

#### V.3.1 - The working principle

The working principle of digital bucking is depicted in Fig. V-30. The signals coming from the same ring are amplified and sampled. In order to recover the b5 harmonic with a resolution at least of 0.1 unit by the digital sum, the conversion process

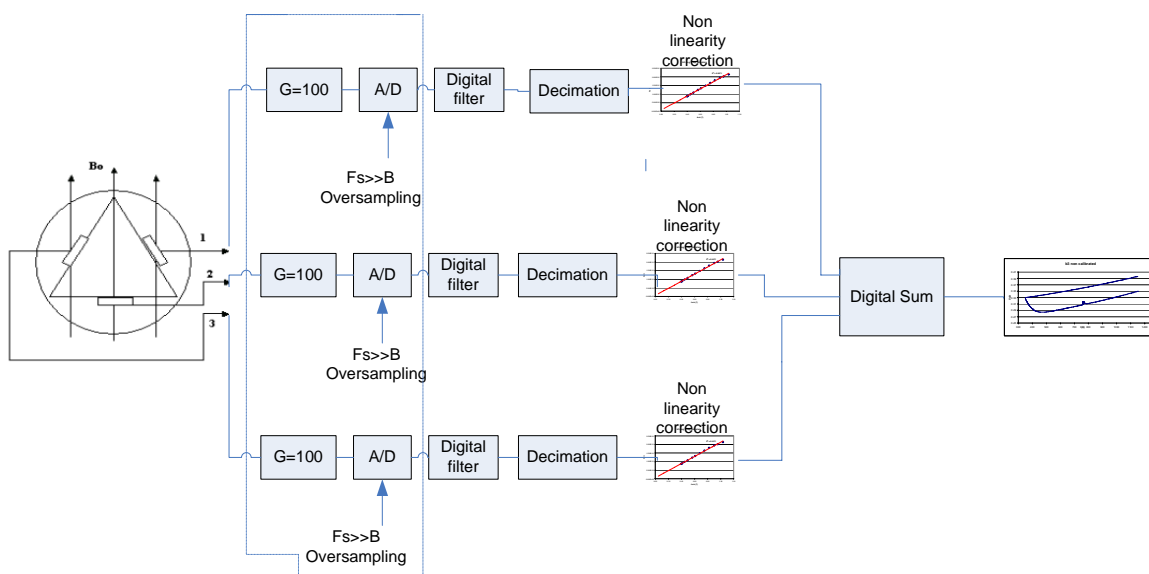


Figure V-30: digital bucking working principle.

should be able to resolve the input voltage at  $10^{-5}$ : in fact, 100 mV is the Hall plate voltage (on the top) due to the injection dipolar field, 0.1 unit field correspond to 1  $\mu$ V on the Hall plate voltage.

The AD converter should have at least 18 bits of resolution. In order to increase the conversion resolution, as well as to reduce the signal noise, a big over-sampling factor and a suitable digital filtering have to be used. In this application the signals to acquire are characterized by a very-slow temporal variation (the snapback phenomena behaves as a variation of some tenths of  $\mu$ V on 60 s time), namely a bandwidth of some Hz. After filtering, the samples array is decimated in order to obtain the required sampling frequency of 10 points/s. Using the transfer function of each Hall plate, the voltage samples are translated into the real field component normal to the Hall plate. By a 18-bit AD converter and about 20 points in all the Hall plate measurement range ( $0.3 \div 1$  T), the non linearity errors can be corrected within 100 ppm. The digital sum of the field samples vectors for each ring will deliver the corresponding  $b_3$ ,  $b_5$  harmonics over the time.

The oversampling and the consequent digital filtering is a technique largely used in the sigma delta modulator to increase the conversion resolution [11].

According to the Nyquist criterion, the sampling frequency must be at least twice the bandwidth of the input signal. Fig. V-31 shows the power density spectrum of a pure sinusoidal tone sampled at  $F_s$  sampling frequency. With an ideal AD converter the noise floor in the spectrum is due only to the quantization noise and uniformly spread on the band  $[0, F_s/2]$ .

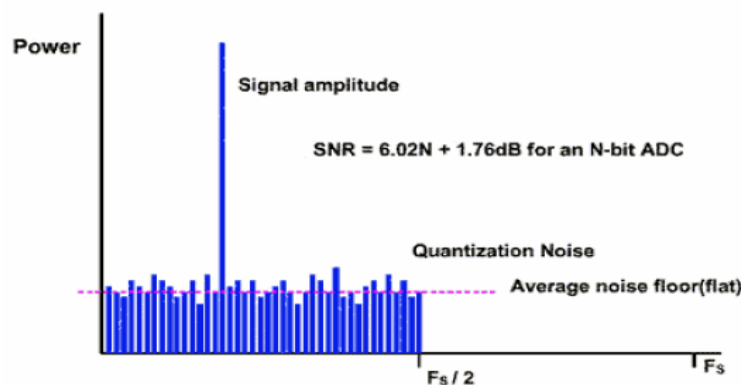
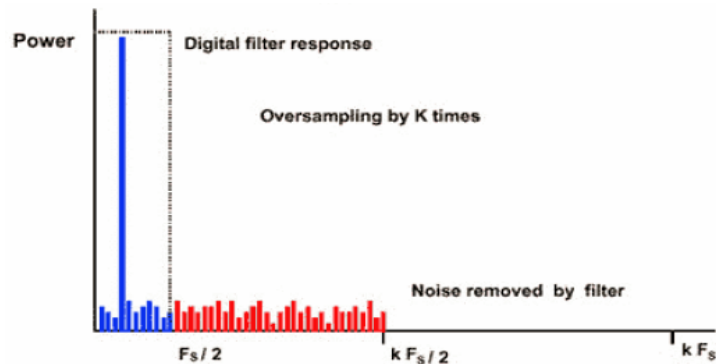


Figure V-31: Power spectrum of a pure sinusoidal tone, sampled at  $F_s$  sampling frequency

The effective number of bit (ENOB) of the ADC converter is estimated through the Signal to Noise Ratio (SNR) evaluation [12]:

$$\text{SNR} = 6.02 N + 1.76 \text{dB} \quad (\text{Eq. V-8})$$

where N is the ENOB and SNR is expressed in db.



**Figure V-32: Effect of the oversampling on the quantization noise**

If the same signal is acquired with a sampling frequency increased by an oversampling factor  $k$ , the SNR remains the same, but the noise energy is spread over a wider frequency range (Fig. V-32).

Hence, by filtering the oversampled signal through an ideal filter with  $F_s/2$  cut-off frequency, the SNR is increased. It is easy to show that for each factor 4 in the oversampling, the SNR is increased of 6 dB. The improvement in terms of effective number of bits is given by:

$$\Delta n = 0.5 \ln(k) \quad (\text{Eq. V-9})$$

Finally, a decimation of a factor  $K$  reestablishes the original time resolution. The overall process is summarized in Fig. V-34.

In this application, since 10 Hz is the signal bandwidth to acquire using a 18-bit ADC, with an oversampling factor 1500 (15 kS/s sampling frequency), a theoretical improvement of 3.5 bits is reachable.

Obviously this has to be considered as an upper limit because:

- the realizable digital filter can only approximate the rectangular frequency response;

- the ADC is supposed to be characterized only by quantization noise, instead, non linearity errors arise actually (INL, DNL, missing codes);
- potential noise overlapped on the signal reduces the conversion resolution.

One of the simplest numerical filters to implement is the moving average filter. Fig. V-33 shows the frequency response of the moving average filter as function of the filter length.

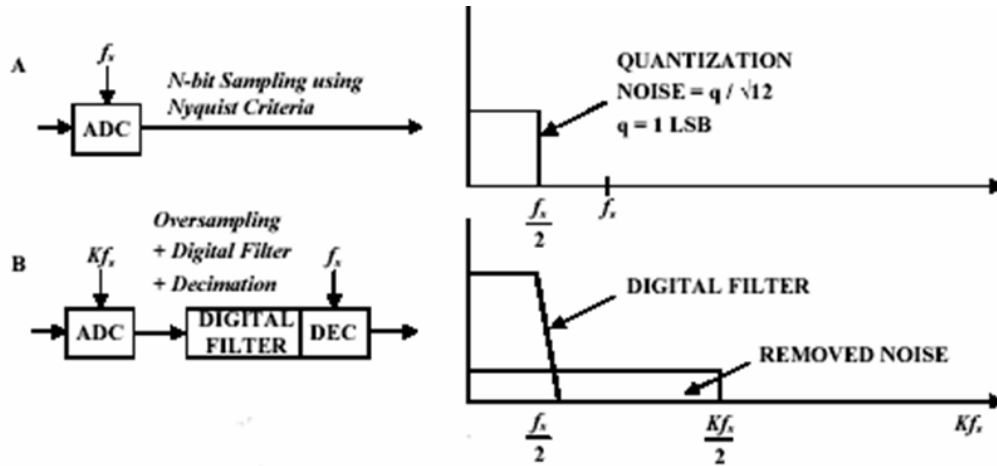


Figure V-34: Summary of the oversampling technique.

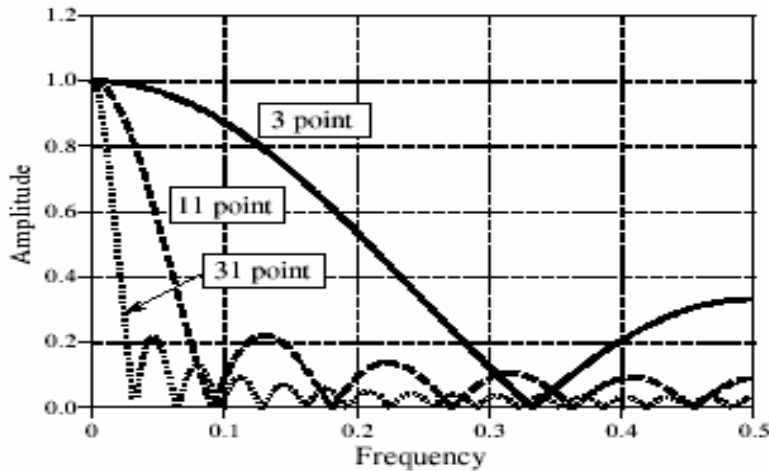


Figure V-33: Frequency response of the moving average filter

The moving average is a very poor low-pass filter, due to its slow roll-off and poor stopband attenuation, but, on the other side, is an exceptionally good smoothing filter (action in time domain).

The frequency response has the following expression:

$$H[f] = \frac{\sin(\pi f M)}{M \sin(\pi f)} \quad (\text{Eq. V-10})$$

The first zero of the frequency response is located at  $1/M$  where  $M$  is the filter length.

At 15 kS/s frequency sampling, to have the first zero at 10 Hz a filter length of 1500 samples has to be considered.

From an implementation point of view, performing the moving average filtering and then decimate for the factor  $k$  is perfectly equivalent to apply decimation with an average every  $k$  samples.

Better results can be obtained by designing a proper FIR filter (Fig. V-35). Fig. V-36, V-37 and V-38 show that on a simulated constant signal with overlapped a  $30 \mu\text{V}$  standard deviation white noise a moving average filter at 1500 samples guarantees a good trade-off between noise reduction and computation complexity (the FIR filter designed has a length of 4500 samples). A moving average filter of 4500 length behaves better than the FIR filter designed ad hoc.

The signals to acquire are at very low frequency thus the ADC converter works almost in static conditions: so the non linearity can be considered as negligible. Nevertheless, particular attention has to be paid to cabling in order to reduce all the noise sources as much as possible.

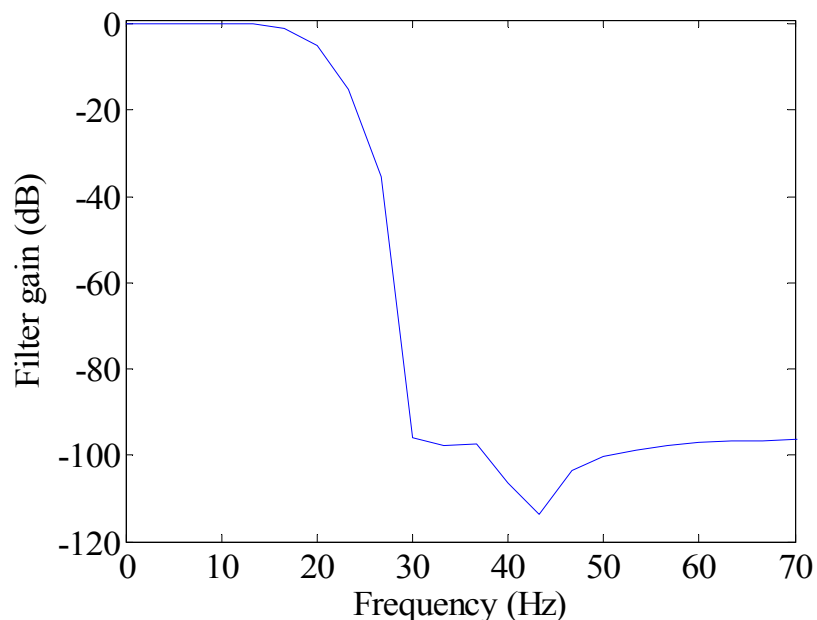


**Figure V-35: Frequency response of a FIR filter at 45 coefficients designed ad hoc.**

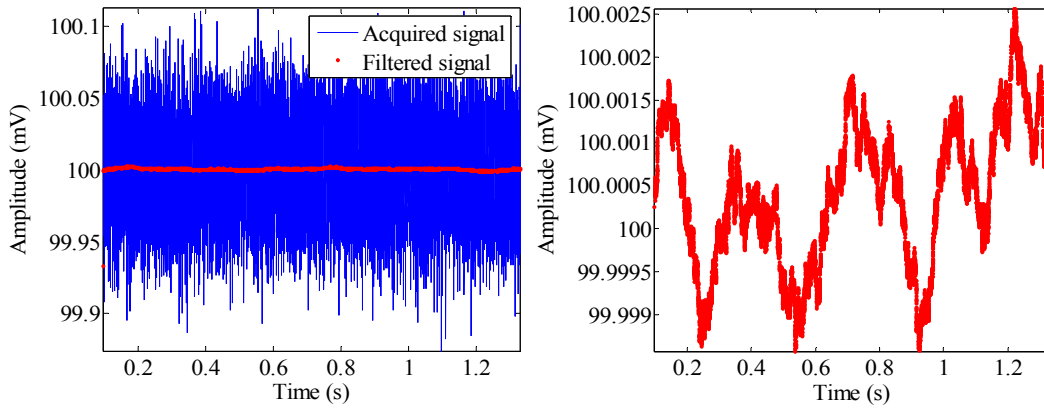


**Figure V-36: Signal filtered with a 1500 samples moving average filter**

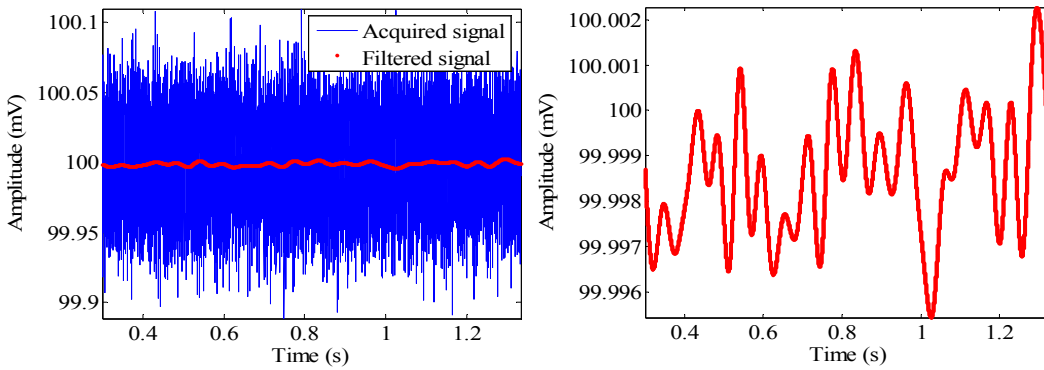


**Figure V-37: Signal filtered with a 4500 samples FIR filter**

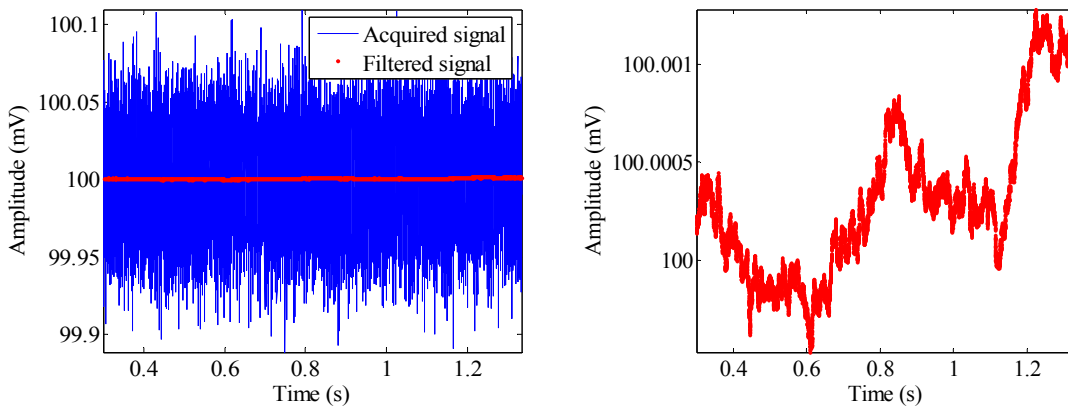


**Figure V-38: Signal filtered with a 4500 samples moving average filter**

### V.3.2 - The proof demonstration

A proof demonstration of the proposed digital bucking was carried out with the 16 bit DAQ system of the snapback analyzer. The Hall plates signals were sampled at 2 kS/s.

On this data, a moving average filter with a decimation of a factor 200 was applied. The voltage samples of each Hall plate are corrected by using the corresponding

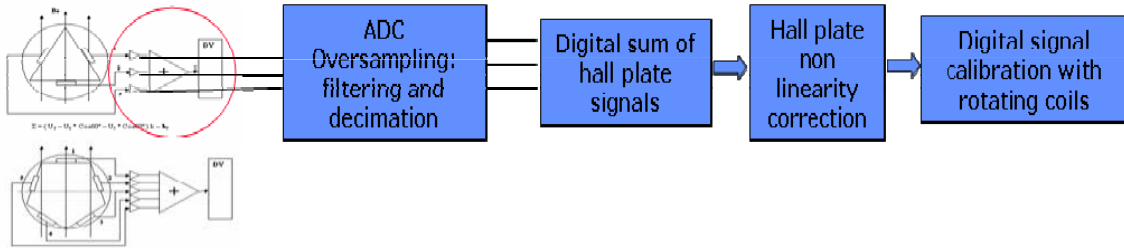


**Figure V-39: Digital bucking layout implemented on the DAQ system 16 bit**

calibration curve, and, subsequently, the digital sum is performed on the channels of the same rings (Fig. V-39).

In Fig. V-40 the b3 snapback curve obtained by applying the off-line calibration both to the digital and analog bucked signal is showed. On the signal corrected by the digital bucking the snapback is clear although the noise overlapped in not negligible. This is mainly quantization noise due to the limited system resolution.

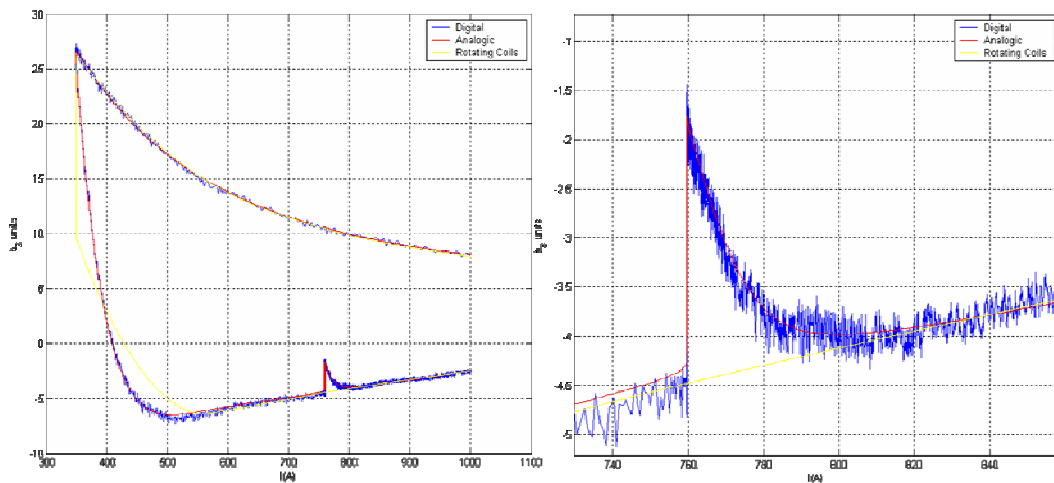


**Figure V-40: Digital bucking after off-line calibration (blue line), comparison with the analog signal (red line).**

### *V.3.3 - The hardware proposed for the digital bucking*

A platform PXI RT equipped with two DAQ cards NI6289 based on an SAR 18-bit ADC multiplexed on 16 differential input channels, analogous as the one used for the integrator proof demonstrator described in the chapter III, was chosen to implement the digital bucking approach.

In multiplexed mode, by taking into account the number of signals to acquire, the maximum frequency sampling selectable is 15 kS/s, assuring an over-sampling factor of 1500. The interchannel delay is negligible, because the signals to acquire are at very low frequency.

The input gain is set to have  $\pm 200$  mV input range (on the injection plateau the top Hall plate have 110 mV output) at which corresponds 1.2  $\mu$ V of LSB.

On the DAQ cards used an automatic calibration procedure is implemented in order to assure over 2 years an absolute accuracy of  $\pm 30$   $\mu$ V on the conversion in the range  $\pm 200$  mV, evaluated taking into consideration:

- the residual PGA gain error;
- the PGA gain stability;
- the residual offset error;
- the ADC INL (integral non linearity) error;
- the random noise on the signal to acquire;
- a variation of 2 degrees with respect to the temperature at which the card auto-calibration was performed.

### *V.3.4 - Digital bucking tests on the new DAQ cards*

Particular tests for the input sensitivity, as well as the analog front end stability, were carried out on the DAQ cards chosen to implement the digital bucking. The experimental setup is shown in Fig. V-41. A voltage calibrator generates a stable 100 mV reference in order to simulate the top Hall plate output on the injection plateau. Particular attention was devoted to the connection on the DAQ card: shielded twisted pair cable, differential input channel, and shielded terminal box were used.

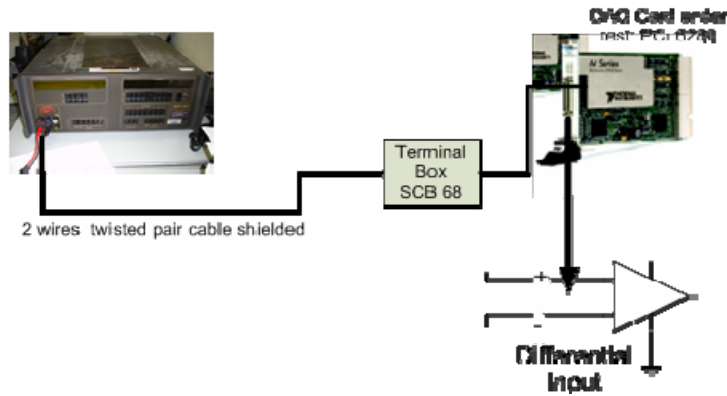


**Figure V-41: Experimental setup for the testing of the 18 bit DAQ cards**

Acquisition of the reference signal at 15 kS/s sampling frequency over 60 s shows a noise of 30  $\mu\text{V}$  standard deviation (Fig. V-42, left). This can represent the main limitation to the conversion sensitivity since with the probe long cable a noise even higher is expected. Many digital filters on the signal acquired were tested in order to reduce the noise to the only quantization noise. Excellent result was obtained using the 1 pole anti-aliasing filter (40 kHz cutoff frequency) on the board and 1500 oversampling factor with consequent decimation and averaging.

As expected, the noise on the signal is reduced by the factor  $\sqrt{k}$ , where  $k$  is the number of samples on which the average is performed (just the oversampling factor in this case).

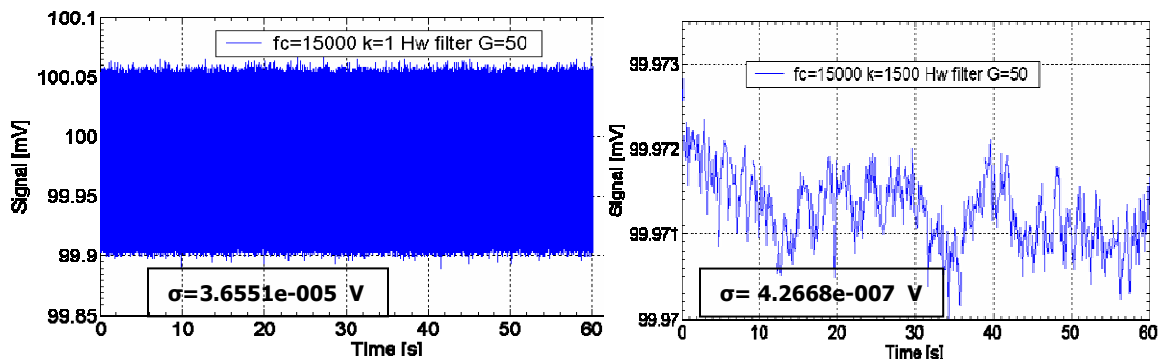


**Figure V-42: The reference signal acquired without filtering (left). The same signal acquired with 1500 over-sampling factor (right).**

As further validation of the oversampling technique, signals very close to the actual measurement target were generated; in particular, the 100 mV reference voltage was increased of  $1\mu\text{V}$  and  $3\mu\text{V}$  steps every 5 s respectively. Fig. V-43 shows the results of the

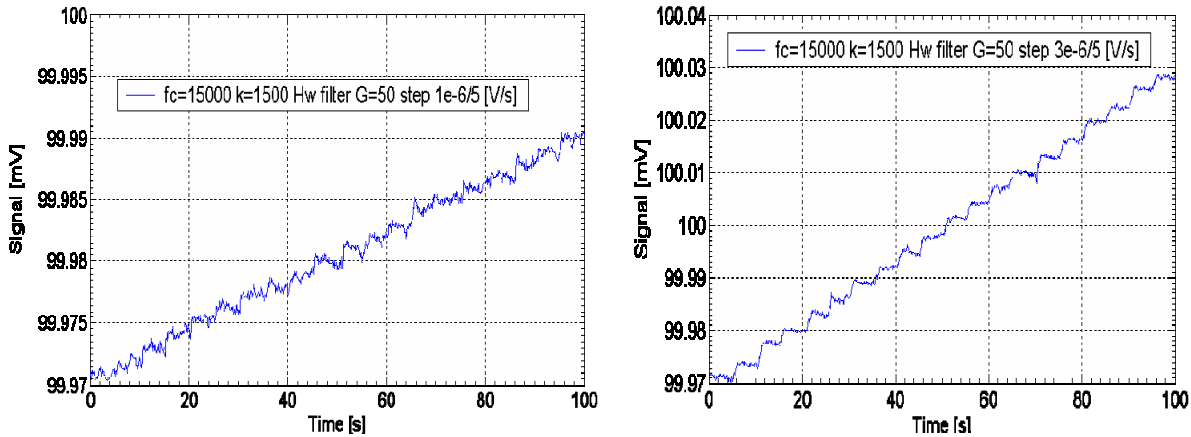


**Figure V-43:** On the left the reference voltage is increased of  $1\mu\text{V}$  every 5s (0.1 b3 unit) whilst on the right of  $3\mu\text{V}$  (0.3 unit of b3).

oversampling earlier detailed on the two signals acquired. Thanks to the noise reduction, the trend imposed appears clear. The acquisition sensitivity was, hence, improved in order to appreciate 0.1 unit of b5 variation on the injection plateau on each Hall plate.

Finally, Fig. V-44 shows the results of the stability tests carried out on the DAQ board.

On the left, the 100 mV reference voltage acquired over 15000 s, is shown. A small drift of few  $\mu\text{V}$  is highlighted; this is due to the voltage generator and not to the instability of

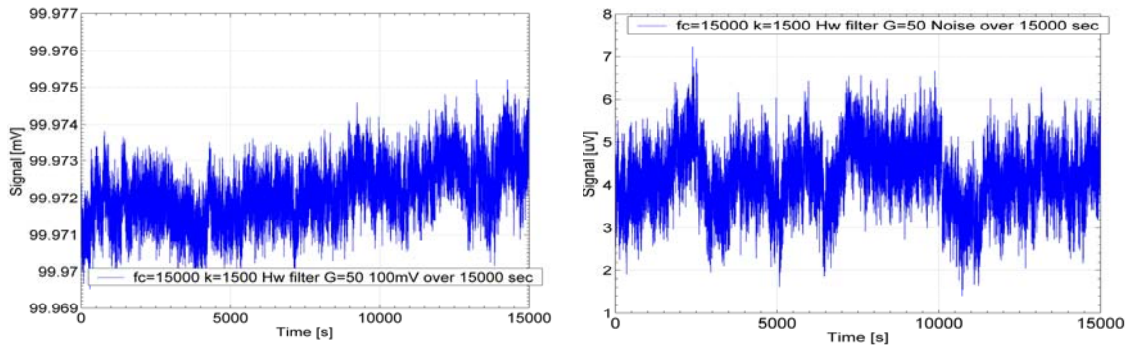


**Figure V-44:** Acquisitions 15000 s long with 1500 over-sampling factor of the 100 mV reference voltage on the left and with the input in short circuit on the right

the DAQ analog front-end. In fact, by connecting the DAQ input in short circuit, (Fig. V-45 on the right), an offset of about 4  $\mu\text{V}$  is evident, and no drift is appreciable.

### V.3.5 - The software developed: architecture overview

A new software for the platform PXI RT was developed in LabView™ RT 7.1 in order to implement the digital bucking approach.

In Fig.V-45, the software architecture is depicted. The main difference with the Snapback Analyzer software, is in the acquisition tasks. Data treatment and correction are performed in RT on the PXI target. On this machine the Snapback Analyzer Graphical

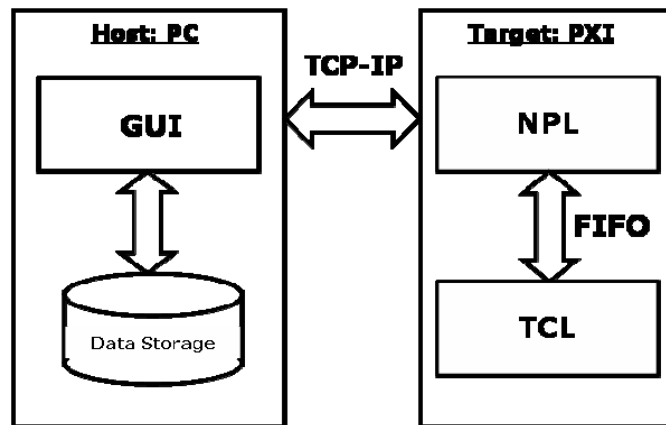


Figure V-45: Digital bucking software architecture.

User Interface runs by achieving the duties of data storage, acquisition parameters setting, data and alarms monitoring, as well as the off-line calibration and analysis.

In particular, on the target machine, two main processes at different priority run.

In the Highest priority process (TCL), the following tasks are carried out:

- Data Acquisition (both the signals coming from each Hall plate and from the output of the compensation cards). The sampling frequency is fixed at 15 kS/s so to assure a 1500 over-sampling factor;
- filtering and decimation to increase the acquisition resolution;
- Hall plate non linearity correction;
- Digital Sum of the Hall plates signal from the same ring;

- Data Integrity Check.

The normal priority process manages the TCP-IP communication with the Host PC, send the data and receive the instrument configuration.

The data transfer between the two processes is carried out through a RT queue.

### *V.3.6 - Conclusions*

A robust instrument to measure and characterize the decay and the snapback phenomena for the b3 and b5 field harmonics was developed implementing both the analog and the digital bucking approach.

In particular, by following a detailed metrological characterization of the measurement probe originally developed at CERN, an automatic calibration procedure was developed in the instrument software in order to compensate the non linearity errors of the Hall plates as well as the analog bucking limitations. This assured measurement repeatability, even if the originally analog compensation cards were affected by stability problems. Measurements carried out on the LHC dipoles proved the robustness of this solution.

At the same time, the innovative digital bucking approach was deeply examined as alternative solution to the compensation in RT of the Hall plates non linearity, as well as the stability of the analog compensation front-end. Preliminary experimental results demonstrated the validity and the feasibility of this approach.

Finally, this approach was implemented on a RT platform by using new 18-bit SAR DAQ cards. Nevertheless, the acquisition resolution was increased thanks to oversampling and suitable digital filtering.

The final result was an instrument where both the techniques were implemented to have measurements cross-check, as well as a instrument self-calibration. In this way, even if automatic, the calibrations using the rotating coils data at each measurement can be avoided.

## V.4 - References

- [1] E. Benedico, “*A fast sextupole and decapole probe for chromaticity corrections*”, Graduation Report, Universitat Politecnica de Catalunya, Spain, April 2002.
- [2] H. Bruck, et al., “*Observation of a periodic field pattern in the persistent-current fields of the superconducting HERA magnets*”, proceedings IEEE Particle Accelerator Conference, 2149-51, San Francisco, USA, 1991.
- [3] L. Walckiers, L. Bottura, M. Buzio, P. Schnizer and N. Smirnov, “*Sensitivity and accuracy of the systems for the magnetic measurements of the LHC magnets at CERN*”, Seventh European Particle Accelerator Conference (EPAC 2000) 26-30 June 2000, Vienna, Austria.
- [4] Formula di magnetizzazione per la baseline.
- [5] T. Pieloni, et al. “*Field decay and snapback measurements using a fast Hall probe sensor*”, IEEE Trans. Appl. Supercond. 14, no.2, 1822-25, 2003.
- [6] L. Bottura, T. Pieloni, S. Sanfilippo, G. Ambrosio, P. Bauer, M. Haverkamp, “*A Scaling Law for Predicting Snap-back in Superconducting Accelerator Magnets*”, 9th European Particle Accelerator Conference (EPAC'04) 5-9 July 2004, Lucerne, Switzerland.
- [7] J.C. Brunet, “*Installation finale des cryo-aimants in situ dans le tunnel ou le SM 18*”, CERN LHC Project Note 64.
- [8] L. Bottura, G. Greco, A. Masi, N. Sammut, “*Snapback Measurements of HCLBBL\_000-IN003164 Dipole Using a Fast Hall Probe Sensor*”, LHC internal note, EDMS no: 555301.
- [9] N. Sammut, L. Bottura, “*Decay and Snapback observed in the Allowe Multipoles of the Latest Dipole Magnets*”, CERN 2004-04-26 EDMS no: 461179.
- [10] <http://www.edacafe.com/books/phdThesis/Chapter-5.5.php>.
- [11] James C. Candy (Editor), Gabor C. Temes (Editor), “*Oversampling Delta-Sigma Data Converters : Theory, Design, and Simulation*”, September 1991, Wiley-IEEE Press.
- [12] IEEE standard 1241.

## **Chapter VI - THE POLARITY CHECKER**

### ***VI.1 - The measurement problem***

The LHC will include about 1750 cryomagnets, up to almost 16 m long, housing a total of about 10000 superconducting magnets, connected in 1612 electrical circuits [1]-[2]. Any construction mistake, leading to an incorrect multipole type or polarity, such as those due to busbar inversion, i.e. connection of a magnet to the wrong circuit, or mechanical installation errors, may seriously compromise the LHC operation and the machine hardware. This kind of errors must be detected by checking carefully all magnets and the instrument used to verify the magnet polarity must have an extremely low failure rate. This is not a trivial test because, in superconducting accelerator magnets, the field can be measured from the outside only via cold bore tubes having a diameter of the order of 50 mm.

It is remarked here that the harmonic coil systems routinely, used on all magnets, could provide the information about the field polarity. In practice, however, the number of parameters involved is so high (i.e. direction of coil rotation, sense of insertion into the magnet, polarity of dozens of cables and connectors, sign conventions used in various coefficients and subroutines within the analysis software) that the polarity information is not sufficiently reliable.

Verifications are carried out at room temperature during and/or at the end of the assembly stage, in order to identify and correct problems as early as possible. In some cases, such as for the corrector spool pieces in the main cryodipole, the polarity check must be deferred to the end of the cold tests, when all connections are finalized. To achieve this task, the probe must be able to measure reliably very low fields, ranging from a fraction of a mT for high-order correctors to a few mT for the main ring magnets. A summary of the magnets families and measurement conditions is shown in Tab. VI-I.

Magnet Type	T.F. [mT/A]	$I_{\max}$ [A]	$B_{\max}$ [mT]	Diode
Main Dipole (MB)	0.66	5.0	3.32	Y
B1 arc Orbit Corrector (MCBV/H)	52.70	0.1	2.64	
B1 IP Orbit Corrector (MCBXH/V)	6.09	2.4	14.62	
Main Quadrupole (MQ)	0.29	3.0	0.88	Y
Tuning Quadrupole (MQT)	0.10	3.0	0.31	
B3 Multipole Corrector (MCS)	0.05	3.0	0.15	Y
B3 Lattice Corrector (MS)	0.02	3.0	0.07	
B4 Multipole Corrector (MCO)	0.40	3.0	1.20	Y
B4 Lattice Corrector (MO)	0.56	1.0	0.56	
B5 Multipole Corrector (MCD)	0.18	3.0	0.55	Y
B6 MultipoleCorrector (MCTX)	0.13	0.5	0.06	

**Table VI-1: Measurement conditions and main parameter of the LHC magnets tested for polarity.**

The general polarity tester described here was developed on the basis of a concept originally devised at BNL [3], and explicitly adapted to the field levels of the LHC magnet assemblies (Tab.VI-1). The basic principle is based on the use of a single Hall plate as field measurement sensor, and on the rotation of this sensor over a turn in order to map the angular dependence of the field. This angle-dependent signal is analyzed in Fourier series in order to extract the field harmonics. Highest priority in the design was given to the basic functionality (polarity), but paying considerable attention also to the following issues:

- determination of all the main characteristics of the magnet under test, and, in particular, automatic detection of the main harmonic order, transfer function (TF), magnet type (normal or skew), and field direction with respect to gravity;
- very low measurement uncertainty on the main field measurement. This is necessary to detect reliably multipolar fields of high-order corrector magnets;

- measurement time below 1 minute, for practical reasons;
- reliability and robustness, focusing on the encasing of the equipment for long-term use;

In this chapter, the working principle of the system and the details of the data analysis procedure are described. The design of the probe, including mechanics, electronics, and data acquisition system, as well as the results of the characterization tests, are reported.

## VI.2 - Measurement principle based on a single rotating hall plate

The order, type, and polarity of a given magnetic field can be identified once the coefficients of the series expansion in the complex plane  $z=x+iy$  are known:

$$\mathbf{B} = B_y + iB_x = \sum_{n=1}^{\infty} C_n \left( \frac{\mathbf{z}}{r_{ref}} \right)^{n-1} = \sum_{n=1}^{\infty} (A_n + iB_n) \left( \frac{\mathbf{z}}{r_{ref}} \right)^{n-1} \quad (\text{Eq. VI-1})$$

where  $r_{ref}=17$  mm. The sign, according to the CERN convention [4], is determined by assuming that the cross product of the unit vectors  $\mathbf{u}_x \times \mathbf{u}_y$  is oriented from the magnet connection side to the end for each magnet, as illustrated in Fig. VI-1 (a).

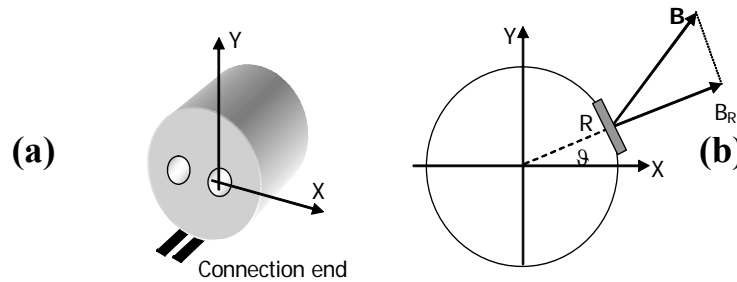


**Figure VI-1: Frame of reference for the magnetic measurements: (a) sign convention and (b) radial component of the field.**

As discussed later, the field probe is mounted tangentially at a radius  $R$  on a rotating support, and it measures the radial component of the field (Fig. VI-1 (b)):

$$B_R(\vartheta) = \vec{B} \cdot \vec{u}_r = \Im(\mathbf{B}e^{i\vartheta}) \quad (\text{Eq. VI-2})$$

The knowledge of this component over the closed boundary of a domain with null current is sufficient to find a unique solution for the field inside the domain (i.e. the field expansion in multipoles given in Eq. VI-1). This is equivalent to a classical Neumann boundary value problem for Laplace's equation in the scalar magnetic potential [4].

The measurement principle is to sample the field at  $N$  uniformly spaced angular positions in anti clockwise direction, with  $N=32, 64, \text{ or } 128$ . The result is the ordered array:

$$B_{R_j} = B_{R_j}(\vartheta_j), \quad \vartheta_j = \frac{2\pi}{N} j, \quad j = 0 \text{ to } N-1 \quad \text{(Eq. VI-3)}$$

In our implementation, the rotation actually starts from  $\vartheta_0=\pi/2$ . The resulting array can be trivially rearranged to correspond to the case  $\vartheta_0=0$ .

The radial field samples can be expressed using the multipoles expansion as follows:

$$B_{R_j} = \sum_{n=1}^{N-1} \left( \frac{R}{r_{ref}} \right)^{n-1} \left( A_n \cos \frac{2\pi}{N} jn + B_n \sin \frac{2\pi}{N} jn \right) \quad \text{(Eq. VI-4)}$$

The series is truncated to the first  $N$  field harmonics with negligible error. At the same time the coefficients of the DFT of the  $B_{R_j}$  vector, defined by:

$$\beta_k = \frac{1}{N} \sum_{j=0}^{N-1} B_{R_j} e^{\frac{2\pi}{N} jk} \quad \text{(Eq. VI-5)}$$

may be shown [App. D] to be proportional to the field coefficients of the same order by first inverting (Eq. IV-5):

$$B_{R_j} = \sum_{k=0}^{N-1} \beta_k e^{-\frac{2\pi}{N} jk} \quad \text{(Eq. VI-6)}$$

and then equating, term by term, the real part of Eq. VI-6 to Eq. VI-4, obtaining finally:

$$C_n = i \cdot \left( \frac{r_{ref}}{R} \right)^{n-1} \beta_n^* \quad (\text{Eq. VI-7})$$

where \* denotes the complex conjugate. The knowledge of the  $C_n$  at just one current level, however, may not be sufficient to derive the correct results, because the residual field in the iron yoke (in some cases a few of mT), might mask completely the main harmonic generated by the current in the superconducting coils and which forms the object of the measurement. Normally, at least two measurements at different currents are taken and fit by a linear regression in order to compute the transfer functions  $\partial C_n / \partial I$ , representing the field produced by the coils (geometric component). From this, following results were obtained:

- magnet order and type, as the order of the dominant term in the arrays  $\partial B_n / \partial I$ ,  $\partial A_n / \partial I$ ;
- magnet polarity, as the sign of the dominant term;
- the main magnet transfer function, as modulus of the dominant term in the arrays  $\partial B_n / \partial I$ ,  $\partial A_n / \partial I$ ;
- the main field magnetic phase, evaluated from the main normal and skew transfer functions.

### ***VI.3 - Instrument description***

The general instrument layout is depicted in Fig. VI-2. The measurement principle is realized with a motorized measurement head. The measurement probe in the head is a Hall generator. The field is obtained at each angular position from the voltage of the Hall generator through a calibration. A stepping motor starting from the zero position sets the angular position. Before the measurement, the hall plate is aligned with respect to the gravity by using an inclinometer to provide an absolute reference for the field direction. A tractor module, based on a DC motor, assures the automatic longitudinal positioning of the measurement probe at the right longitudinal point in the cryoassembly.

In the following the measurement probe mechanical layout, the architecture of the control electronic, as well as the instrument software, are described.

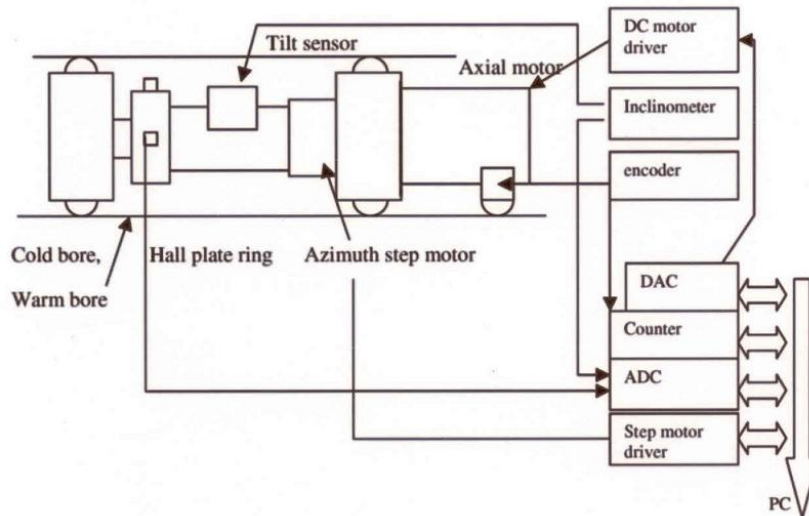


**Figure VI-2: Layout of the field polarity tester.**

### VI.3.1 - The mechanical layout

The main issue in the conception of the measurement head was the modularity.

The probe is composed by the following modules (Fig. VI-3): measurement, radial positioning, the tractor, the encoder, and the output connector;

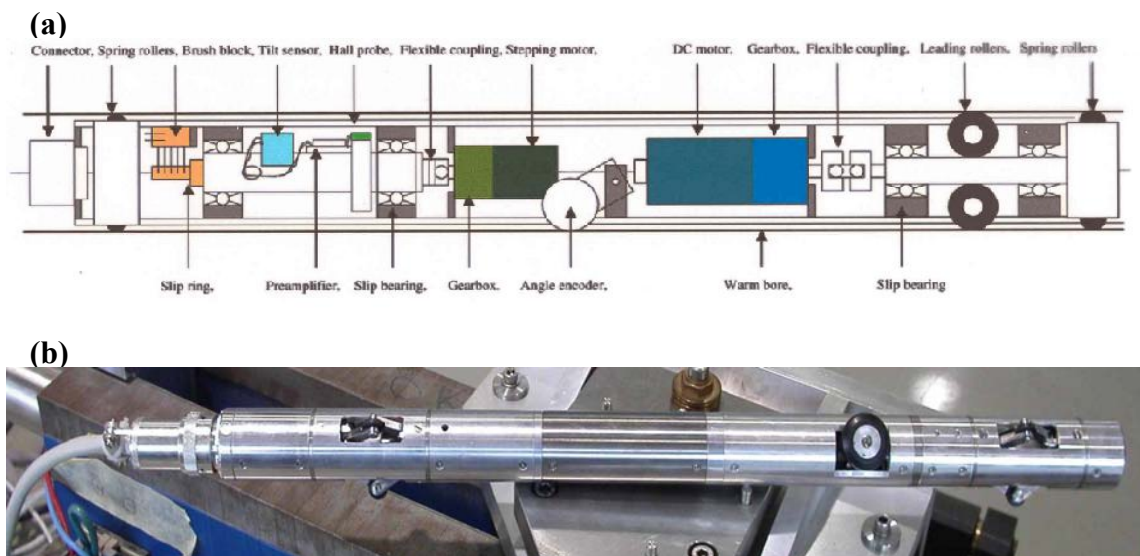


**Figure VI-3: Internal layout (a) and external view (b) of the Polarity Checker probe.**

The *measurement module* (Fig. VI-4) is based on a G10 support holding the hall plate, a signal preamplifier, and the inclinometer for the alignment to gravity. The hall plate used for this application requires a current source of 50 mA, and at this current value is characterized of a sensitivity of  $233.8 \text{ mV}^{-1}$ . By considering that the gain of the preamplifier is approximately 500, the measurement sensitivity becomes about  $100 \text{ mV}(\text{mT})^{-1}$ . This value insures that with magnetic fields as low as 0.1mT (case of sextupoles correctors with a protection resistance in parallel of  $0.1 \Omega$ ) the voltage output is 10 mV, which can be treated easily by the acquisition. As it is demonstrated later, with a suitable instrumentation amplifier and an efficient noise software filtering also this worst case is characterized by a sigma of two orders of magnitude lower than the magnetic field amplitude measured.

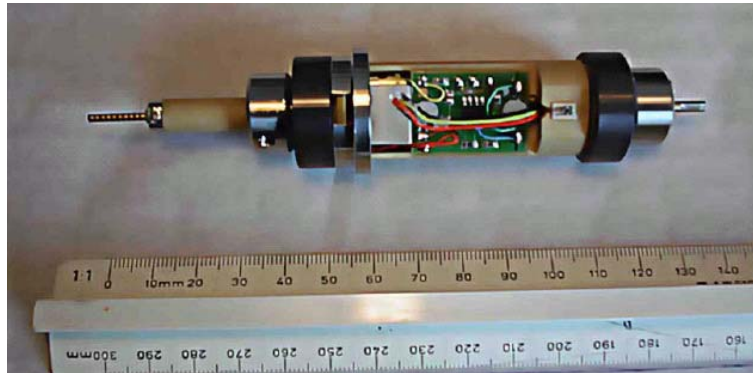


**Figure VI-4: A detail of the probe assembling: the module containing the hall plate, the amplifier and the tilt sensor.**

The used inclinometer is a tilt sensor of electrolytic type, having a resolution of a measurement range of  $\pm 45$  degree, and a resolution of 0.1 mrad. This permits a theoretical resolution in the alignment to the gravity lower than 1 mrad. In practice the alignment resolution depends also on the stepper motor, which is controlled in open loop, and by the response time of the tilt sensor as discussed later. To solve this problem, for each measurement both the initial and final radial positions are acquired, and an eventual positioning error is corrected via software.

*The module for the radial positioning* is composed by a stepper motor and by a gearbox to demultiply the motion of the motor. The motor has 24 steps per revolution, and the gearbox has a gear ratio of 22, thus a complete turn of the hall plate is obtained in 528

motor steps. Therefore, by programming the motor driver firmware, each step can be divided into 256 microsteps. In this way, in each measurement resolution (32, 64 and 128 measurement points per turn), the turn angle will be divided always in equal parts, and the spatial sampling period will be constant.

The encoder module provides the information about the longitudinal position of the probe, inside the magnet aperture. The conversion factor between the pulses counted (by the counter on the acquisition card) and the probe distance from a reference point (in millimetres), is obtained after a calibration procedure. The encoder wheel is mounted on a spring loaded arm specially developed to assure a contact with the surface of the cold bore. The tractor module is based on a DC motor controlled by the software in closed loop by using the encoder positioning information. With both the encoder and the tractor module, the probe longitudinal positioning is completely automated: after putting the probe in the reference position (the downstream magnetic side, for example) the software automatically moves the probe in the exact longitudinal measurement position for each magnet to test. Many efforts have been done (and are still in progress) to improve the repeatability of the encoder, crucial for this application: as a matter of fact, the maximum longitudinal error allowed for the correctors measurement is 2 centimetres. This value is very small if compared to the measurement range of the encoder (the maximum length of the assemblies), that is about 15 meters.

Finally, the connector module takes out all the cables, by a slip ring for the electrical connection to the rotating parts.

The probe is supported by a spring loaded roller system. The wheels that allow the longitudinal motion are on springs mounted in symmetric way. They are sized for use in an aperture in the range of 40 to 50 millimetres. The symmetry minimizes the feed down effect in the magnetic field acquisition [5].

### *VI.3.2 - The electronic hardware architecture*

In the Fig. VI-5, all the instrument electronic modules are illustrated. The majority are commercial components. Only the current source for the hall plate of 50 mA and the circuit for the conditioning of the encoder signals have been developed ad hoc. This latter provides two TTL signals: the first, with frequency proportional to the angular speed of

the encoder, and the second, a binary signal giving the information about the turn direction.

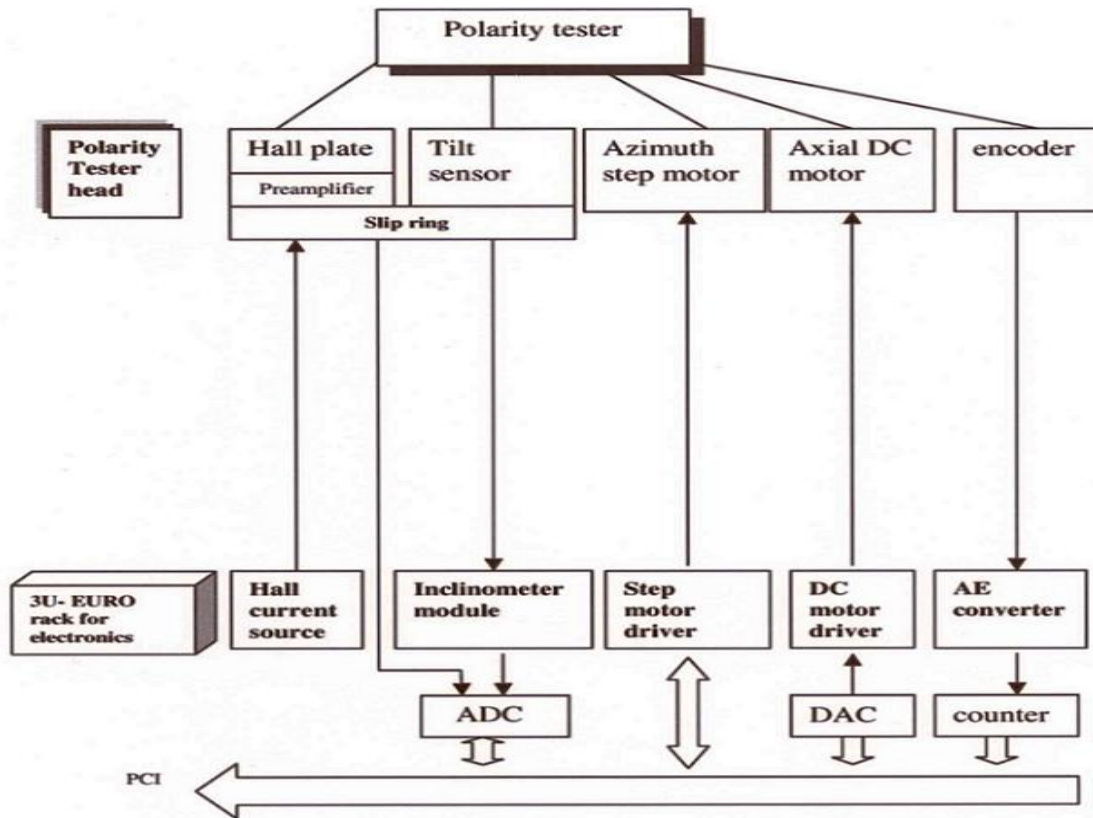


Figure VI-5: General scheme of the hardware modules used

The stepper motor driver requires a particular attention. It is characterized from the possibility to divide the normal motor step until 256 microsteps. This allows the positioning resolution of the motor to be increased by a factor 256.

The heart of all the system is the ADC acquisition card, the NI 6036 E. It is characterized by an ADC of 16 bit (that assures a conversion resolution optimal for the specific application), 16 analog channels (in single ended or 8 in differential mode) with



Figure VI-6: The front panel of the polarimeter electronic rack. (from left to right: the voltmeter for the tilt sensor, 50 mA hall plate supply, and, finally the power supplies for rack, DC motor, tilt sensor, stepping motor.

a sampling frequency maximum of 200 kS/s. This cards permits to acquire the signals of the hall plate and the inclinometer, and also to count the pulses from the encoder.

The communication with the stepper motor driver is carried out via serial port RS232.

### *VI.3.3 - The instrument software*

The Polarity Checker software is a collection of LabView <sup>TM</sup> modules for the management of the instrument hardware and the measurement of the magnetic field characteristics: harmonic order, transfer function, mounting angle of the magnet (normal or skew), the polarity and an estimation of the magnetic field main phase.

After the probe longitudinal positioning in the longitudinal center of the magnet the following steps are performed:

- radial alignment of the hall plate respect to the gravity;
- measurement current value setting;
- field acquisition;
- field harmonics evaluation.

#### *-Hall plate Radial alignment procedure-*

Before a measurement, the Hall plate is levelled by a closed-loop motor control system, based on feedback from a tilt sensor.

Because of the limited measurement range, the inclinometer may be in an overrange position at the beginning of the measurement. Two expedients are used to decrease the setting time. First by the sign of the inclinometer output voltage is detected in order to decide the motor motion direction characterized by a lower distance to zero position. Furthermore, the motor speed is changed as function of the angular radial position, increasing the motion resolution (the number of micro steps per step is modified) when approaching the zero level.

The motor is driven at maximum speed when the hall plate is far from the measurement range of the tilt sensor ( $\pm 30$  degrees). When inside the interval, the radial position reading is compared with two other threshold values, corresponding to two different speed values. The lowest speed is set when the Hall plate is within 2 degree of the zero position, in order to obtain a fine positioning with respect to the gravity. The procedure ends when the angle is lower than a threshold, fixed at 0.05 degree. The

control algorithm also takes into account the finite response time of the tilt sensor. In principle, between two consecutive steps of the motor, a waiting time of about 600 ms is necessary. This time could give rise to very long alignment time in the worst case (hall plate at 180 degree position), where 264 motor steps are needed to come in zero position.

To achieve alignment times within 45 seconds in the worst case are, a trade-off between inclinometer response time and motor speed has been adopted. This is done in practice changing the waiting time as the rotation speed. Around the zero position, the information read by the inclinometer has to be exact and a longer time is used.

The alignment procedure described was found to achieve positioning error as low as 0.5 degree. This is satisfactory because both the starting and the final angles are measured, for each magnetic field acquisition so that a correction (rotation of the reference system by the error angle) can be carried out before the evaluation of the  $C_n$ .

#### *-Measurement current value setting-*

In low magnetic field measurement (i.e. for transfer functions of about 0.1 mT in corrector magnets), the contribution of the residual magnetization is eliminated by measuring at two different current values at least (possibly at different polarities). The measurement time is reduced by a programmable power supply. The measurement current values for the magnet under test are read from a database file.

#### *Field Acquisition*

This procedure gives directly the vector of the  $N$  magnetic field normal values equally spaced in angle for a complete turn.

By starting from a hall plate zero position, the following steps are repeated for a complete turn:

- turn the motor with the necessary number of microsteps in order to obtain a  $2\pi/N$  rotation, and then switch it off, in order to avoid the influence of the motor magnetic field;
- acquire 1000 samples at 10 kHz of the hall plate output voltage, then low-pass filter at 20 Hz cutoff in order to obtain an average value of  $B_{Rj}$  at the end of the transient. Fig. VI-7 shows the signal read and the response of the filter;

The complete motor switching off and the hall plate response time require a time interval at 750 ms between two consecutive measurements. The overall acquisition time for a resolution of 64 points/turn is finally about 50 sec.

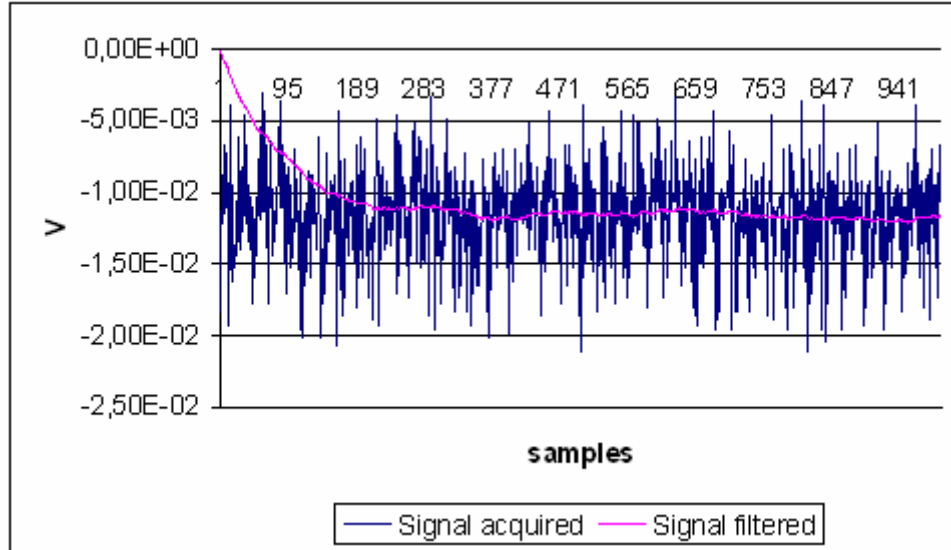


**Figure VI-7: Hall plate output signal and output of the digital filter**

*-Field harmonics evaluation-*

The following operations are performed in order to determine the transfer functions of each field harmonics on the acquired samples vector:

- compute the harmonic coefficients  $\beta_n$  using the FFT according the Eq. VI-5;
- compute the field coefficients  $C_n^k$  using eq. VI-7;
- repeat the samples vector acquisition the prescribed number of current steps; compute a linear regression through each set  $\{C_n^k, I_k\}$ , in order to obtain the transfer functions  $\partial C_n / \partial I$ .

After the FFT evaluation on the two vectors  $A_n$  and  $B_n$  a rotation of the reference system of a  $\pi/2$  angle to transfer the measurement reference system is performed since the hall plate starts aligned with the gravity (Fig.VI-1 (b)). In addition the Hall plate angle errors are compensated, namely:

- Hall plate mounting error, established by calibrating in a reference dipole;
- initial positioning angle error, as measured from the inclinometer.

The former is a constant of a measurement probe (ranging around few tenth of degree). The latter, instead, changes for each measurement because of alignment uncertainty; therefore, for each field acquisition, both the starting ( $\theta_i$ ) and the final angle ( $\theta_f$ ) of the hall plate are measured. The difference  $\theta_f - \theta_i$  represents the angle error to be corrected.

On the two vectors  $\partial \mathbf{A}_n / \partial I$ ,  $\partial \mathbf{B}_n / \partial I$ , the following automatic analysis is performed:

1. the index of the maximum element in both arrays is the harmonic order of the magnet measured;
2. the corresponding values are the transfer functions of the main skew and normal components. By comparison of  $A_n$  and  $B_n$  is clear to determine the magnet mounting angle;
3. the main TF sign gives the polarity of the field;
4. from the main TF skew and normal, with the convention previously illustrated, an estimation of the field main phase is evaluated.

## ***VI.4 - System characterization***

In this section the characterization of the polarity tester is presented divided in the calibration of the Hall plate and followed by the determination of the overall measurement error. To characterize the system a number of measurements have been carried out, on dedicated calibration benches with all the possible magnet types (dipole, quadrupole, sextupole, octupole, decapole); the issue has been the measurement uncertainty evaluation for the magnetic transfer function measurement as well as for the main field phase. At the same time, the systematic errors were investigated, and an appropriate correction implemented.

### *VI.4.1 - Hall plate static characteristic evaluation*

The gain of the chain of the Hall plate and amplifier was calibrated in a reference dipole used as variable magnetic field source. A teslameter based on NMR (Nuclear Magnetic Resonance) was used for each supply current value to measure the exact field inside the dipole (the measurement uncertainty is around  $10^{-7}$  T), while the instrument output voltage was measured directly by the software.

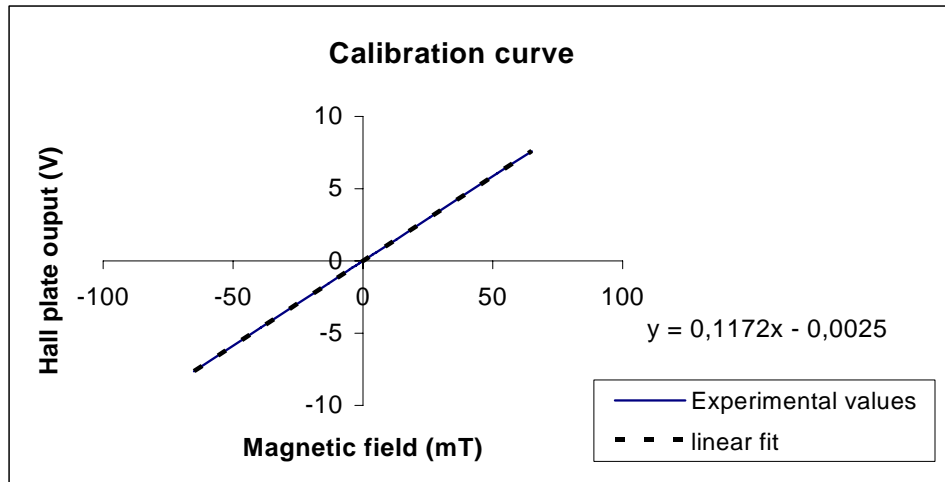


Figure VI-8: Calibration curve of the hall plate used in the instrument prototype

To deal with alignment issues, the harmonic analysis procedure described earlier was used to determine the main field component. In this specific case, only the main skew component of the waveform read was taken (as the reference dipole is skew).

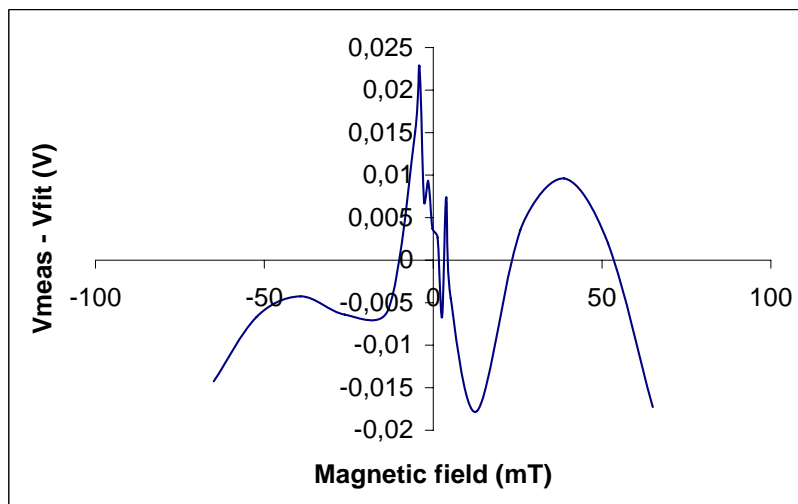


Figure VI-9: Hall plate non linearity versus the field

In this way, all the non linearity effects of the sensor are not considered. Fig.VI-8 shows the calibration curve obtained. At the same time the interpolation line at minimum rms was evaluated in order to obtain the calibration factor for the software and for testing the linearity of the system of the Hall plate and amplifier.

The linearity error results of the order of 0.3% (Fig.VI-9).

#### VI.4.2 - Systematic errors investigation

The systematic errors of the system were determined by performing repeated measurement on a set of calibration magnets whose characteristics (field, transfer function, polarity) and orientation (field direction) were well known. Two major systematic errors were found:

- radial positioning error during a measurement;
- Hall plate mounting angle error.

The source of the former error was investigated by repeated measurements. For each calibration magnet type, the hall plate radial positions recorded before and after a revolution were analyzed.

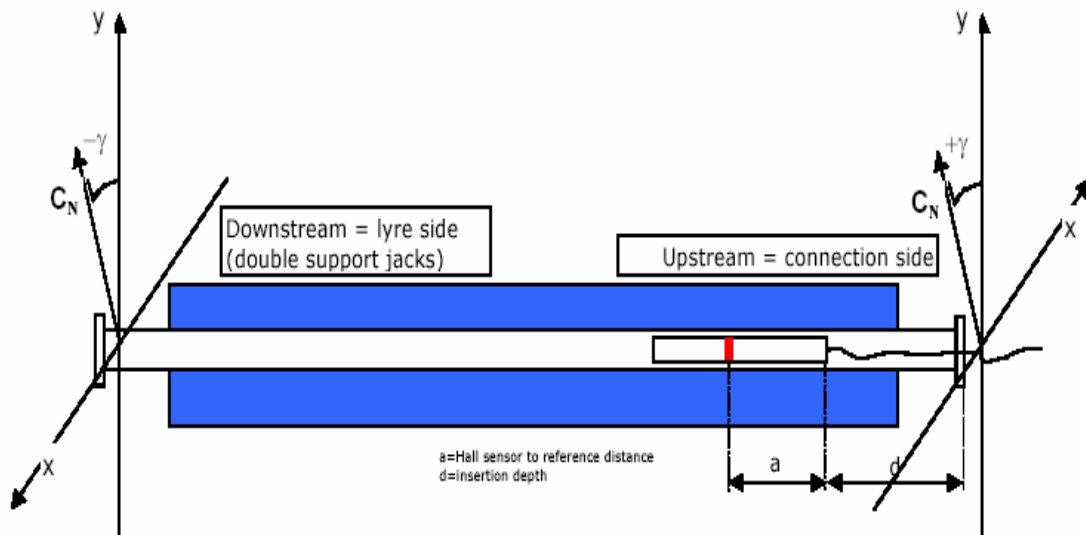


**Figure VI-10: Relation between the reference systems upstream and downstream side in a main dipole**

In Fig. VI-11 these values for measurements from upstream and downstream side, respectively, on a reference quadrupole are reported. The initial angle for each measurement  $\theta_I$  is always less than 0.05 degree (threshold set in the alignment procedure). The final angle  $\theta_F$  should be 0 because the hall plate, after  $N$  steps, comes

back in the starting position. In reality the measured value was found to have a random spread as large as 1 degree. The effect of this radial positioning error on the magnetic phase evaluation is examined in Fig. VI-12, which shows the relation between the main field phase measured and the value  $\theta_F - \theta_i$ . The measured reference magnet is a normal calibration quadrupole with main phase practically zero. The direct relation between the final positioning error of the Hall plate and the error on the evaluated phase is evident. In other words, the error in the field phase measured is just the quantity  $\theta_F$  ( $\theta_i$  is always negligible).

In Fig. VI-12 the same data corrected subtracting the value of the final angle  $\theta_F$  are shown. The measurement variability is decreased and all the measurements are closer to the expected value (the sign of the field angles is inverted measuring upstream and downstream). The error in the final position of the Hall plate gives the same effects as a rotation of the measurement reference system of an angle  $\theta_F$ .

Whatever are the sources of the angular positioning error (mostly uncertainty on the hall plate alignment caused by problems in the motor control are suspected) a simple reference system rotation by the final angular error allows the random error on the main phase to be corrected.

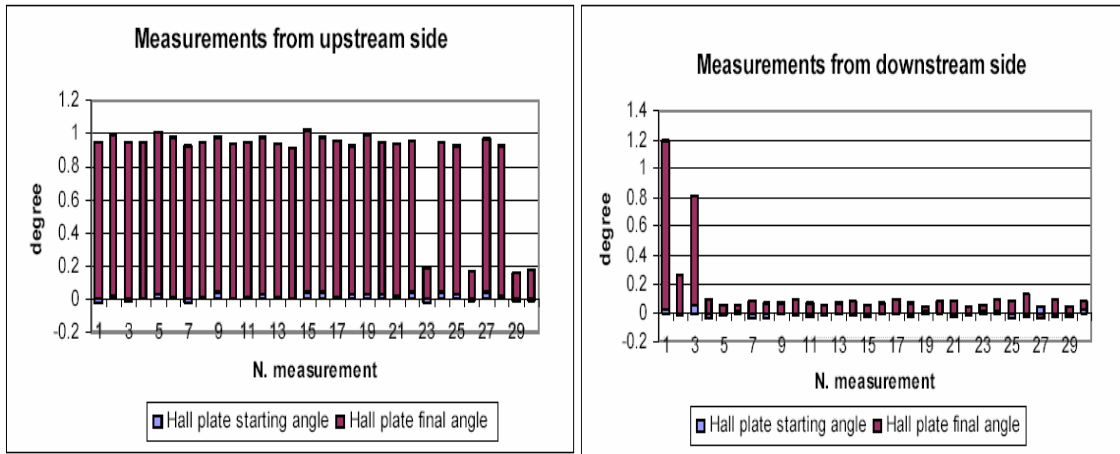


**Figure VI-11: Initial and final hall plate radial position in 30 repeated measurements from upstream and downstream side in a reference quadrupole**

After the correction, a further systematic error on the main phase, due to the hall plate mounting angle, is still present (Fig.VI-10).

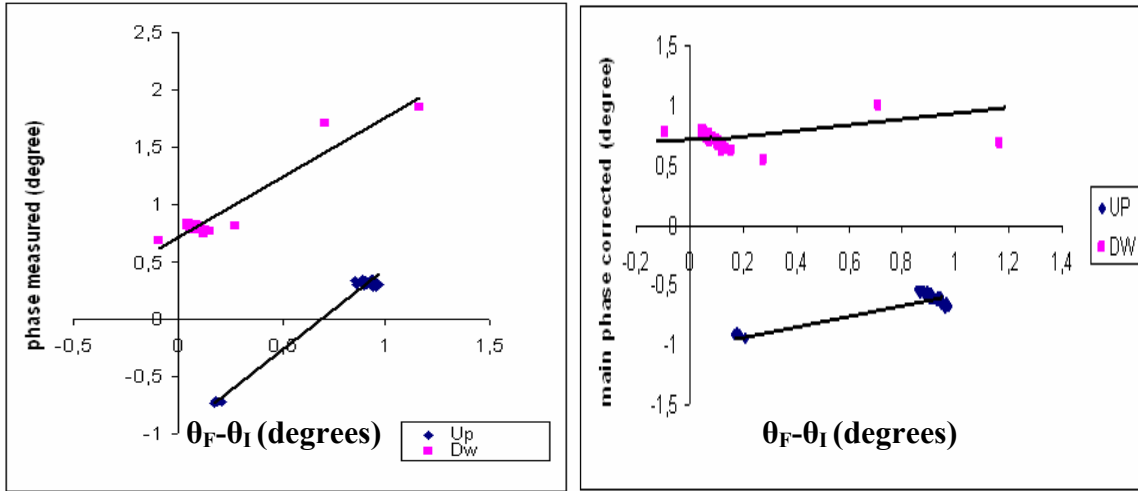


**Figure VI-12: On the left relation between the phase measured on a reference normal quadrupole in repetitive measurements and the  $\theta_F - \theta_I$  value. On the right the same main phases with the  $\theta_F - \theta_I$  correction**

Using the above procedure, the random error on the field direction to a fraction of degree is decreased. However, the systematic error is not yet removed. To do this, the phase symmetry respect to  $y$  axis (reference for the angles) for a normal magnet was used, as shown in Fig. VI-10. The magnetic phase measured from the upstream side of the magnet under test is the same in absolute value, but with opposite sign in the case of the downstream side of the same magnet.

Let  $\alpha_{UP}$  and  $\alpha_{DW}$  be the main magnetic angles measured from upstream and downstream side respectively,  $\alpha_{ERR}$  the systematic error on the angle measurement (e.g. a Hall plate mounting error), and  $\gamma$  the real value of the field direction. The following relations are derived:

$$\alpha_{UP} = \gamma + \alpha_{ERR} \quad ; \quad \alpha_{DW} = -\gamma + \alpha_{ERR}$$

the systematic error can be determined adding the two results above:

$$\alpha_{ERR} = \frac{\alpha_{up} + \alpha_{DW}}{2}.$$

Therefore, the system error can be evaluated easily by two measurements from opposite sides of the magnet under test. The angle error sign is always the same because the

reference system agrees with the measurement probe: this means that the angle between the hall plate normal (in the average point) and the normal axes of the polar reference system is always the same (Fig.VI-13).

This calibration was done performing 30 measurements from each side of reference magnets in order to evaluate the angle error by means of average. On the first prototype the systematic angle error estimation has been found to be in the range  $0,4 \pm 0,75$  degree. The value of 0.6 degree was considered for the software correction of this error.

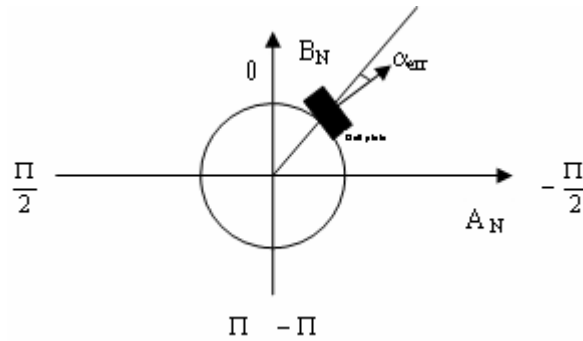


**Figure VI-13: Angle error in the hall plate mounting**

#### VI.4.3 - Measurement uncertainty evaluation

As a final step, the measurement uncertainty was evaluated both for the field harmonics measurement as well as for field direction estimation. A statistical approach was applied: after instrument systematic errors correction, the average and standard deviation in 60 repeated measurements on different reference magnet types were computed (Table VI-2). Even in the case of a main field value of about 0.1 mT (B3 for the calibration sextupole), the standard deviation is at least of two orders of magnitude lower than the average (measured value).

Magnet Order	Main Field (mT)		Field direction (mrad)
	Avg.	Std. Dev.	Std. Dev.
1	-25.58	0.024	1.79
2	8.60	0.010	1.70
3	0.10	0.001	4.19
4	-0.85	0.001	7.55
5	0.42	0.001	2.04

**Table VI-2: Repeatability test results**

In this range of field, the maximum linearity error, estimated at 3% from the calibration measurement, becomes important. However, even in the worst case (dodecapole), the field to be measured is 6 times higher than the measurement uncertainty, and, since in LHC magnets all multipole errors are at least two orders of magnitude below the main harmonic, the identification of main harmonic order and polarity (for the field range in Table VI-2) is virtually error-free.

Measured quantity	Value
Main Field accuracy (mT)	0.001
Field linearity	3%
Main harmonic order	error-free
Main harmonic polarity	error-free
Main harmonic type	error-free
Field direction accuracy (mrad)	8

**Table VI-3 : Measurement estimated accuracy**

For the field direction measurements, the maximum standard deviation measured is around 8 mrad (0.4 degree). Whilst this accuracy is inadequate for field direction measurements in LHC magnets, it is nevertheless well below the threshold necessary to correctly attribute normal or skew field type, i.e. at least  $\pi/12 \approx 262$  mrad.

The instrument accuracy is summarized in Table VI-3.

### ***VI.5 - The automatic polarity test***

The final goal of the measurement system is the error-free test of interconnections of all the magnets of the LHC by means of field polarity checking. This test was to be short, easy, and reliable. The realized instrument satisfies these requirements: in fact, it exhibits very short measurement times (a measurement for two different current values, with a resolution of 64 points/turn, has a maximum measurement time of 2 minutes, including

the alignment procedures), measurement uncertainty practically zero for this measurement target, and, finally, it is a very robust instrument.

In the same line of approach, the probe described was complemented by other auxiliaries to produce a completely automatic polarity test which eliminates human errors and meets the previous requirements.

The following equipment was used:

- a bipolar Kepco power supply for magnet excitation;
- a computer-controlled Keithley 2001 multiplexer and a custom-built data switching unit, able to route the input current through up to 9 channels in each of 6 different cables (provided with ad-hoc connectors) to the appropriate magnets in the cryoassemblies;
- a PC that runs the software for polarity checker control and to automatically carry out the test.

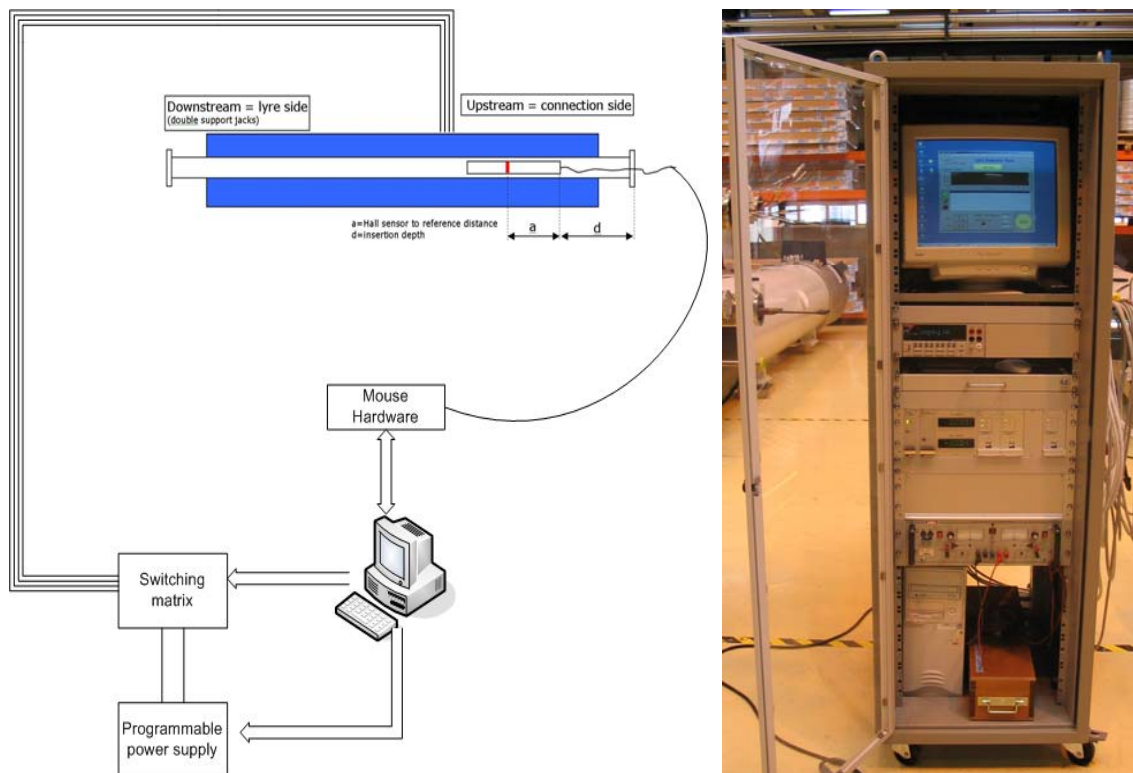


**Figure VI-14: Automatic polarity test bench.**

The automatic polarity test bench software is a collection of LabView™ modules that perform two basic tasks:

a) control the polarity checker to execute a field measurement and return the magnet parameters;

b) guide the operator through the full test of a given assembly, returning a conformity report. Operation is supported by an Excel configuration file that lists the existing types of assembly and their composition, the physical properties and positions of the various magnets in the assembly, the nominal transfer function, multipole type and polarity of each. The expected results depend on the presence of a parallel protection resistor, on the polarity of the power supply (which may be constrained due to a protection diode) and on the side from which the probe is inserted (the polarity of even normal and odd skew multipole fields changes with a 180° rotation around the y axis).

The Database architecture is illustrated in Fig. VI-15.

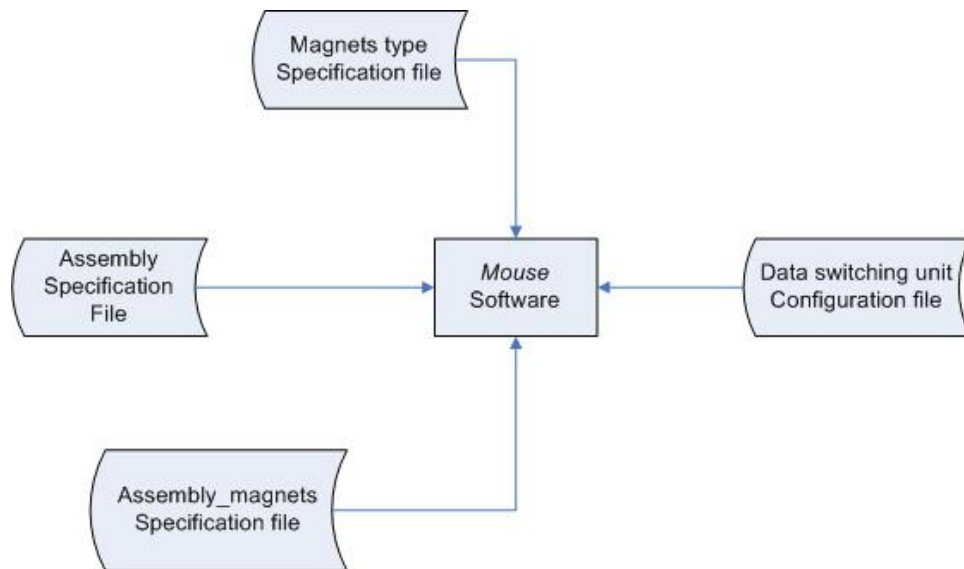


**Figure VI-15: Database files architecture.**

The file called *Assembly Specification file* contains the list of all the assemblies that have to be tested, both dipole assemblies and corrector assemblies. For each assembly type, its composition (in terms of apertures number and magnets type present from upstream to downstream assembly side) is given. The file *Assembly\_magnets Specification file* stores

all the magnets data useful for the polarity test and related to the magnet type mounted in a particular assembly. In particular, the magnet longitudinal position, the mounting angle, and the expected polarity. All the magnetic and electrical characteristics (main transfer function, measurement current values, harmonic order) for the magnet to test are stored in the *Magnets type Specification file*. In this last one, the search key is the magnet type name.

The test bench software is designed to have a wizard-style interface that guides the operator through the test preventing omissions and mistakes (Fig.VI-16).

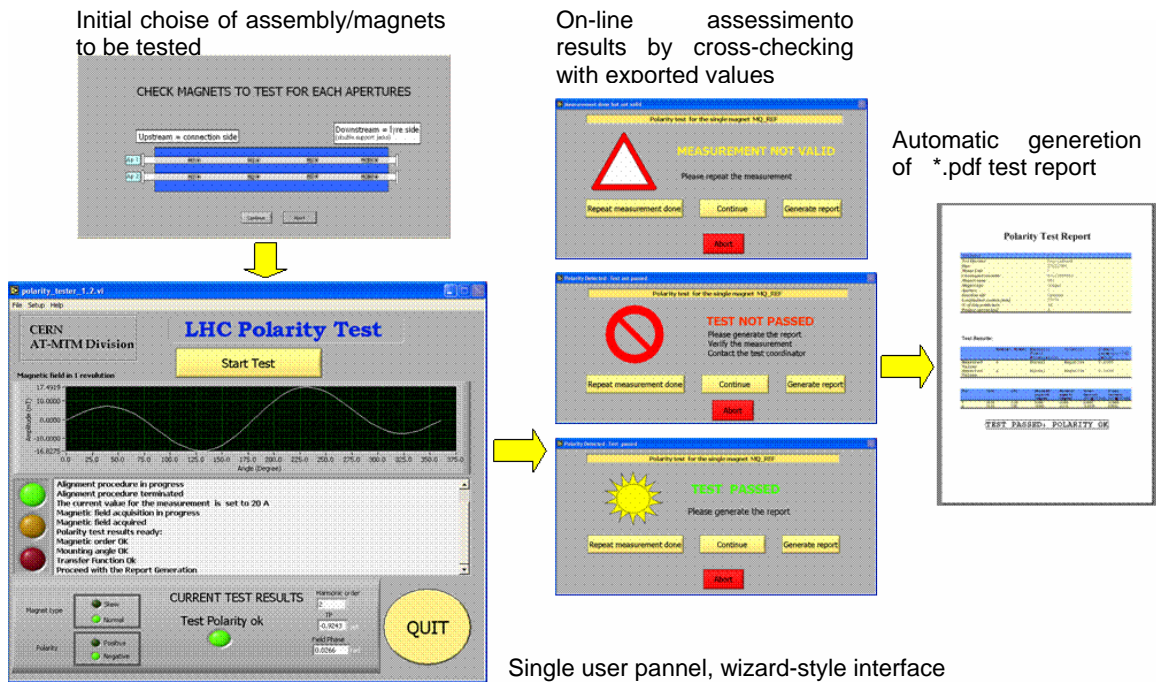


Figure VI-16: Polarity test LabView User interfaces.

## VI.6 - Results

The polarity checker is presently used to test errors in the interconnections of all the magnets that will compose the LHC. 5 units have been built to accommodate the workload during series tests.

To date, a total of 505 cryoassemblies have been checked at CERN. A summary of results is shown in Tab. IV-4.

About 3% of all corrector magnets were found to have polarity or aperture inversions. This fault rate, if undetected, would have led to a loss of 6% of correcting capability, which could be acceptable in some cases (e.g. for the dipole spool pieces), recoverable in others (e.g., the dipole correctors, which are individually powered) but catastrophic for some (e.g., skew quadrupoles or main dipoles).

Predictably, the fault rate was much higher in 2003 and 2004 than it is today. All faults could be corrected based on the measurements performed, which is a major achievement of this instrument.

<b>Magnet Type</b>	<b>Tested</b>	<b>Faults</b>	<b>Type</b>
<b><i>Cryodipoles</i></b>	330	3	Any
- Main dipoles (MB)	330	0	-
- Spool piece correctors	990	3	Polarity
<b><i>Short Straight Sections</i></b>	175	34	Any
- Main Quadrupoles (MQ)	175	0	-
- Dipole Correctors (MCB)	175	3	Polarity
		28	Aperture
- Tuning Quadrupoles	71	0	-
- Skew Quadrupoles (MQS)	1	0	-
- Sextupole Correctors	175	8	Polarity
		28	Aperture
- Octupole Correctors (MO)	103	2	Polarity
		2	Aperture
<b>Total Cryoassemblies</b>	<b>505</b>	<b>37</b>	<b>Any</b>
<b>Total magnets</b>	<b>2020</b>	<b>61</b>	<b>Any</b>

**Table VI-4: Polarity test summary on 505 cryoassemblies.**

## **VI.7 - References**

- [1] M. Modena, M. Bajko, M.Cornelis, et al., “*LHC Superconducting Dipoles Production Follow-up: Results of Audit on QA aspects in industry*”, MT-19.
- [2] The LHC Team, *LHC Design Report*, CERN 2004-003.
- [3] R. Thomas, W. Louie, G. Ganetis, A. Jain, P. Wanderer, “*Automated Polarity Checking for RHIC Magnet Assemblies*”, Proceedings of the 11th International Magnet Measurement Workshop (IMMW-XI) Brookhaven National Laboratory, Upton, NY, September 21st-24th, 1999.
- [4] P. Proudlock, P. Burla , “*LHC Magnet Polarities*”, CERN Engineering Specification, EDMS no: 90041.
- [5] A. Masi, L.Bottura, M. Buzio, A. Tikhov , “*A new instrument for the magnets polarity test*”, AT-MTM Internal note 2004-141, EDMS no:475522, 2004-06-01.
- [6] M Buzio, A Masi *et al*, “*Checking the Polarity of Superconducting Multipole LHC Magnets*”, Submitted for publication to IEEE Trans. on Applied Superconductivity.

## **CONCLUSION AND OUTLOOK**

Digital technologies were successfully applied at magnetic measurements systems at different accuracy level.

At the *high-accuracy* end, i.e. the systems based on rotating coils and on the Faraday-Lenz's law, a new fast numerical integrator (FDI) based on ADC and numerical integration performed on DSP was proposed. Experimental validation carried out on a system PXI Real Time showed an effective improvement of the resolution with respect to the old PDI integrators, based on voltage to frequency conversion principle. According to the ADC resolution and the sampling rate chosen, the theoretical flux resolution of the new integrator is five orders of magnitude higher than the old integrator. A time measurement for improving integration accuracy was proposed. In agreement with the strict requirements of drift and stability, the guidelines of the integrator analog front-end design was defined, taking into account features as automatic gain commutation, offset auto-calibration and automatic fine gain adjustment. A first prototype of the analog front-end was developed and is being tested.

Two new analysis algorithms improving the standard analysis in dynamic field measurements were presented. The first one applies quadrature detection and short time Fourier transform (STFT) to the acquired magnetic flux samples in a combined way. The second approach extrapolates magnetic flux samples outside those covering three complete coil turns, thus giving the possibility of reconstructing the magnetic flux over a complete coil turn at a given time instant, to obtain, in principle, the field harmonics at each given time. The performances of the approaches proposed were assessed in simulation on reference field harmonics typical of the LHC superconducting dipoles. Different ramp current types are taken into account, principally the ones of the LHC

nominal cycle ( $10 \text{ As}^{-1}$  ramp rate) and a linear ramp up to  $100 \text{ As}^{-1}$ . The comparison between the standard analysis shows that the algorithm based on the extrapolation of the flux samples, despite its simplicity, provides the best results both on the main harmonic and on the higher order multipoles, with a reduction of the absolute errors on nominal LHC linear ramp of one order of magnitude. The method based on demodulation also exhibits encouraging results, which is interesting as this is a new technique that was never applied before to rotating coils measurements. We expect that this fully digital approach, complemented by suitable signal processing, will enlarge considerably the measurement capability, and we are eagerly waiting for the accurate experimental validation of the algorithm proposed which are foreseen in the near future.

The performance improvement on the measurement system based on the rotating coils is summarized in Fig. 1. The measurement time is now significantly faster both because the new integrators are compatible with a higher coil speed and, thanks to the extrapolation approach, the field harmonics can be evaluated at each given time. In dynamic fields measurements the absolute errors were reduced at least of one order of magnitude according to the current ramp rate

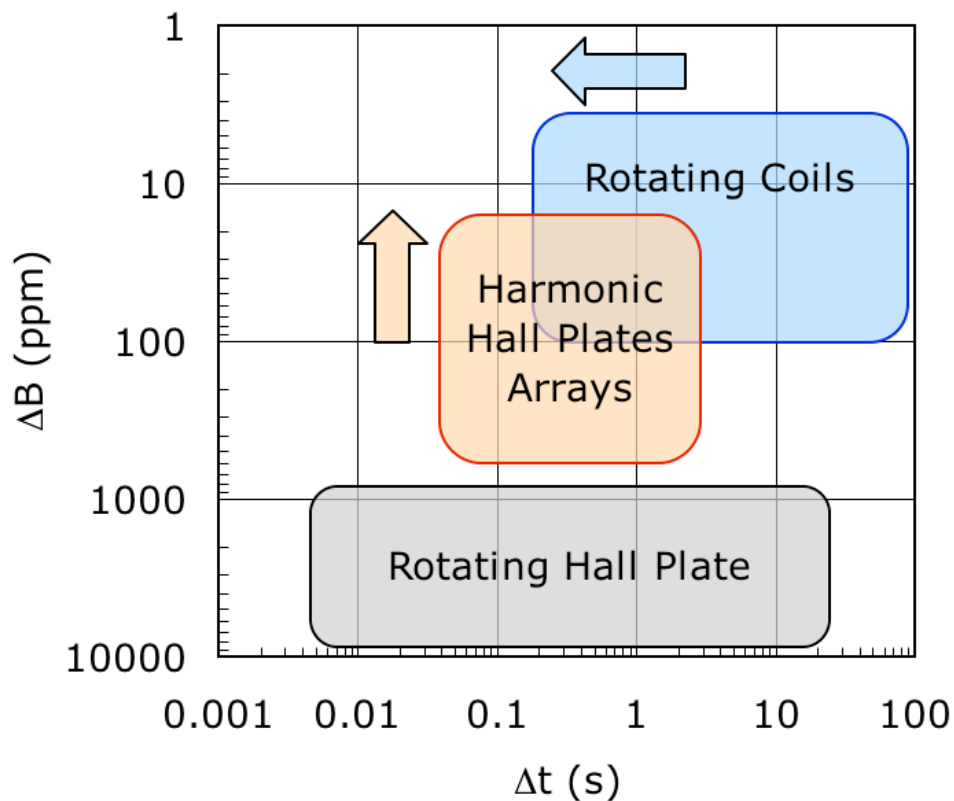


**Figure 1: Improvement of the measurement system analyzed following the application of digital technologies**

Concerning the array of Hall probes to measure the sextupolar and decapolar field components in the LHC dipoles, i.e. the system with *medium accuracy* performance, the instrument was fully characterized. The main uncertainties sources were discovered to be a lack of compensation associated with the Hall plates non linearity and the instability of the analog compensation cards (variation of gain and offset in the short term). This latter was responsible also for the scarce instrument repeatability. According to the characterization results, an automatic calibration procedure, using rotating coil measurement as reference, was implemented in the new instrument realization. New measurements, carried out on two different LHC dipoles, showed good results. Nevertheless, design guidelines were defined for a new analog bucking cards, expected to guarantee higher stability even over the long term. An alternative solution based on digital bucking, namely the compensation of the main field after the sampling of each Hall plate signal by means of numerical sum, was explored. Over-sampling and filtering techniques were applied in order to increase the sampling resolution and a real time compensation of the Hall plates non linearity at better than 100 ppm was implemented. A proof demonstration on the sextupolar harmonic was achieved using a DAQ system 16 bit resolution. Finally, this approach was implemented on a PXI system equipped with 18-bit DAQ cards and real time operating system. The combined use of both the digital approach and the analog one based on the new cards and the automatic calibration procedure, is expected to assure a global accuracy improved of one order of magnitude (see Fig. 1).

The last result concerns the polarity checker, i.e. the instrument with *low accuracy*. An instrument to measure the polarity of all the LHC magnets types at warm (i.e. at environment temperature) was developed. By means of a meticulous metrological characterization of the first prototype realized, systematic measurement errors were discovered and characterized. Their correction in the instrument software assured a virtually error-free polarity measurement. A fully automatic test bench based on this instrument was developed. This is become the standard to test errors in the interconnections of all the magnets that will compose the LHC (about 8400). Up to now 5 devices were produced and about 2020 magnets were tested. About 3% of all corrector magnets were found to have polarity or aperture inversions. This fault rate, if undetected, would have lead to a loss of 6% of correcting capability, which could be acceptable in some cases (e.g. for the dipole spool pieces), recoverable in others (e.g., the dipole correctors, which are individually powered) but catastrophic for some (e.g., skew quadrupoles or, for that matter, also main dipoles).

## **Appendix A- THE MEASUREMENT STATION**

PXI (PCI eXtensions for Instrumentation) is a rugged PC-based platform for measurement and automation systems. PXI combines PCI electrical-bus features with the rugged, modular, Eurocard mechanical-packaging of CompactPCI; therefore it adds specialized synchronization buses and key software features. This makes it a high-performance and low-cost deployment platform for measurement and automation systems. These systems serve applications such as manufacturing test, military and aerospace, machine monitoring, automotive, and industrial test.

PXI systems are comprised of three basic components: the chassis, the system controller, and peripheral modules (Fig. A-1).



**Figure A-1: A standard 8-Slot PXI chassis with an embedded system controller and seven peripheral modules**

## PXI Chassis

The chassis provides the rugged and modular packaging for the system. Chassis generally range in size from 4-slots to 18-slots, and are also available with special features such as DC power supplies and integrated signal conditioning. The chassis contains the high-performance PXI backplane, which includes the PCI bus and timing and triggering buses (Fig. A-2 ). These timing and triggering buses enable users to develop systems for applications requiring precise synchronization. For more information on the functionality of the PXI timing and triggering buses, refer to the PXI Hardware.

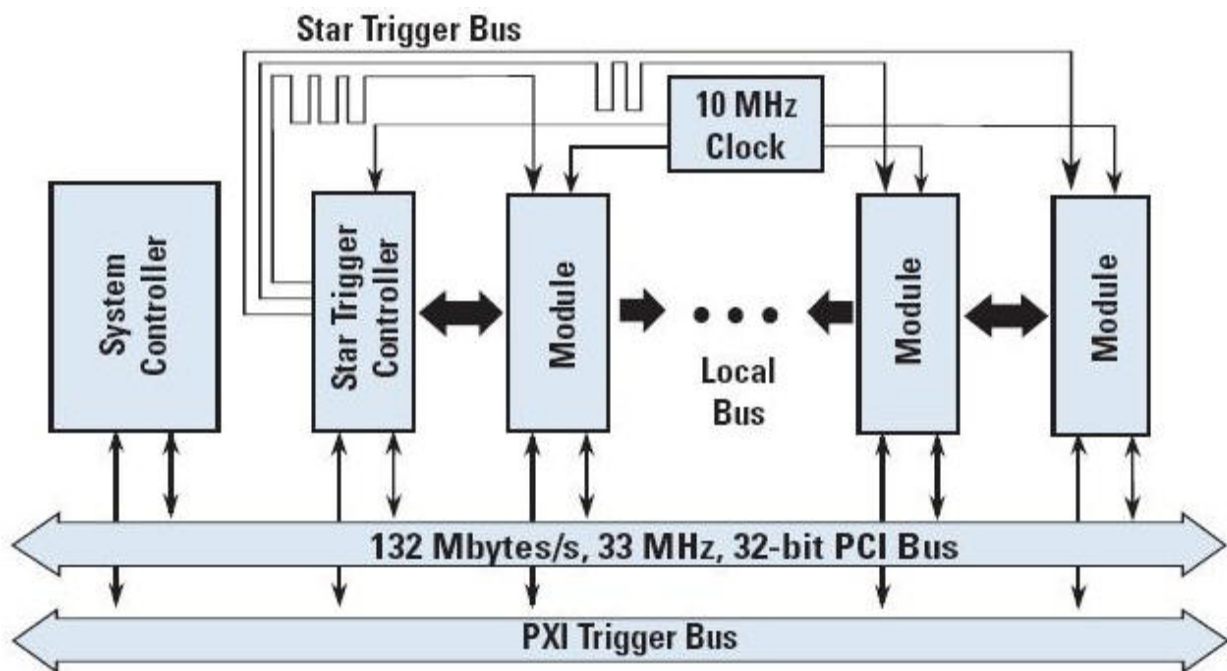


Figure A-2: PXI Timing and Triggering Buses. PXI combines industry-standard PC components, such as the PCI bus, with advanced triggering and synchronization extensions on the backplane.

## PXI Controllers

As defined by the PXI Hardware Specification, all PXI chassis contain a system controller slot located in the leftmost slot of the chassis (slot 1). Controller options include remote control from a standard desktop PC or a high-performance embedded control with either a Microsoft operating system (such as Windows 2000/XP) or a Real-Time operating system (such as LabVIEW Real-Time). The controller used in the proof demonstrator platform is the NI 8173: a Pentium IV 2.5 Ghz with 1 Gbyte RAM, 40 Mb Hard Disk and Pharlap Operating system RT.

The RT tasks running on the target system are developed in LabView<sup>RT</sup> 7.1, the data are displayed on a Host computer (Windows Xp PC) on which the Graphical User Interface is installed and finally the data communication between the target and the host is based on TCP/IP protocol.

### PXI Peripherals Modules

As already anticipated the PXI system is equipped with two PXI 6289 Analog to Digital cards. Here their main characteristics:

- 18 bit resolution SAR (Successive Approximation Register) A/D converter based
- Up to 16 differential channel (or 32 in single ended acquisition)
- Programmable Gain Amplifier to vary the input range from +/- 100 mV to +/- 10 V (+/- 0.1, +/-0.2, +/- 0.5, +/- 1, +/- 2, +/- 5, +/- 10)
- Hardware anti-aliasing filters at 40 Khz cut-off frequency
- 625 KS/s maximum sampling frequency on single channel or 500 KS/s in multiplexed mode
- Two 32 bit 80 Mhz counters/timers
- Up to 4 analog outputs at 16 bits, 2.8 MS/s (3 us full-scale settling)
- Analog and digital triggering
- 6 DMA channels for high speed data throughput

On the cards an automatic calibration procedure is implemented so to assure an improved measurement accuracy. The data about the acquisition accuracy, guaranteed over 2 years, are summarized in Fig. A-3.

**AI Absolute Accuracy Table (Filter On)**

Nominal Range		Residual			Residual	Offset			Absolute	
Positive Full Scale	Negative Full Scale	Gain Error (ppm of Reading)	Gain Tempco (ppm/°C)	Reference Tempco	Offset Error (ppm of Range)	Tempco (ppm of Range/°C)	INL Error (ppm of Range)	Random Noise, $\sigma$ (pV <sub>rms</sub> )	Accuracy at Full Scale <sup>1</sup> (pV)	Sensitivity <sup>2</sup> (pV)
10	-10	40	17	1	8	11	10	60	960	24
5	-5	45	17	1	8	11	10	30	510	12
2	-2	45	17	1	8	13	10	12	210	4.8
1	-1	55	17	1	15	15	10	7	120	2.8
0.5	-0.5	55	17	1	30	20	10	4	70	1.6
0.2	-0.2	75	17	1	45	35	10	3	38	1.2
0.1	-0.1	120	17	1	60	60	10	2	28	0.8

**Figure A-3: PXI 6289 DAQ card Analog Input absolute accuracy with filter input on**

For instance for 200 mV bipolar input range taking into account:

- The residual PGA gain error;
- The PGA gain stability;
- The residual offset error;
- The ADC INL (integral non linearity) error;
- The random noise on the signal to acquire;
- A variation of 2 degrees respect the temperature at which the card autocalibration was performed;

An acquisition sensitivity of 1.2 uV is reached with 30 uV absolute accuracy.

## **Appendix B- SCXI DATA ACQUISITION SYSTEM FOR THE SNAPBACK ANALYZER**

The data acquisition system chosen for the Snapback analyzer is a National Instrument SCXI system connected to a DAQ card PCI 16 bit (model 6052 E) installed in a Personal Computer Windows Xp. Its main structure is the SCXI-1000 chassis that houses power and different modules which communicate via an analog bus (Fig. V-7). Chassis control circuitry manages this bus, assuring the synchronization between each module and the DAQ device.

The SCANCLK signal from the DAQ device synchronizes the SCXI multiplexing with the DAQ board internal clock that triggers the A/D conversions. SCXI Slot 0 enables and disables the modules according to the pre-programmed list. In this way, the system multiplexes channels from several modules to a only analogic input channel of the DAQ device at very high rates.

SCXI 1000 chassis has 4 slots available; the modules used for this application are two:

1. **SCXI 1100 module:** This module is a 32-channel differential-input multiplexer with an onboard programmable-gain instrumentation amplifier (PGIA). It has 32 differential voltage or current input channels, an analog

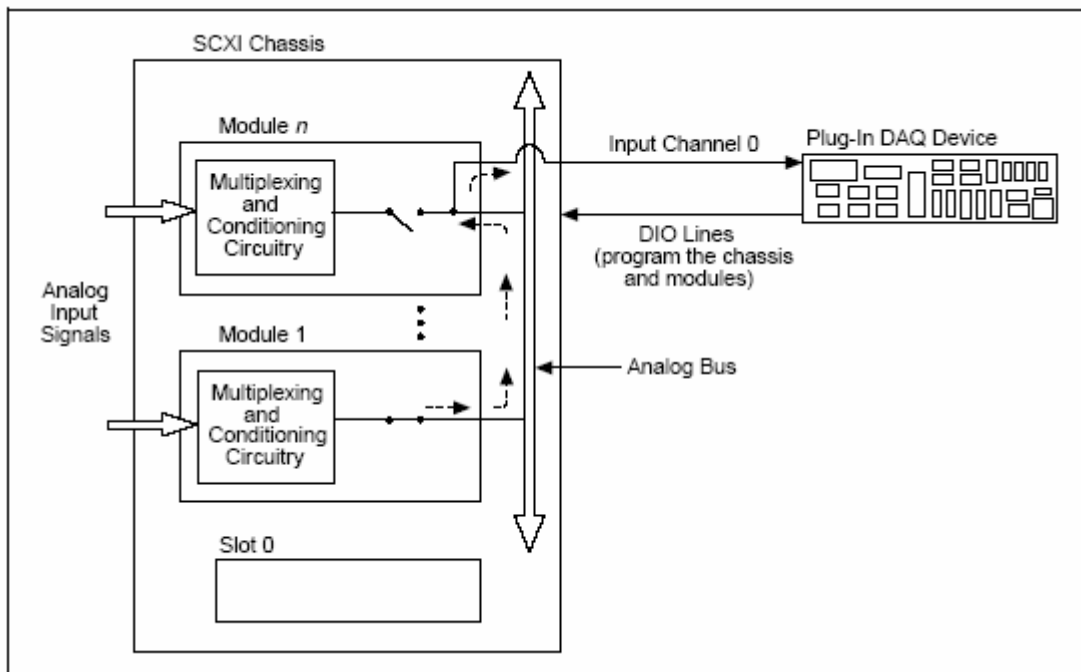


**Figure B-1: SCXI signal routing.**

input range of  $\pm 10$  V and two jumper-selectable lowpass, one-pole resistance-capacitor (RC) filter, with bandwidths of 10 kHz and 4 Hz, positioned after the amplifier. The instrumentation amplifier is characterized by the following software-selectable gains: 1, 2, 5, 10, 20, 50, 100, 200, 1,000, and 2,000. It is

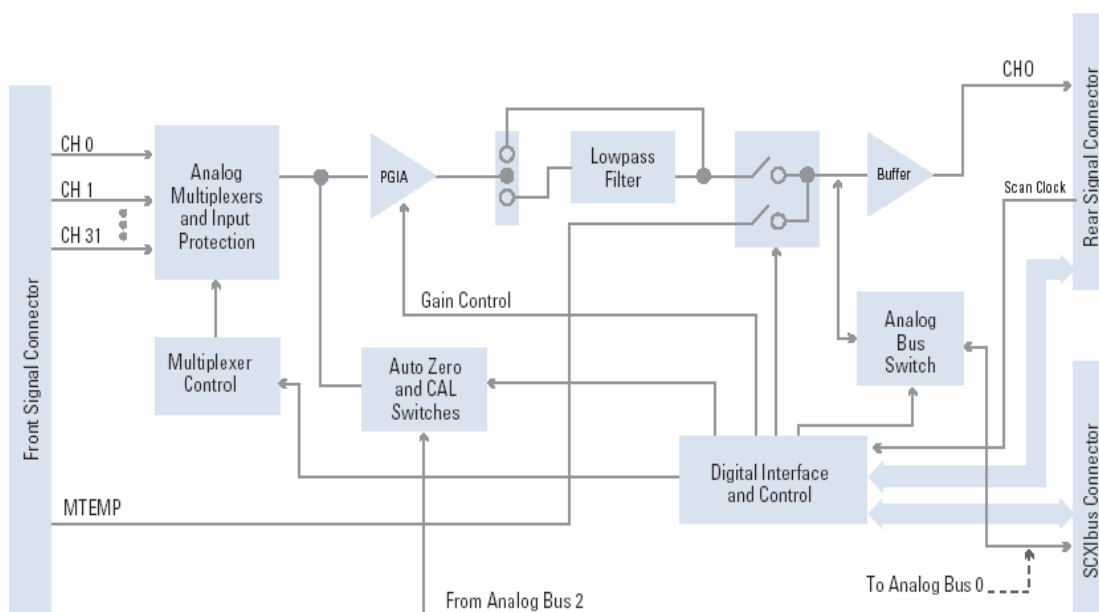


**Figure B-2: Scheme for input module for Hall plates outputs acquisition.**

used to acquire the 28 signals coming from each Hall plate plus the inclinometer and the hall plates current signal, all in differential mode. In Fig. B-2 the module architecture is showed: the signal is first multiplexed then amplified and filtered.

2. **SCXI 1102 module:** The SCXI-1102 is a 32-channel amplifier module designed for measuring thermocouples and other low-bandwidth signals. Each one of the 32 channels includes input protection circuitry to 42 VAC peak and a software-selectable gain of 1 or 100. The SCXI-1102 has lowpass filters with cut-off frequencies of 2 Hz, 200 Hz, and 10 kHz respectively. The SCXI-1102

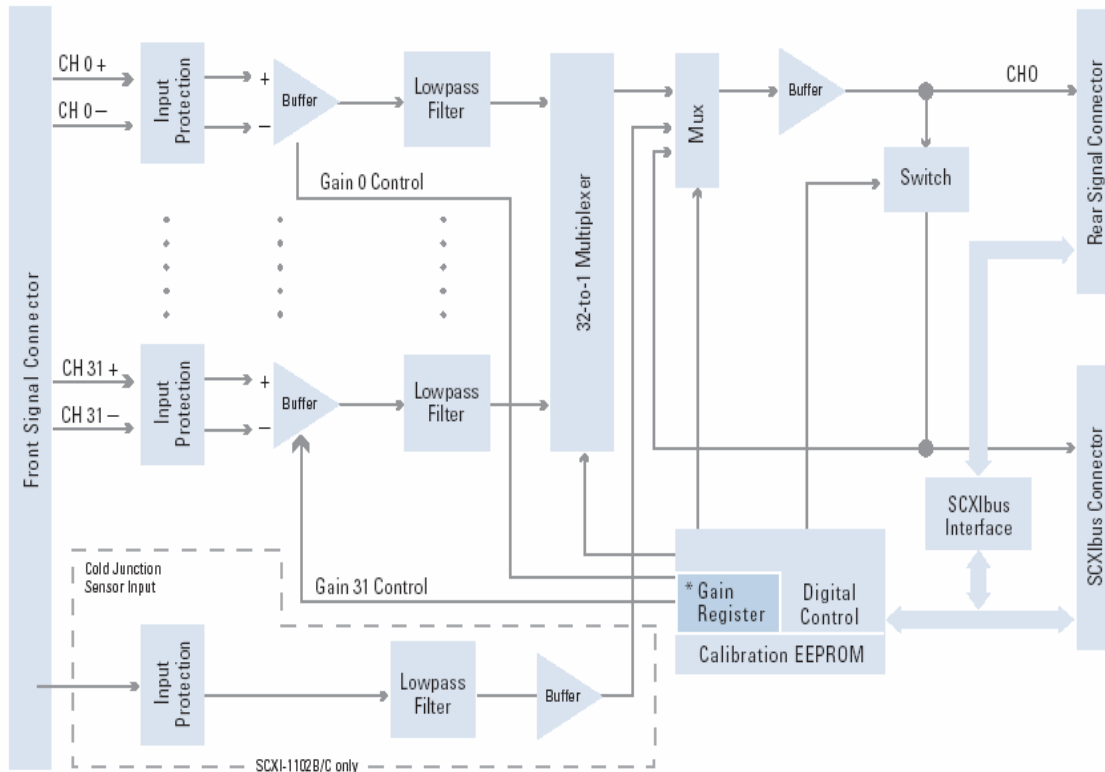


**Figure B-3: Scheme of the input module for rings output acquisition**

works only in multiplexed mode and drives a single analog input channel on the DAQ device (channel 0). The SCXI-1102 is software configurable and contains no jumpers. It is used to acquire rings outputs that are, the signal proportional to the sextupole and decapole fields compensated by the analogical cards, and the monitor signal of the magnet excitation current. The architecture of this module (Fig. B-2), shows that each analog input channel passes through its own programmable gain instrumentation amplifier and lowpass filter before it is multiplexed.

**DAQ acquisition card PCI-6052E:** this acquisition board is based on a 16-bit ADCs with 16 analog inputs, a 16-bit DACs, eight lines of TTL-compatible digital I/O, and two 24-bit counter/timers for timing I/O. His maximum sample rate is 333 kS/s.

## Appendix C- THE DATA ACQUISITION SOFTWARE FOR THE SNAPBACK ANALYZER

The module regarding the acquisition of the output signals of the compensation cards can be seen as a classical software of data acquisition particularly tailored for this application. Fig. C-2 shows the main panel of the acquisition section.

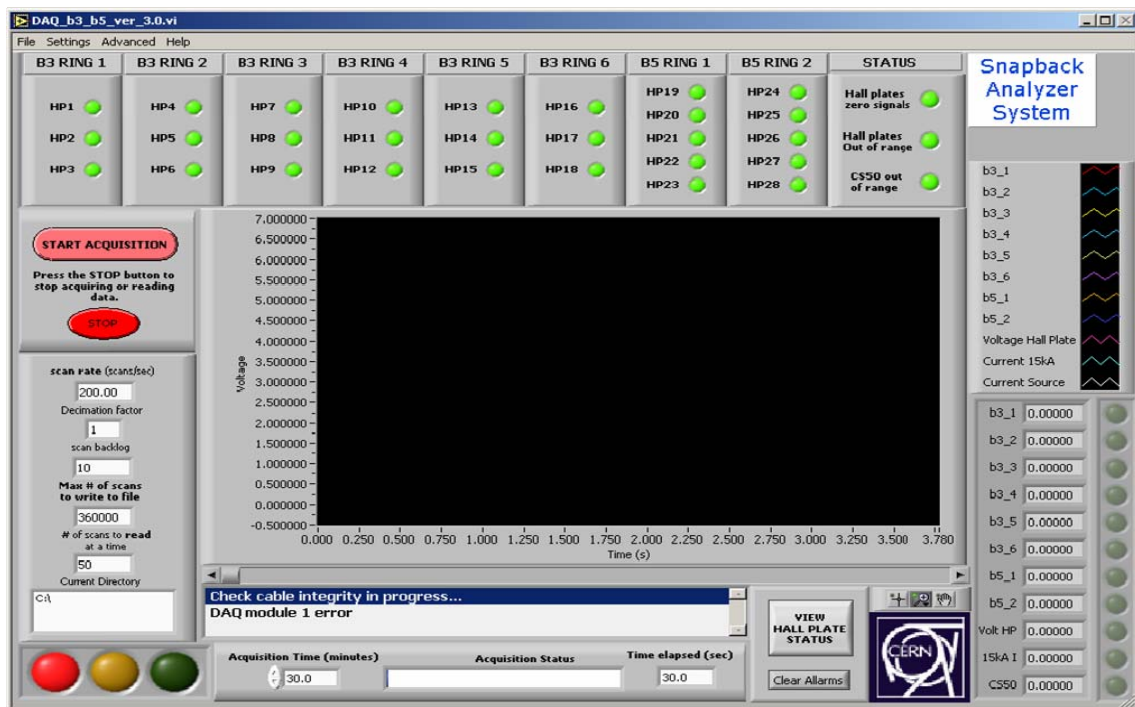


Figure C-2: Snapback Analyzer Main panel.

The main functionalities can be so summarized:

- Data display- The eight hall plates rings signals as well as the magnet excitation current (important to reconstruct the current cycle shape), the current monitor that supplies the 28 hall plates and the voltage measured on the series of the hall plates chain are showed on the main chart for all the measurement length (typically 2000 s) at selectable update rate (typically 10 point/s);
- Data integrity check- The saturation of each b3 or b5 signals is detected on-line and warned by means of specific leds; in particular the status of every single hall plate is verified since all the 28 hall plates voltage are acquired. These are compared with proper thresholds in order to detect situations of zero signal (wires disconnected) or amplitude out of nominal ranges (for instance in case of short circuit between the hall plates supply wires and the output wires). The signals of each hall plates can be displayed in a dedicated monitor chart.

Data Storage- All the data acquired (the b3, b5 signals as well as the 28 signals coming from each hall plates) are logged on file at 10 Hz sampling frequency. To reduce the signal noise after the acquisition a decimation is carried out. The oversampling factor can be set up to 200.

- Acquisition Parameters Setting- All the main acquisition parameters (e.g. oversampling factors, measurement duration, monitor channel limits) are completely selectable by the user. In particular the gain of each single channel is managed through a configuration file.
- Cable checking- Before starting the acquisition this procedure makes a fast check of each hall plate channel as well as the current source channel, with the probe put in a no field zone. The voltage signals should be zero, unless short circuits between the cable strands (i.e. between the hall plate output and the supplying strands).
- Probe alignment- A particular procedure using the tilt sensor guides the operator in the alignment of the measurement probe respect to the gravity

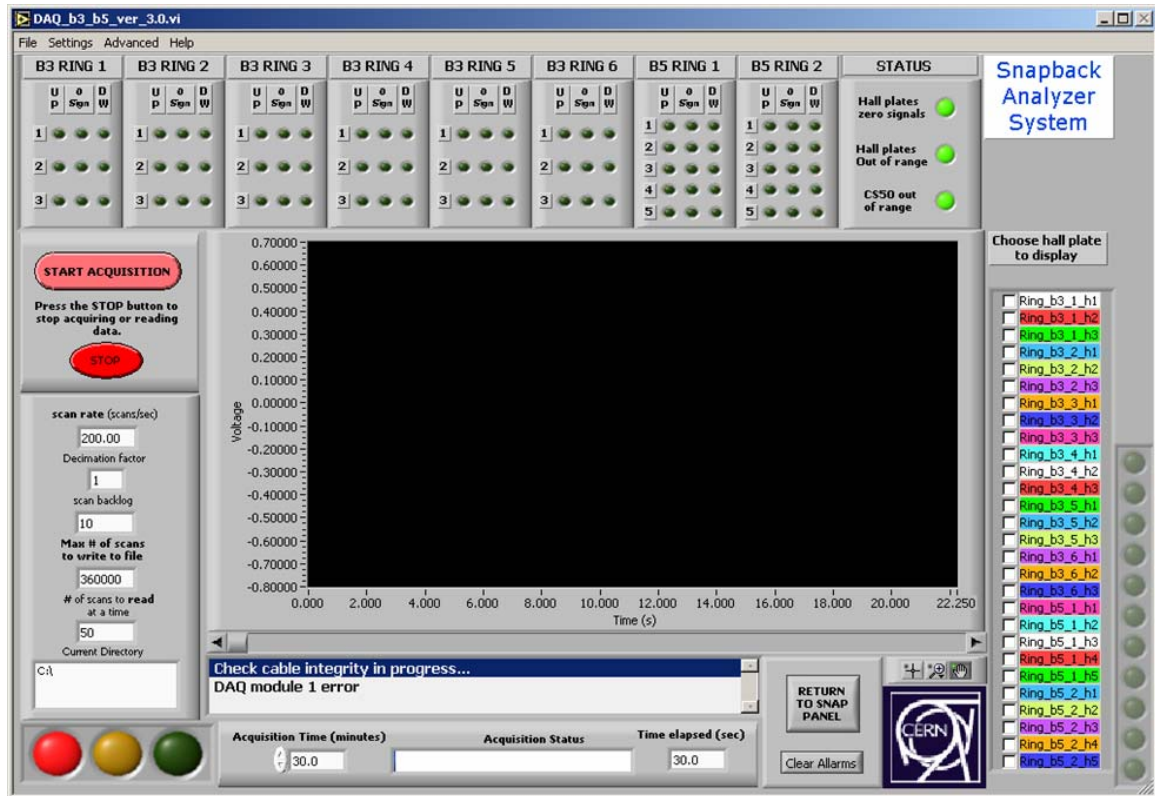


Figure C-1: Hall plates monitor panel.

## **Appendix D- CORRESPONDENCE BETWEEN DFT COEFFICIENTS AND MULTIPOLES EXPANSION COEFFICIENTS**

The relation between the normal component of the field  $Br(R_{mis}, \theta)$  in the hall plate centre and, the field  $B$  in the same point:

$$Br(\theta) = \text{Im}(Be^{i\theta}) \quad (\text{Eq. D-1})$$

This is a periodic function of the angular position  $\theta$  (with period  $2\pi$ ) and then can be expanded in Fourier series as follows:

$$Br(\theta) = \sum_{m=-\infty}^{\infty} \Delta_m e^{im\theta} \quad (\text{Eq. D-2})$$

where the complex quantities  $\Delta_m$  are the Fourier coefficients of the expansion, and are obtained by projection of the function  $Br(\theta)$  on the basis of the expansion:

$$\Delta_m = \frac{1}{2\pi} \int_0^{2\pi} Br(\theta) e^{-im\theta} d\theta \quad (\text{Eq. D-3})$$

Keeping in mind the expression Eq. D-3 of the multipoles expansion of the magnetic field:

$$Br(\theta) = \text{Im} \left[ \sum_{n=1}^{\infty} C_n \left( \frac{R_{mis}}{R_{ref}} \right)^{n-1} e^{in\theta} \right] \quad (\text{Eq. D-4})$$

and therefore the Fourier coefficients are:

$$\begin{aligned}\Delta_m &= \frac{1}{2\pi} \int_0^{2\pi} Br(\theta) e^{-im\theta} d\theta = \\ &= \frac{1}{2\pi} \int_0^{2\pi} \mathbf{Im} \left[ \sum_{n=1}^{\infty} \mathbf{C}_n \left( \frac{R_{mis}}{R_{ref}} \right)^{n-1} e^{in\theta} \right] e^{-im\theta} d\theta\end{aligned}\tag{Eq. D-5}$$

Because of the operators of integration, summation and imaginary part are linear it is allowed to exchange their orders as follows:

$$\Delta_m = \frac{1}{2\pi} \sum_{n=1}^{\infty} \left\{ \int_0^{2\pi} \mathbf{Im} \left[ \mathbf{C}_n e^{in\theta} \left( \frac{R_{mis}}{R_{ref}} \right)^{n-1} \right] e^{-im\theta} d\theta \right\}\tag{Eq. D-6}$$

Evaluating the imaginary part of the term in square brackets and decomposing all complex exponential functions in their harmonic functions components it results:

$$\begin{aligned}\Delta_m &= \frac{1}{2\pi} \sum_{n=1}^{\infty} \int_0^{2\pi} \left\{ \mathbf{Im} \left[ \mathbf{C}_n \left( \frac{R_{mis}}{R_{ref}} \right)^{n-1} \right] \cos(n\theta) \cos(m\theta) \right. \\ &\quad - i \mathbf{Im} \left[ \mathbf{C}_n \left( \frac{R_{mis}}{R_{ref}} \right)^{n-1} \right] \cos(n\theta) \sin(m\theta) \\ &\quad + \mathbf{Re} \left[ \mathbf{C}_n \left( \frac{R_{mis}}{R_{ref}} \right)^{n-1} \right] \sin(n\theta) \cos(m\theta) \\ &\quad \left. - i \mathbf{Re} \left[ \mathbf{C}_n \left( \frac{R_{mis}}{R_{ref}} \right)^{n-1} \right] \sin(n\theta) \sin(m\theta) \right\} d\theta\end{aligned}\tag{Eq. D-7}$$

Let remember the following properties of the harmonic functions:

$$\begin{aligned}\int_0^{2\pi} \cos(n\theta) \cos(m\theta) d\theta &= \pi \delta_{n|m|} \\ \int_0^{2\pi} \sin(n\theta) \sin(m\theta) d\theta &= \begin{cases} \pi \delta_{n|m|} & \text{for } m > 0 \\ -\pi \delta_{n|m|} & \text{for } m < 0 \end{cases} \\ \int_0^{2\pi} \cos(n\theta) \sin(m\theta) d\theta &= 0 \\ \int_0^{2\pi} \sin(n\theta) \cos(m\theta) d\theta &= 0\end{aligned}\tag{Eq. D-8}$$

where  $\delta_{ij}$  is the Kronecker delta function. In its definition we have taken into account the fact that while  $n$  is non-zero and always positive,  $m$  can span the positive and negative integer sets. Using the properties Eq. D-8 into Eq. D-7 we finally obtain that:

$$\Delta_m = \begin{cases} \frac{1}{2} \left( \text{Im} \left[ \mathbf{C}_m \left( \frac{R_{mis}}{R_{ref}} \right)^{m-1} \right] - i \text{Re} \left[ \mathbf{C}_m \left( \frac{R_{mis}}{R_{ref}} \right)^{m-1} \right] \right) & \text{for } m > 0 \\ \frac{1}{2} \left( \text{Im} \left[ \mathbf{C}_{|m|} \left( \frac{R_{mis}}{R_{ref}} \right)^{|m|-1} \right] + i \text{Re} \left[ \mathbf{C}_{|m|} \left( \frac{R_{mis}}{R_{ref}} \right)^{|m|-1} \right] \right) & \text{for } m < 0 \end{cases} \quad (\text{Eq. D-9})$$

that leads finally to the following result:

$$\Delta_m = \begin{cases} \frac{1}{2} \left( \frac{R_{mis}}{R_{ref}} \right)^{m-1} [\mathbf{Im}(\mathbf{C}_m) - i \mathbf{Re}(\mathbf{C}_m)] & \text{for } m > 0 \\ \frac{1}{2} \left( \frac{R_{mis}}{R_{ref}} \right)^{|m|-1} [\mathbf{Im}(\mathbf{C}_{|m|}) + i \mathbf{Re}(\mathbf{C}_{|m|})] & \text{for } m < 0 \end{cases} \quad (\text{Eq. D-10})$$

The equation (A1.10) shows clearly that the spectrum of Fourier coefficients of the real function  $Br(\theta)$  has symmetric real part and anti-symmetric imaginary part. As common practice in signal analysis theory, half of the spectrum amplitude is contained in the *positive* frequencies semi-axis (positive values of  $m$ ), and the other half is in the *negative* frequencies semi-axis (negative values of  $m$ ). Only one half of the spectrum is sufficient to describe the expansion completely, and therefore it's possible to write:

$$\begin{cases} \mathbf{Im}(\mathbf{C}_m) = A_m = 2 \left( \frac{R_{ref}}{R_{mis}} \right)^{m-1} \mathbf{Re}(\Delta_m) \\ \mathbf{Re}(\mathbf{C}_m) = B_m = -2 \left( \frac{R_{ref}}{R_{mis}} \right)^{m-1} \mathbf{Im}(\Delta_m) \end{cases} \quad (\text{Eq. D-11})$$

$m = 1 \dots \infty$

The considerations above are valid for a continuous, periodic signal  $Br(\theta)$ . In our case however we are dealing with a regularly spaced, discrete sample of this periodic signal. It is therefore necessary to introduce a further relation.

Let be  $N$  the resolution used in the sampling and  $\Delta\theta = \frac{2\pi}{N}$  the sampling period, from the

(A1.2) the sampled value are given by:

$$Br(n\Delta\theta) = \sum_{m=-\infty}^{\infty} \Delta_m e^{imn\frac{2\pi}{N}} = \sum_{m=-\infty}^{\infty} \Delta_m W_N^{mn} \quad (\text{Eq. D-12})$$

where  $W_N = e^{i\frac{2\pi}{N}}$ , and  $n=0, \dots, N-1$  obviously.

Now the integer m can be written as a sum:

$$m=k+rN \quad \text{with } k=0,\dots,N-1 \quad \text{and } r=\dots,-1,0,1,\dots$$

then, since  $W_N^N = 1$

$$W_N^{mn} = W_N^{(k+rN)n} = W_N^{kn}$$

Therefore the Eq. D-12 becomes:

$$Br(n\Delta\theta) = \sum_{k=0}^{N-1} \sum_{r=-\infty}^{\infty} \Delta_{k+rN} W_N^{kn} \quad (\text{Eq. D-13})$$

Defining the ‘‘aliased’’ coefficients  $\bar{\Delta}_k$  by:

$$\bar{\Delta}_k = \sum_{r=-\infty}^{\infty} \Delta_{k+rN} \quad (\text{Eq. D-14})$$

We obtain

$$Br(n\Delta\theta) = \sum_{k=0}^{N-1} \bar{\Delta}_k W_N^{kn} \quad n=0,\dots,N-1 \quad (\text{Eq. D-15})$$

The expression at the second member of the Eq. D-15 is, except for the factor N, the IDFT of the sequence  $\bar{\Delta}_k$ . Being this transformation bidirectional:

$$\bar{\Delta}_k = \frac{1}{N} \sum_{n=0}^{N-1} Br(n\Delta\theta) W_N^{-kn} = \sum_{m=-\infty}^{\infty} \Delta_m e^{-imn\frac{2\pi}{N}} \quad k=0,\dots,N-1 \quad (\text{Eq. D-16})$$

In other words:

$$\bar{\Delta}_k = \frac{1}{N} \mathbf{Br}_k \quad k=0,\dots,N-1 \quad (\text{Eq. D-17})$$

where  $\mathbf{Br}_k$  are the DFT coefficients of the sequence  $Brn$ .

Now it is possible to do the hypothesis that the function  $Br(\theta)$  is a trigonometric polynomial, that is a function with a Fourier series made of a finite number of terms. In fact, in the multipole expansion of the magnetic field  $B(\theta)$  it is usual to consider until the 15<sup>th</sup> harmonic order. Therefore:

$$Br(\theta) = \sum_{m=-M}^M \Delta_m e^{im\theta} \quad (\text{Eq. D-18})$$

with  $M=15$ .

It is also true that:

$$N > 2M + 1$$

in fact as resolution the values 32,64,128 has been used. Then it follows from the definition of  $\bar{\Delta}_k$  that:

$$\Delta_k = \begin{cases} \bar{\Delta}_k & |k| \leq \frac{N}{2} \\ 0 & |k| > \frac{N}{2} \end{cases} \quad (\text{Eq. D-19})$$

In other words in this case the difference  $\Delta_k - \bar{\Delta}_k$ , the aliasing error, is zero. Finally we conclude that:

$$\Delta_k = \frac{1}{N} \mathbf{Br}_k \quad (\text{Eq. D-19})$$

and then:

$$\begin{cases} A_k = \frac{2}{N} \left( \frac{\text{Rref}}{\text{Rmis}} \right)^{k-1} \mathbf{Re}(\mathbf{Br}_k) \\ B_k = -\frac{2}{N} \left( \frac{\text{Rref}}{\text{Rmis}} \right)^{k-1} \mathbf{Im}(\mathbf{Br}_k) \end{cases} \quad (\text{Eq. D-20})$$

with  $k=1, \dots, \frac{N}{2}$  being N even.

And, as previously said,  $\mathbf{Br}_k$  are the FFT (N is chosen power of 2) complex coefficients of the sequence  $Br_n$ . This last one is the vector of the N sampled values of the function  $\text{Br}(\theta)$  with sampling period  $\frac{2\pi}{N}$ .